NOTE TO USERS

This reproduction is the best copy available.

UMI®

UNIVERSITÉ DE SHERBROOKE

AXIAL AND FLEXURAL BEHAVIOUR OF REINFORCED CONCRETE-FILLED FRP TUBES: EXPERIMENTAL AND THEORETICAL STUDIES

By

Hamdy Mahmoud Hamdy Mohamed

A Dissertation

Submitted in Partial Fulfilment of the Requirement for the Degree

Doctor of Philosophy

Specialty: Civil Engineering
Faculty of Engineering
University of Sherbrooke

Jury members:

Radhouane Masmoudi	Advisor	Sami Rizkalla	Examiner
Yixin Shao	Examiner	Richard Gagne	Examiner
Jean Proulx	Reporter	Mourad Karray	President

Sherbrooke, Québec, Canada, March 2010

Library and Archives Canada

Published Heritage Branch

395 Wellington Street
Ottawa ON K1A 0N4
Canada

Bibliothèque et Archives Canada

Direction du Patrimoine de l'édition

395, rue Wellington
Ottawa ON K1A 0N4
Canada

Your file Votre référence
ISBN: 978-0-494-62815-7
Our file Notre référence
ISBN: 978-0-494-62815-7

NOTICE:

The author has granted a non-exclusive license allowing Library and Archives Canada to reproduce, publish, archive, preserve, conserve, communicate to the public by telecommunication or on the Internet, loan, distribute and sell theses worldwide, for commercial or non-commercial purposes, in microform, paper, electronic and/or any other formats.

The author retains copyright ownership and moral rights in this thesis. Neither the thesis nor substantial extracts from it may be printed or otherwise reproduced without the author's permission.

AVIS:

L'auteur a accordé une licence non exclusive permettant à la Bibliothèque et Archives Canada de reproduire, publier, archiver, sauvegarder, conserver, transmettre au public par télécommunication ou par l'Internet, prêter, distribuer et vendre des thèses partout dans le monde, à des fins commerciales ou autres, sur support microforme, papier, électronique et/ou autres formats.

L'auteur conserve la propriété du droit d'auteur et des droits moraux qui protège cette thèse. Ni la thèse ni des extraits substantiels de celle-ci ne doivent être imprimés ou autrement reproduits sans son autorisation.

In compliance with the Canadian Privacy Act some supporting forms may have been removed from this thesis.

While these forms may be included in the document page count, their removal does not represent any loss of content from the thesis.

Conformément à la loi canadienne sur la protection de la vie privée, quelques formulaires secondaires ont été enlevés de cette thèse.

Bien que ces formulaires aient inclus dans la pagination, il n'y aura aucun contenu manquant.

Canada

PUBLICATION DISSERTATION OPTION

This dissertation consists of the following seven articles that have been submitted for publication as follows: The first paper is presented in Chapter 2 and it has been published in the American Concrete Institute (ACI) – Special Publication SP-257-6, pp. 91-109. The second paper is presented in Chapter 3 and it has been accepted for publication in *Journal of Composite for Construction*–American Society of Civil Engineers (ASCE). The third paper is presented in Chapter 4 and it has been accepted for publication in the American Concrete Institute (ACI) – *ACI structural Journal* (MS ID S-2009-225.R2). The fourth and fifth papers present most of contents of chapter 5 and they have been submitted for publication February 2010 in *Journal of Composite for Construction* –American Society of Civil Engineers (ASCE) and *Journal of Engineering Structures*-Elsevier (accepted). Chapter 6 presents the content of the sixth paper that has been published in MESC-5, the fifth Middle East Symposium on structural composites for infrastructure applications, Innovations & Applications, Egypt, 2008. Finally, the seventh paper is included in Chapter 7 that it has been published in American Society for Composites and Canadian Association for Composite Structures and Materials, University of Delaware, Delaware, USA, 2009.

ABSTRACT

Corrosion of steel reinforcement causes continual degradation to the worldwide infrastructures and it has prompted the need for challenges to those involved with reinforced concrete structures. Recently, the use of fibre-reinforced polymers (FRP) tubes as structurally integrated stay-in-place forms for concrete members, such as beams, columns, bridge piers, piles and fender piles has emerged as an innovative solution to the corrosion problem. In such integrated systems, the FRP tubes may act as a permanent form, often as a protective jacket for concrete, and especially as external reinforcement in the primary and secondary directions such as for confinement. Furthermore, the use of concrete-filled FRP tubes (CFFT) technique is predicated on performance attributes linked to their high strength-to-weight ratios, expand the service life of structures, enhance corrosion resistance, and potentially high durability.

This dissertation evaluates the axial and flexural performances of reinforced CFFT through experimental and analytical investigations. The details description and the findings of the investigations are presented through seven articles. To fulfill the objectives of this research, an experimental program has been designed including pure compression tests (33 specimens), axial-eccentric load tests (4 specimens) and pure flexure tests (10 specimens). Experimental investigations of the behaviour of CFFT have generally been carried out without using internal longitudinal reinforcement. The CFFT system of this study consists basically of filament-wound glass FRP tubes filled with concrete and reinforced internally with steel or FRP bars. Five types of new FRP tubes have been used with different thicknesses and two different diameters, 152 and 213 mm.

Pure compression tests have been conducted on 40 specimens with a total height ranging from 305 mm to 1520 mm. One of the main objectives of testing these specimens is to evaluate the design equations of the North American codes and design guidelines to predict the ultimate load capacities of reinforced and unreinforced short CFFT columns. In addition, the effect of three parameters and their interactions on the buckling behaviour were investigated for these specimens; namely, the FRP tube thickness, concrete compressive strength, and slenderness ratio. The effect of eccentric load on the behaviour of four CFFT

specimens of diameters 152mm and long 912mm, has been evaluated using four different eccentricity values (15, 30, 45 and 60 mm).

Based on the finding of experimental and theoretical investigation for the CFFT columns, a new confinement model is proposed for the confined concrete compressive strength of the CFFT cylinders. Also, the design equations are modified to accurately predict the ultimate and yield loads capacities of internally reinforced and unreinforced short CFFT columns. In addition, the theoretical analysis was utilized to correlate the slenderness ratio of the CFFT columns to various material characteristics and geometric properties of the FRP tubes and concrete. It was found that a slenderness ratio of 12 gave a safe value for the design purposes. However a more precise formula for the slenderness ratio was proposed to control the buckling mode of failure.

Pure flexural tests have been conducted on 10 RCFFT and RC beams of a total length 2000 mm with constant diameter 213 mm. The test variables were the type of internal reinforcements (steel or GFRP bars), the FRP tube thickness, concrete compressive strength and the type of transverse reinforcements (spiral steel or FRP tubes). The influence of the considered variables on the flexural behaviour of the tested RCFFT beams is presented. A simplified analytical method is developed to predict the yield and resisting moments corresponding to the failure modes of the tested RCFFT beams. The analysis was conducted according to the equations derived from linear elastic analysis. This analysis was found to be acceptable for predicting the ultimate and yield moments capacities of the FRP or steel-RCFFT beams. In addition, an analytical investigation to examine the validity of the available design provisions for predicting the load-deflection response of CFFT is conducted. The effective moments of inertia of the tested beams are analyzed using the different available code, manuals and design guidelines equations. The results of the analysis are compared with the experimental values. It has been found that the predicted tension stiffening for steel or FRP-RCFFT beams using the conventional equations (steel or FRP-RC member) is underestimated and hence the predicted deflections are overestimated. Based on the experimental data obtained in this study, new proposed equations and a modified expression for the effective moment of inertia of a simply supported CFFT beams reinforced with steel or GFRP bars are introduced.

During the course of the research work, the candidate has participated in the following related papers and reports that have been published:

Journal Papers

1. Masmoudi, R., **Mohamed, H** and Metiche. S, (2008) "Finite Element Modeling For Deflection and Bending Responses of GFRP Poles" Journal of Reinforced Plastics and Composites, Vol. 27, No. 6, pp. 639-658.

Refereed Conference Publications:

2. **Mohamed, H.**, and Masmoudi, R. (2009) "Design Optimization of GFRP Pole Structures Using Finite Element Analysis" COMPOSITES & POLYCON 2009, American Composites Manufacturers Association, proceedings on CD-Rom, January 15-17, Tampa, FL, USA, 10p.
3. **Mohamed, H.**, Abou Hashish, A., Moussa, A., Masmoudi, R., and Salama, A. (2008) "Punching Shear Behavior Of Prestressed Flat Slabs" CSCE 2008 Annual General Meeting, proceedings on CD-Rom, Québec, QC, Canada, 10 to 13 Jun, 10p.
4. **Mohamed, H.**, and Masmoudi, R. (2007) "Behavioral Characteristics for FRP Composites Pole Structures: Nonlinear Finite Element Analysis" CSCE 2007 Annual General Meeting,Yellowknife, Northwest Territories, Canada, June 6-9, 10p.
5. Masmoudi, R., and **Mohamed, H**. (2006) "Finite Element Modeling of FRP-Filament Winded Poles" Third International Conference on FRP Composites in Civil Engineering (CICE 2006), proceedings on CD-Rom, December 13-15, Miami, Florida, USA, 4p.

Technical Reports

6. Masmoudi, R., Patrick Girard, **Mohamed, H.**, Metiche S., "Développement des règles de calcul pour la conception de nouveaux poteaux de distribution en matériaux composites", Rapport technique no. 07-2, soumis à Hydro-Québec Distribution, Département de génie civil, Université de Sherbrooke, 148p. 2007.
7. **Mohamed, H.**, and Masmoudi, R. "Finite Element Analysis of FRP-PVHO Chamber" technical report, submitted to HEMATO MAX inc., 1838 pie-IX, Montreal, Qc, H1V 2C6, Département de génie civil, Université de Sherbrooke, 32p. 2007.
8. **Mohamed, H.**, and Masmoudi, R. "Finite Element Analysis For 20 ft GFRP Poles Under Pressure Load" technical report, submitted to FRE Composites inc., 75 Wales Street, St-Andre-d'Argenteuil (Quebec) Canada J0V 1X0, Département de génie civil, Université de Sherbrooke, 30p. 2007.

Also the candidate has participated in the following publications during his doctorate study at the University of Sherbrooke:

Journal Papers

9. **Mohamed, H.**, and Masmoudi, R. (2010) "Axial Load Capacity of Reinforced Concrete-Filled FRP Tubes Columns: Experimental versus Theoretical Predictions" *Journal of Composites for Construction*, ASCE, Vol. 14, No. 2, pp. 1-13.
10. **Mohamed, H.**, and Masmoudi, R. (2008) "Compressive Behaviour of Reinforced Concrete Filled FRP Tubes" *ACI Special Publications* (SP), SP-257-6, pp. 91-109.
11. **Mohamed, H.**, Abdel Baky, H.M., and Masmoudi, R. Nonlinear Stability Analysis of CFFT Columns: Experimental and Theoretical Investigations. Accepted for publication at *ACI Structural Journal* (S-2009-225.R2).
12. **Mohamed, H.**, and Masmoudi, R. "Deflection Prediction of Steel and FRP-Reinforced Concrete-Filled FRP Tubes Beams: Experimental and Theoretical Investigations."*Journal of Composite for Construction*, ASCE (submitted at February 2010)
13. **Mohamed, H.**, and Masmoudi, R. Flexural strength and behaviour of Steel and FRP-Reinforced Concrete-Filled FRP Tubes Beams. Accepted for publication at *Journal of Engineering Structures*-Elsevier (ENGSTRUCT-D-10-00180).
14. **Mohamed, H.**, and Masmoudi, R. "Moment-Interaction Diagram of Concrete Filled FRP Tubes Columns: Experimental and Theoretical Investigation." *Journal of Engineering Structures*, Elsevier, (to be submitted at April 2010).

Refereed Conference Publications:

15. **Mohamed, H.**, El Zefzafy, H., and Masmoudi, R. (2010) "Review of ACI 440.2R Design Method for Strength and Axial Load Capacity of Concrete Filled-FRP Tubes Columns" CSCE 2010 Annual General Meeting, proceedings on CD-Rom, Winnipeg, Manitoba, Canada, 9 to 12 Jun, 10p.
16. **Mohamed, H.**, El Zefzafy, H., and Masmoudi, R. (2010) "Experimental Investigation on the Behaviour of Concrete-Filled FRP Tubes under Flexural Load" CSCE 2010 Annual General Meeting, Winnipeg, Manitoba, Canada, 9 to 12 Jun, 10p.
17. **Mohamed, H.**, and Masmoudi, R. (2009) "Assessment of Confinement Models for Concrete Confined with FRP Tubes" American Society for Composites and Canadian Association for Composite Structures and Materials, proceedings on CD-Rom, September 15 to 17, University of Delaware in Newark, Delaware, USA.
18. **Mohamed, H.**, and Masmoudi, R. (2009) "Behavior of FRP Tubes-Encased Concrete Columns under Concentric and Eccentric Loads" COMPOSITES & POLYCON 2009, American Composites Manufacturers Association, proceedings on CD-Rom, January 15-17, Tampa, FL, USA, 10p.
19. **Mohamed, H.**, and Masmoudi, R. (2009) "Strength and Ductility of CFFT Beams Reinforced with Steel / GFRP Rebars" 9th International Symposium on Fiber

Reinforced Polymer Reinforcement for Concrete Structures, proceedings on CD-Rom, Sydney, Australia, Monday 13 – Wednesday 15 July, 4p.

20. **Mohamed, H.**, and Masmoudi, R. (2009) "Experimental Versus Guidelines Prediction Values for Load Capacity of the Concrete Columns Confined by Fiber-Reinforced Polymer Tubes" 9th International Symposium on Fiber Reinforced Polymer Reinforcement for Concrete Structures, proceedings on CD-Rom, Sydney, Australia, Monday 13 –Wednesday 15 July, 4p.
21. **Mohmed, H.**, and Masmoudi, R. (2008) "Experimental Study for the Slenderness Ratio of the Axially Loaded CFFT Columns" Fourth International Conference on FRP Composites in Civil Engineering (CICE2008), proceedings on CD-Rom, 22-24 July 2008, Zurich, Switzerland, 6p.
22. **Mohamed, H.**, and Masmoudi, R. (2008) "Compressive Behaviour of Filament Winded GFRP Tube-Encased Concrete Columns" Fourth International Conference on FRP Composites in Civil Engineering (CICE2008), proceedings on CD-Rom, 22-24 July 2008, Zurich, Switzerland, 6p.
23. **Mohamed, H.**, and Masmoudi, R. (2008) "Characteristic Behaviors of GFRP Tube-Encased Concrete Columns" CSCE 2008 Annual General Meeting, proceedings on CD-Rom, Québec, QC, Canada, 10 to 13 Jun, 10p.
24. **Mohamed, H.**, and Masmoudi, R. (2008) "Behaviour Concrete Filled GFRP Tube Columns under Eccentric Loading" MESC-5, the fifth Middle East Symposium on structural composites for infrastructure applications 2008. Innovations &Applications, proceedings on CD-Rom, Hurghada, Egypt 23-25th May 2008, 10p.
25. **Mohamed, H.**, El Zefzafy, H., and Masmoudi, R. (2008) "Effect of columns parameters on the slenderness ratio of the axially loaded CFFT columns" ACMBS-V, the Fifth International Conference on Advanced Composite Materials for Bridges and Structures, proceedings on CD-Rom, Winnipeg, Canada, 10p.

HONOURS AND AWARDS

The candidate has been received the following honours and awards during his doctorate study at the University of Sherbrooke:

1. La médaille du mérite de la Faculté de génie (Médaille Leonardo de Vinci), Université de Sherbrooke, 2009.
2. Bourse du vice-doyen de la Faculté de génie, Université de Sherbrooke, 2009.
3. Award for one of the top 5 papers, American Composites Manufacturers Association, in ACMA Jan 2009.
4. La bourse Ingénieurs-professeurs de la Faculté de genie, Université de Sherbrooke, 2008.
5. Bourse institutionnelle, Université de Sherbrooke, QC, 2007.
6. Bourse institutionnelle, Université de Sherbrooke, QC, 2006.

RÉSUMÉ

Comportements axial et en flexion de tubes en matériaux composites remplis de béton armé : des études expérimentales et théoriques

Les infrastructures au monde entier ont connu des dégradations majeures à cause de la corrosion des barres d'acier. Ce problème représente un vrai défi pour ceux intéressés aux structures en béton armé. Récemment, l'utilisation des tubes en polymères renforcés de fibres (PRF) en tant que d'éléments structuraux en béton tels que les poutres, les colonnes, les piliers de ponts, les pieux et les pieux de défense, est devenu comme une solution innovatrice au problème de la corrosion. Dans tels systèmes intégrés, les tubes en PRF peuvent fonctionner comme une forme permanente, souvent comme une veste de protection pour le béton, et particulièrement comme renforcement externe dans les directions principales et secondaires tel que le confinement. En outre, l'utilisation de la technique des tubes en PRF remplis de béton (CFFT) est fondée sur les attributs de performances liés à leur rapport élevé de résistance au poids, elle augmente la durabilité des structures et leur durée de vie, et améliore la résistance à la corrosion.

L'objectif de cette thèse est d'évaluer les performances axiales et en flexion des tubes CFFT à travers les études expérimentales et analytiques. La description détaillée de ces études est présentée dans 7 articles publiés. Pour réaliser l'objectif de cette recherche, un programme expérimental a été élaboré incluant les essais de compression (33 échantillons), les essais de charges axiales et excentriques (4 échantillons) et les essais de flexion pure (10 échantillons). Les études expérimentales du comportement des tubes CFFT ont été réalisées sans l'utilisation des armatures longitudinale internes. Dans cette étude, le système des tubes CFFT est essentiellement composé de tubes en PRF remplis du béton armé de barres d'acier

ou de PRF. Cinq nouveaux types de tubes en PRF ont été utilisés avec différentes épaisseurs et deux différents diamètres (152 mm et 213 mm).

Les essais de compression pure ont été effectués sur 33 échantillons avec une hauteur totale variant de 305 à 1520 mm. L'une des objectifs principaux de ces essais de compression est d'évaluer les équations de conception des codes Nord-Américain et des guides de conception pour prédire la capacité des charges ultimes des colonnes courtes en PRF remplies du béton qu'il soit armé ou non armé. D'autre part, l'effet des trois paramètres (l'épaisseur des tubes en PRF, la résistance à la compression du béton et le taux d'élancement) et leurs interactions sur le comportement au flambement ont été examinés pour ces 33 échantillons. L'effet des charges excentriques sur le comportement des 4 échantillons de tubes CFFT de 152 mm de diamètre et de 912 mm de longueur, a été évalué en utilisant 4 différentes valeurs d'excentricité (15, 30, 45 et 60 mm).

Sur la base des résultats obtenus à partir de l'étude expérimentale et théorique effectuées sur les colonnes CFFT, un nouveau modèle de confinement est proposé pour la résistance à la compression du béton confiné de cylindres en PRF. Aussi, les équations de conception sont modifiées pour prédire avec précision les capacités de charges ultimes et limites pour les colonnes courtes intérieurement armées ou non armées. De plus, l'analyse théorique a été utilisée pour corréler le taux d'élancement des colonnes CFFT aux diverses caractéristiques des matériaux et propriétés géométriques des tubes en PRF et du béton. On a trouvé qu'un taux d'élancement de 12 a donné une valeur sécuritaire pour la conception de ces colonnes. Cependant, une formule plus précise pour le taux d'élancement a été proposée pour contrôler le mode de rupture par flambement.

Les essais de flexion ont été effectués sur un total de 10 échantillons constitués de tubes en PRF remplis du béton armé et des poutres en béton armé de 2000 mm de longueur et de 213 mm de diamètre constant. Les variables d'essais étaient le type de renforcements internes (barres d'acier ou de PRF de verre), l'épaisseur des tubes en PRF, la résistance à la compression du béton, et les renforcements transversales (acier spiral ou tubes en PRF). L'influence de ces variables sur le comportement de flexion des poutres CFFT testées est présentée. Une méthode d'analyse simplifiée est développée pour prédire les valeurs des moments résistants et des moments limites correspondantes au mode de rupture pour ces poutres testées. L'analyse est faite selon les équations déduites de l'analyse élastique linéaire.

Cette analyse est acceptable pour prédire les capacités des moments ultimes et limites des poutres CFFT renforcées en PRF ou en acier. D'autre part, une étude analytique est effectuée pour examiner la validité des dispositions de conception pour prédire la réponse charge - déflection des CFFT. Les moments d'inertie efficace des poutres testées sont analysés en utilisant les différentes équations existantes des codes, manuels et guides de conception. Les résultats de cette analyse sont comparés avec les valeurs expérimentales obtenues. Il a été constaté que la raideur en tension prédite en utilisant les équations conventionnelles pour les poutres CFFT renforcées en PRF ou en acier est sous-estimé et par conséquent les valeurs de déflection prédites sont sur-estimées. Des nouvelles équations proposées et des expressions modifiées validées par les résultats expérimentaux obtenus sont introduites pour l'évaluation du moment d'inertie efficace des poutres CFFT renforcées avec des barres d'acier ou de PRF de verre.

Mots-clés : axial, flexion, tubes, matériaux composites, béton armé, expérimentales et analytiques.

ACKNOWLEDGEMENTS

All Praise be to Allah Almighty and Peace be upon His Prophet Mohammed.

I would like to express my sincere and deepest gratitude to my supervisor, Prof. Radhouane Masmoudi, for his unwavering support and guidance throughout this research project. His patience, leadership, and never ending encouragement gave me the confidence to focus and proceed. I owe him an unbelievable amount of gratitude for his prominent role in helping me to achieve one of the greatest accomplishments in my life.

I would like to thank the structural laboratory technical staff in the Department of Civil Engineering at the Université de Sherbrooke, in particular Mr. Nicolas Simard for his help in my experimental work. Special thanks to the manufacturer (FRE Composites, Saint-André d'Argenteuil, QC, Canada) for providing the FRP Tubes.

Also, we are thankful to The Natural Sciences and Engineering Research Council of Canada (NSERC) for supporting this research and to the Canadian Foundation for Innovation (CFI) for the infrastructure used to conduct testing, which without such infrastructure, this research work could not be possible.

Many thanks also go to all my colleagues and friends at the Université de Sherbrooke. Their friendliness streamlined and supported my studies and life style during the period of my doctoral studies.

I would like to express my deep appreciation and thanks to my brothers and sisters from the bottom of my heart for their support, endless love and encouragement. Special thanks are due my mother, for her prayers, encouragement and endless love. The spiritual support of all of them cannot be praised enough. Finally, I would like to mark my deep love and appreciation to my wife for her steadfast support throughout these years. She was always there to give me the push for this challenge. I cannot present this work without expressing my love to my son Mahmoud and my daughter Razan who enlightened my life with their smile; to them this thesis is dedicated.

Dedication

To the memory of my father

To the memory of my friend Gomaa Shaban

To my mother who taught me faith and love

To my brothers and my sisters

To my wife, my son and my daughter

To those who work hard to make the world a better place to live in

Table of Contents

ABSTRACT iii

RÉSUMÉ viii

ACKNOWLEDGEMENTS xi

Table of Contents xiii

List of Tables xx

List of Figures xxi

Chapter 1 Introduction 1

1.1 Introduction 1

1.2 Objectives and Originality 6

1.3 Methodology 8

1.4 Organization of the Dissertation 10

Chapter 2 Compressive Behavior of Reinforced Concrete Filled FRPTubes 13

2.1 Synopsis 13

2.2 Introduction 14

2.3 Research Significance 15

2.4 Experimental Program 16

2.4.1 Materials 16

2.4.1.1 FRP tubes 16

2.4.1.2 Concrete mixtures 19
2.4.2 Test specimens and parameters 19
2.4.3 Instrumentation and test setup 22
2.5 Experimental Results and Discussion 24
2.5.1 Behavior of CFFT cylinders 25
2.5.1.1 Failure mode 25
2.5.1.2 Axial stress_strain relationship 26
2.5.1.3 Compressive strength: 27
2.5.1.4 Dilation properties 27
2.5.2 Behavior of CFFT Columns 28
2.5.2.1 Failure modes 28
2.5.2.2 Axial stress-strain relationship 30
2.5.2.3 Compressive strength 32
2.5.2.4 Axial displacement 33
2.5.2.5 Lateral displacement 34
2.5.2.6 Confinement effect on the load-strain relationship of steel reinforcement 36
2.5.2.7 Dilation properties 37
2.6 Conclusions 39

Chapter 3 Axial Load Capacity of Concrete-Filled FRP Tubes Columns: Experimental versus Theoretical Predictions 41

3.1 Abstract 41
3.2 Introduction 42
3.3 Objectives 43
3.4 Experimental Program 44
3.4.1 Properties of materials 44

3.4.2 Specimen preparation 46
3.4.3 Instrumentation and test setup 47
3.5 Experimental Results 48
3.5.1 Stress–axial and hoop strains behavior 48
3.5.2 Failure modes 50
3.6 Theoretical Predictions of the Axial Load Carrying Capacity 55
3.6.1 Review of codes and design guidelines 55
3.6.2 ACI 440.2R-08 guide for the design and construction of externally bonded FRP systems 56
3.6.3 Canadian Standard Association CAN/CSA-S6-06-Canadian Highway Bridge Design Code 57
3.6.4 Canadian Standard Association CAN/CSA-S806-02-Building Code 58
3.6.5 Theoretical versus experimental confined concrete compressive strength 58
3.6.6 Proposed confinement model for CFFT 60
3.6.7 Predicted versus experimental values of the axial load carrying capacity 63
3.6.8 Modified equations for the axial load resistance of the CFFT columns 68
3.7 Conclusions 73

Chapter 4 Nonlinear Stability Analysis of Concrete Filled FRP-Tubes Columns: Experimental and Theoretical Investigation.....75

4.1 Abstract.....75
4.2 Introduction and Background 76
4.3 Research Significance 77
4.4 Experimental Program 78
4.4.1 Materials 78
4.4.2 Test specimens 79
4.4.3 Instrumentations and test set-up 81
4.5 Test Results and Discussion 83
4.5.1 Failure modes 83
4.5.2 Ultimate load carrying capacity and slenderness ratio effect 84

4.5.3 Load-deformation characteristics of CFFT columns 88
4.5.4 Effect of concrete compressive strength and FRP tube thickness 93
4.6 Theoretical Investigation 95
4.6.1 Buckling loads 96
4.6.2 CFFT columns strength curve 99
4.6.3 Design example 101
4.7 Conclusions 103

Chapter 5 Flexural Behaviour of Reinforced CFFT Beams 104
5.1 Abstract 104
5.2 Introduction and Background 105
5.3 Experimental Program 111
5.3.1 Materials 111
5.3.1.1 Concrete 111
5.3.1.2 Reinforcing steel 112
5.3.1.3 FRP bars 112
5.3.1.4 FRP tubes 114
5.3.1.5 Mechanical properties of the FRP tubes 116
5.3.1.5.1 Axial tension test 116
5.3.1.5.2 Axial compression test 118
5.3.2 Test specimens 120
5.3.3 Fabrication of specimens 122
5.3.4 Instrumentation 124
5.3.5 Test setup 126
5.4 Test Results and Discussions 129
5.4.1 General behaviour 129
5.4.2 Cracking and yield loads 129
5.4.3 Load-deflection response 133
5.4.4 Load-strain relationships 142

5.4.4.1 The flexural longitudinal compression and tension strains 142
5.4.4.2 The flexural hoop strain response 147
5.4.4.3 The shear strain rosette response 148
5.4.5 Failure modes and crack patterns 153
5.5 Effect of Test Parameters on Flexural Strength and Ductility 164
5.5.1 Effect of type of transverse reinforcement 164
5.5.2 Effect of type of longitudinal reinforcing bars 166
5.5.3 Effect of reinforcement ratio of FRP tubes 166
5.5.4 Effect of concrete compressive strength 169
5.6 Theoretical Analysis 171
5.6.1 Cracking moment of RCFFT beams 172
5.6.2 Theoretical development for yield and ultimate moment of test RCFFT beams 175
5.6.3 Defection calculation of steel and FRP-RCFFT beams 186
5.6.3.1 Review of deflection formulas for steel and FRP-RC members 187
5.6.3.2 Evaluation of moment of inertia equations for deflection prediction of RCFFT beams 191
5.6.3.3 Modified Branson's equation for steel-RCFFT beams 192
5.6.3.4 Modified Branson's equation for FRP-RCFFT beams 194
5.6.3.5 Proposed equation for FRP-RCFFT beams 198
5.6.3.6 Experimental verification of the modified and proposed equations 198
5.7 Conclusions 203

Chapter 6 Behavior of Concrete-Filled FRP Tubes Columns under Eccentric Loads 205

6.1 Abstract 205
6.2 Introduction 206
6.3 Experimental Program 207

6.3.1 Materials 207
6.3.1.1 GFRP tubes 207
6.3.1.2 Concrete 207
6.3.2 Reinforcing steel 209
6.3.3 Test matrix and specimen preparation 210
6.3.4 Test setup 212
6.4 Test Results and Discussion 214
6.4.1 Axial and lateral strain behaviour 214
6.4.2 Load–strain relationship of internal reinforcements 215
6.4.3 Axial and horizontal deformation 218
6.4.4 Failure modes 221
6.4.5 Interaction diagram 224
6.5 CONCLUSIONS 226

Chapter 7 Assessment of Confinement Models for Concrete Confined with FRP Tubes 227

7.1 Abstract 227
7.2 Introduction 228
7.3 Review of Strength Models of FRP- Confined Concrete 229
7.4 Experimental Work 232
7.5 Assessment of Selected FRP-Confined Models 234
7.6 Conclusions 240

Chapter 8 Summary and Conclusions 241

8.1 Summary 241
8.2 Conclusions 242
8.2.1 Reinforced CFFT columns 243
8.2.1.1 Short CFFT columns under concentric loading 243
8.2.1.2 Slender CFFT columns under concentric loading 245

8.2.1.3 Short CFFT columns under eccentric loading 245

8.2.2 Reinforced CFFT beams 246

8.3 Recommendations for Future Work 258

REFERENCES 259

List of Tables

Table 2-1 Dimension and mechanical properties of fiber reinforced polymer tubes 16
Table 2-2 Details of specimens and summary of test matrix..... 20
Table 2-3 Test results..... 24
Table 3-1 Dimension, details and mechanical properties of the FRP tubes 45
Table 3-2 Details of specimens and test results for the confined strength..... 52
Table 3-3 The experimental and theoretical results at the yield and maximum load levels... 69
Table 4-1 Dimension and mechanical properties of fiber-reinforced polymer tubes 79
Table 4-2 Configuration and characteristics of the tested specimens and test results 80
Table 5-1 Mix proportion of concrete..... 111
Table 5-2 Properties of reinforcing steel bars..... 113
Table 5-3 Properties of reinforcing FRP bars. 115
Table 5-4 Mechanical and physical properties of fibres and resin. 115
Table 5-5 Dimension and details of the GFRP tubes..... 116
Table 5-6: Test matrix and details of beam specimens..... 121
Table 5-7 Test results of RC and RCFFT beams 132
Table 5-8 Experimental and predicted cracking moment for test RCFFT beams 175
Table 5-9 The theoretical results of moment capacities, η and ξ values..... 183
Table 6-1 Properties of reinforcing steel bars..... 209
Table 6-2 Details of specimens and summary of test matrix..... 212
Table 6-3 Test results for the eccentrically and concentrically loaded CFFT columns..... 214
Table 7-1 Existing confining models for FRP-confined concrete 230
Table 7-2 Test matrix and specimens details..... 233
Table 7-3 Experimental test results..... 234
Table 7-4 Performance of selected confined models and compression with test data..... 236
Table 7-5 Statistical performance of strength model for CFFT specimens 239

List of Figures

Figure 2-1 Test procedures for split-ring test. 17
Figure 2-2 Load and strain -strain relationship for split-disk test 18
Figure 2-3 Fabrication of CFFT cylinders 21
Figure 2-4 Fabrication of CFFT columns 22
Figure 2-5 Test setup for concentric axial load 23
Figure 2-6 Failure mode of CFFT cylinders 25
Figure 2-7 Stress-strain relationships for the plain and CFFT cylinders 26
Figure 2-8 Experimentally observed dilation behavior for CFFT cylinders 28
Figure 2-9 Failure modes of CFFT columns of Group No. 3, 5 and 6. 29
Figure 2-10 Stress-strain relationships for specimens of Group No. 3 31
Figure 2-11 Stress- strain relationships (Group No. 5 and 6) 32
Figure 2-12 The relationship between the axial load and slenderness ratio 33
Figure 2-13 Axial load-axial displacement relationships 35
Figure 2-14 Axial Load-axial displacement relationships 35
Figure 2-15 Load-lateral displacement relationships 36
Figure 2-16 The relationship between the axial load on the column and axial strain in the longitudinal steel bars (Group No. 3 and 6) 38
Figure 2-17 The relationship between the axial load on the column and axial strain in the longitudinal steel bars for specimens of Group No. 4 38
Figure 2-18 Experimentally observed dilation behavior for specimens of Group No. 5. 39
Figure 3-1 Load-strain (hoop) behavior of the FRP tubes for the split-disk test 45
Figure 3-2 Typical steel cages for CFFT specimens 47
Figure 3-3 Schematic of the test setup 48
Figure 3-4 Stress–strain behavior of CFFT specimens. 51

Figure 3-5 The typical load-axial strain in the longitudinal steel bars relationships for the reinforced CFFT columns 53
Figure 3-6 Failure mode of CFFT cylinders 54
Figure 3-7 Failure modes of CFFT columns 54
Figure 3-8 Predicted-versus-experimentally observed ultimate strength for different confinement models (Series-I) 62
Figure 3-9 Predicted-versus-experimentally observed ultimate and yield loads 67
Figure 3-10 In-place confined strength of concrete-versus-FRP volumetric ratio 70
Figure 3-11 Load-displacement behavior for RC and FRP confined concrete columns 72
Figure 3-12 Predicted-versus-experimentally observed yield load 72
Figure 4-1 Test specimens 81
Figure 4-2 Instrumentation and test setup 82
Figure 4-3 (a) Failure modes of CFFT specimens 85
Figure 4-4 Experimental ultimate load carrying capacity-versus-slenderness ratios (kl/r) 86
Figure 4-5 Load–axial displacement behavior of CFFT columns 90
Figure 4-6 Load–lateral displacement behavior of CFFT columns 92
Figure 4-7 Effect of various parameters on the ultimate strength of CFFT columns 94
Figure 4-8 Effect of the slenderness ratio on the critical buckling stress 100
Figure 4-9 Critical slenderness ratio 102
Figure 5-1 Stress-strain relationship for concrete. 112
Figure 5-2 types of steel reinforcing bars and test set up. 113
Figure 5-3 Stress-strain relationships for the steel reinforcement 113
Figure 5-4 Sand coated GFRP reinforcing bars. 115
Figure 5-5 Filament wound GFRP tubes. 115
Figure 5-6 Test procedures for coupon tension test. 117
Figure 5-7 Stress-strain behaviour of the FRP tubes for the coupon tensile test. 118
Figure 5-8 Test procedures for coupon compression test. 119
Figure 5-9 Stress-strain behaviour of the FRP tubes for the coupon compression test 120

Figure 5-10 FRP and cardboard tubes for beam specimens. 123
Figure 5-11 Typical steel and glass FRP cages for RC and RCFFT beams 124
Figure 5-12 Instrumentation of the reinforcing bars with strain gauges..... 125
Figure 5-13 Different types of instrumentation for the beam specimens. 126
Figure 5-14 Steel frame of the test setup 126
Figure 5-15 Schematic of test setup for RCFFT and control beams..... 127
Figure 5-16 Overview for the test setup. 128
Figure 5-17 Moment-curvature relationships for RC and RCFFT beams 131
Figure 5-18 Load–deflection curves for Specimens (CO-S-N, COS-S-N and D-S-N) 135
Figure 5-19 Load–deflection curves for Specimens (CO-G-M, COS-G-N and D-G-M) 135
Figure 5-20 Load–deflection curves for Specimens (D-S-N and D-G-N)..... 137
Figure 5-21 Load–deflection curves for Specimens (D-S-M and D-G-M) 137
Figure 5-22 Load–deflection curves for Specimens (D-G-N and E-G-N) 139
Figure 5-23 Load–deflection curves for Specimens (D-G-M and E-G-M) 139
Figure 5-24 Load–deflection curves for Specimens (D-S-N and E-S-M) 140
Figure 5-25 Load–deflection curves for Specimens (D-G-N and D-G-M) 141
Figure 5-26 Load–deflection curves for Specimens (E-G-N and E-G-M) 141
Figure 5-27 Load-flexural compression and tension relationships (Series 1) 144
Figure 5-28 Load-flexural compression and tension relationships (Series 2) 144
Figure 5-29 Strain profile at mid-span section of control and CFFT beams (Series No. 1) 145
Figure 5-30 Strain profile at mid-span section of control and CFFT beams (Series No. 2) 146
Figure 5-31 Mid-span hoop strain of reinforced CFFT beams (Series No. 1)..... 149
Figure 5-32 Mid-span hoop strain of reinforced CFFT beams (Series No. 2)..... 150
Figure 5-33 load-strain rosette relationships at mid-height of tested beams (Series 1) 151
Figure 5-34 load-strain rosette relationships at mid-height of tested beams (Series 2) 152

Figure 5-35 Failure mode and concrete crack pattern of RC beam CO-S-N 154
Figure 5-36 Failure mode and concrete crack pattern of RC beam CO-G-M 154
Figure 5-37 Failure mode and concrete crack pattern of RC beam COS-S-N 156
Figure 5-38 Failure mode and concrete crack pattern of RC beam COS-G-M 156
Figure 5-39 Failure mode and concrete core crack pattern of RCFFT beam D-G-N 157
Figure 5-40 Failure mode and concrete core crack pattern of RCFFT beam D-S-N 157
Figure 5-41 Failure mode and concrete core crack pattern of RCFFT beam D-G-M 160
Figure 5-42 Failure mode and concrete core crack pattern of RCFFT beam D-S-M 160
Figure 5-43 Failure mode and concrete core crack pattern of RCFFT beam E-G-N 161
Figure 5-44 Failure mode and concrete core crack pattern of RCFFT beam E-G-M 161
Figure 5-45 Load-end rotations of RC and CFFT beams 162
Figure 5-46 Load-concrete end slippages of reinforced RCFFT Beams 163
Figure 5-47 Effect of type of transverse reinforcement on the flexural strength 165
Figure 5-48 Effect of type of transverse reinforcement on the energy absorption 165
Figure 5-49 Experimental flexural strength versus Young's modulus of bars 167
Figure 5-50 Energy absorption versus Young's modulus of bars 167
Figure 5-51 Experimental flexural strength versus FRP-tube reinforcement ratio 168
Figure 5-52 Energy absorption versus FRP-tube reinforcement ratio 168
Figure 5-53 Experimental flexural strength versus concrete compressive strength 170
Figure 5-54 Energy absorption versus concrete compressive strength 170
Figure 5-55 The Typical cross section of the RCFFT beams 172
Figure 5-56 Details of RCFFT beam cross section and its strain and stress profiles 178
Figure 5-57 The experimental to theoretical monument ratio versus the neutral axis depth ratio 182
Figure 5-58 The experimental to the theoretical moment capacities of RCFFT beams 186
Figure 5-59 Deflected shape of simply supported beam subjected to two equal concentrated loads 187
Figure 5-60 Effective to gross moment of inertia versus Ma / Mcr, (Steel-RCFFT beams) 195

Figure 5-61 Effective to gross moment of inertia versus Ma / Mcr, (FRP-RCFFT beams) 197
Figure 5-62 Effective to cracking moment of inertia versus Ma/Mcr, (FRP-RCFFT beams) 199
Figure 5-63 Mid-span moment versus deflection measurements and predictions 202
Figure 6-1 stress-strain curve for the split-disk 208
Figure 6-2 Stress-strain curve for coupon tensile test 208
Figure 6-3 Stress-strain relationships for the steel reinforcement 209
Figure 6-4 Formwork and casting procedures 211
Figure 6-5 Test set up for eccentric axial load 213
Figure 6-6 Load–axial and lateral strains relationships of Specimen B90SN15 216
Figure 6-7 Load–axial and lateral strains relationships of Specimen B90SN30 216
Figure 6-8 Load–axial and lateral strains relationships of Specimen B90SN45 217
Figure 6-9 Load–axial and lateral strains relationships of Specimen B90SN60 217
Figure 6-10 Load–strain relationships of internal steel reinforcements (tension–side) 218
Figure 6-11 Load-axial deformation relationships for the eccentrically and concentrically loaded CFFT columns 220
Figure 6-12 Load-horizontal deformation relationships for the eccentrically and concentrically loaded CFFT columns 220
Figure 6-13 Failure modes of eccentrically loaded CFFT column specimens 223
Figure 6-14 Load-eccentricity relationships 225
Figure 6-15 Experimentally interaction diagram for CFFT columns 225

Chapter 1 Introduction

1.1 Introduction

The corrosion of steel reinforcement in an aging highway and marine infrastructure is a major problem currently facing the transportation and civil engineering structure community. Further, the existing of these structures in harsh environments has resulted in steady deterioration that shortens the lifetime serviceability of concrete structures. Harsh environments, such as those found in cold regions or Canadian climates, may expose structures to freeze-thaw cycles, marine sea spray or winter de-icing salts. In Canada and the United States, maintenance and replacement costs of bridge and marine substructures are measured in billions of dollars. Government agencies and industrial firms are looking for infrastructure systems that are stronger, last longer, are more resistance to corrosion, cost less to build, maintain and repair. Engineers all over the world are challenged and in search of new and affordable construction materials as well as innovative approaches and systems to problem solving.

Since the 1970s, research projects and field studies have been conducted on different methods for protecting reinforced concrete structures from deterioration and corrosion damage. Several techniques, including epoxy coating of reinforcing bars, cathodlic protection, increased concrete cover thickness, polymer concrete overlays have been used to inhibit or eliminate corrosion. None of these techniques, however, has been proven to be cost-effective or a long-term solution. A significant research effort over the past twenty years has shown that fibre reinforced polymer (FRP) materials can be effectively used to reinforce and/or strengthen deteriorated or understrength reinforced concrete structures. FRP reinforcement is made from high tensile strength fibres such as carbon, glass, and aramid embedded in polymeric matrices and produced in the form of bars, tubes, grids, in a wide variety of shapes and characteristics. FRPs are corrosion-free

materials and have been used worldwide for new structures to avoid the deterioration of concrete structures caused by corrosion of steel reinforcement.

Over the past decade there has been increased consideration and field use of composites for the rehabilitation of existing structural components and systems. However, despite similar levels of efforts being made for the introduction of composites into new construction applications there has been only limited success with most projects being at the level of demonstrations, rather than bid competitively with conventional materials, or being specified because of the inherent and essential advantages of FRP composites over conventional materials. In part their application in new construction has been limited due to high costs in comparison with components fabricated from conventional materials such as concrete and steel. Further there is a reluctance to use these materials for primary structural elements in new construction without sufficient data on long-term structural response and durability. There is however, no doubt, that these materials have significant advantages for use in new construction ranging from lighter weight which would translate to greater ease in construction without heavy construction equipment and use of smaller sub-structural elements, to their greater capacity to meld form and function thereby providing for ease in integration of aesthetics with functionality (Karbhari 2004).

In the last decade, considerable efforts have been made to apply FRP composites in the construction industry, and recently, structural applications of FRP composites started to appear in civil infrastructure systems. FRP composite materials have been used as internal and external reinforcement in the field of civil engineering constructions. It has been used as internal reinforcement for beams, slabs and pavements (Masmoudi et al. 1998; Rizkalla et al 2003; Benmokrane et al. 2006), and also as external reinforcement for rehabilitation and strengthening different structures (Demers and Neale 1998; Teng et al. 2002). Application of FRP in infrastructural systems has come about as a result of the many desirable characteristics of composites that are superior to those of conventional materials such as steel, concrete, and wood. FRP composites are very attractive materials to structural engineers due to their high specific stiffness and high specific strength. The

high corrosion resistance of FRP composites makes them ideal alternative materials to resolve a number of problems that the worldwide infrastructures are now facing.

To most effectively utilize the advantages of FRP materials, which are light weight and improve constructability, innovative structural designs are needed which either incorporate ''composites-efficient'' forms or which combine these materials with conventional ones. One promising innovative structural system is concrete-filled FRP tubes (CFFT). In recent years, CFFT system has been widely studied for their use in civil infrastructure. In the early 1980s, the concept of CFFT was proposed by Fardis and Khalili 1981 and 1982, who analyzed the behaviour of circular and rectangular FRP tube-encased concrete columns and beams. CFFT are constructed by simply filling prefabricated FRP tubes with concrete. CFFT technique represents a formwork-free, steel-free, and corrosion-resistant alternative for construction of new infrastructure. This system provides an excellent alternative to conventional reinforced concrete or steel components for several structural applications in aggressive and corrosive environments, including fender piles, bridge girders and piers, poles, and overhead sign structures. The most common characteristics of the integrated systems are as follows:

- FRP shape acts as permanent form for concrete; hence, will save the cost of formworks involved in conventional cast-in-place or pre-cast industries.
- Main reinforcement for concrete is provided externally by the FRP shape, even though additional reinforcement of other types of materials such as steel may be provided internally. In concrete-filled FRP tubes, the tube acts as reinforcement for both shear and flexure, utilizing the multi-direction fibre orientation. This would save the time and cost involved in conventional construction in assembling longitudinal rebars together with stirrups. The closed composite shells provide passive confinement to the concrete, which significantly improves the strength and ductility.
- Depending on the nature of loading, the capacity and performance of the system may depend on the composite action between the concrete and FRP shape.
- The system lends itself to optimization based on material properties of each component. The hybrid system provides the designers with several flexible

parameters, which can be controlled to achieve optimum design in individual applications including type of fibres, orientation of the fibres, number of layers in the composite shell, and the concrete wall thickness.

- The contained concrete, in case of concrete-filled tubes, is protected from moisture intrusion that could otherwise deteriorate the concrete core
- Reduces the expense of maintaining new infrastructure
- Increases the life span and safety of new infrastructure

The general process used to manufacture FRP tubes is one of placing and retaining fiber reinforcements in the direction and form needed to provide the finished product its desired shape and properties. It can be done by pultrusion, filament winding, centrifugal casting or resin infusion. Pultrusion is a highly automated, low-labor, closed-mold process for manufacturing FRP shapes having a uniform cross section. The process is well suited for high-volume commercial production of both custom and standard shapes because it can be operated continuously.

The filament winding technique is the most common manufacturing method for producing FRP tubes. Filament winding was invented in 1946 and incorporated into missile applications in the 1950s (Daniel and Ishai 1994). Filament winding is an automated low-labor process typically used to manufacture cylindrical, conical, parabolic, box beam, and other FRP tube shapes. Such shapes are made by continuously wrapping resin-impregnated fibre reinforcements around a mandrel. In basic terms, the process involves a winding machine that pulls dry fibre reinforcement from supply racks through a resin applicator system and winds the wet fibre around the mandrel. In the filament winding process, the placement of the primary fibre-glass reinforcement is tightly controlled and can be oriented in either a circumferential or longitudinal direction or anywhere in between as needed to develop the necessary strength properties in the circumferential (hoop) direction. Controlling fibre tension and winding angle is an integral part of the filament winding process because these factors greatly determine the performance of the finished FRP tube is usually somewhat rougher than the smooth interior.

The use of FRPs in new structures is still somewhat limited, mainly because of their relatively higher initial cost, lack of design codes in some area. However, CFFT technique provides an emerging and promising system for a variety of structural applications in which the tubes serve as structural formwork. Circular CFFT have already been implemented in the field as bridge piers, marine piles, and girders, where FRP tubes were essentially the sole reinforcement for the system (Mirmiran and Shahawy 1996; Mirmiran, et al., 1999; Seible et al. 1999; Fam et al 2003a, and b; Zhao et al. 2004). Fam et al. 2003c presented eight field applications of a total 1162 CFFT composite piles in marine environments in different location of the United States of America. These piles were without internal reinforcements. The diameter of the used CFFT composite piles ranged from 300 mm to 450 mm, and the length ranged from 14 m to 25 m. Whereas, these composite piles were used as a fender walls to protect the piers of a bridge in a lake; to support new docking facilities; in a structural application to support a wharf extension; dauphin clusters; structural battered. In other applications, FRP tubes have been used in conjunction with internal steel reinforcement (Pando et al. 2003). In 2000, the Virginia Department of Transportation (VDOT) employed the CFFT composite piles for an entire bent of new route 40 Bridge over the Nottoway River in Sussex Country, Virginia. Also, in 2001, VDOT started a bridge replacement project at the Route 351Bridge crossing of the Hampton River in Hampton, Virginia. The VDOT has decided to use a CFFT composite pile. Internal longitudinal steel reinforcement was included in the used CFFT composite pile to increase the flexural stiffness (Pando et al. 2003). In addition, the concept of concrete-filled FRP tubes has been used in field applications as bridge girders. Whereas, the flexural behaviour of large and full-scale a two-span concrete-filled carbon FRP tube bridge girders combined with either a conventional RC deck or a lightweight GFRP modular deck was investigated by Karbhari et al. 2000. Based on the findings of the previous research work, a field application of CFFT with carbon FRP tubes as bridge girders was implemented to construct the Kings Stormwater Channel Bridge, along Highway 86, near the Salton Sea. (Burgueno et al. 1998; Seible et al. 1999; Karbhari et al. 2000; Zahao et al. 2000). The bridge is 20 m long and comprises a two-span slab-on-

girder system for the superstructure, which in turn comprises six longitudinal 340 mm diameter CFFT girders with 9.50 mm thick carbon FRP tubes.

The axial and flexural studies on CFFT, however, have mostly been conducted without using internal reinforcements. Although valuable research has been conducted on CFFT under flexural and axial loads, and in some other areas it has been quite limited, leaving research gaps in need of further investigations to introduce appropriate provisions in guidelines and codes for the design issues of CFFT under axial and flexural loads. The main focus of the present study is on the reinforced concrete-filled FRP tubes. It basically consists of a filament-wound FRP tubes filled with concrete and reinforced internally with steel or FRP rebar. The scope is primarily focused on the structural feasibility of reinforced CFFT. The following issues are examined:

- Confinement of concrete with FRP tubes.
- Composite action of FRP tube, internal rebar and concrete in columns under concentric and eccentric loads.
- Composite action of FRP tubes internal rebar and concrete in beams under flexural load.
- Comparison of its behaviour with conventional RC columns and beams.
- Design issues such as ultimate load carrying capacity and deformation.

1.2 Objectives and Originality

Recently, the concrete-filled FRP tubes (CFFT) technique has been used successfully for different concrete structures in the field of civil engineering. Nevertheless, the ultimate load carrying capacities of short and slender reinforced CFFT columns have not yet been fully explored. Several codes and design guidelines addressing the strengthening and rehabilitation issues of RC columns using confinement by FRP sheets have been recently published. Most of the design provisions for predicting the ultimate axial load incorporated in these codes and design guidelines are based on the design formulas of members reinforced with conventional steel considering some modification. On the other hand, the design provisions for predicting the yield and ultimate moment capacities as well as the load-deflection response of the circular reinforced CFFT under flexural load have not yet

been introduced in codes and design guidelines. For example, the recommended equations for estimating the effective moment of inertia for deflection calculation in the current codes and design guidelines do not take into consideration the effect of confinement.

This present study is aimed at providing basic technical information on axial and flexural behaviour of CFFT members. A number of research objectives are identified and systematically listed below in the two stated areas for the proposed experimental and analytical development.

1. Reinforced CFFT columns

a. Short

- To evaluate the compression behavior of small and medium-scale CFFT columns under pure axial load and eccentric load using new filament wound GFRP tubes.
- To evaluate the confinement models and the design equations provided by the three different North American codes and design guidelines (ACI Committee 440.2R 08, CAN/CSA-S6-06 and CAN/CSA-S806-02), for the predictions of the confined concrete compressive strength and the ultimate load capacities of the short CFFT columns.
- To propose a new confinement model and to introduce appropriate modifications to the existing design equations for the reinforced and unreinforced short (non-slender) CFFT columns.

b. Slender

- To investigate the influence of the slenderness ratio of CFFT columns on the critical buckling load and the ultimate capacity of such columns.
- To investigate the relative importance of internal reinforcement, concrete compressive strength and thickness of the FRP tubes on the buckling mode of failure of CFFT columns.
- To verify the accuracy of existing critical buckling load formulas and then to propose a threshold for the slenderness ratio for CFFT columns.

2. Reinforced CFFT beams

- Evaluating the contribution of FRP tubes to the flexural capacity, compared to

conventional RC beams with and without steel spiral reinforcement.

- To evaluate the effects of the following specific experimental parameters on the flexural response of CFFT beams:
  1) The effect of type of the internal reinforcements (steel or GFRP bars) on the flexural performance of RCFFT beams.
  2) The effect of the FRP tube thickness
  3) The effect of concrete compressive strength by using the two types of concrete batches.
- To develop an analytical procedure to predict the yield and ultimate moment of RCFFT beams.
- To examine the validity of the available design provisions for predicting the load-deflection response of CFFT beams.
- To develop new equations and update the existing design equations for predicting the effective moment of inertia of CFFT beams reinforced with steel or GFRP bars.

1.3 Methodology

To achieve the objectives of this research, experimental and analytical programs were designed. The experimental program consisted of two types of structural members. The first and second type comprised reinforced concrete filled FRP tubes columns and beams, respectively.

Experimental investigations of the axial behaviour of the CFFT columns have generally been carried out without using internal longitudinal reinforcement. While there is abundant experimental and theoretical research information on the small (cylinder) scale specimens, there are few data on the behaviour of large scale CFFT columns. In addition, limited experimental works have been carried out on specimens with internal longitudinal reinforcements.

Therefore, as regards columns, 35 CFFT columns and five control reinforced concrete columns of different size and with internal longitudinal reinforcements were cast

and tested under concentric and eccentric loading in the experimental investigation of this study. The experimental program of the CFFT columns was characterized to four stages. The first and the second stage were designed to study the behaviour of short and long CFFT columns respectively under concentric loads, while the third stage was focused on the behaviour of short CFFT columns under eccentric loads. The fourth stage was developed to serve as control conventional spiral-steel reinforced concrete columns for CFFT specimens.

The analytical investigation for CFFT columns included analysis test results using the different available design provisions of axial load capacity pertinent to members confined with FRP materials. The results of each analysis were compared to the experimental values. Based on the results of this comparison and the experimental findings, proposed modifications to the North American codes and design guidelines for the predictions of the ultimate load capacities of the short CFFT columns are presented. On the other hand, for the slender CFFT columns, simplified formula for the limit slenderness ratio was proposed for the design purposes. The predicted value according to the proposed formula agrees with the observed critical slenderness ratio and with the recommended value in the literature.

As regards beam, the test beams were divided into two series. The first and second series were cast using normal and medium concrete strength, respectively. Each series included five beams, one conventional reinforced concrete (RC) circular beams without spiral reinforcement and one RC beam with spiral reinforcement, while the remaining three specimens were RCFFT. The specimens of each series were reinforced with steel or glass FRP bars with the same reinforcement ratio. Two types of FRP tubes different in thickness were used as stay-in-place form works for the beam specimens.

The analytical investigation for CFFT beams included step by step simplified formulations to predict the yield and ultimate moment of tested RCFFT beams. In addition, the experimental values of the moment-deflection response of tested CFFT beams were analyzed and compared with the available design equations. Based on the

results of this comparison and the experimental findings, new equations and proposed modifications to the existing equations for predicting the effective moment of inertia in the literature and codes for the predictions of the moment-deflection response of tested CFFT beams are presented.

1.4 Organization of the Dissertation

This dissertation consists of eight chapters. The following is a brief description of the contents of the thesis:

Chapter 1: This chapter serves as an introduction, outlines the advantages and applications of concrete filled FRP tubes in civil engineering infrastructures, followed by the objective and scope of this study.

Chapter 2: This chapter presents the first paper in this dissertation, which is titled "Compressive Behavior of Reinforced Concrete Filled FRP Tubes." It presents the results of an experimental investigation on the axial behaviour of 16 small- and medium-scale reinforced CFFT columns. Factors influencing the strength and ductility enhancement such as: the effect of laminate thickness, concrete strength and presence of longitudinal steel bars are addressed. Research findings indicate the longitudinal steel reinforcements enhance the ductility of CFFT columns. The ultimate strength of the CFFT is mainly dependent on the stiffness of the FRP tubes in the hoop direction, and it is more effective for normal concrete strength.

Chapter 3: This chapter presents the second paper in this dissertation, which is titled "Axial Load Capacity of Reinforced Concrete-Filled FRP Tubes Columns: Experimental versus Theoretical Predictions" The purpose of this study is to present a constructive critical review of the state-of-the-art design methodologies available for the case of confined concrete RC short columns using FRP tubes and to indicate a direction for future developments. Comparisons between the experimental test results and the theoretical predictions values by the three North American codes and design guidelines are performed. Based on the test results and the analysis a new confinement model is

proposed for the confined concrete compressive strength of the CFFT cylinders. Also, the design equations are modified to accurately predict the ultimate and yield loads capacities of internally reinforced and unreinforced short CFFT columns.

Chapter 4: This chapter presents the third paper in this dissertation, which is titled "Nonlinear Stability Analysis of Concrete Filled FRP-Tubes Columns: Experimental and Theoretical Investigation" In this study, 18 CFFT columns of different heights, 305, 608, 912, 1216 and 1520 mm and 4 control RC columns were tested under uniaxial compression load. The main objective of this paper is to investigate experimentally and theoretically the influence of the slenderness ratio of CFFT columns on the critical buckling load and the ultimate capacity of such columns. Simplified formula for the limit slenderness ratio was proposed for the design purposes of CFFT columns in this paper.

Chapter 5: This chapter describes the experimental program and the theoretical analysis conducted to test 10 control beams reinforced with FRP or steel bars in the longitudinal direction and with FRP tubes or spiral steel in the transverse direction. In this chapter the details of test specimens, materials, configurations, test setup, and instrumentations are given. The results obtained from the experimental investigation are presented in this chapter. The influence of each test parameter on the flexural behaviour of the tested beams is analyzed. A simplified analytical method is developed to predict the yield and resisting moments corresponding to the failure modes of the tested RCFFT beams. In addition, an analytical investigation to examine the validity of the available design provisions for predicting the load-deflection response of CFFT is conducted. The effective moments of inertia of the tested beams are analyzed using the different available code, manuals and design guidelines equations. The results of the analysis are compared with the experimental values. Based on the experimental data obtained in this study, new proposed equations and a modified expression for the effective moment of inertia of a simply supported CFFT beams reinforced with steel or GFRP bars are introduced. Finally, most of the content of this chapter are included in two papers.

Chapter 6: This chapter presents the sixth paper in this dissertation, which is titled "Behavior of Concrete Filled FRP Tubes Columns under Eccentric Loads." It presents

the results of an experimental investigation on the behaviour of CFFT columns under eccentric load. The new test setup is described in the experimental program. The results obtained from the experimental investigation are presented in this chapter. The test results for four CFFT columns tested with different eccentric values are compared to the test results of CFFT and RC columns tested under concentric load.

Chapter 7: This chapter presents the main contribution of the seventh paper in this dissertation, which is titled "Assessment of Confinement Models for Concrete Confined with FRP Tubes." In this chapter fourteen selected FRP-confined models for prediction the ultimate strength of CFFT have been reviewed. A comparison between the experimental results and those predicted by the selected models is presented. The assessment has been based on the prediction of the ultimate axial strength of the CFFT specimens, rather than on its strain or whole stress-strain relationships.

Chapter 8: A summary of this investigation is given in this chapter. The chapter also presents the general conclusions drawn from the work presented in this dissertation. Recommendations for future research are also given.

Chapter 2
Compressive Behavior of Reinforced Concrete Filled FRP Tubes

2.1 Synopsis

In recent years, the application of concrete-filled fiber reinforced polymer (FRP) composites tubes (CFFTs) for different structural applications (piles, column, girder, bridge piers) has been started. The FRP tubes benefits are in confinement, protective jackets, providing shear and/or flexural reinforcement and permanent formwork. Most of the experimental investigations conducted to study the behavior of the CFFT columns under compression load, were without internal longitudinal reinforcement. This paper presents the experimental results of small and medium height CFFT columns with internal steel bars. The parameters used in this investigation include the effect of laminate thickness of FRP tubes, concrete strength, slenderness ratio (height to diameter ratio) and presence of longitudinal steel bars. Sixteen CFFT specimens and one steel spiral reinforced concrete column were tested under axial compression load. The diameter of the tubes used was 152 mm (6 in), and the fiber orientations were mainly in the hoop direction. The results indicate that significant decrease of the ultimate load capacity by increasing the slenderness ratio, which also yields to different failure modes. The internal longitudinal reinforcements improve the ductility of the CFFT columns, as well as the load carrying capacity. The ultimate strength of the reinforced CFFT columns is mainly dependent on the stiffness of the GFRP tubes. The benefit of CFFT technique is more effective for normal than that medium strength concrete.

2.2 Introduction

In recent years, the application of concrete filled fiber reinforced polymer (FRP) tubes (CFFT) for different structural applications piles, column, girder, bridge piers has proved to be one of the more promising system (Mirmiran and Shahawy 1997a; Mirmiran and Shahawy 2003; Fam et al 2003a,b; Karbhari 2004; Fam and Rizkalla 2003). Filament winding is one of the oldest composite manufacturing methods to fabricate FRP tubes. In this process, the placement of the fiber is tightly controlled and can be oriented in any direction as needed, to develop the necessary strength properties in the hoop or axial direction. Confinement of the concrete is produced by the reaction of FRP tubes normal to the hoop direction for structural members under uniaxial loads. The fiber layers in the hoop direction are activated to provide the confinement of the concrete. The axial layer is not economic for CFFT columns, due to the earlier local buckling under the compression load. Kaynak et al. 2005 conducted a split-disk test for specimens produced with five different winding angle to investigate the processing parameters of continues FRP tubes. The results indicate that both hoop tensile strength and hoop tensile modulus of elasticity depend strongly on the fiber direction of specimens. Specimens having 90° and ±65° had much higher values compared to the ones having ±45°, ±25° and 0°.

Several researchers had studied many parameters for FRP closed forms, particularly CFFT. Presence of internal steel bars on axial compression behavior of CFFT were studied (Zhu et al. 2005). The results indicated that unreinforced CFFT columns failed by local rupture of FRP tube. The dowel actions of steel bars enhanced the ductility of the reinforced CFFT columns. A total of 42 CFFT cylinders were tested in uniaxial compression to investigate the dilation characteristics of the confined concrete (Mirmiran and Shahawy 1997b). It was concluded that, the dilation rate of CFFT reaches a maximum value which corresponds to a reversal in volumetric strain response. The dilation rate finally stabilizes at an ultimate value, which is a function of the FPR tubes stiffness. Mirmiran et al. 2001 tested seven fixed-fixed long CFFT with different slenderness ratios as a column under uniaxial compression. The CFFT columns were not internally reinforced, and the study was aimed to establish slenderness limits in CFFT

similar to those developed for conventional reinforced concrete columns. The results clearly showed that increasing the slenderness ratio (height to diameter ratio) from 5.5 to 18.6, the strength dropped rapidly from 1396 kN (314 kip) to 493 kN (111 kip), respectively. Yuan and Mirmiran 2001 presented an analytical and experimental study of the static buckling of thin-walled FRP tubes filled with concrete and bent in single curvature. The tubes had a core diameter of 147.3 mm (5.8 in) and a wall thickness of 3.68 mm (0.144 in), and their lengths ranged between 813 mm (32 in) and 2743 mm (108 in). The study showed that CFFT are much more susceptible to buckling than concrete columns with internal steel reinforcement. Also, it was recommended that the current slenderness ratio limit of 11 for steel-reinforced concrete columns bent in single curvature be reduced to 5.5 for CFFT, for this particular type of FRP tubes.

While many research works have been reported related to the axial behavior of CFFT columns, few experimental works were done on specimens with internal longitudinal reinforcements. Also, most of these studies were on small cylinder specimens 152 x 305 mm (6x12 in). In this paper, the experimental results of eight CFFT cylinders, eight CFFT columns and one control specimen are presented. Short and medium height CFFT columns were tested under uniaxial loads with different parameters. The effect of FRP-tube thickness, concrete strength, slenderness ratio (height to diameter ratio) and presence of longitudinal steel bars are evaluated in this investigation.

2.3 Research Significance

From the available literature on the CFFT technique, it is clear that the amount of the experimental work on specimens reinforced with longitudinal steel bars is limited, compared to specimens without internal reinforcement. It is obvious that further experimental research is required on large scale CFFT with internal reinforcement. In this study, new GFRP tubes are used as an FRP-stay in place structural formwork for concrete columns. This study takes into account the effect of concrete strength, thickness of FRP tubes and the slenderness ratios of the columns. The benefits of this work is the evaluation of the structural performance of new GFRP tubes, as well as the evaluation of

the load-axial and lateral deformation, the failure modes, the stress-strain and the dilation (ratio of hoop to axial starin) behavior of medium scale CFFT columns.

2.4 Experimental Program

2.4.1 Materials

2.4.1.1 FRP tubes

Three types of glass-fiber reinforced polymer (GFRP) tubes were used. The GFRP tubes were fabricated using filament winding technique; E-glass fiber and Epoxy resin. The internal diameter for all tubes is constant and equal to 152 mm (6 in). Table 2-1 presents the details for the three types A, B and C of the tubes, where E_X and E_Y are the Young's modulus in the longitudinal and hoop direction, respectively. Different fiber angles with respect to the longitudinal axis of the tubes were used: (±60°), for tube type A and B, and (±65°, ±45°) for tube type C. The laminate theory is used to calculate the Young's modulus in the axial and transverse directions based on the mechanical properties of the fibers and the resin which were provided by the manufacture. The split-disk test was performed according to ASTM D-2290-08 (ASTM 2008a) test-method on five specimens from each type of the tubes to determine the hoop tensile strength and modulus of these specimens (see Figure 2-1). Figure 2-2 shows the load and stress-strain relationship for each type of the tubes for the split-disk test, and as expected, the highest hoop tensile force values were obtained for the specimens of tube type C, which has the largest thickness. The load-strain curve for the split-disk test was linear up to failure for tubes A and B, but bilinear for tube C with a small reduction of the stiffness at 80 kN (18 kip).

Table 2-1 Dimension and mechanical properties of fiber reinforced polymer tubes

Tube type	Internal diameter (mm)	Thickness (mm)	Number of layers	Stacking sequence	E_X (MPa)	E_Y (MPa)
A	152	2.65	6	$[\pm 60°]_3$	8785	20690
B	152	2.85	8	$[\pm 60°]_4$	8787	20860
C	152	6.40	14	$[\pm 65_3, \pm 45, \pm 65_3]$	9270	23630

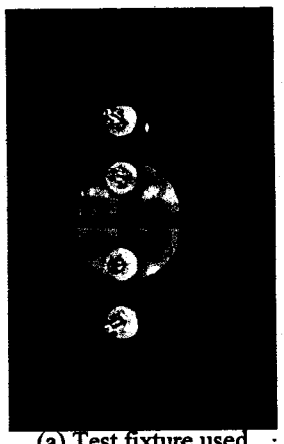

(a) Test fixture used

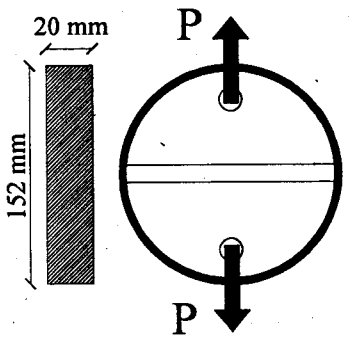

(b) Specimen dimension

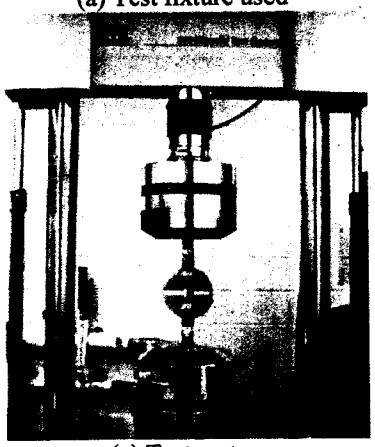

(c) Tests setup

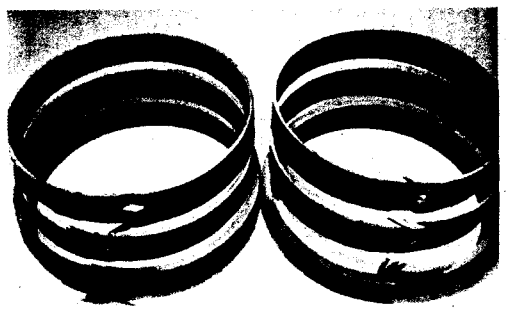

(d) Dominant failure mechanisms

Figure 2-1 Test procedures for split-ring test.

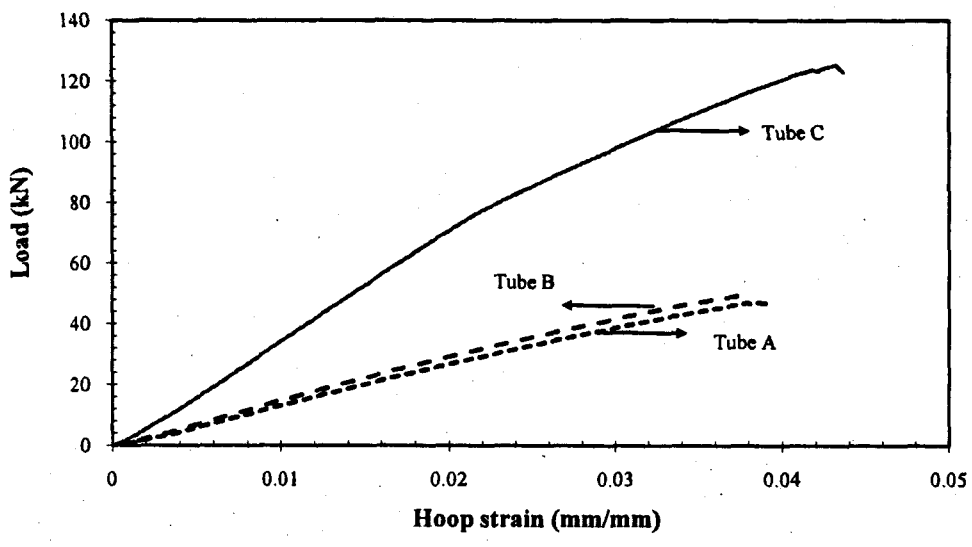

(a) Load-strain relationships for split-disk test.

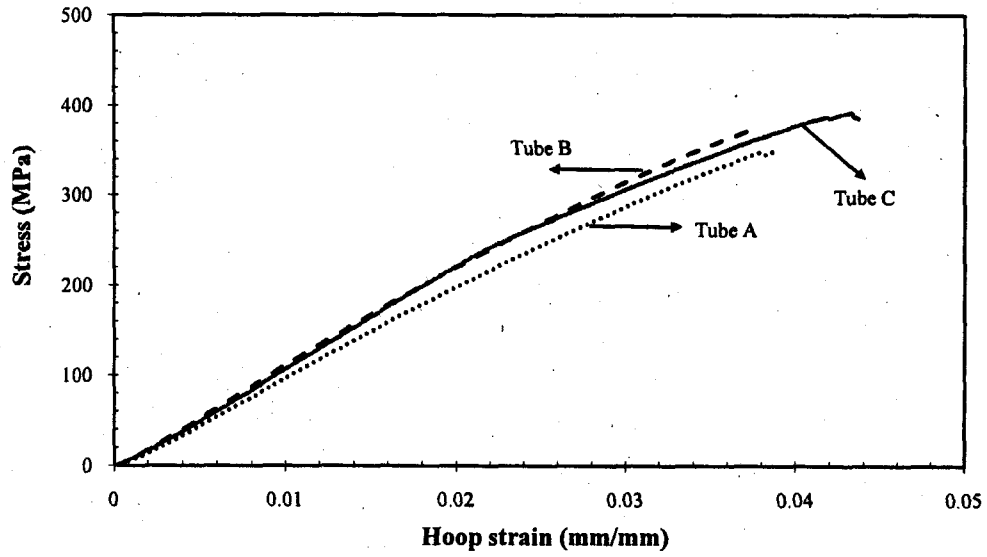

(b) Stress-strain relationships for split-disk test.

Figure 2-2 Load and strain -strain relationship for split-disk test

2.4.1.2 Concrete mixtures

All specimens were constructed from two concrete batches (N and M) to take into consideration the effect of concrete strength on the compressive behavior of the CFFT columns. The target strengths of batches N and M were intended to provide normal and medium concrete strength of 30 and 45 MPa (4.35 and 6.525 ksi), respectively. Both concrete batches were supplied by ready mix concrete supplier. The maximum size of the coarse aggregates was about 20 mm (0.788 in) and 16 mm (0.63 in) for the N and M concrete batches, respectively. Ten plain concrete cylinders (152 x 305 mm) were prepared from each batch N and M. The 28-day average concrete strengths were found to be equal to 29.6 and 44.7 MPa (4.3 and 6.48 ksi) and standard deviation equal to 0.84 and 0.68 for batches N and M, respectively.

2.4.2 Test specimens and parameters

The test matrix and the specimen identification are shown in Table 2-2. The first letter indicates the tube type used from Table 2-1, the first number shows the height of the column ranged from 300 to 1200 mm (11.82 to 47.28 in), and the second letter presents the type of concrete mix.

The parameters considered in this study are concrete strength, thickness of the GFRP tubes, presence of internal steel bars and slenderness ratio. Group No. 1 consists of ten plain concrete cylinders for each type of the concrete. Group No. 2 has eight CFFT cylinders 152x305 mm (6x12 in), two cylinders were cut from tubes A, B and C (different wall thicknesses), see Figure 2-3. These CFFT cylinders were tested to obtain the stress-strain behavior of the confined concrete. Also, the results of Group No.2 will be used to compare the ultimate strength capacities for the short and medium CFFT columns (Groups No. 3 and 4), having the same type of concrete and GFRP tubes. The percentage of the GFRP reinforcement ratio ($4t/D$) is equal to 6.97, 7.50, and 16.84, respectively for tubes A, B, and C, where t is the thickness of the GFRP tube.

Group No. 3 is composed of three different heights CFFT columns: 608, 912 and 1216 mm (23.95, 35.93 and 47.9 in). The variation in the heights was chosen to give

slenderness ratios (*H/D*) equal to 4, 6 and 8 for each height, respectively; where *H* and *D* are the height and the internal diameter of the columns, respectively. The three columns were cast with concrete type (N) and tube A. These columns were reinforced with six deformed steel bars No. 10 M, so the reinforcement ratio is equal to 2.60%. The bars were distributed uniformly inside the cross section of the tubes. The bars were welded at the top and bottom by two steel 3.2 mm (0.126 in)-diameter stirrup, to fix the bars inside the tube during casting. The distance between the bars and the tubes was 8 mm (0.315 in). Also, a concrete cover of 10 mm (0.394 in) was provided between the ends of the longitudinal steel bars and the top and bottom surfaces of the specimens to avoid the stress concentration at the steel bars area (Figure 2-4). This group is aimed to study the effect of the slenderness ratio on the behavior of the reinforced CFFT columns.

Table 2-2 Details of specimens and summary of test matrix

Group No.	Specimen ID	Height (mm)	Tube type	4t/D‡ %	(H/D)	Steel bars	Concrete strength (MPa)	No. of specimens
1	Cyl-.N	305	-	-	2	----	30	10
	Cyl-.M	305	-	-			45	10
2	A30N	305	A	6.97	2	----	30	2
	B30N		B	7.50				2
	C30N		C	16.8				2
	A30M		A	6.97			45	2
3	A60N	608	A	6.97	4	6 No. 10	30	1
	A90N	912			6			1
	A120N	1216			8			1
4	A60M	608	A	6.97	4	6 No. 10	45	1
	A90M	912			6			1
	A120M	1216			8			1
5	B90N	912	B	7.50	6	6 No. 10	30	1
	B90N-W	912				without		1
6	Control	912	Steel spiral		6	6 No. 10	30	1

‡ RFP tube reinforcement ratio

Group No. 4 is similar to specimens of Group No. 3 except that the concrete mix type M is used. Group No. 5 is composed of two 912 mm (35.93 in)-height CFFT columns using tube type B and concrete type N. Specimen B90N was internally reinforced with six

steel bars No. 10 M; However specimen B90N-W was cast without internal steel bars. This group is proposed to study the effect of the longitudinal steel reinforcement.

Finally, the specimen of Group No. 6 is a spirally-steel reinforced concrete column with height equals to 912 mm (35.93 in), and concrete type N. The specimen was reinforced with 6 longitudinal conventional steel bars No. 10 M. In addition, mild steel bars of diameter 3.2 mm (0.126 in) are used for the spiral reinforcement. The pitch equals to 50.6 mm (1.99 in) of the spiral is designed to give approximately the same hoop stiffness as the GFRP tube type A (Fam et al. 2007). The pitches of the spiral are reduced to 25 mm (0.985 in) over a distance of 125 mm (49.25 in) at both ends of the column. This is to avoid the local failure at both ends, close to loading regions. All the specimens were cast with concrete in a vertical position. This is performed by fixing the GFRP tubes in a vertical position inside the wooden box formwork. Two holes were drilled at the top and bottom of the wooden box to fix the specimen vertically. Also, the bottom surface area of the wooden box is attached with a horizontal wood plate to prevent the leakage of the concrete.

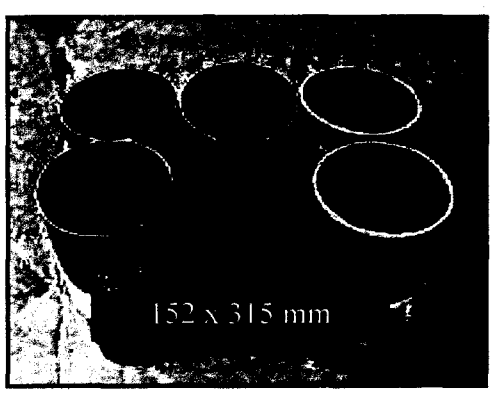

(a) GFRP tubes before casting

(b) Capping and instrumentation

Figure 2-3 Fabrication of CFFT cylinders

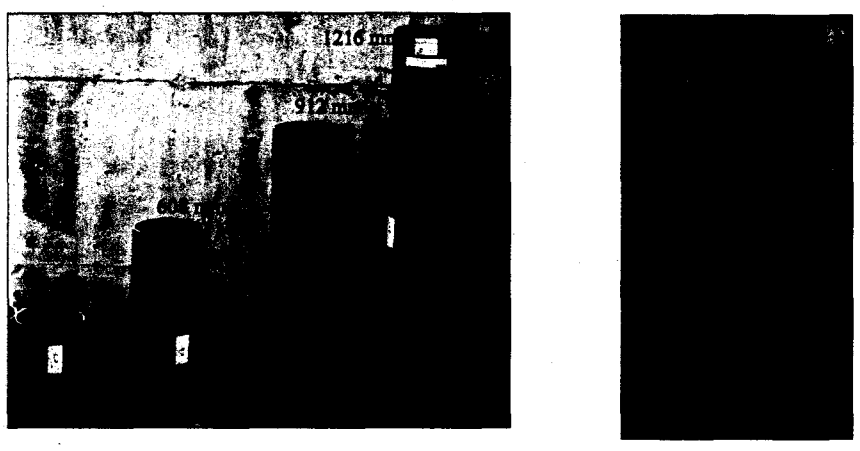

(a) GFRP tubes for different height.

(b) rebar cages for control specimen

Figure 2-4 Fabrication of CFFT columns

2.4.3 Instrumentation and test setup

Internal and external instrumentations were used in this study to capture the local strain distributions of the CFFT specimens. Before casting, two of the longitudinal steel bars, 180 degree apart, were instrumented with electrical strain gauges at the mid height. The spiral steel reinforcements were also integrated with strain gauges, two at the mid height. Before testing, two axial and two hoop electrical strain gauges were mounted, 180 degree apart, along the hoop direction on the external surface of the specimens. Additional two pairs of strain gauges were also mounted at the quarter height level for the 1200 mm (47.28 in) height specimens. Strain gauges of 6 mm (1.41 in) length were used to monitor the strain distribution of the GFRP tubes. Also, 30 mm (35.46 in)-strain gauges were bonded on the surface of the concrete cylinders and control spirally-steel specimen.

The axial displacement for each column was measured by two linear variable displacement transducers (LVDTs) 180 degrees apart along the hoop direction of the specimen. The LVDTs used have a maximum range of 100 mm (3.94 in) with an accuracy of 0.01mms (0.000394 in). Also, to measure the horizontal displacement, four LVDTs were mounted horizontally at the mid-height of the column 90 degrees around the column. All specimens were prepared before the test by a thin layer of the high

strength sulfur capping on the top and bottom surfaces to insure the uniform stress distribution during the test. Two circular steel tie raps of 4.0 mm (0.157 in) thickness and 60.0 mm (2.364 in) width were used to confine the two ends of the loading for each specimen. They were also used to avoid the local failure of the specimens at its both ends. The specimens were tested using a 6,000 kN (1350 kip) capacity FORNEY machine, where the CFFT columns were setup vertically at the center of loading plates of the machine. The FORNEY machine, strain gauges and LVDTs were connected by a 20 channels Data Acquisition System and the data were recorded every second during the test. The loading rate range was 2.0 to 2.50 kN/s (2.45 to 0.56 kip/s) during the test by manually controlling the loading rate of the hydraulic pump. Figure 2-5 shows the experimental test setup used in this study.

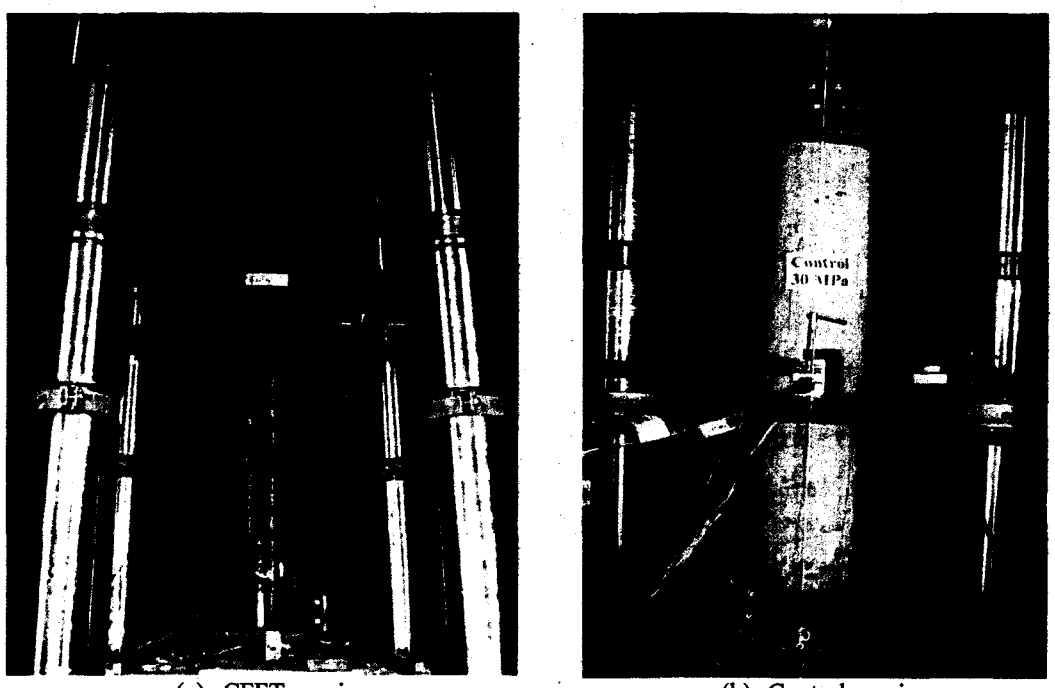

(a) CFFT specimen (b) Control specimen

Figure 2-5 Test setup for concentric axial load

2.5 Experimental Results and Discussion

Table 2-3 presents a summary of experimental results in terms of the maximum axial load P_{max}, the confined concrete compressive strength f'_{cc}, the ratio of f'_{cc} to unconfined concrete strength f'_c, the ultimate axial strain ε_{cc} and hoop strain ε_{ch} and the different failure modes of the CFFT specimens. The test results for CFFT cylinders and columns are discussed below.

Table 2-3 Test results

Group No.	Specimen ID	P_{Max} (kN)	f'_c (MPa)	f'_{cc} (MPa)	Axial (ε_{cc})	Hoop (ε_{ch})	$\frac{f'_{cc}}{f'_c}$		Failure mode
1	Cyl-.N	537.7‡	29.65‡	--	--	--	--	--	Compression failure
	Cyl-.M	811.0‡	44.72‡	--	--	--	--	--	Compression failure
2	A30N-1	1350	30	74.40	0.045	0.038	2.48	2.42*	Tube rupture
	A30N-2	1283		71.00	0.030	0.027	2.37		Tube rupture
	B30N-1	1490		81.88	0.039	0.034	2.73	2.70*	Tube rupture
	B30N-2	1450		80.00	0.040	0.023	2.67		Tube rupture
	C30N-1	2160		119.1	0.046	0.033	4.00	4.11*	Tube rupture
	C30N-2	2302		128.0	0.041	0.028	4.23		Tube rupture
	A30M-1	1620	45	89.40	0.041	0.034	1.98	1.90*	Tube rupture
	A30M-2	1502		82.50	0.035	0.033	1.82		Tube rupture
3	A60N	1302	30	70.98	0.021	0.015	2.37		Tube rupture
	A90N	1454		80.23	0.042	0.028	2.67		Tube rupture with buckling
	A120N	1201		66.00	0.025	0.020	2.2		Buckling
4	A60M	1741	45	95.00	0.025	0.014	2.11		Tube rupture
	A90M	1595		87.00	0.032	0.043	1.93		Tube rupture with buckling
	A120M	1366		75.27	0.018	0.017	1.70		Buckling
5	B90N	1597	30	88.00	0.038	0.031	2.93		Tube rupture with shear sliding
	B90N-W	1182		65.00	0.033	0.027	2.16		Tube rupture with buckling
6	Control	822	30	-----					Compression failure

‡ The average value for 10 plain concrete cylinders' * the average ratio for two CFFT cylinders.

2.5.1 Behavior of CFFT cylinders

2.5.1.1 Failure mode

Figure 2-6 shows the failure mode for the three types of the CFFT cylinders. All specimens failed due to the rupture of the fiber in the hoop direction at the ultimate hoop stress, resulting from the dilation of the concrete. The fracture of the GFRP tubes occurred along the total height of the cylinders started from top or bottom and extended to the opposite direction. The shape of the failure was "zigzag" pattern normal to the direction of fibers in the hoop direction. Low sounds heard during the early-to-middle stages of loading were referred to the dilation, micro-cracking of concrete and offset of the aggregate. At higher levels of confining pressure; sounds were heard clearly due to rupture of the fibers in GFRP tubes. The ultimate failure was very explosive for specimens of tubes A and B; however, ductile failure was observed for tube C. The concrete fell out of the tube in a crushed state, immediately after failure especially for tubes A and B.

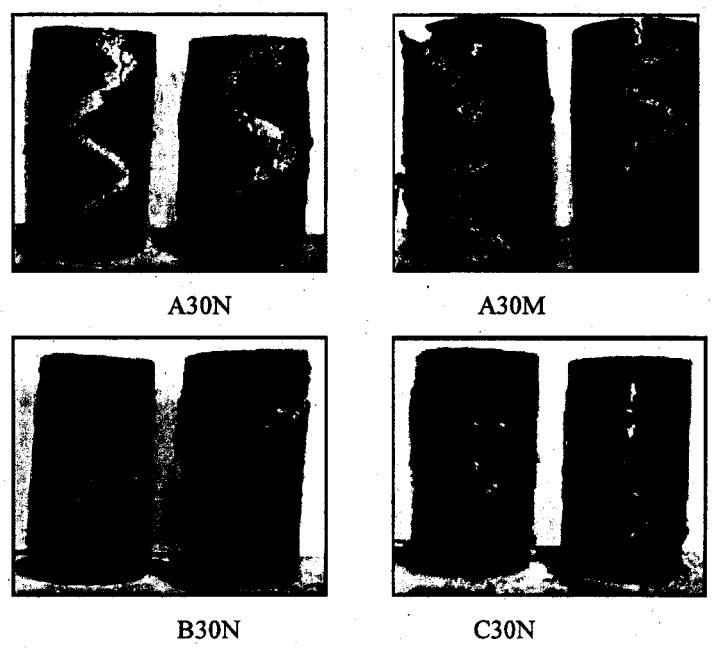

Figure 2-6 Failure mode of CFFT cylinders

2.5.1.2 Axial stress-strain relationship

The axial stress-axial and hoop strain behaviors for the CFFT cylinders are practically bilinear, as shown in Figure 2-7. The stress-strain curve at the first stages of loading is similar to the unconfined concrete. After achieving the approximate unconfined concrete strength, the stress-strain curve of CFFT cylinders get softened and eventually exhibit linear behavior until sudden failure due to the rupture of the GFRP tube. Figure 2-7 shows sharp transition for CFFT cylinders of tubes A and B, however gradual and smooth transition for tube C between the first and second stages of the stress-strain curve was observed.

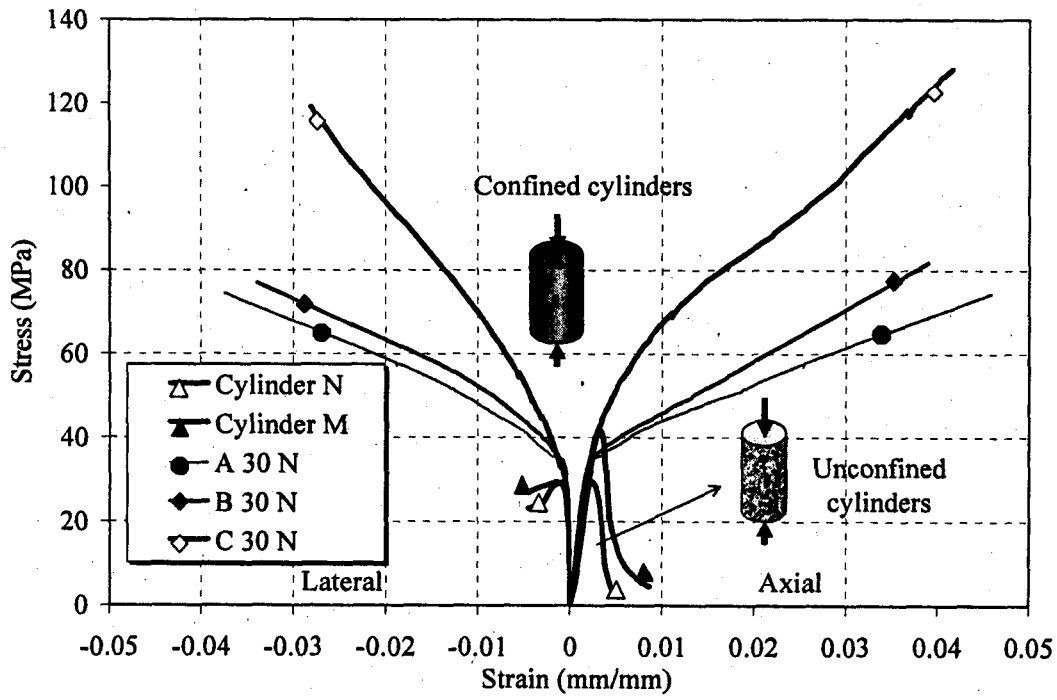

Figure 2-7 Stress-strain relationships for the plain and CFFT cylinders

2.5.1.3 Compressive strength:

The average ratios of confined to unconfined concrete strength (f'_{cc}/f'_c) were 2.42, 2.7, and 4.11 for CFFT cylinders casted in tubes A, B and C, respectively, with concrete mix type (N). As expected, significant enhancement of the strength as well as the ductility for the CFFT cylinders was achieved by increasing the thickness of FRP tubes. The maximum confined concrete strength was observed for specimen C30N-2 reaching up to 128 MPa (18.56 ksi). These results indicate that a 7.5% increase in the thickness of GFRP tubes (type B compared to type A), and a 142% increase (type C compared to type A), yield an increase of the (f'_{cc}/f'_c) ratios, of 12% and 70%, respectively, in average. Also, note that an increase of 50% of the compressive strength of concrete (Specimens A30M compared to specimens A30N), yields an increase of only 18 % for the confined compressive strength f'_{cc}, in average. Also, the (f'_{cc}/f'_c) ratios for A30M and A30N are equal to 1.90 and 2.42, respectively. This shows that the confinement action is more effective for normal, than medium strength concrete.

2.5.1.4 Dilation properties

Figure 2-8 shows the axial strain-dilation relationships for the CFFT cylinders. Dilation (η) is defined as the ratio of hoop strain (ε_{ch}) to axial strain (ε_{cc}).

$$\eta = \frac{\varepsilon_{ch}}{\varepsilon_{cc}}$$

The observed dilation behavior of the CFFT cylinders is consistent with the general dilation behavior discussed in previous studies by (Mirmiran and Shahawy 1997a; Shawn et al. 2005). At the first stage of loading, the confinement of the GFRP tubes was not fully activated. Therefore, the initial dilation rate remained relatively constant, with a value approximately equal to 0.3, 0.28 and 0.2 for CFTT cylinders A30N, B30N and C30N, respectively. It is clear that these values are similar to the Poisson's ratio of the unconfined concrete. In addition, the initial dilation ratios of the CFFT cylinders depend mainly on the concrete core. Increasing the load on the cylinders, the axial and hoop strains increased resulting from the micro-cracking of the concrete. At axial strain approximately equals 0.0015, 0.0018 and 0.0024 the dilation ratios increased rapidly

upward and approached to the peak value at axial strain approximately equal to 0.007, 0.011 and 0.01 for CFTT cylinders A30N, B30N and C30N, respectively. At this point, the confinement of the GFRP tube was fully activated. The peak dilation value is dependent on the stiffness of the GFRP tubes, whereas, the peak dilation values are 0.86, 0.77 and 0.58 for CFTT cylinders A30N, B30N and C30N, respectively. Figure 2-8 shows the effect of the tube thickness on the dilation ratios. The dilation rate decreased at all load levels with increasing the thickness of the tubes.

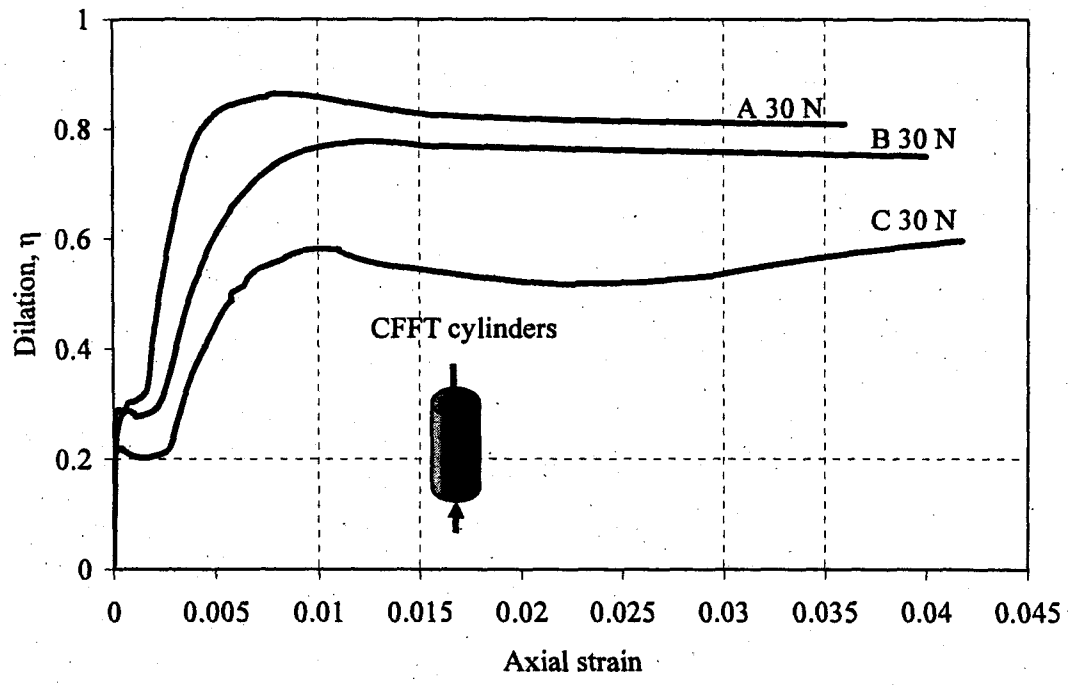

Figure 2-8 Experimentally observed dilation behavior for CFFT cylinders.

2.5.2 Behavior of CFFT Columns

2.5.2.1 Failure modes

Different failure modes were observed for the three slenderness ratios (4, 6 and 8), that are investigated in this study. Figure 2-9 shows the failure modes for CFFT columns of Groups No. 3 and 5 as well as that of the control specimen. First, for CFFT columns with

slenderness ratio (H/D = 4), specimen A60N was tested without using protective tie-steel-rap at its both ends. A premature failure for specimen A60N at 1302 kN (292.95 kip) was observed. The failure occurred at the top end of the specimen due to rupture of the tube accompanied by crushing of the concrete. The rupture of the tube extended to the third height of the specimen. Specimen A60M with protective tie-steel-rap failed due to the rupture of the tube, at higher ultimate load 1741 kN (391.725 kip) than specimen A60N. The increase in the strength resulted from using the steel-tie-rap at both ends of this specimen. Specimens A60N and A60M failed in compression without any buckling phenomenon, as expected.

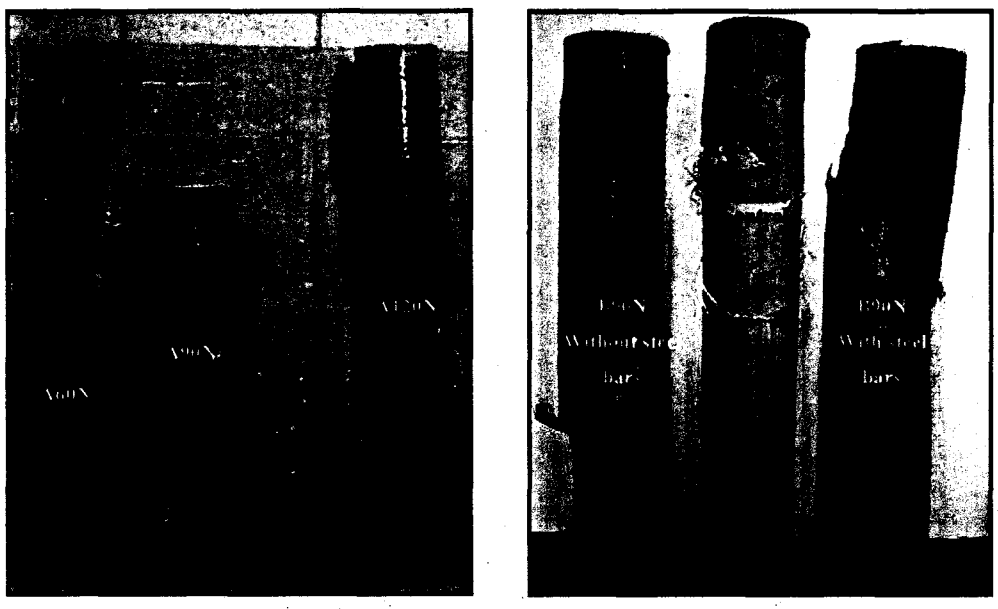

Figure 2-9 Failure modes of CFFT columns of Group No. 3, 5 and 6.

Second, for CFFT columns of slenderness ratio (H/D = 6), typical failure was generally observed by rupture of the tubes, between one end of the steel-tie-rap and the mid-height of the specimen. The failure occurred due to single curvature buckling mode, immediately followed by the rupture of the tube. Distortions of the cross section and outward bulging of the tube occurred near the mid height for all specimens before the failure. This was resulted from sliding of the concrete core and local buckling of the steel bars inside the tube. Snapping sounds were heard even after stopping the test and removal

of the specimens from the setup. This continued until the stored energy in the hoop direction and the interaction between fiber and the prestressed concrete core was released. Specimens A90N and A90M failed at ultimate loads of 1454 and 1595 kN (327.15 and 358.87 kip), respectively. The difference between these ultimate loads is due to the compressive strengths of the used concrete types. Shear failure occurred as the primary mode of failure for the specimen B90N-W. The ultimate load of specimen B90N is 35% higher than that of specimen B90N-W. It is the result of the dowel action of the steel bars which gives ductility to the concrete and resists the sliding of the concrete core inside the tube at 45 degree for specimen B90N. Compression failure occurred for the control specimen, whereas, vertical cracks were observed around the hoop direction at the bottom region of the column in a uniform pattern.

After 80 % of the ultimate loads, the horizontal deformation for specimens A120N and A120M started increasing until buckling with a single curvature occurred. At this load level, distortion of the cross section at the mid height occurred, and the load decreased with significant increase of the horizontal displacement. The failure mode for specimens with slenderness ratio (H/D = 8) was permanent, even after removal the load and without rupture of the GFRP tube.

2.5.2.2 Axial stress-strain relationship

The axial stress versus axial and lateral strains relationships for Groups No. 3 and 5 are shown in Figure 2-10 and Figure 2-11, respectively. The stress-strain behaviors for CFFT columns showed a typical bilinear response composed mainly of three regions; that are similar to the CFFT cylinders behaviors. The initial slope of the curves has a similar appearance to concrete core, regardless of the difference in the slenderness ratios. As shown in Figure 2-10, the bend point on the curves is at the same confinement stress level for all specimen of Group No. 3. Also, the ultimate hoop strains for CFFT specimens are similar to those of the spit disk tests of tube A and B. The response curve of specimen A120N becomes softer than that of specimens A60N and A90N, after the bend point. It is clear that the ultimate strain of specimen A90N is higher than that of specimen A120N.

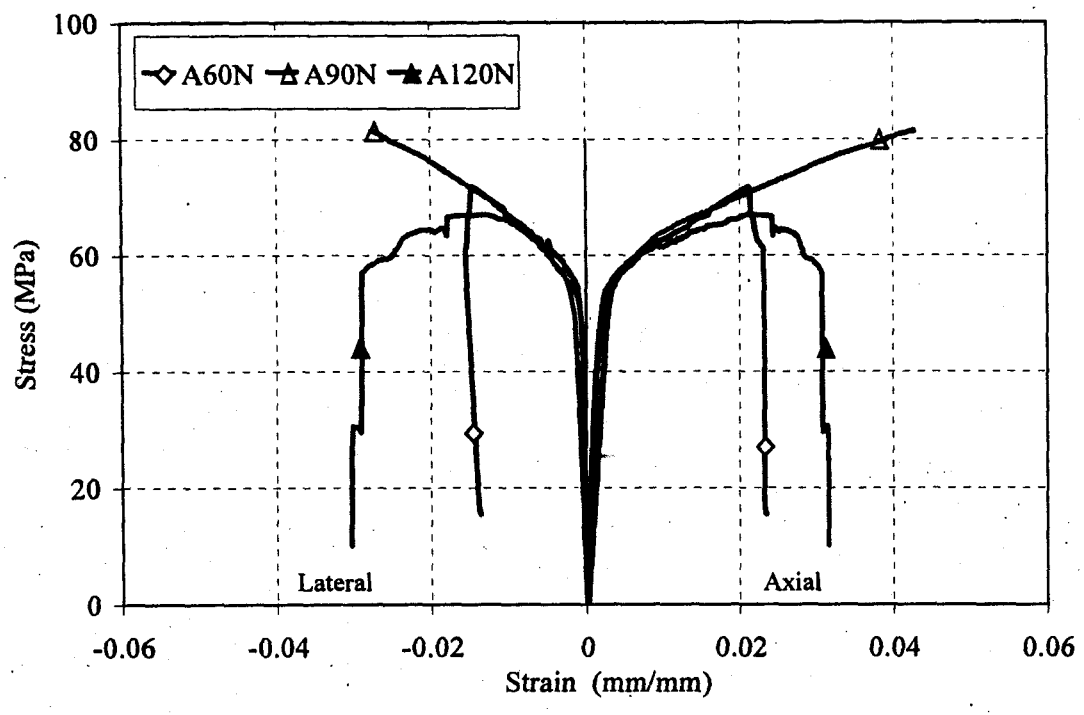

Figure 2-10 Stress-strain relationships for specimens of Group No. 3

Figure 2-11 compares the axial stress-axial and hoop strain behaviors of CFFT columns with and without internal longitudinal steel reinforcement, which are also compared to the control specimen (confined using spiral steel). It is significantly clear that the enhancement in the ductility of the CFFT columns increased due to the confinement action provided by steel reinforcement. The maximum strains for the control and CFFT columns are approximately 0.002 and 0.035 respectively. On the other hand, the bend point for specimen B90N is higher than that of specimen B90N-W, because of the contribution of the longitudinal steel bars, as expected.

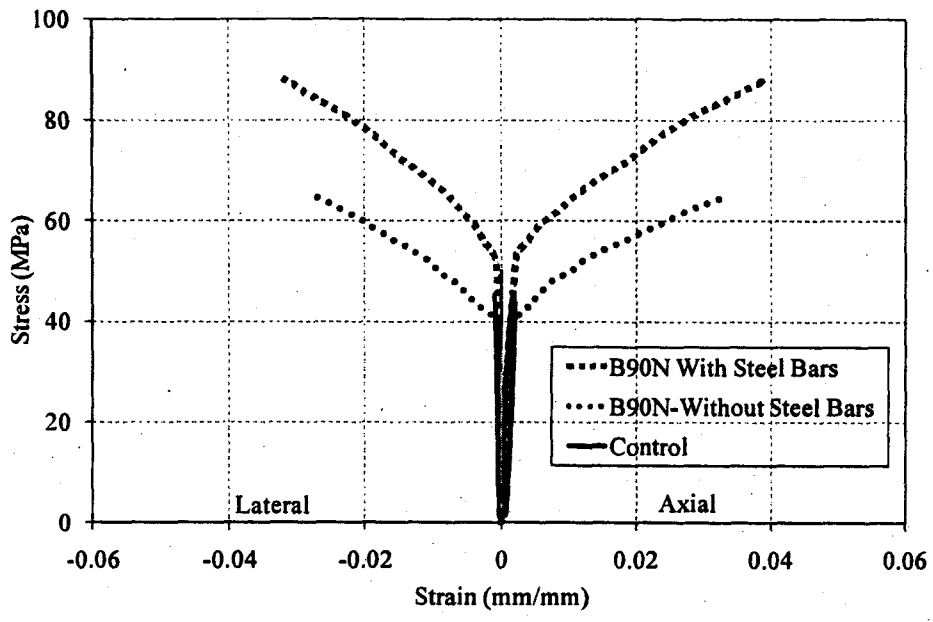

Figure 2-11 Stress- strain relationships (Group No. 5 and 6)

2.5.2.3 Compressive strength

Figure 2-12 presents the relationship between the ultimate load capacity and the slenderness ratio for the CFFT columns of Group No. 4. Note that while doubling the slenderness ratio from 2 (specimen A30M) to 4 (specimen A60M), an increase of 12 % in average, in the ultimate-load-carrying capacity is achieved by using internal steel reinforcement. The ultimate-load-carrying capacity of specimen A30M is approximately the same when using a slenderness ratio equal to 6 and internal steel reinforcement (specimen A90M). A 13% reduction of the ultimate load carrying capacity is observed when using a slenderness ratio equal to 8 (specimen A120M compared to specimens A30M). Generally, the ultimate load capacities for all specimens of Group No.4 are higher than specimens of Group No.3, due to the difference in the concrete compressive strength used for each group. On the other hand, the ultimate strength of CFFT specimen with longitudinal steel bars (B90N) is higher than for specimen without longitudinal steel bars (B90N-W). The increase in the ultimate strength is resulting from the dowel action of the steel bars, which prevents the sliding of the concrete core. The steel bars also improve the flexural capacity of the CFFT specimens to resist the induced moments resulting from the lateral deformation

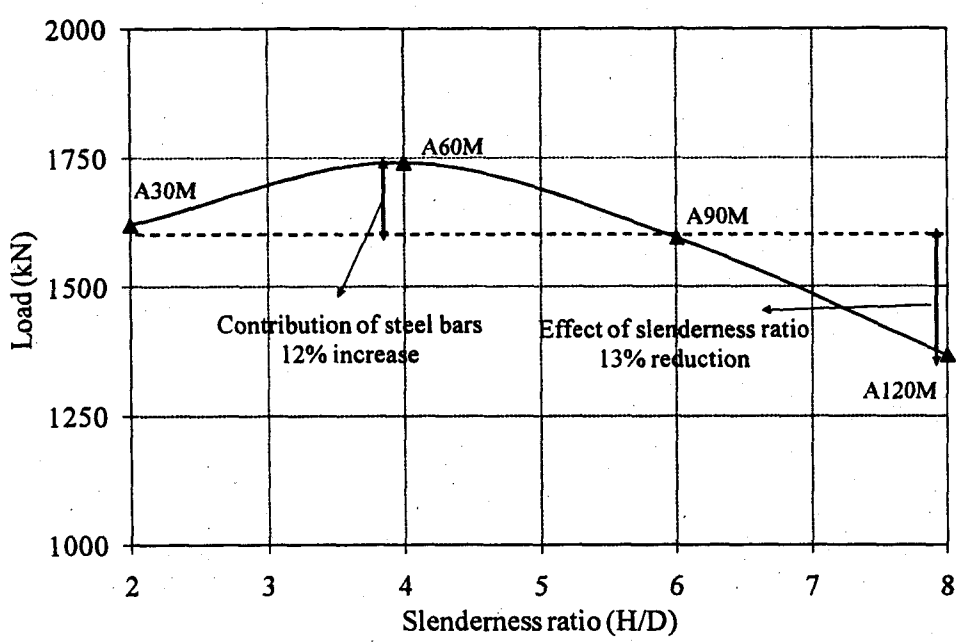

Figure 2-12 The relationship between the axial load and slenderness ratio

2.5.2.4 Axial displacement

The load versus axial displacement curve for specimens of Group No. 4 is shown in Figure 2-13. It is clear that the initial tangent modulus for specimens A60M and A90M is slightly higher than that of specimen A120M. The axial displacement increased slowly and showed a linear response up until yielding or softening stages. Yielding occurred at almost the same load level for all specimens. After that level, the axial displacement increased rapidly up to failure. However, in the case of *H/D* equal to 8 for specimen A120M no gain in the load carrying capacity was achieved after yielding. Also, due to the small slenderness ratio (*H/D = 4*) for specimen A60M, the maximum axial displacement was significantly low 17.54 mm (0.69 in) compared to the other specimens.

Energy absorption is one of the important deformational characteristics of concrete structure to determine the ductility of the structure. The energy absorption was determined as the area under the load displacement curve. The integration of the area

under the load-displacement was performed numerically from the experimental data of the load versus displacement along the whole load history. The values of the energy absorption for the control, B90N-W and B90N specimens are 2.668, 26.478 and 41.516 kN.m (1.968, 19.54 and 30.63 ft.·kipf) , respectively. The energy absorption for the B90N-W and B90N specimens is 9.92 and 15.5, respectively, times that of the control specimens. The ductility indexes of the CFFT specimens were much higher than that of the control specimen. This observation confirms the superior ductile response of the CFFT columns than that of the reinforced concrete columns. In addition, the energy absorption for the B90N specimens is 1.56 times that of the B90N-W specimens. This observation confirms the importance of the longitudinal steel reinforcement to increase the ductility of the CFFT columns.

2.5.2.5 Lateral displacement

The lateral displacement produces additional moment on the column and reduces the ultimate load carrying capacity of the specimens. Figure 2-15 shows the axial load-lateral displacement relationships for specimens A120N and A120M. It is clear that the lateral displacement approached to zero up to load level 85% of the ultimate load. After that level, the lateral displacement started to increase rapidly up to the ultimate load. Beyond the ultimate load, the lateral displacement increased progressively with a significant decrease in the load until buckling of a single curvature was occurred. Also, Figure 2-15 shows the effect of the concrete strength on the ultimate load capacity of the two specimens. Whereas, the ultimate load of specimen A120M is 13.73% higher than that of specimen A120N. On the other hand, the lateral displacement of 912 mm-height specimens was observed immediately before the failure. However, the lateral displacement for 610 mm-height specimens was not significant up to failure.

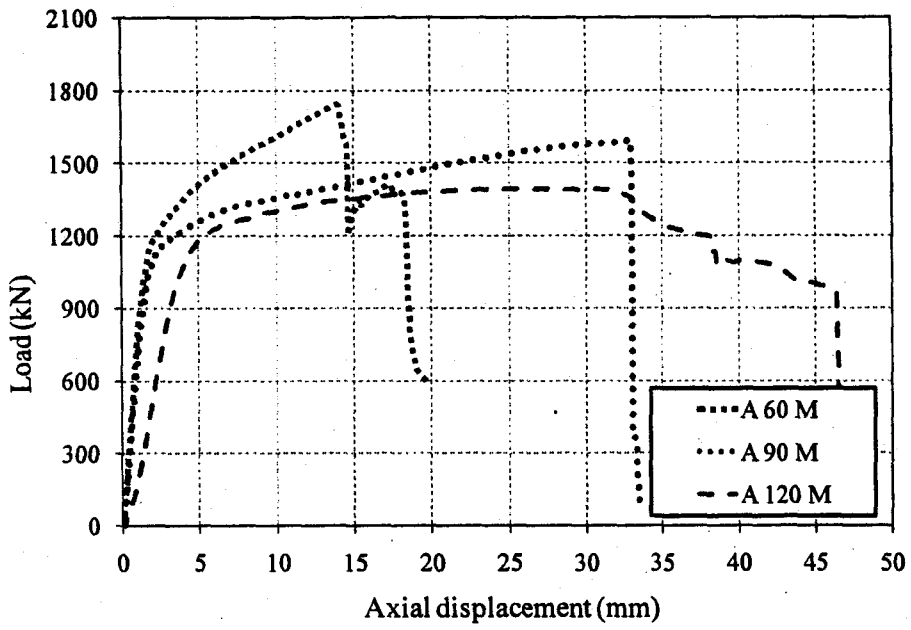

Figure 2-13 Axial load-axial displacement relationships

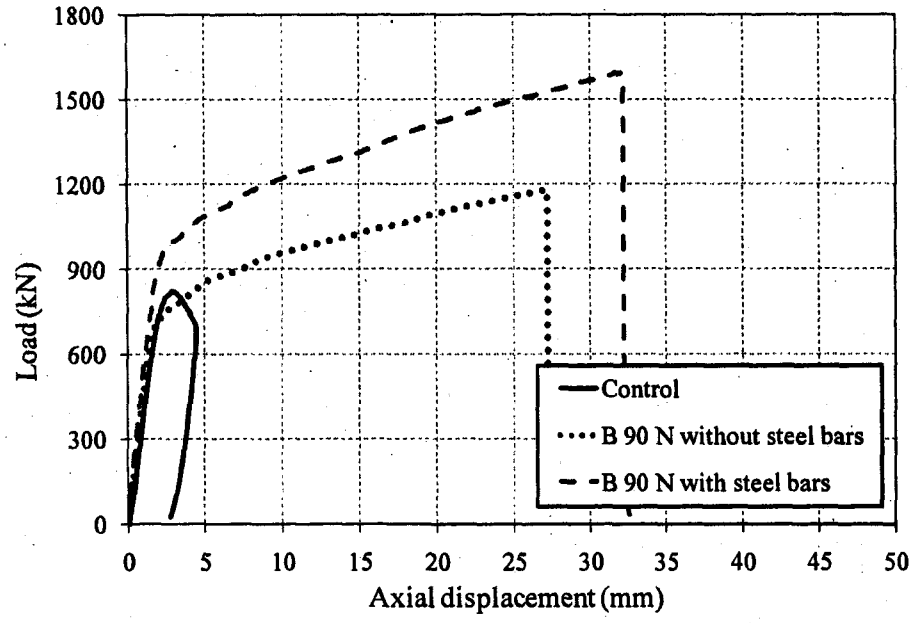

Figure 2-14 Axial Load-axial displacement relationships

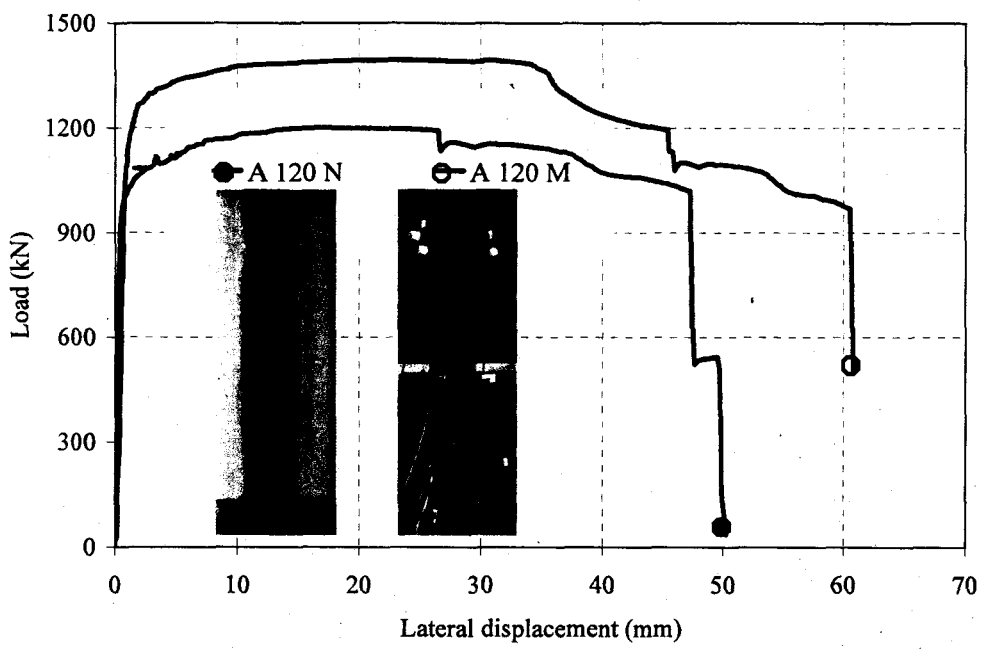

Figure 2-15 Load-lateral displacement relationships

2.5.2.6 Confinement effect on the load-strain relationship of steel reinforcement

In order to capture the deformation behavior of steel reinforcement inside the CFFT columns, two steel bars were instrumented for each specimens of Groups No. 3 and 4. Figure 2-16 and Figure 2-17 present the relationship between the axial load on the columns and axial strain in the longitudinal steel bars for specimens of Group No. 3 and 4, respectively. The curve for each specimen was cut as shown in Figure 2-16 and Figure 2-17 by dashed line. This line presents the failure of the strain gauges. The load-strain curve exhibited a linear response until earlier yielding of the steel bars approximately at strain equals 0.002, and at 65-75% of the ultimate load capacity.

The yield loads for specimens A60N, A90N and A120N are equal to 985, 944 and 966 kN (221.6, 212.4 and 217.35 kip), respectively, while for specimens A60M, A90M and A120M the yield load are equal to 1250, 1136 and 1147 kN (281.25, 255.6 and 258 kip), respectively. It appears that the yield loads occurred at the same concrete stress level

of $1.25f'_c$ for different slenderness ratios. It can be concluded that the yield load of the steel bars inside CFFT specimens depends mainly on the unconfined concrete compressive strength. Therefore, the importance of the longitudinal steel bars in CFFT column is not only to increase the strength but to improve the flexural and shear capacity of the CFFT columns. The yield strain of the steel bars for control specimen occurred at 0.002, accompanied by the failure of the specimen. The load-strain curves for CFFT specimens presented reverse action due to the expected local buckling of the steel bars at yielding, after that the strain was continued aggressively in the horizontal direction up to failure.

2.5.2.7 Dilation properties

Figure 2-18 shows the dilation ratio versus axial strain for the CFFT columns of Group No.5. It is obvious that the initial dilation ratios for the two CFFT specimens with and without internal reinforcement appear to be the same and equals 0.3. Whereas, at the first stages of the loading, the axial load was carried by the concrete core and the GFRP tube was not fully activated. At axial strain approximately equals 0.003, the dilation ratios increased rapidly and approached to the peak value at axial strain approximately equals 0.007. After that level, the dilation value remained constant for specimen B90N, while a decrease was observed for specimen B90N-W up to the failure. The peak dilation ratio of specimens B90N-W and B90N is 0.92 and 0.70, respectively. It is clear that the peak dilation of specimen B90N-W 1.31 times that of specimen B90N. This presents contribution of the longitudinal steel bars inside the CFFT columns to increase the shear capacity of the CFFT specimens.

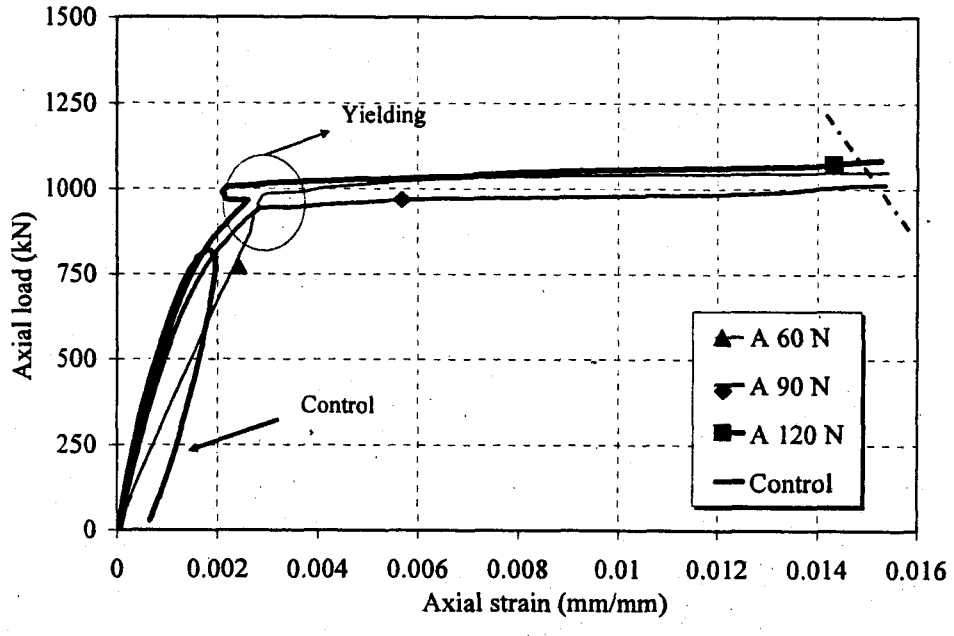

Figure 2-16 The relationship between the axial load on the column and axial strain in the longitudinal steel bars (Group No. 3 and 6)

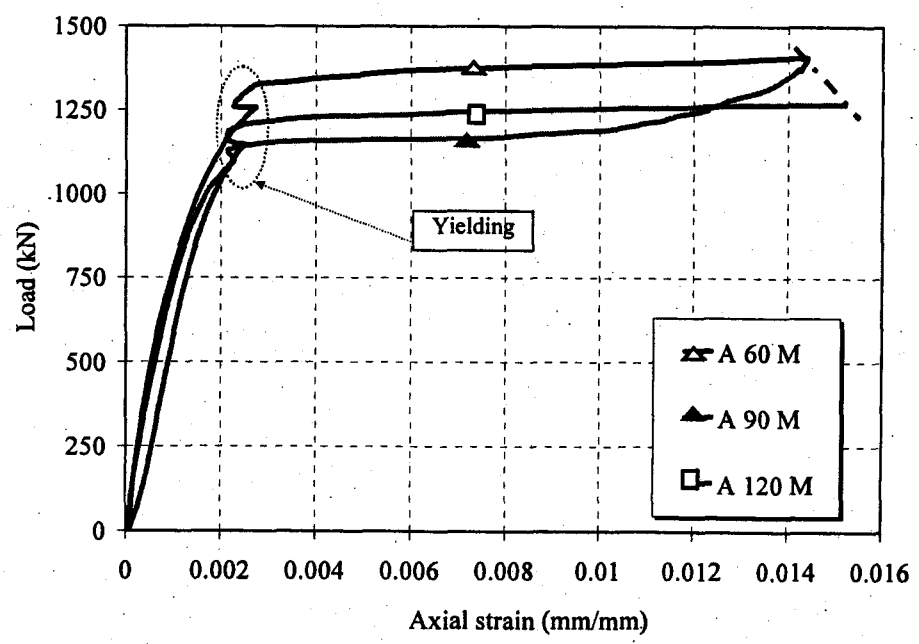

Figure 2-17 The relationship between the axial load on the column and axial strain in the longitudinal steel bars for specimens of Group No. 4

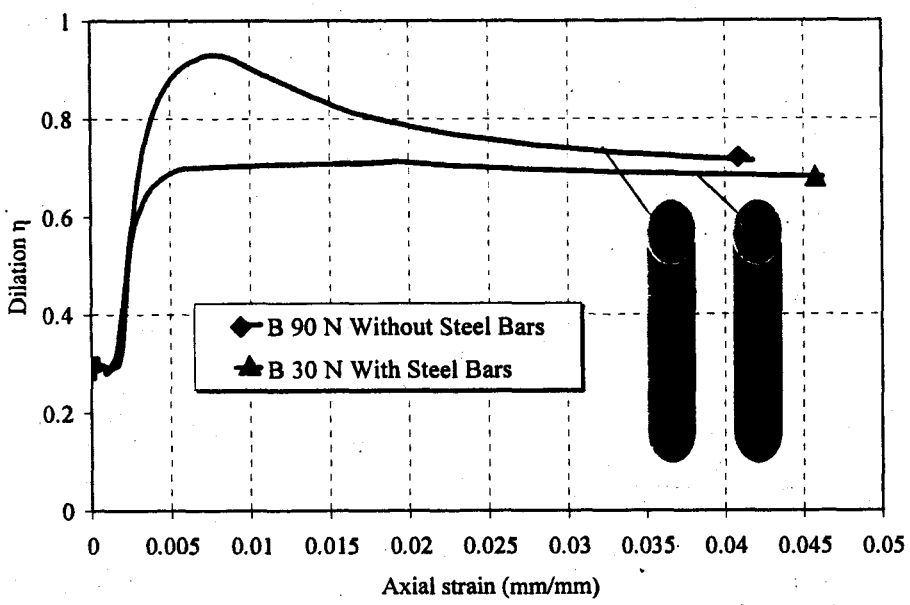

Figure 2-18 Experimentally observed dilation behavior for specimens of Group No. 5.

2.6 Conclusions

The behaviors of small and medium internally reinforced CFFT columns with different slenderness ratios under concentric axial loading and two types of concrete were presented. The experimental results for 20 unconfined cylinders, eight CFFT cylinders, eight CFFT columns and one control specimen were investigated. The slenderness ratios ranged between 2, 4, 6 and 8 were examined in the present study. The findings of this research can be summarized as follows:

- The longitudinal steel bars provided significant dowel action, which delayed the dilation of concrete core inside CFFT, thereby improving the ductility of CFFT columns.
- The ultimate strengths of the CFFT columns were mainly dependent on the hoop stiffness of the GFRP tubes, and it was more effective for normal than medium strength concrete.
- The failure modes for CFFT are affected by the slenderness ratio.

- Increasing the slenderness ratio (*H/D*) of the reinforced CFFT specimens more than six significantly reduces the ultimate load carrying capacities due to the buckling phenomenon.
- The average ultimate rupture strain of the GFRP tubes is close to the rupture strain obtained from split-disk test.

Notation

The following symbols are used in this paper:

E_X	= Young's modulus in the longitudinal direction of the FRP tubes (MPa)
E_Y	= Young's modulus in the hoop direction of the FRP tubes (MPa)
H	= height of the specimens (mm)
D	= diameter of the FRP tube (mm)
t	= thickness of FRP tube (mm)
f'_{cc}	= confined concrete compressive strength (MPa)
f'_c	= unconfined concrete compressive strength (MPa)
ε_{cc}	= ultimate axial strain of the confined CFFT specimens
ε_{ch}	= ultimate hoop strain of the confined CFFT specimens
ε_c	= ultimate axial strain of the unconfined concrete cylinders
P_{Max}	= Maximum axial load (kN)
η	= Dilation ratio

Chapter 3
Axial Load Capacity of Concrete-Filled FRP Tubes Columns: Experimental versus Theoretical Predictions

1 Abstract

This paper presents the experimental and theoretical results of small and medium-scale concrete filled fiber-reinforced polymer (FRP) tubes (CFFT) columns. A total of 23 CFFT specimens were tested under axial compression load. Five different types of new FRP tubes were used as stay-in-place formwork for the columns. The effects of the following parameters were examined: the FRP-confinement ratio, the unconfined concrete compressive strength, the presence of longitudinal steel reinforcement, and the height to diameter ratio. Comparisons between the experimental test results and the theoretical predictions values by the three North American codes and design guidelines (ACI 440.2R 08, CSA-S6-06 and CSA-S806-02) are performed in terms of confined concrete strength and ultimate load carrying capacity. The results of this investigation indicate that the design equations of the ACI 440.2R-08, CAN/CSA S6-06 and CAN/CSA S806-02 overestimate the factored axial load capacity of the short CFFT columns as compared to the yield and crack load levels. Also, the CAN/CSA S6-06 and CAN/CSA S806-02 confinement models showed conservative predictions, while the ACI 440.2R-08 was slightly less conservative. A new confinement model is proposed for the confined concrete compressive strength of the CFFT cylinders. Also, the design equations are modified to accurately predict the ultimate and yield loads capacities of internally reinforced and unreinforced short CFFT columns. Two new factors are

introduced in the modified equations, (k_{cc}) accounts for the in-place-strength of CFFT columns to CFFT cylinder strength, and (k_{cr}) accounts for the initiation of the steel yielding and concrete cracking for the FRP-confined columns.

3.2 Introduction

Fiber-reinforced polymer (FRP) composite materials have recently been used as internal and external reinforcement in the field of civil engineering constructions. It has been used as internal reinforcement for beams, slabs and pavements (Masmoudi et al. 1998; Benmokrane et al. 2006), and also as external reinforcement for rehabilitation and strengthening different structures (Demers and Neale 1998). In addition, the concrete-filled FRP tubes (CFFT) technique has been used successfully for different concrete structures. The most highly developed application to date is the use of CFFT as pier column and girder for bridges (Fam and Mandal 2006; Son and Fam 2008), also as fender piles in marine structures (Karbhari 2004). FRP tubes provide different advantages such as confinement, protecting the concrete from aggressive environments, act as permanent formwork, and provide shear and/or flexural reinforcement. In some of the field applications, CFFT has also been utilized as a compression and flexural members without internal reinforcement (Karbhari et al. 2000). Experimental investigations of the axial behavior of the CFFT columns have generally been carried out without using internal longitudinal reinforcement. While there is abundant experimental and theoretical research information on the small scale specimens (mainly FRP-concrete cylinders), there is few data on the behavior of medium and large scale CFFT columns (Saafi et al. 1999; Sheikh et al. 2007). In addition, limited experimental works have been carried out on specimens with internal longitudinal reinforcements (Zhu et al. 2005; Mohamed and Masmoudi 2008a, b and c).

During the last two decades, a number of confinement models were developed for circular CFFT and FRP wrapped cylinders to predict the ultimate confined concrete compressive strength (Samaan 1998; Lam and Teng 2003 and 2004). These models have been utilized to predict the ultimate axial load of non-slender, normal weight concrete columns confined with FRP jackets by different design guidelines. The current North

American codes and design guidelines provide design equations for the short circular columns strengthened or retrofitted with the FRP confinement wrapping (ACI 440.2R 2008; CSA-S806-02; CSA-S6-06). In fact, all of the mentioned codes and design guidelines were introduced to strengthen or rehabilitate the existing steel reinforced concrete columns. In addition, they are based on the confined concrete compressive strength resulting from the FRP wrapping and neglecting the effect of the existing transverse steel reinforcements. However, the presence of the existing internal longitudinal and transverse steel reinforcements leads to conservative design. Despite the difference between the structures of the fibers in the tubes and sheets which are used to confine the concrete columns, the previous studies have shown that the behavior of CFFT is similar to those of wrapped concrete columns. On the other hand, for FRP-wrapped concrete, different research works have been conducted to evaluate the confinement models of the different codes to predict the confined concrete compressive strength (Bisby et al. 2005; Carey and Harries 2005; Chaallal et al. 2006). However, more research work is still needed to evaluate the design equations of the different codes and design guidelines to predict the ultimate load capacities of the reinforced and unreinforced short CFFT columns.

3.3 Objectives

Generally, in the CFFT columns technique, FRP tubes act mainly as the transverse reinforcement and its axial resistance is neglected due to the local buckling of the fibers. Regarding the design provisions adopted by several structural concrete design codes, concrete columns must contain minimum amounts of longitudinal reinforcements. In this study, twenty three reinforced and unreinforced specimens were tested under axial load to provide a better understanding of the behavior of the CFFT columns. The objectives of this paper can be summarized as follows:

- To evaluate the compression behavior of small and medium-scale CFFT columns under pure axial load, using new filament wound GFRP tubes.
- To evaluate the confinement models and the design equations provided by the three different North American codes and design guidelines (ACI Committee

440.2R 08, CAN/CSA-S6-06 and CAN/CSA-S806-02), for the predictions of the confined concrete compressive strength and the ultimate load capacities of the short CFFT columns.

- To propose new model and appropriate modifications to the existing design equations for the reinforced and unreinforced short (non-slender) CFFT columns.

3.4 Experimental Program

3.4.1 Properties of materials

Two types of reinforcing steel bars were used in this study: deformed steel bars No. 10M and 13M, (nominal diameter 11.3 and 12.7 mm, respectively). The mechanical properties of the steel bars were obtained from the standard tests carried out according to ASTM A615/A615M-09 (ASTM 2009), on five specimens for each type of the steel bars. The results indicated that the yield tensile strengths were 462 MPa and 360 MPa, also the ultimate tensile strengths were 577 MPa and 538 MPa for steel bars No. 10M and 13M, respectively. On the other hand, new filament wound FRP tubes manufactured from glass fiber and epoxy resin were used as structural stay in place formwork for the columns. Five types of the FRP tubes have been used in this study with different thicknesses and diameters.

Table 3-1 shows the dimensions, mechanical properties and the details for each tube. The winding angles of the tubes A, B and D were optimized for the underground pipe applications. While tubes C and E were designed for pipe telecommunication applications. The split-disk test was performed according to ASTM D-2290-08 (ASTM 2008a), on five specimens for tubes Type A, B and C. The load-strain relationships for the split-disk test are shown in Figure 3-1. The test results for those tubes were compared against the theoretical results of the classical laminate theory using the software (Laminator). The theoretical results showed good agreement with the test results. Based on this agreement, the software was used to predict the tensile strength in the hoop direction for tubes Type D and E. Also, the coupon tensile test was performed according to ASTM D 638-08 (ASTM 2008b) standard, on five specimens from each type of the

tubes (Type A, B, C, D and E). All CFFT specimens were fabricated from two concrete batches (1 and 2) to take into consideration the effect of concrete strength on the compressive behavior of the CFFT columns. The target strength of the first and second batches was intended to provide 30 MPa and 45 MPa, respectively.

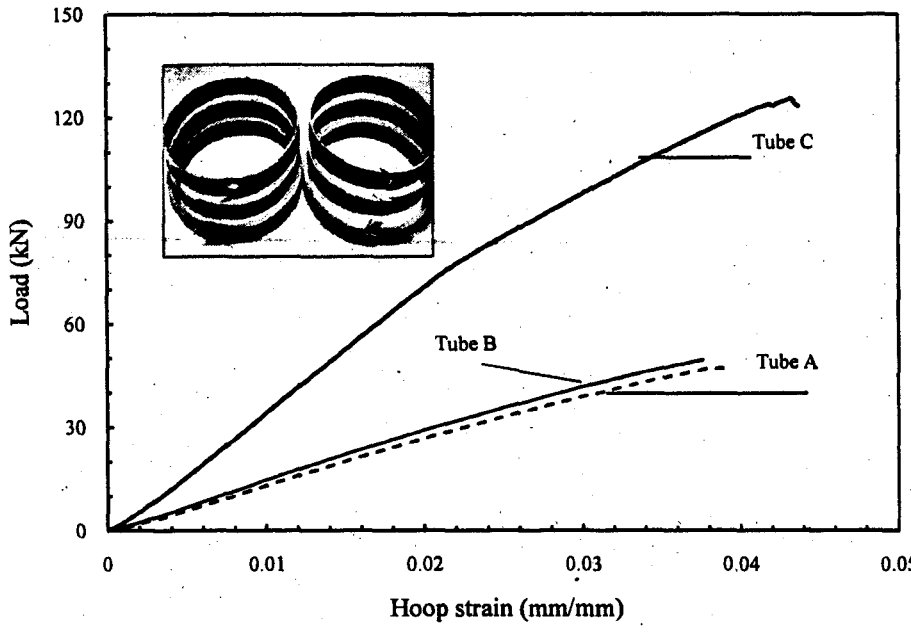

Figure 3-1 Load-strain (hoop) behavior of the FRP tubes for the split-disk test

Table 3-1 Dimension, details and mechanical properties of the FRP tubes

Tube type	D (mm)	t_{FRP} (mm)	No. of layers	Stacking sequence	E_{FRP} *(MPa)*	F_{FRPu} *(MPa)*	E_x (MPa)	F_x (MPa)
A	152	2.65	6	$[\pm 60]_3$	20690§	345§	8785*	57.90*
B	152	2.85	8	$[\pm 60]_4$	20860§	370§	8787*	59.76*
C	152	6.40	14	$[\pm 65_3, \pm 45, \pm 65_3]$	23630§	390§	9270*	60.15*
D	213	2.90	6	$[60, 90_4, 60]$	32260†	537†	8865*	55.16*
E	213	. 0	12	$[\pm 60, 90, \pm 60, 90_6]$	30200†	498†	7897*	59.24*

E_x and E_{FRP} are, respectively, the Young's modulus in the longitudinal and hoop directions; F_x and F_{FRPu} are, respectively, the ultimate tensile strength in the longitudinal and hoop directions; † Calculated using lamination theory; *Based on coupon test; § Based on split-disk test

3.4.2 Specimen preparation

For a compression member in a non-sway frame, the effective slenderness ratio (kH/r) is used to determine whether the column is short or slender. For this calculation, H is the unbraced length of the column, k is the effective length factor for the compression element and r is the radius of gyration. The effect of slenderness can be ignored for short columns as reported in ACI 318-08 and CSA S6-06 if (kH/r) is less than 22. For circular section, the radius of gyration, r, is equal to 0.25 times the diameter (D). The slenderness ratio (kH/r) can then be calculated for the fixed-fixed end conditions with $k = 0.5$ which leads to $(H/D \leq 11)$. Based on this limitation, the test matrix for this particular study was limited to the short columns subjected to concentric axial loads with height to diameter ratio (H/D) ranging from 2 to 7. These values were designed to avoid the effect of the slenderness ratio (buckling instability) on the behavior of the CFFT columns. The CFFT specimens were classified into five series, Table 3.2 shows the details for each specimen in each series. The following parameters were considered in the experimental test program: (1) Concrete strength, (2) FRP tube thickness, (3) The presence of longitudinal steel reinforcement and (4) Height to diameter ratio.

Series (I) consists of twelve CFFT cylinders (152x305 mm) with slenderness ratio (H/D) equal to 2. The specimens of this series are identified in Table 3-2, (column No. 2). The first letter indicates the tube type used from Table 1, the first number indicates the unconfined concrete compressive strength of batch No. 1 (30 MPa) or No. 2 (45 MPa), the second number indicates the replica of this specimen. The slenderness ratios (H/D) for the CFFT specimen's of Series II, III, IV and V varied from 4 to 7. The specimens notations are identified as follows: the first letter indicates the tube type, the first number indicates the height of the specimens in (cm), the second letter indicates the presence of steel bars (S) or without longitudinal steel reinforcement (W), and the second number indicates the unconfined concrete compressive strength of batch No. 1 or 2. Three series of the test matrix were designed with internal steel bars. Specimens of Series (II and III) were reinforced with six deformed steel bars No. 10M, with reinforcement ratio equal to 3.30%, while specimens of Series (IV) were without internal bars. Specimens of Series

(V) were reinforced with six deformed steel bars No. 13M, with reinforcement ratio equal to 2.17%. The steel bars were distributed uniformly inside the cross section of the tube. The bars were welded at the top and bottom by two steel stirrups with 3.2 mm diameter, to fix the bars inside the tube during casting. Figure 3-2 shows the typical steel cage which has been used to reinforce the CFFT specimens.

3.4.3 Instrumentation and test setup

Internal and external instrumentations were used in this study to capture the local strain distributions of the CFFT specimens. Before casting, two of the longitudinal steel bars were installed with electrical resistance strain gauges at the mid height. Also, before testing, axial and lateral strain gauges were mounted, along the hoop directions on the external surface of the specimens at the mid and quarter height. Figure 3-3 shows the schematic of the test setup in addition to the instrumentation layout used during the test. The specimens were tested using a 6,000 kN capacity testing Forney machine.

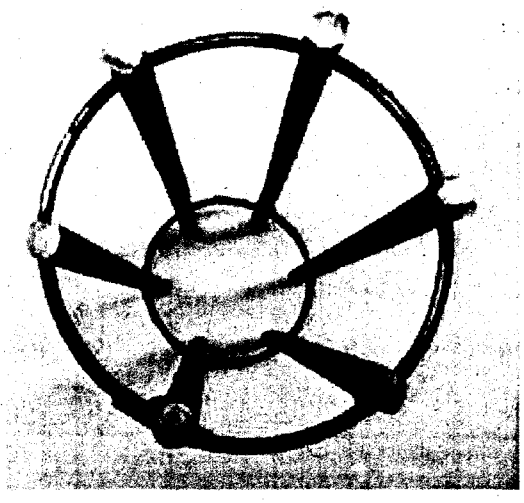

Figure 3-2 Typical steel cages for CFFT specimens

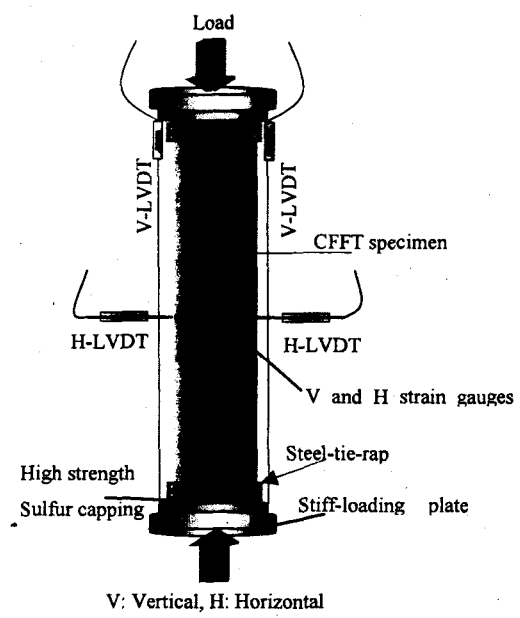

Figure 3-3 Schematic of the test setup

3.5 Experimental Results

3.5.1 Stress–axial and hoop strains behavior

The stress-axial and hoop strains behavior for the CFFT cylinders are practically bilinear, as shown in Figure 3-4, (a and b). The stress–strain curve at the first stages of loading is similar to the unconfined concrete. Stress-strain hardening behavior occurred after achieving the approximate unconfined concrete strength, and eventually exhibit linear behavior until sudden failure due to the rupture of the tube. It is clear that a significant enhancement of the strength as well as the ductility for the CFFT cylinders was achieved by increasing the thickness of FRP tubes. Table 3-2 shows the test results for the confined concrete compressive strength, f'_{cc}. Table 3-3 presents a summary of the experimental test results in terms of the maximum axial load (P_{max}), the yield load (P_y), the confined compressive strength at yielding stages, f'_{ccy} for the short reinforced and unreinforced CFFT columns. The f'_{cc} values were obtained using Equations 3-1.a and 3-1.b for unreinforced and reinforced specimens respectively. Also, Equations 3-1.c was used to present the confined compressive strength at yielding level.

$$f'_{cc} = \frac{P_{Max}}{A_g} \qquad 3\text{-}1.a$$

$$f'_{cc} = \frac{P_{Max} - f_y A_s}{A_g - A_s} \qquad 3\text{-}1.b$$

$$f'_{ccy} = \frac{P_y - f_y A_s}{A_g - A_s} \qquad 3\text{-}1.c$$

Depending on the level of the confinement, the ACI 440 2R-08 supported by (Rocca et al. 2008) classified the stress-strain behavior of the reinforced concrete column to unconfined, lightly confined, heavily confined with softening, and heavily confined with hardening. The stress versus axial and lateral strain relationships for specimens of Series (IV) are shown in Figure 3-4.c. This figure presents typical stress-strain behavior for all tested CFFT columns in this study. The stress–strain behavior showed a typical quasi-bilinear response composed mainly of three regions that are similar to the CFFT cylinders behavior. The initial slope of the curves has a similar appearance to concrete core. As shown in Figure 3-4.c, the bend point on the curves depends mainly on the unconfined concrete compressive strength. According to the ACI 440.2R-08 classification, the uniaxial stress-strain curves of the reinforced and unreinforced CFFT columns in this study can be characterized as heavily confined with hardening.

Figure 3-5 presents typical load-axial strain behavior for the longitudinal steel bars for two specimens of each concrete batch (1 and 2). The dashed lines at the end of the curves represent the failure of the strain gauges. The load-strain curve exhibited a linear response until yielding of the steel bars occurred at strains approximately equal to 0.002, and for load level that ranged from 43 to 72% of the ultimate load capacities of the columns. Table 3-3 presents the yield load for the reinforced concrete columns, the ratio of this load to the ultimate load, and the ratios of the confined concrete compressive strength at the yield level f'_{ccy} to the unconfined concrete compressive strength f'_c. This indicates that, in average the yield load occurred at $1.21\,f'_c$ and $1.66\,f'_c$ for CFFT columns with normal (tubes Type A, B and D) and high (tubes Type C and E) FRP volumetric ratio, respectively. It can be concluded that the confinement using FRP tubes delayed the start of steel bars yielding. Also, the increase in the FRP volumetric ratio

increases significantly the level of the confined strength at the yielding f'_{ccy} as compared to the unconfined concrete compressive strength f'_c.

3.5.2 Failure modes

Figure 3-6 shows the failure modes for the three types of the CFFT cylinders (Series I). The cylinder specimens failed due to the rupture of the fibers in the hoop direction. The ultimate failure was very explosive for specimens of tubes Type A and B (thickness 2.65 and 2.85 mm, respectively); however, ductile failure was observed for tube Type C (thickness 6.40). Figure 3-7.a shows the different failure modes which were observed for specimens of Series II to IV. A sudden compression failure for specimens of Series (II and III) was observed at the ultimate load. Typical failure was generally characterized by the rupture of the tubes between one end and the mid-height of the specimen. The failure occurred due to the local buckling of the steel bars immediately followed by the rupture of the tubes. On the other hand, shear failure occurred as the primary mode of failure for specimens of Series (IV), which were without internal reinforcements. The ultimate load of Specimen (B90S30) of Series (III) was higher than that of Specimen (B90W30) of Series (IV). It is the result of the dowel action of the steel bars which gave ductility to the concrete and resisted the sliding of the concrete core inside the tube at 45 degree.

Horizontal deformation was observed for specimens of Series III to IV just before the failure occurred. In fact, it was observed that the concrete compressive strengths (30 MPa or 45 MPa) did not affect the mode of failure of the tested specimens of this study. Figure 3-7.b shows the failure modes for the specimens of Series (V). At 90% of the ultimate load, the horizontal deformation increased and the failure occurred due to the rupture of the FRP tubes. The rupture was through the total height of Specimen (E150S30, FRP tube thickness 6.40 mm), while it was only at the mid height of Specimen (D150S30, FRP tube thickness 2.90 mm).

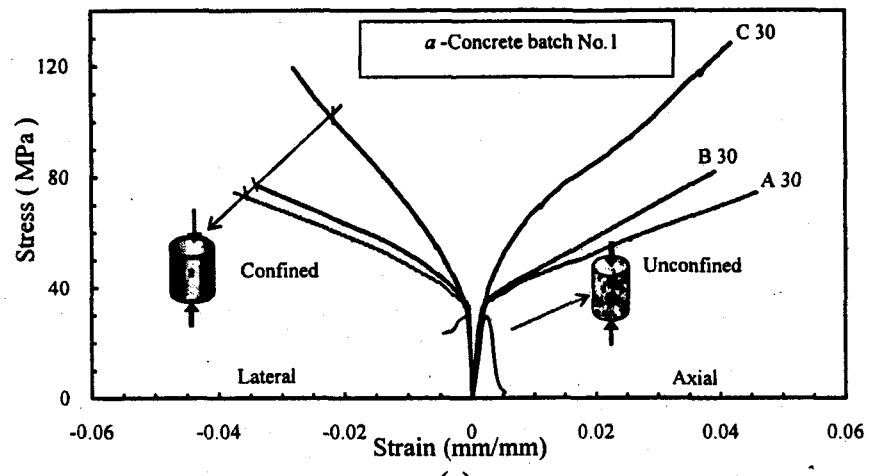

(a)

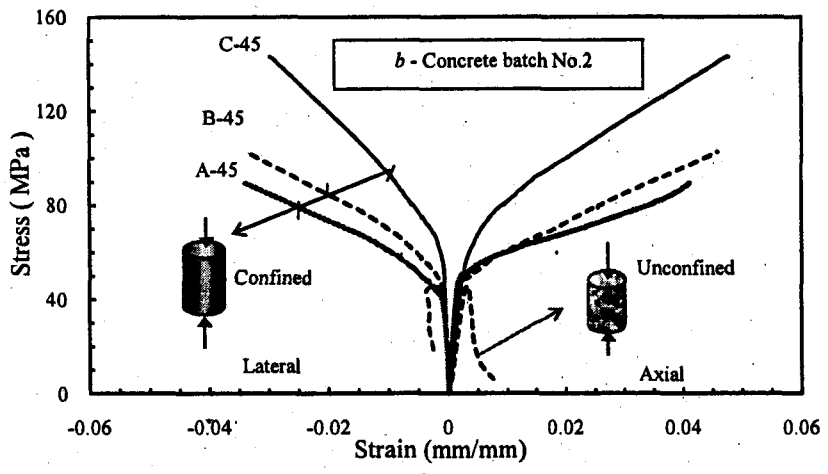

(b)

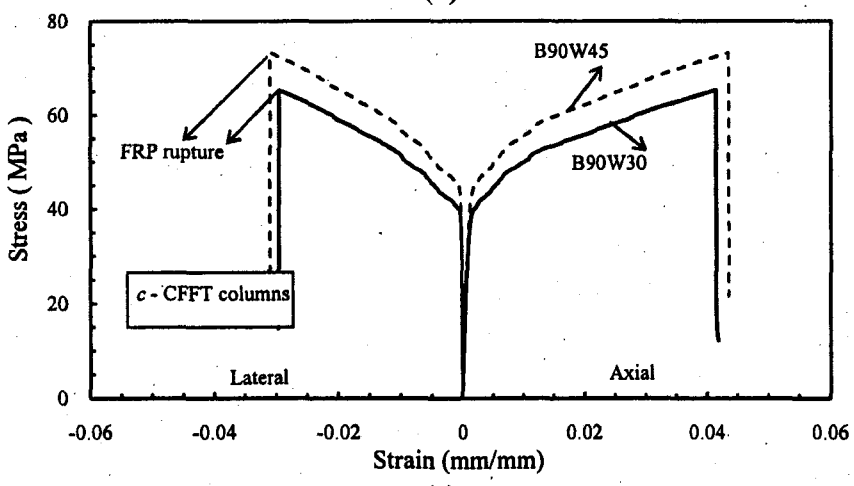

(c)

Figure 3-4 Stress–strain behavior of CFFT specimens.

Table 3-2 Details of specimens and test results for the confined strength

Series No.	ID	H (mm)	D (mm)	Tube type	H/D	Steel bars	f_c' (MPa)	f_{cc}' (MPa)	f_{cc}'/f_c'
I	A-30-1	305	152	A	2	--	30	74.40	2.48
	A-30-2	305	152	A			30	71.00	2.37
	B-30-1	305	152	B			30	81.88	2.73
	B-30-2	305	152	B			30	80.00	2.67
	C-30-1	305	152	C			30	119.1	4.00
	C-30-2	305	152	C			30	128.0	4.23
	A-45-1	305	152	A	2	--	45	89.40	1.98
	A-45-2	305	152	A			45	82.50	1.82
	B-45-1	305	152	B			45	101.7	2.26
	B-45-2	305	152	B			45	103.5	2.30
	C-45-1	305	152	C			45	142.6	3.17
	C-45-2	305	152	C			45	148.5	3.30
II	A60S30	608	152	A	4	6 No 10M	30	78.42	2.61
	A60S45	608	152	A			45	83.50	1.86
	C60S30	608	152	C			30	122.7	4.09
III	A90S30	912	152	A	6	6 No. 10M	30	67.14	2.23
	A90S45	912	152	A			45	75.17	1.67
	C90S30	912	152	C			30	117.52	3.90
	B90S30	912	152	B			30	75.29	2.50
IV	B90W30	912	152	B	6	--	30	65.14	2.17
	B90W45	912	152	B			45	73.73	1.64
V	D150S30	1500	213	D	7	6 No. 13M	30	61.37	2.04
	E150S30	1500	213	E			30	97.19	2.65

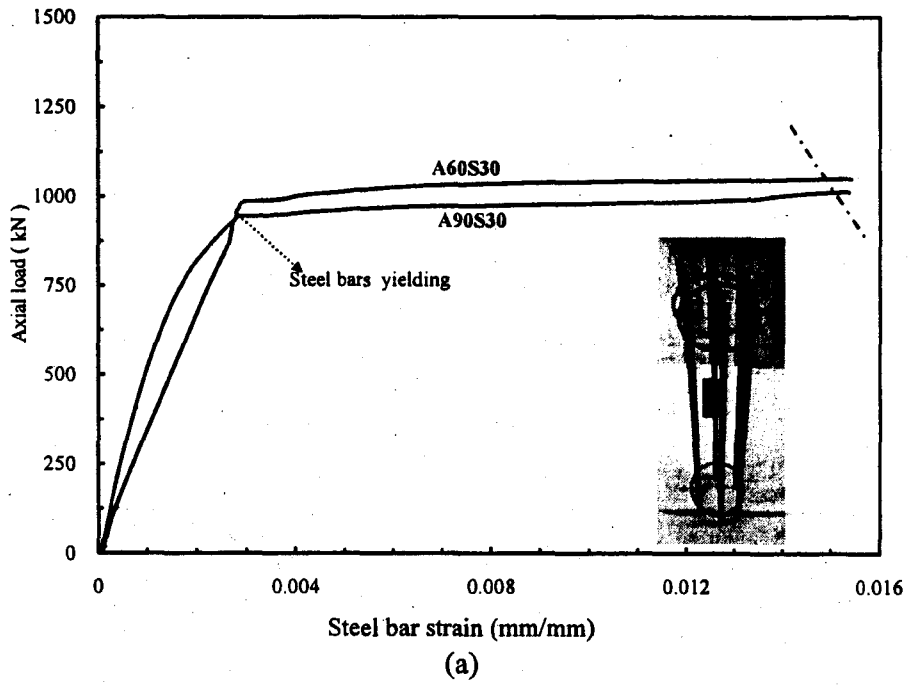

(a)

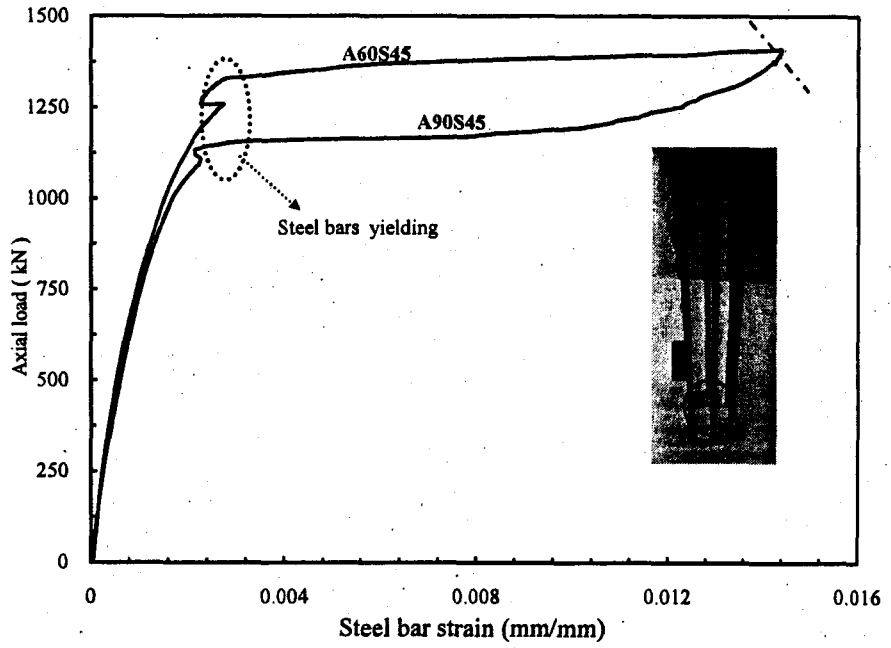

(b)

Figure 3-5 The typical load-axial strain in the longitudinal steel bars relationships for the reinforced CFFT columns

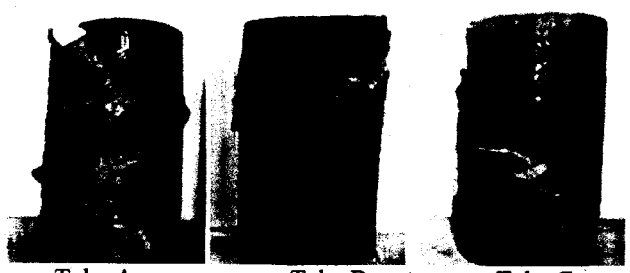

Tube A Tube B Tube C

Figure 3-6 Failure mode of CFFT cylinders

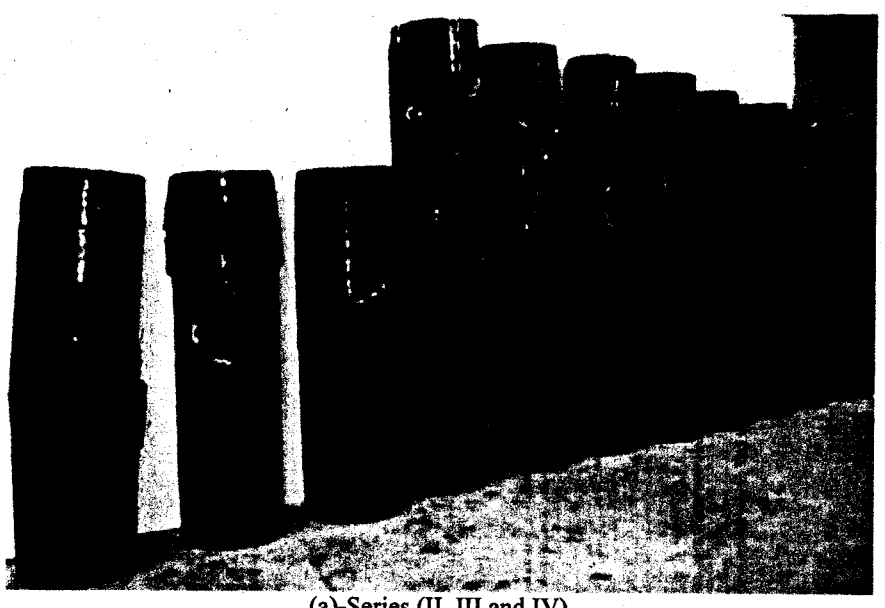

(a)-Series (II, III and IV)

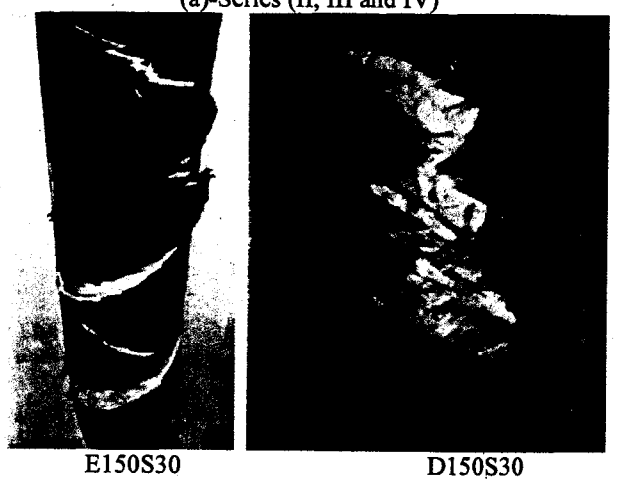

E150S30 D150S30

(b)-Series (V)

Figure 3-7 Failure modes of CFFT columns

3.6 Theoretical Predictions of the Axial Load Carrying Capacity

3.6.1 Review of codes and design guidelines

The North American codes represent the nominal axial load capacity, P_o of the conventional reinforced concrete (RC) column under concentric loading by the following rational equation:

$$P_o = k_c f_c'(A_g - A_s) + f_y A_s \qquad 3\text{-}2$$

In Equation 3-2, the concrete and steel strengths at ultimate and yielding, respectively, are added together to compute the theoretical nominal strength or yield point of short loaded RC columns under pure axial load. It was possible to express the column capacity in this simple form because both the concrete and steel reached their plastic states at approximately the same strain level (Ozbakkaloglu and Saatcioglu 2004). The parameter k_c is defined as the ratio between the in-place-strength of concrete to concrete cylinder strength, (f_{co}' / f_c'). The difference is usually attributed to the size effect, shape and concrete cast practice between columns and concrete cylinders. In 1930, an extensive experimental program was conducted on reinforced concrete columns; as a result, a value of 0.85 was suggested for k_c (Lyse and Kreidler 1932).

In fact, a perfect axially loaded column does not exist, unintentional eccentricity occurs on the column section due to the end condition, inaccuracy of construction, and normal variation in material properties. To take these factors into consideration, the ACI 318-08 code specifies a reduction factor of 20% and 15% in the maximum nominal load P_o, for tied and spiral column, respectively. Introducing the strength reduction factor (ϕ), the axial load capacity of the reinforced concrete columns according to the ACI 318-08 code, is as follows:

For spiral columns (ϕ *= 0.75)*

$$P_r = \phi P_n = 0.85\phi\left[0.85 f_c'(A_g - A_s) + f_y A_s\right] \qquad 3\text{-}3.a$$

For tied columns (ϕ *= 0.65)*

$$P_r = \phi P_n = 0.80\phi\left[0.85 f_c'(A_g - A_s) + f_y A_s\right] \qquad 3\text{-}3.b$$

The two Canadian codes CSA S6-06 and CSA S806-02 provide similar equations to the ACI 318-08 equations, except that they introduced a material resistance factor for steel and concrete instead of the strength reduction factor specified in the ACI 318-08. In addition, the Canadian codes use the factor α_1 instead of k_c, which depends on the value of the unconfined concrete compressive strength. In essence, the ACI 440.2R-08 and the two Canadian codes use the same equations of the conventional RC columns to predict the compressive strength of externally bonded FRP reinforced concrete columns using (f'_{cc}) instead of (f'_c). The following section presents a summary of the confinement models and the design equations for short FRP-confined-reinforced concrete columns under axial load, as reported by the ACI 440.2R design guidelines and the two Canadian codes CSA S6-06 and CSA S806-02. In the presentation of the different models and equations of each code, a uniform set of parameters, which may be different from the original ones, has been adopted for consistency and comparison purposes.

3.6.2 ACI 440.2R-08 guide for the design and construction of externally bonded FRP systems

Chapter 12 of the ACI 440.2R-08 design guidelines deals with the strengthening by FRP jackets of RC members subjected to axial force, or combined axial and bending forces. This chapter gives the following equations for the axial compressive strength of short (non-slender), normal weight concrete member confined with an FRP jacket, using the confined concrete strength:

For nonprestressed members with existing steel spiral reinforcement

$$P_r = \phi P_n = 0.85\phi\left[0.85 f_c'(A_g - A_s) + f_y A_s\right] \qquad 3\text{-}4$$

The strength reduction factor for RC columns confined internally with spiral steel (ϕ) is the same as mentioned before in Equation 3-3.a. The approach adopted by the current ACI 440.2R-08 for the maximum confined concrete compressive strength (f'_{cc}) is based on a model proposed by Lam and Teng 2003 as follows:

$$f'_{cc} = f'_c + \Psi_f 3.3 \kappa_a f_{lFRP} \qquad 3\text{-}5.a$$

where, $\Psi_f = 0.95$ is an additional reduction factor, and the efficiency factor (κ_a) accounts for the geometry of the section, circular and noncircular, ($\kappa_a = 1.0$, for circular columns) and

$$f_{lFRP} = \frac{2 E_{FRP} n t_{FRP} \varepsilon_{fe}}{D} \qquad 3\text{-}5.b$$

where $\varepsilon_{fe} = \kappa_\varepsilon \varepsilon_{fu}$, and $\kappa_\varepsilon = 0.55$.

ε_{fe} is the effective strain level in the FRP at failure. A strain efficiency factor (κ_ε) is provided based on the experimental results, which were carried out by (Pessiki et al. 2001). This factor accounts for the difference between in-situ jacket rupture strains, and FRP rupture strains determined from tensile coupon tests. On the other hand, the minimum level of lateral pressure f_{lFRP} is limited to be not less than $0.08 f'_c$. This is the minimum level of confinement required to assure a non-descending second branch in the stress-strain behavior (Lam and Teng 2003). In addition, to prevent excessive cracking and the resulting loss of concrete integrity, the maximum ultimate strain is limited to 0.01.

3.6.3 Canadian Standard Association CAN/CSA-S6-06-Canadian Highway Bridge Design Code

According to the Canadian Highway Bridge Design Code (CAN/CSA S6-06), the factored axial load resistance P_r of a confined column is given by the following equation:

$$P_r = k_e \left[\alpha_1 \phi_c f'_{cc} (A_g - A_s) + \phi_s f_y A_s \right] \qquad 3\text{-}6$$

where k_e is a strength reduction factor applied for unexpected eccentricities, which equal to 0.80, and $\phi_c = 0.75$, $\phi_s = 0.9$. The value α_1 depends on the unconfined concrete compressive strength, $(\alpha_1 = 0.85 - 0.0015 f'_c \geq 0.39)$

The compressive strength of the confined concrete f'_{cc} shall be calculated as follows:

$$f'_{cc} = f'_c + 2 f_{lFRP} \qquad 3\text{-}7$$

where, $f_{lFRP} = 2t_{FRP}\phi_{FRP}f_{FRPu}/D$, and $\phi_{FRP} = 0.65$ are the material resistance factors for concrete, steel and FRP, respectively.

The CAN/CSA S6-06 limits the confinement pressure f_{lFRP} at the ultimate limit state (ULS) that shall be designed to be between $0.1f_c'$ and $0.33f_c'$. Note that Equation 3-7 is valid only for concrete strength less than 50 MPa.

3.6.4 Canadian Standard Association CAN/CSA-S806-02-Building Code

The factored axial load resistance P_r of the confined columns provided by CAN/CSA S806-02 Building Code is the same as mentioned before by CAN/CSA S6-06, except for the value of k_e and the material resistance factors. The values of $k_e = 0.85$, $\phi_c = 0.60$, $\phi_s = 0.85$ and $\phi_{FRP} = 0.75$ are adopted by the CSA S806-02 leading to the following equation:

$$P_r = 0.85\left[\alpha_1\phi_c f_{cc}'(A_g - A_s) + \phi_s f_y A_s\right] \quad 3\text{-}8$$

The CAN/CSA S806-02 uses Equation 3-9 to evaluate the confined concrete compressive strength f_{cc}',

$$f_{cc}' = 0.85f_c' + k_1 k_s f_{lFRP} \quad 3\text{-}9$$

where $k_1 = 6.7(f_{lFRP})^{-0.17}$, and factor k_s accounts for the shape of the cross section, which is equal to 1.0 for circular section.

The CAN/CSA S806-02 limits the FRP hoop strain to 0.004 times its elastic modulus E_{FRP}.

$$f_{lFRP} = \frac{2t_{FRP}\phi_{FRP}f_{FRPu}}{D} \le \frac{2t_{FRP}E_{FRP}0.004}{D} \quad 3\text{-}10$$

3.6.5 Theoretical versus experimental confined concrete compressive strength

One of the main objectives of this study is to evaluate the applicability of the confinement models of the two Canadian codes and the ACI 440.2R-08 design guidelines

to the CFFT technique. The objective of this section is to identify the most and least conservative model's predictions of the two Canadian codes and ACI design guidelines for the confined concrete strength f'_{cc}. Figure 3-8.a to Figure 3-8.c are graphs of values of f'_{cc} / f'_c, determined by the three confinement models versus the experimental f'_{cc} / f'_c values of the CFFT cylinder specimens tested in this study. The theoretical f'_{cc} values were calculated considering $\phi_{FRP} = 1.00$, then respecting the ϕ_{FRP} as provided by the two CSA codes and the ACI design guidelines. In case of CSA S806-02 model, the f'_{cc} value for limiting FRP tensile strength to 0.004 times its elastic modulus E_{FRP} was considered. The ACI 440.2R-08 provides additional FRP environmental reduction factors which depends on the type of the FRP and the exposure condition. However, in the present analysis, this factor is set to 1.0 because the specimens were tested after one month from the date of the casting and no degradation occurred during this period. The confining pressure f_{lFRP} was calculated using Equation 3-10 based on the ultimate hoop tensile strength f_{FRPu}, which equal to the value obtained from the split-disk test (see Table 3-1). The trend lines accompanied by the coefficient of regression R^2 values for specimens of batch No.1 and 2 were plotted for each case in Figure 3-8. The two dashed lines represent the ±10% accuracy of predicted versus experimentally observed ultimate strength for different confinement models.

It is observed that the ACI 440.2R-08 and CSA S806-02 unfactored predictions values (without reduction factor) are less conservative than that of CSA S6-06. Figure 3-8.a shows that the unfactored ACI 440.2R-08 f'_{cc} / f'_c predictions are close to the experimental values; in spite of some individual values which were overestimated. On the other hand, it is observed that the CSA S6-06 unfactored predictions values for the two batches are 20% less than that the experimental values (see Figure 3-8.b). However, the unfactored CSA S806-02 f'_{cc} / f'_c predictions overestimate the experimental results, especially for normal strength concrete specimens (30 MPa). On the other hand, as taking into account the recommended value of the FRP reduction factor ϕ_{FRP}, and the strain efficiency factor (κ_ε), the predictions values become more conservative. However,

it is observed that the ACI 440.2R-08 factored predictions values are less conservative than that CSA S6-06 and CSA S806-02, particularly for specimens cast with tube Type C. On the other hand, it should be mentioned that the f'_{cc} provided by CSA S806-02 is governed by limiting the hoop tensile strain to be not more than 0.004; otherwise the predicted values may overestimate the strength values. In addition, limiting the confinement pressure $f_{lFRP} \leq 0.33\, f'_{cc}$ according to the CSA S6-06 for the specimens cast with tube Type C leads to more conservative predictions.

3.6.6 Proposed confinement model for CFFT

The previous section showed that the unfactored predictions with the ACI 440.2R-08 and CSA S806-02 confinement models for some individual values were slightly overestimated the experimental values. The three confinement models of the ACI 440.2R-08 design guidelines and two Canadian codes are presented by linear regression equations. In fact, the test results of this study and those available in the literature show that the ultimate strength of CFFT cylinders mainly depends on the confinement ratio (f_{lFRP}/f'_c), and the confinement efficiency is reduced with the increase in this ratio (Samaan et al. 1998; Saafi et al. 1999). Also, it has been proven that the FRP tubes have higher confinement efficiency than FRP sheet (Wu et al. 2006). In this study, a new model to account for the confinement using FRP tubes is proposed to predict the peak stress of the CFFT cylinders as follows:

$$f'_{cc} = f'_c\left[0.7 + 2.7\left(\frac{f_{lFRP}}{f'_c}\right)^{0.7}\right] \qquad 3\text{-}11$$

The proposed model was calibrated using the regression analysis method and based on the test results of the CFFT cylinders of this study and those available in the literature. The accuracy of the proposed model depends significantly on the ultimate hoop strength

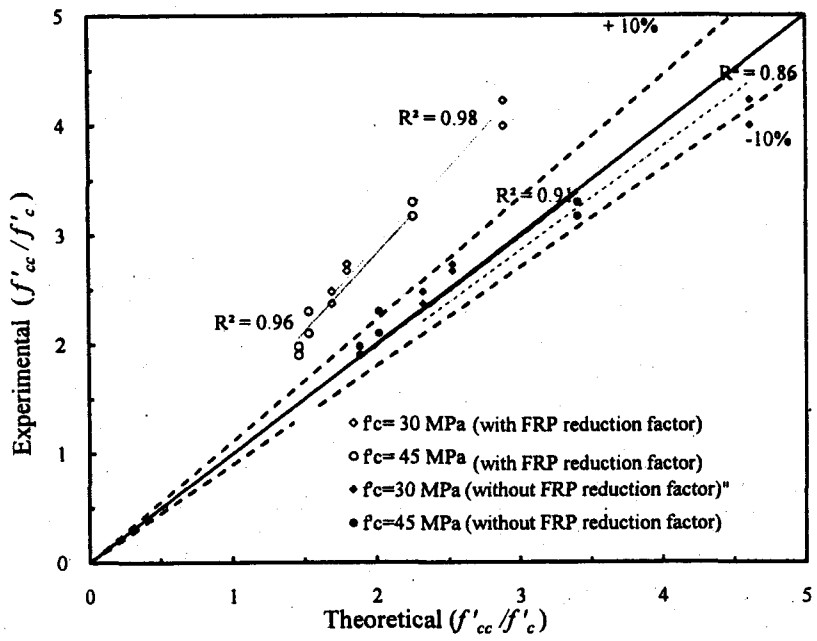

(a) Model by ACI 440.2R-08

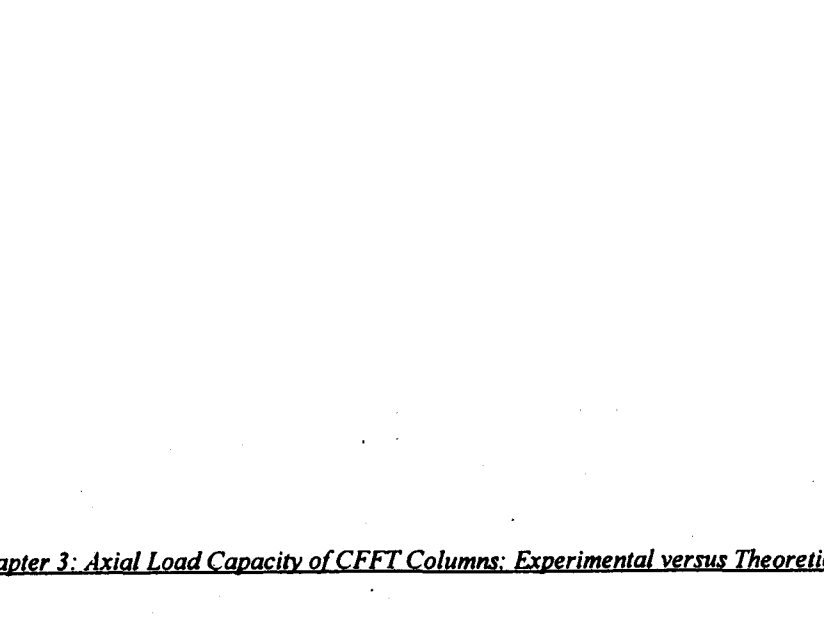

(b) Model by CSA S6-06

Figure 3-8 Predicted-versus-experimentally observed ultimate strength for different confinement models (Series-I)

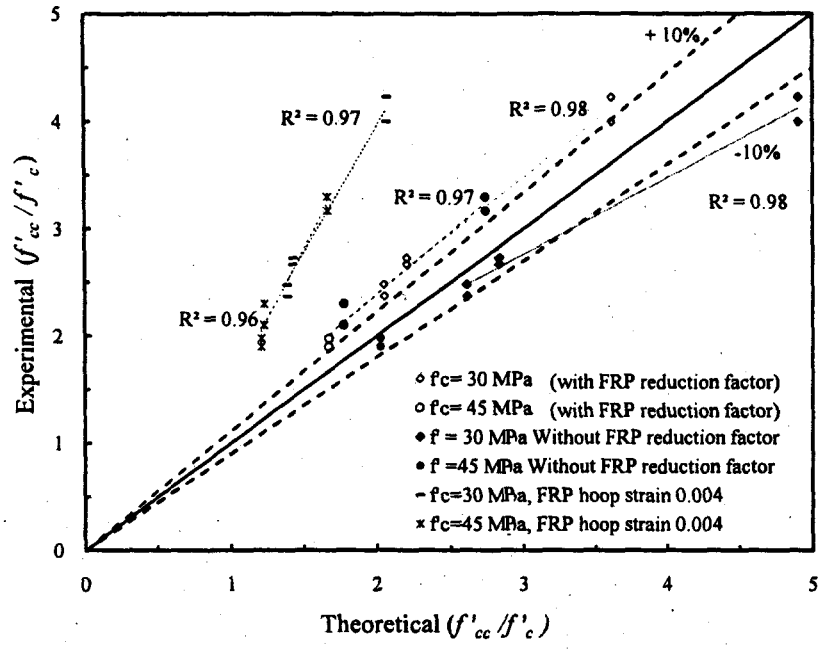

(c) Model by CSA-S806-02

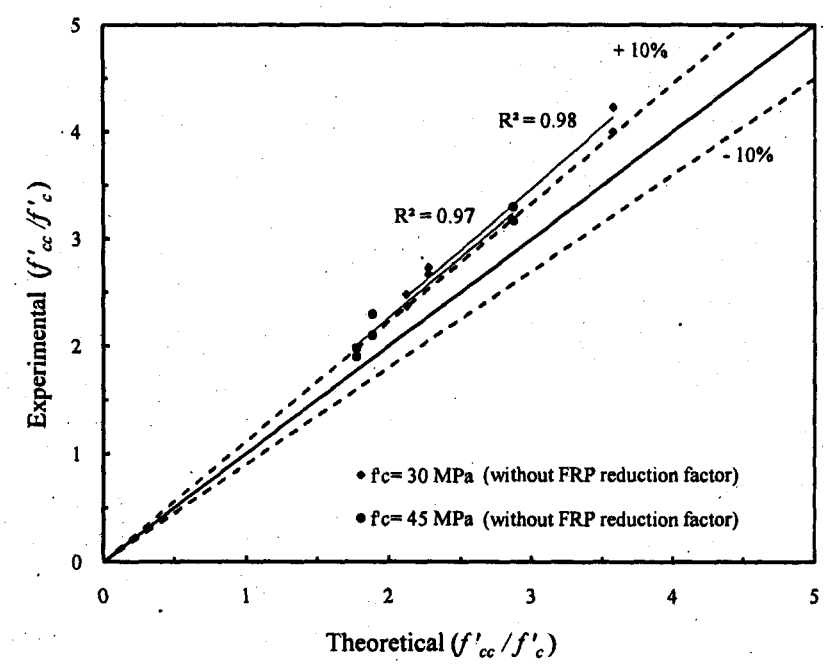

(d) Proposed Model

Figure 3-8 Predicted-versus-experimentally observed ultimate strength for different confinement models (Series-I)

of the FRP tubes. Also, this model accounts for the variation in the unconfined concrete compressive strength in the range of 25 MPa to 60 MPa. Figure 3-8.d presents a comparison between the ratios of f'_{cc} / f'_c, determined by the proposed model versus the experimental values. A good correlation is noted between the experimental and predicted values. In addition, it is observed that the ratios of the experimental values for the two batches are 10% over than the predictions values, which leads to a conservative prediction. On the other hand, this study shows the effectiveness of the split–disk test to obtain accurate values for the ultimate hoop tensile strength f_{FRPu} of the FRP tubes, which were used to calculate the FRP lateral pressure ($f_{lFRP} = 2t_{FRP}f_{FRPu}/D$). However, the tensile coupon test is not suitable for the FRP tubes to determine the hoop properties. Hence, it is recommended to use the split-disk test to evaluate the (f_{lFRP}) for the CFFT technique.

3.6.7 Predicted versus experimental values of the axial load carrying capacity

In terms of application of the confinement models in the design equations, an important concern yet to be addressed is the size effect of tested CFFT cylinders, and how such results are correlated to different-size of the CFFT columns. The column definition according to the CSA standard A23.3-04 for the reinforced concrete structures is that the height-to-diameter ratio, should be greater than or equal to three to be considered as a column; otherwise, it is considered to be a cylinder. Accordingly, the 305 mm height specimens were considered as cylinders, while the other specimens presented in Table 3-2 are considered as short columns. To verify the validity of the design equations of the two Canadian codes and ACI design guidelines, the factored axial load values for the tested CFFT columns were calculated. The minimum and maximum allowable confinement limits, material resistance factors and the strength reduction factors which were provided by the three codes have been incorporated into the current investigation. Since a ductile failure was assured, the spiral-column resistance factor was accounted in the calculation. Figure 3-9.a to Figure 3-9.c present the predicted normalized load carrying capacities determined by the ACI 440.2R-08, CSA S6-06 and CSA S806-02 versus, the normalized ultimate experimental values. In Figure 3-9, the solid line (45°) and dashed line (+50%)

represent the values of the predicted factored axial loads that equal to 100% and 50% of the experimental values, respectively. It can be observed that the ACI 440.2R-08 predictions are less conservative than that the CSA S6-06 and CSA S806-02. However, the predicted factored maximum axial loads are roughly 50%, 40% and 30% the experimental values according to ACI 440.2R, CSA-S6-06 and CSA-S806-02, respectively. Figure 3-9.b and Figure 3-9.c show that the predictions using CSA S6-06 and CSA S806-02 for the columns C60S30, C90S30 and E150S30 are overly conservative, whereas these specimens had FRP reinforcement ratios higher than the allowable limits.

Based on the Ultimate Limit State (ULS) design method, failure of the conventional reinforced concrete columns is assumed to occur when the compressive concrete strain reaches 0.003 or when the tensile and/or compressive stress in the steel reaches f_y. In addition, at the cracking load level which corresponds to the initiation of spalling of concrete cover, the longitudinal reinforcements reach yielding for most of the circular columns, (Kim 2007). Based on this assumption, the yield load or nominal load of the conventional reinforced concrete columns has been represented by Equation 3-2. On the other hand, the same equation has been used to predict the nominal load of the FRP-confined concrete columns with f'_{cc} instead of f'_c. However, in case of FRP-confined concrete columns, the cracking load and yielding load occur at a load level lower than the ultimate load. Figure 3-5 shows that the steel reinforcements started to yield just after reaching the unconfined concrete compressive strength, or after the knee on the load-displacement curve. Regarding to the axial-load behavior of the confined columns, when the unconfined concrete strength level is surpassed, the stiffness is reduced down to 10%-30% of the initial stiffness, depending on the FRP volumetric ratio. Table 3-3 presents the experimental percentage ratios of the yield to the ultimate load for the reinforced CFFT columns. It is observed that for high (tubes Type C and E) and normal (tubes Type A, B and D) FRP volumetric ratio, the yield to the ultimate load ratios in average are equal to 50% and 64%, respectively. This indicates that the factored ACI 440.2R and CSA-S6-06 prediction's values are approximately equal to or close to the experimental yield loads. From the previous discussion, it is unsafe that the ACI 440.2R-08 and the two Canadian codes use Equation 3-2 as a base for the design of the FRP-confined concrete columns

(equations. 3-4, 3-6 and 3-8, respectively), because their yield and crack loads levels are different from those of conventional RC columns. Hence, it is recommended that the factored axial load resistance of the FRP-confined columns must be related to the yield load or the confined concrete compressive strength at the yield level f'_{ccy}.

Figure 3-9.d to Figure 3-9.f are graphs of predicted normalized load carrying capacities determined by the ACI 440.2R-08, CSA S6-06 and CSA S806-02 versus, the experimental yield values. In fact, the ratios of the experimental to the factored predicted values present the overall reduction factors for the load carrying capacities of the columns. Figure 3-9.d to Figure 3-9.f show that the ratios of the experimental yield to the predicted values were decreased as compared to the values in Figure 3-9.a to Figure 3-9.c. Again it can be observed that the ACI 440.2R-08 predictions are less conservative than that of the CSA S6-06 and CSA S806-02. Figure 3-9.d shows that the ACI prediction values for the three specimens (C60S30, C90S30 and E150S30) are close to the yield loads. On the other hand, substituting by the material resistance factor and reduction factor in the ACI 440.2R-08, CSA S6-06 and CSA S806-02 equations, we can get the imposed overall reduction factors for the FRP-confined column multiplied by $f'_{cc} A_g$ as follows:

$$P_{rACI\,440} = \phi P_n = 0.85\phi 0.85(f'_{cc} A_g) = 0.85 \times 0.75 \times 0.85(f'_{cc} A_g) = 0.54(f'_{cc} A_g) \quad 3\text{-}12$$

$$P_{rS\,6-06} = 0.80\alpha_1\phi_c(f'_{cc} A_g) = 0.80 \times 0.80 \times 0.75(f'_{cc} A_g) = 0.48(f'_{cc} A_g) \quad 3\text{-}13$$

$$P_{rS\,806-02} = 0.85\alpha_1\phi_c(f'_{cc} A_g) = 0.85 \times 0.80 \times 0.6(f'_{cc} A_g) = 0.40(f'_{cc} A_g) \quad 3\text{-}14$$

The additional gain in the strength after the steel yielding of the steel bars is not accounted in the above equations, and this gives a certain degree of conservativeness. The previous equations (Equation 3-12 to 3-14) show that the overall reduction factors are 54, 48 and 40% for the ACI 440.2R, CSA S6-06 and CSA S806-02, respectively.

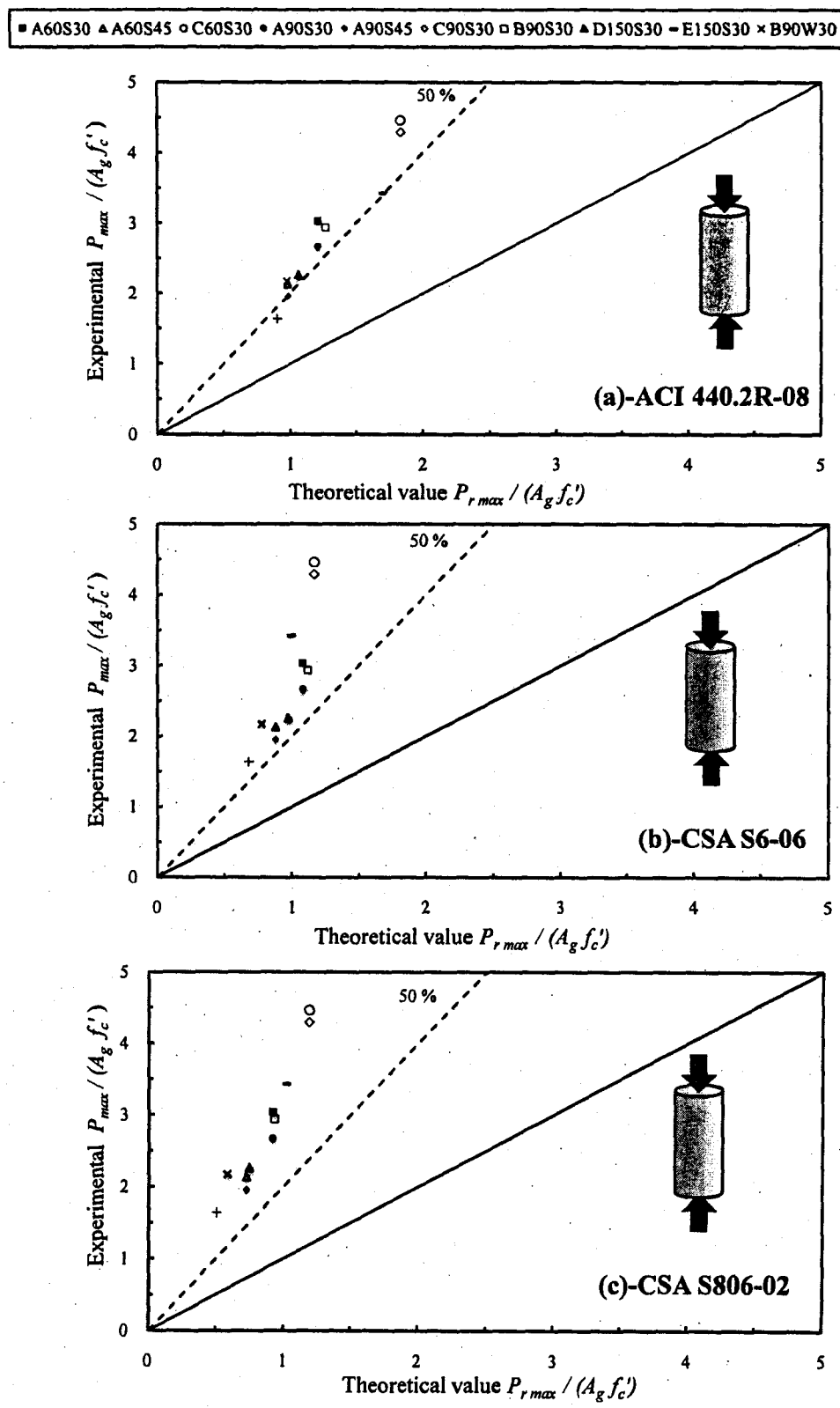

Figure 3-9 Predicted-versus-experimentally observed ultimate and yield loads

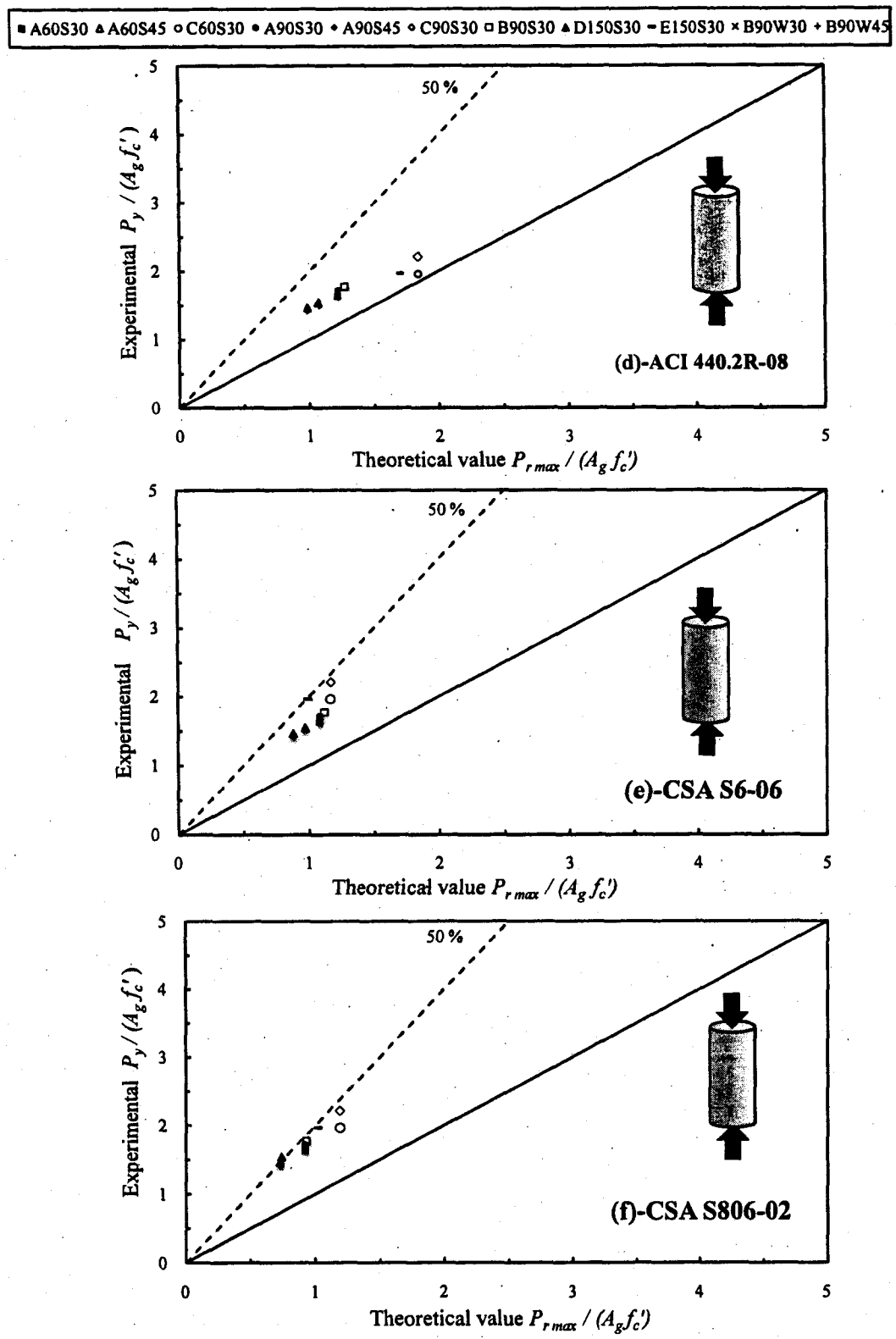

Figure 3-9 Predicted-versus-experimentally observed ultimate and yield loads

However, the predicted factored axial loads are roughly 80, 60 and 55% of the experimental yield loads according to the ACI 440.2R, CSA-S6-06 and CSA-S806-02, respectively (see Figure 3-9.d, Figure 3-9.e and Figure 3-9.f). These results show that the intended overall reduction factors are not achieved.

3.6.8 Modified equations for the axial load resistance of the CFFT columns

Equation 3-2 is updated with a new factor k_{cc} instead of k_c as shown in Equations. 3-15.a and 3-15.b for the reinforced and unreinforced CFFT columns, respectively. This factor is defined as the ratio of the in-place-strength of CFFT columns $(f'_{cc(column)})$ to CFFT cylinder strength $(f'_{c(cylinder)})$.

$$P_o = k_{cc} f'_{cc} (A_g - A_s) + f_y A_s \qquad 3\text{-}15.a$$

$$P_o = k_{cc} f'_{cc} (A_g) \qquad 3\text{-}15.b$$

The k_{cc} factor is proposed because all the existing confinement models were established and verified based on the experimental test results of the small scale cylinder specimens, to provide f'_{cc}. Data from reinforced and unreinforced CFFT columns tested in this study, along with the reported by others (Jaffry 2001; Mirmiran et al. 1998; Zhu et al. 2005; Fam et al. 2003c), were examined to evaluate k_{cc} factor. However, it is believed that the presence of the longitudinal steel may provide more restraining action against an inclined shear failure as compared to the unreinforced CFFT columns (Zhu et al. 2005). Therefore, two values for the k_{cc} factor are proposed for the reinforced and unreinforced CFFT columns. Figure 3-10.a and Figure 3-10.b show the variation of in-place-strength of confined concrete k_{cc} for the reinforced and unreinforced specimens, respectively, versus the FRP volumetric ratio. However, the figures show that the trend in strength reduction for the unreinforced specimens is higher than that of the reinforced specimens. The statistical analysis of the data (Figure 3-10) indicates that the k_{cc} can be taken 0.80 and 0.75 for the reinforced and unreinforced specimens, respectively, for f'_c up to 60 MPa.

Figure 3-11 shows a comparison between RC and FRP-confined columns in terms of the design, yield and ultimate load levels. Failure of the RC columns is assumed to occur when the compressive concrete strain reaches 0.003 or when the tensile stress in the steel reaches f_y. It oes not matter whether the concrete or the steel approaches its ultimate strength first.

Table 3-3 The experimental and theoretical results at the yield and maximum load levels

Series No.	ID	f'_{ccy} (MPa)	$\frac{f'_{ccy}}{f'_c}$	Experimental values			Proposed (unfactored)		$\frac{P_{y(Exp)}}{P_{y(Proposed)}}$	$\frac{P_{Max(Exp)}}{P_{o(Proposed)}}$
				P_y (kN)	P_{Max} (kN)	$\frac{P_y}{P_{Max}}$	(P_y or P_{cr}) (kN)*	(P_o) (kN)**		
II	A60S30	34.99	1.16	890	1652	0.53	789	1314	1.13	1.26
	A60S45	52.37	1.16	1195	1741	0.68	915	1525	1.31	1.14
	C60S30	45.14	1.50	1068	2430	0.43	1244	2072	0.86	1.17
III	A90S30	37.56	1.25	935	1454	0.64	789	1314	1.19	1.11
	A90S45	50.32	1.11	1159	1595	0.72	915	1525	1.27	1.05
	C90S30	52.83	1.76	1203	2338	0.51	1244	2072	0.97	1.13
	B90S30	39.27	1.30	965	1597	0.60	848	1412	1.14	1.13
IV	B90W30	---	---	---	1182	---	661	1102	--	1.07
	B90W45	---	---	---	1338	---	841	1401	--	0.95
V	D150S30	39.36	1.31	1650	2417	0.68	1405	2341	1.17	1.03
	E150S30	52.27	1.74	2100	3665	0.57	2308	3846	0.91	0.95
Average									1.10	1.09
Standard deviation									±0.16	±0.09

*Eqs. 3-16.a and3-16.b; ** Eqs. 3-15.a and 3-15.b

For the FRP-confined concrete columns, it should be emphasized that the excessive cracking, steel yielding and the resulting loss of concrete integrity must be prevented. Therefore it is recommended to limit the factored load resistance of the FRP-confined columns relative to the yield load not to the failure load, as it is provided in case of RC columns. A new factor k_{cr} is proposed to account for the initiation of the steel yielding and concrete cracking of the FRP-confined columns. This factor is assumed to be the same for the reinforced and unreinforced CFFT columns, because the steel and concrete reach yielding and cracking, respectively, approximately at the same load level. Based on the ratios of the ultimate load to the yield load for the CFFT specimens of this study (refer to Table 3-3), the statistical analysis of the test data indicates that the k_{cr} can be

taken equal to 0.60. The following expressions give the yield load P_y and cracking load P_{cr} for the reinforced and unreinforced CFFT-columns, respectively:

$$P_y = k_{cr} P_o = k_{cr}\left[k_{cc} f_{cc}^{'}(A_g - A_s) + f_y A_s\right] \qquad 3\text{-}16.a$$

$$P_{cr} = k_{cr} P_o = k_{cr}\left[k_{cc} f_{cc}^{'} A_g\right] \qquad 3\text{-}16.b$$

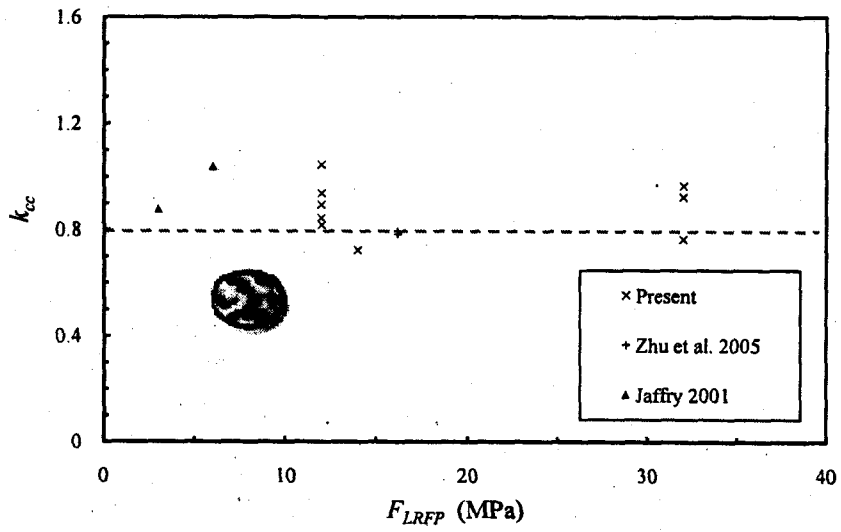

(a) - Reinforced CFFT specimens

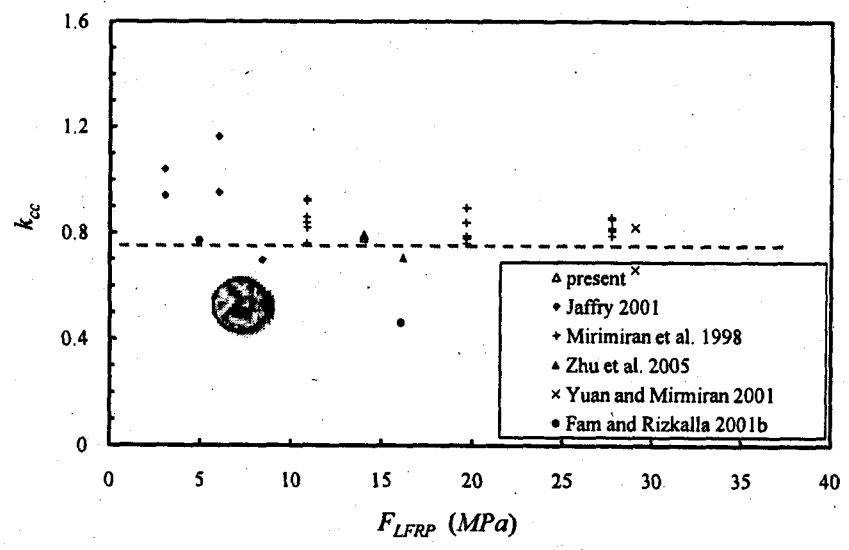

(b) -Unreinforced CFFT specimens

Figure 3-10 In-place confined strength of concrete-versus-FRP volumetric ratio

The values of 0.85 and 0.80 are introduced as strength reduction factors for unexpected eccentricities for the reinforced and unreinforced CFFT-columns, respectively as follows:

$$P_n = 0.85P_y \qquad 3\text{-}17.a$$

$$P_n = 0.80P_{cr} \qquad 3\text{-}17.b$$

Finally, introducing the strength reduction factor (ϕ), the factored axial load resistance of the reinforced and unreinforced CFFT columns can be presented as follows:

$$P_r = 0.85\phi k_{cr}\left[k_{cc}f'_{cc}(A_g - A_s) + f_y A_s\right] \qquad 3\text{-}18.a$$

$$P_r = 0.80\phi k_{cr}\left[k_{cc}f'_{cc}A_g\right] \qquad 3\text{-}18.b$$

In fact, the failure of the concrete can be initiated due to either creep or fatigue. Whereas, design of the conventional reinforced concrete columns, concrete and steel may undergo creep if the stress reaches 80% of the ultimate strength for the concrete and steel. However, the actual total service load on the conventional reinforced concrete columns according to the ULS is imposed to be less than 40% of its ultimate strength (refer to Figure 3-11) (Thériault and Neale 2000). In fact, this is the same load level that ensures creep failure will not occur. On the other hand, with regard to fatigue failure, the concrete must be stressed to at least 40% of its ultimate strength before fatigue failure can take place (Thériault and Neale 2000).

Table 3-3 presents the unfactored predicted load carrying capacities of the tested CFFT columns using the proposed equations, Equations 3-15.a and 3-15.b for the maximum loads and Equations 3-16.a and 3-16.b for the yield loads. It was found that the ratios of the experimental load carrying capacities to the unfactored predicted values using the proposed equations, at the yield and maximum load levels were equal to 1.10 ±0.16 and 1.09 ±0.09, respectively, (see Table 3-3). It is clear that the predictions of the nominal and yield loads for the reinforced and unreinforced short CFFT columns using the proposed equations are in good agreement with the experimental results and conservative. On the other hand, Figure 3-12 presents the factored predicted normalized load carrying capacities determined by

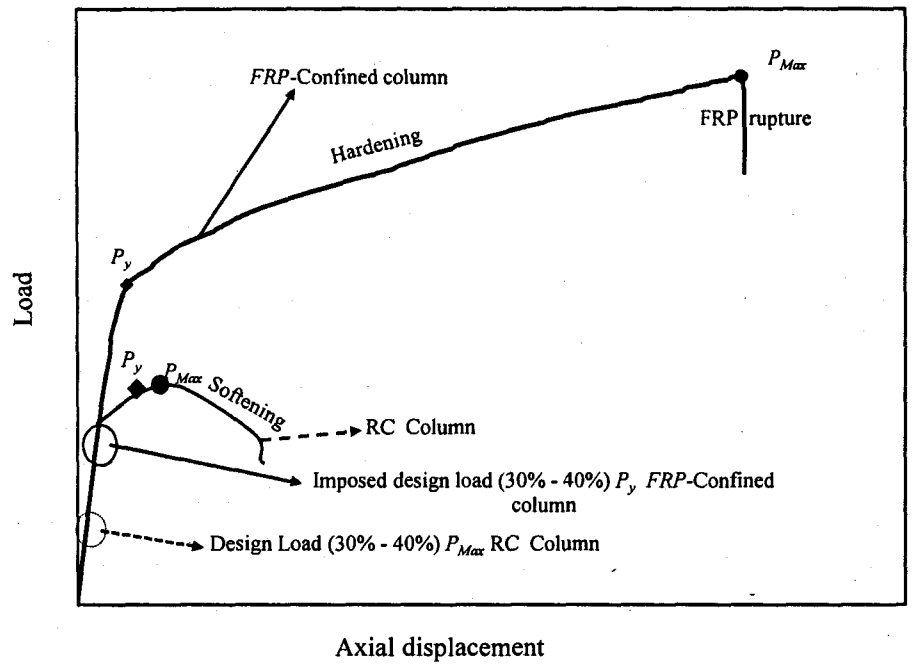

Figure 3-11 Load-displacement behavior for RC and FRP confined concrete columns

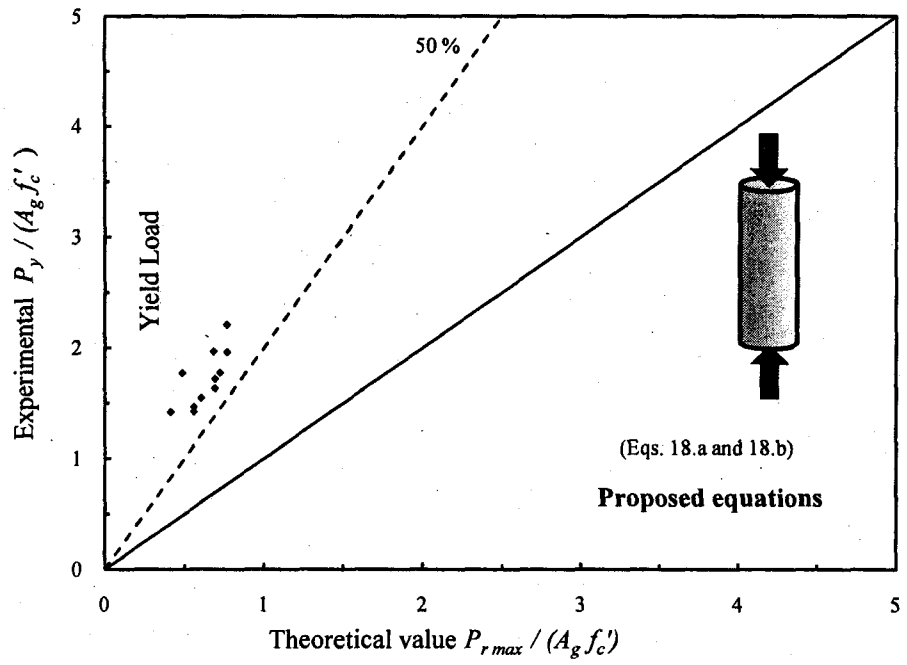

Figure 3-12 Predicted-versus-experimentally observed yield load

the proposed equations (Equations 3-18.a and 3-18.b), versus, normalized yield experimental values of the tested short CFFT columns of this study. The confined strength f'_{cc} was calculated according to the proposed confined model, with $\phi_{FRP} = 0.65$. Also, the strength reduction factor (ϕ) was taken as 0.75 according to the ACI provisions. However, the f_{lFRP} values were limited to be less than $0.33f'_c$ which lead to a conservative prediction, especially for specimens cast in tubes Type C and E. Figure 3-12 shows that the predicted values of the factored axial load varied from 30% to 40% of the experimental yield load. In fact, the proposed equation can ensure a design load level away from the concrete cracking, steel yielding and the resulting loss of concrete integrity. Moreover, the service design load at 30% to 40% of the yield load can be safely used against the creep and fatigue initiation for the concrete and steel.

3.7 Conclusions

The behavior of short CFFT columns subjected to concentric axial compression loading conditions was investigated in this study. The test results of this study combined with other reported data in the literature were evaluated using regression analysis and a number of comparisons. These analyses were used to evaluate the validity of the confinement models and design equations of the three North American codes and design guidelines, ACI 440.2R-08, CSA S6-06 and CSA S806-02. A nonlinear empirical model for confined ultimate strength of CFFT has been proposed. In addition, step-by-step design equations were proposed to predict the factored ultimate and yield loads resistance of the CFFT columns. The findings presented in this paper can be summarized as follows:

1. The failure modes of the CFFT specimens tested in this study of height to diameter ratios ranged from 2 to 7 resulted mainly from the rupture of the FRP tubes.
2. The test results indicated that the yield load of CFFT columns occurred on average at a load level equal to 54 to 60% of the ultimate load.
3. Limiting f_{lFRP} to be less than $0.33\,f'_c$ by CAN/CSA S6-06, and limiting the FRP hoop tensile strength to 0.004 its elastic modulus E_{FRP} by CAN/CSA S806-02 leads to a conservative predictions for the confined concrete compressive strength.

4. The CAN/CSA S6-06 and CAN/CSA S806-02 confinement models showed conservative predictions, while the ACI 440.2R-08 was slightly less conservative.
5. The design guidelines of the ACI 440.2R-08, CAN/CSA S6-06 and CAN/CSA S806-02 overestimate the factored axial load capacities of the reinforced and unreinforced CFFT columns as compared by the yield and crack load levels. It is recommended that the code design equations for the factored axial load capacities should deal with the cracking or yielding load levels of the FRP-confined concrete columns.
6. For concrete strength up to 60 MPa a new confined model is proposed for the CFFTcylinder specimens. Also, based on the test results of this study together with the other reported data in the literature, the design equations are modified to predict the yield and ultimate load carrying capacities of the internally reinforced and unreinforced short CFFT columns. K_{cc} is a new factor introduced to account for the in-place-strength of CFFT columns to CFFT cylinder strength. K_{cc} is taken 0.80 and 0.75 for the reinforced and unreinforced CFFT columns, respectively. Also, a new factor (K_{cr}) is proposed to account for the initiation of the steel yielding and concrete cracking for the short CFFT columns.

Chapter 4

Nonlinear Stability Analysis of Concrete Filled FRP-Tubes Columns: Experimental and Theoretical Investigation

4.1 Abstract

This paper presents experimental results and theoretical analysis for buckling responses of concrete filled FRP tubes (CFFT) columns. The analysis intended to understand the effect of the slenderness ratio on the critical buckling load of axially loaded CFFT columns. The effect of three parameters and their interactions on the buckling behavior were investigated; namely, the FRP tube thickness, concrete compressive strength, and slenderness ratio. The experimental program consisted of testing twenty-two circular CFFT columns with a total height ranging from 305 mm to 1520 mm (12 in to 60 in) with an internal tube diameter of 152 mm (6 in). The experimental results showed that the uniaxial compressive strength of CFFT columns was reduced by 13% to 23% with increasing the slenderness ratio from 4 to 20 depending on the three tested parameters. The analysis in this paper aimed to correlate the slenderness ratio of the CFFT columns to various material characteristics and geometric properties of the FRP tubes and concrete. It was found that a slenderness ratio of 12 gave a safe value for the design purposes. However a more precise formula for the slenderness ratio was proposed to control the buckling mode of failure.

4.2 Introduction and Background

Using FRP sheets to confine concrete columns in the construction industry came back to the early 1980's owing to the distinct characteristics of fiber-reinforced polymer (FRP) materials. Various experimental results showed that using FRP tubes to confine concrete columns can enhance the ultimate load carrying capacity by 300% (Mirmiran and Shahawy 1997a; Fam and Rizkalla 2002 and 2003; Fam et al. 2003a, b). Besides their structural advantages, FRP tubes work to protect the plain concrete core from environmental conditions and to prevent the internal steel bars from corrosion. Recently, various industrially projects have been witnessed in the area of construction engineering in the form of piles, columns, girders or bridge piers (Karbhari 2004; Fam et al. 2007). CFFT are also proposed to be used for cable-stayed pedestrian bridges (Seible 1998). Numerous experimental investigations have been conducted to understand the axial behavior of CFFT columns under pure axial load. Although these studies were of great interest to provide extensive results for ultimate capacity and ductility index of CFFT columns, the buckling modes of failure of such columns have not been recorded in enough experimental work. Few studies have been conducted on large scale columns under different load combinations (Toutanji 1999; Mirmiran et al. 2001; Carey and Harries 2005; Sheikh et al. 2007).

The significant increase of the ultimate capacity of CFFT columns highlights the fact that the slenderness ratio of such columns might be a critical factor that controls the mode of failure of these columns (Mirmiran and Shahawy 1997a). Few studies observed that instability of CFFT columns might occur at a lower slenderness ratio than that of ordinary RC columns (without FRP tubes), however, the ultimate capacity of the former might be higher than that of the earlier. This attributed to the bilinear stress-strain behavior of the CFFT columns where the buckling mode of failure initiated at the plastic branch of the curve that characterized by a lower Young's modulus (Yuan and Mirmiran 2001). These results drew conclusion that the increase of the slenderness ratio of CFFT columns might prevent such columns from attaining their ultimate load capacity. A questionable aspect is the design slenderness ratio of these columns to avoid buckling as

this topic has not yet included in any design guidelines. Further experimental and theoretical studies are still necessary to better understand the buckling responses of CFFT columns and to correlate their critical buckling loads to the material and geometric properties of the confining FRP tubes.

The plastic behavior assumption is quite accurate to represent the response before buckling and it is widely accepted in stability analysis of CFFT columns using tangent Euler formula or the yield load. Some experimental results revealed that CFFT columns might failed by buckling at a load level higher than the tangent Euler load. It was observed experimentally that CFFT columns started to deform at a load level corresponding to the tangent Euler formula. With the further increase in the applied axial load, the lateral deformation increased as a result of the flexural stiffness of the CFFT columns. The failure modes were almost to be controlled by instability at load levels that were higher than the tangent Euler critical load (Mirmiran et al. 2001; Yuan and Mirmiran 2001). Mirmiran et al. 2001 investigated experimentally and theoretically the effect of the slenderness ratio of CFFT columns on the buckling behavior of such columns. It was obvious that the CFFT columns were much more susceptible to buckling phenomena than unconfined-concrete columns. Yuan and Mirmiran in 2001 recommended that the slenderness ratio limit of CFFT columns had to be reduced to 11, for a particular type of FRP tubes that was employed in their experimental program. Despite the fact that there is a significant number of valuable experimental research that have been carried out to understand the response of CFFT columns (Fam 2000; Fam and Rizkalla 2001; Karbhari 2004), these studies were mainly oriented to short columns without internal longitudinal reinforcement. In this study, 18 CFFT columns of different heights, 305, 608, 912, 1216 and 1520 mm (12, 24, 36, 48 and 60 in) and 4 control RC columns were tested under uniaxial compression load.

4.3 Research Significance

The objectives of this paper can be summarized as follows:

- To investigate the influence of the slenderness ratio of CFFT columns on the critical

buckling load and the ultimate capacity of such columns;

- To investigate the relative importance of internal reinforcement, concrete compressive strength and thickness of the FRP tubes on the buckling mode of failure of CFFT columns;
- To verify the accuracy of existing critical buckling load formulas and then to propose a threshold for the slenderness ratio for CFFT columns.

4.4 Experimental Program

4.4.1 Materials

In this study, two types of steel bars were used to reinforce the CFFT and control specimens, deformed steel bars No. 10 M and mild steel bars 3.2 mm (0.125 in) diameter. Steel bars No. 10 M was used as a longitudinal reinforcement, while steel bars 3.2 mm (0.125 in) diameter were used as spiral reinforcement for the control specimens. The mechanical properties of the steel bars were obtained from the standard tests according to the ASTM A615/A615M-09 (ASTM 2009). Five specimens for each diameter were tested. The average values of the yield tensile strength, f_y, were 462 and 675 MPa (66.99 ksi and 97.875 ksi) for steel bars No. 10 M and 3.4 mm diameter, respectively with an ultimate tensile strength, f_{su}, 577 and 820 MPa (83.66 and 118.9 ksi), respectively. Two different concrete batches (A and B) were used in the experimental program. The average actual cylinder compressive strengths after 28-day and their standard deviation were 30 ±0.5 MPa and 45 ±0.5 MPa for batches A and B, respectively.

Two types of FRP tubes with an internal diameter of 152 mm (6.0 in) were used in the experimental program taken the names throughout the manuscript Type I and Type II. The GFRP tubes were fabricated using filament winding technique; E-glass fiber and Epoxy resin were utilized for manufacturing these tubes. The two tubes had different thicknesses with various numbers of layers and fiber orientations as shown in Table 4-1. The split-disk and coupon tensile tests were performed on five specimens from each type according to the ASTM D-2290-8 and ASTM D 638-08 standard to determine the

Table 4-1 Dimension and mechanical properties of fiber-reinforced polymer tubes

Tube type	D (mm)	t_{frp} (mm)	No. of layers	Stacking sequence	E_x (MPa)	E_y (MPa)	f_{ua} (MPa)	f_{uhfrp} (MPa)
I	152	2.65	6	$[\pm 60°]_3$	8785	20690	57.90	345
II	152	6.40	14	$[\pm 65_3, \pm 45, \pm 65_3]$	9270	23630	60.15	390

D and t_{frp} are the internal diameter and thickness of the FRP tubes, respectively. f_{uhfrp} and f_{ua} are, respectively, the ultimate strength in the hoop and axial direction; E_x and E_y are, respectively, the Young's modulus in the longitudinal and hoop directions.*(Note: 1 mm = 0.04 in, 1 MPa = 0.145 ksi)*

strength and Young's modulus in the axial and transverse directions. More details regarding the mechanical characteristics and material properties of these tubes can be found in (Mohamed and Masmoudi 2008a and c).

4.4.2 Test specimens

Table 4-2 summarizes different configurations of the tested specimens. The experimental program was carried out on twenty two specimens, eighteen CFFT columns and four RC columns. The twenty two specimens were included through six series. The tested columns had a circular cross-section of 152 mm (6 in) diameter. In the specimens ID shown in the second column of Table 4-2, the numbers indicate the column height in cm and the letter I or II refers to the tubes type. The symbols A and B in the specimen ID stand for the concrete strength 30 and 45 MPa (4.35 ksi and 6.525 ksi), respectively.

Each series included three specimens with the same height and different concrete strengths or FRP types as shown in Table 4-2. The first two specimens in each series were casted in the FRP tube of Type I with the two different concrete batches while the third specimens in each series was made of the concrete batch of Type A ($f_c' = 30\,\text{MPa}$ (4.35 ksi)) and was cast in the FRP tube of Type II. The column height ranged from 305 mm (12 in) (Series No. 1) to 1520 mm (60 in) (Series No. 5). Series No. 1 had two replicas for each specimen with a total number of six specimens in this series. The objective of this particular series was to measure the ultimate capacity of short concrete column (the target failure mode of the column in this series was rupture in the FRP tube).

This particular series intended to measure the mechanical characteristics (Ultimate load, initial and tangent young's modulus) of the concrete confined with two FRP tubes types. Series No. 6 included control specimens with internal spirally steel reinforcements (pitch = 50.6 mm (2 in)) instead of FRP tubes. In this series, two replicas were taken for each column. The pitches of the steel were designed to have approximately the same hoop stiffness of the FRP tube of Type I, (Fam et al. 2007). Series No. 2 to No. 5 represented long CFFT columns with a slenderness ratio ranged from 8 to 20, as shown in Figure 4-1. All the columns in these series were internally reinforced with six deformed steel bars (10 M) with a reinforcement ratio equal to 3.30 %. The bars were distributed uniformly inside the cross section of the GFRP tube. Two steel stirrups were used at the top and the bottom of each specimen to fix the bars in their positions during casting (Figure 4-1.b). Note that, the specimens of Series No. 2 to No. 5 did not have internal distributed steel stirrups along the column height.

Table 4-2 Configuration and characteristics of the tested specimens and test results

Series No	ID	Tube	l (mm)	kl/r	f'_c (MPa)	f'_{cc} (MPa)	f'_{cc}/f'_c	ε_{cc}	ε_{ch}	P_y (kN)	P_u (kN)	P_y/P_u %	Failure mode
1	30IA*	I	305	4	30	72.50	2.47	0.045	0.038	--	1316	---	C-R
	30IB*	I	305	4	45	85.95	1.91	0.041	0.034	--	1561	---	C-R
	30IIA*	II	305	4	30	123.5	4.11	0.041	0.028	--	2231	---	C-R
2	60IA	I	610	8	30	78.42	2.61	0.035	0.025	890	1652	53.87	C-R-L
	60IB	I	610	8	45	83.50	1.85	0.022	0.013	1195	1741	68.63	C-R-L
	60IIA	II	610	8	30	122.7	4.09	0.029	0.019	1068	2430	43.95	C-R-L
3	90IA	I	912	12	30	67.14	2.23	0.033	0.025	935	1454	64.30	C-R-L
	90IB	I	912	12	45	75.17	1.67	0.017	0.010	1159	1595	72.66	C-R-L
	90IIA	II	912	12	30	117.5	3.92	0.031	0.019	1203	2338	51.45	C-R-L
4	120IA	I	1216	16	30	52.77	1.76	0.021	0.013	996	1202	82.86	B
	120IB	I	1216	16	45	62.12	1.38	0.014	0.008	1150	1366	84.18	B
	120IIA	II	1216	16	30	99.17	3.30	0.021	0.012	1153	2016	57.19	C-R-B
5	150IA	I	1520	20	30	46.50	1.55	0.015	0.011	1086	1127	96.36	B
	150IB	I	1520	20	45	52.83	1.17	0.014	0.009	1167	1203	97.00	B
	150IIA	II	1520	20	30	94.78	3.16	0.026	0.018	1217	1939	62.76	C-R-B
6	Cont-A*	Spiral steel	912	12	30	31.34	1.04	--	--	805	826	97.45	C
	Cont-B*		912	12	45	33.34	0.74	--	---	838	861	97.32	C

* The results are the average of the two spicemens; *l is the length of the specimen; k* is the column effective length factor (equal 0.5 in our analysis: Fixed-fixed columns); *r* is the radius of gyration of the cross section; (C) concrete compression failure (crushing); (R) FRP-tube ruptures; (L) steel bar local buckling; (B) buckling. *(Note1 mm = 0.04 in, 1 kN = 0.225 kips, 1 MPa = 0.145 ksi)*

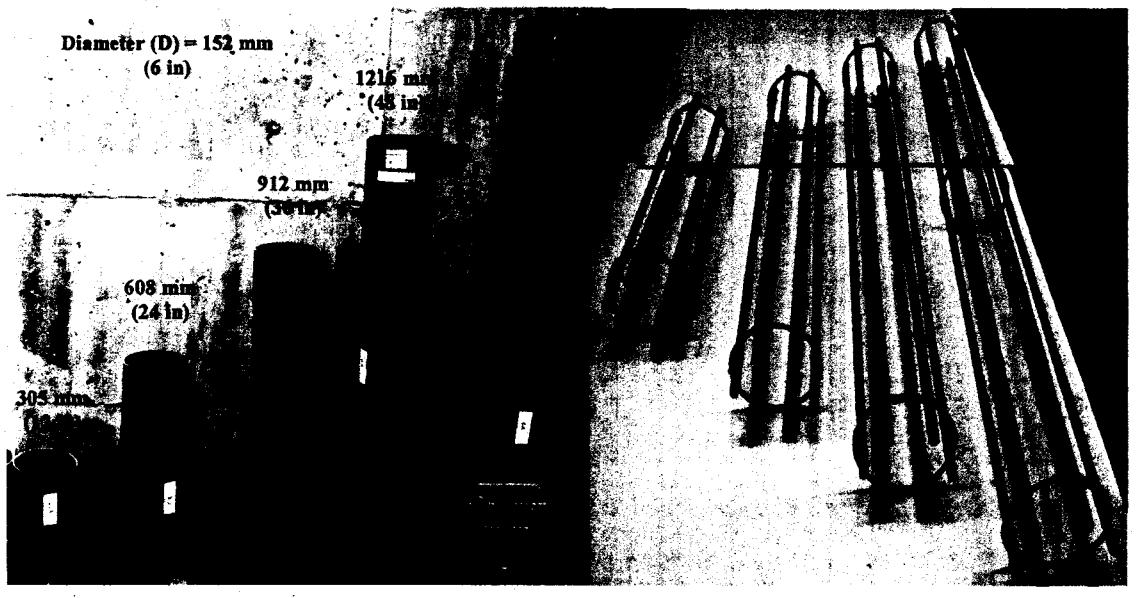

a. FRP tubes b. Steel cages

Figure 4-1 Test specimens

4.4.3 Instrumentations and test set-up

Vertical and horizontal displacements of all specimens at their mid-height were monitored using linear variable displacement transducers (LVDTs). Strains in the longitudinal steel reinforcement and FRP tubes were recorded using electric strain gauges, 6.0 mm in length. Two strain gauges were bonded to the mid-height of two longitudinal steel bars, 180 degree apart. Two axial and two transversal strain gauges were installed on the FRP tubes on two opposite sides at the mid and quarter height of each column (see Figure 4-2.a). All the specimens were prepared before testing using a thin layer of the high strength sulphur capping at both ends to insure the uniform stress distribution during the test. In addition, steel collars (4.0 mm thickness and 60.0 mm width) were attached to the ends of the specimens to confine and prevent premature failure at these locations. The specimens were tested using a 6,000 kN (1350 kips) capacity FORNEY machine, where the CFFT columns were setup vertically at the center of loading plates of the machine as shown in Figure 4-2.b. Due to the fact that the upper and lower clamp of the testing machine were prevented from rotation (no special set-up was used to allow the rotation), the tested specimens represented the case of fixed-fixed columns.

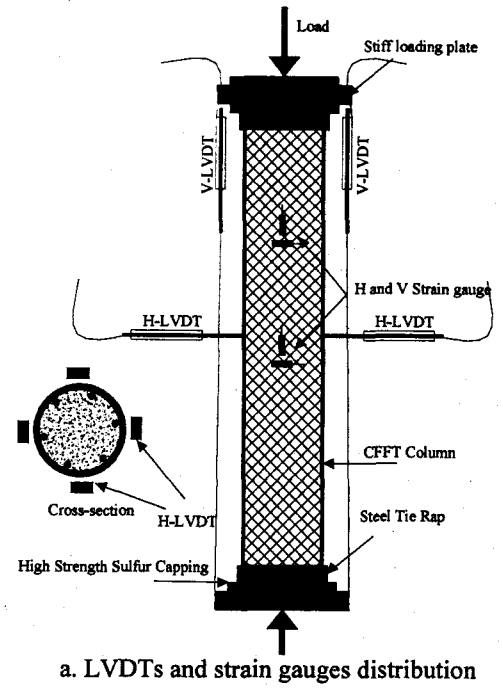

a. LVDTs and strain gauges distribution

b. Test setup

Figure 4-2 Instrumentation and test setup

4.5 Test Results and Discussion

4.5.1 Failure modes

The modes of failure of the CFFT specimens were characterized either by FRP tubes rupture (Series No. 1) or columns instability (Series No. 4 and 5). For the columns in Series No. 2 and No. 3, a combination of the both modes of failure was recorded. Figure 4-3 shows the modes of failure of all tested specimens. For short columns or CFFT cylinders ($l = 305$ mm - Series No. 1) the modes of failure were characterized by rupture of the tubes (Figure 4-3.a). The rupture of the GFRP tubes was followed by concrete crushing. As shown in Figure 4-3.a, the rupture cracks in the confining FRP tubes were propagated along the longitudinal vertical axis of the column indicating that these tubes failed when the lateral strain values exceeded the ultimate strain values of FRP materials. For the columns with a slenderness ratio 8 and 12 ($l = 610$ mm and $l = 912$ mm), the failure modes were a combination of rupture of the confining FRP tubes and local buckling of internal steel bars at the column mid-height. Yet the CFFT columns have not failed due to instability and the column response was similar to that of short columns. However, the columns with these two slenderness ratios started to buckle at load level that was slightly less than the failure load of the column. This mode of failure is shown in Figure 4-3.b for the columns in Series No. 2 and No. 3. It is of interest to mention that for specimens in the Series No. 3, the CFFT columns buckled just before the rupture of the tube.

Increasing the slenderness ratio to 16 ($l = 1216$ mm and longer) changed the modes of failure to instability of the CFFT columns (Figure 4-3.c). The columns of Series No. 4 and 5 failed at a load level that was much less then the ultimate capacity of the corresponding cylinder (Series No. 1). The instability was evident in the shape of a single curvature mode at a load level around 85% of the final failure load of each specimen. This indicated that these specimens behaved as long columns. Although the column started to buckle at a load level 85% of the failure load, the deflected column was still stable and carried more axial load. Loading the specimens continued until the specimens could not maintain the applied axial force or until reaching the maximum displacement capacity of the testing machine. The recorded failure modes of the CFFT columns tested in Series No.

4 or No. 5 showed that the greater the slenderness ratio, the more significant the curvature of the FRP tube. As far as the mode of failure of the control specimens (columns that are confined with internal transversal steel stirrups instead of FRP tubes) are considered, Figure 4-3.d shows the modes of failure of the tested specimens with the two different concrete batches (Series No. 6). The failure mode was typical for unconfined concrete columns. It is characterized by concrete crushing with concrete cover splitting. The failure mode took place once the internal steel bars were yielded.

4.5.2 Ultimate load carrying capacity and slenderness ratio effect

The experimental yielding and ultimate loads, (P_y and P_u respectively) of all tested specimens are given in Table 4-2. In this table, the confined concrete compressive strength f'_{cc} ; i.e., the maximum compressive strength just before failure, and the corresponding axial strain $\varepsilon_{cc}$and the lateral strain hoop direction ε_{ch} are shown in the seventh to the thirteenth columns. This table also presents the effectiveness of the confining technique, f'_{cc}/f'_c, and the ratio of yielding and ultimate load. The stress–strain behaviors of the CFFT specimens showed a typical bilinear response. More details regarding the stress-strain curves can be found in (Mohamed and Masmoudi 2008c).

The confined strength values for CFFT specimens without and with internal reinforcement were calculated as follow:

$$f'_{cc} = \begin{cases} \dfrac{p_u}{A_g} & \text{Without internal reinforcement} \\ \dfrac{p_u - f_y A_s}{A_g - A_s} & \text{With internal reinforcement} \end{cases} \qquad 4\text{-}1$$

where A_g is the column cross-section (internal area of FRP tubes). For each specimen, the failure mode is shown in the last column. The ultimate capacity of all specimens was depicted versus the slenderness ratio in Figure 4-4. In this paper, the slenderness ratio kl/r was calculated based on the geometric characteristics of the concrete neglecting the

30IA 30IB 30IIA

Series No. 1

(a) Concrete crushing

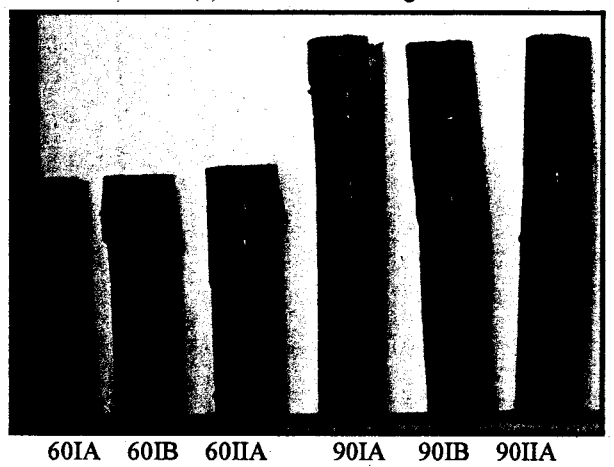

60IA 60IB 60IIA 90IA 90IB 90IIA

Series No. 2 Series No. 3

(b) Combined mode of failure

120IA 120IB 120IIA 150IA 150IB 150IIA

Series No. 4 Series No. 5

(c) Bulking mode of failure

Figure 4-3 (a) Failure modes of CFFT specimens

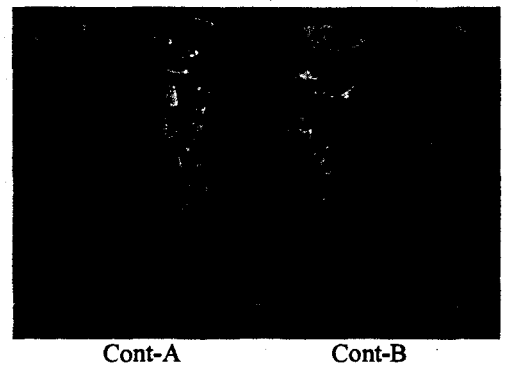

Cont-A Cont-B

Series No. 6

(d) Specimens with steel stirrups

Figure 4-3 (b) Failure modes of control specimens

contribution of the FRP tubes (k and l are, respectively, the column effective length factor and height). The radius of gyration r is computed as $\sqrt{I/A_g}$. This assumption was based on the small thickness of the FRP tubes besides the fact that the fiber orientations of the tubes were oriented mainly toward the hoop direction rather than the axial direction. Another assumption was taken throughout the manuscript that was the tested specimens represent the case of fixed-fixed columns with ($k = 0.5$).

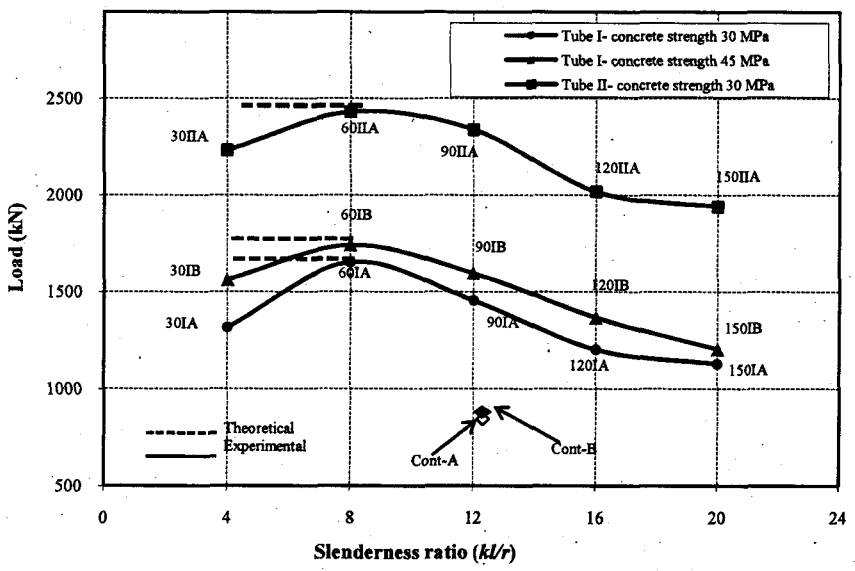

Figure 4-4 Experimental ultimate load carrying capacity-versus-slenderness ratios (kl/r)

Despite the fact that the two control specimens (Cont-A and Cont-B in Series No. 6 with steel stirrups) purported to represent the same lateral confining pressure resulting from steel stirrups as that coming from the FRP tubes of Type I, the ultimate capacity of these two specimens were significantly lower than that of all other specimens. For example, for specimens with the same slenderness ratio (kl/r=12) the ultimate load carrying capacity of the control specimens (with steel stirrups) were 826 kN and 861 kN (185.85 kips and 193.72 kips), for concrete batches A and B, respectively. However using the FRP tubes to confine the same concrete columns instead of internal steel stirrups increased the ultimate capacity to 1600 kN and 2400 kN (360 kips and 540 kips), respectively. This can be attributed to the continuity of the FRP tubes rather than the discontinuity of the steel stirrups. In fact, this reflects the superior confining behavior of FRP tubes compared to steel stirrups to increase the ultimate load carrying capacity of concrete columns. Specimens in Series No. 1 represented case of short columns without internal longitudinal reinforcement (concrete cylinders). Although the mode of failure of the specimens in this series were similar to that of the specimens in Series No.2 (rupture in the FRP tubes) their ultimate capacity were around 20% less than that of the specimens in Series No. 2. The difference in the ultimate capacities between the specimens of the two series resulted from the contribution of the internal reinforcement bars (neglecting the size effect). Theoretically speaking, considering the contribution of the internal reinforcement in calculating the ultimate capacity of the specimens in Series No. 1 ($f_y A_s$) makes their failure loads similar to that of the specimens of Series No. 2 (horizontal line at the beginning of the curves in Figure 4-4).

For all specimens, using FRP tubes to confine concrete columns increased the axial load carrying capacities regardless the slenderness ratio of the CFFT columns. Figure 4-4 confirms the fact that the ultimate load capacities of the CFFT specimens significantly decreased with increasing the slenderness ratio (kl/r) over 8. For example, the decrease of the ultimate capacity of the Specimens 90IA, 120IA and 150IA (with a slenderness ratio changed from 12 to 20) compared to Specimens 60IA was, respectively, 12%, 27% and 32%. This highlighted the fact that the recommended slenderness ratio for design purposes of CFFT columns should be reduced to 12. On the other hand, changing the

concrete compressive strength from 30 to 45 MPa (4.35 ksi and 6.525 ksi) did not significantly enhance the ultimate capacity of any two identical specimens (having the same height and FRP tube type). For example comparing the ultimate capacity of Specimen 150IA with that of Specimen 150IB showed that increasing the concrete compressive strength by 50% the failure load (buckling load) increased only by 6.70%.

4.5.3 Load-deformation characteristics of CFFT columns

The plotted results in Figure 4-5.a to Figure 4-5.d represent the load–deflection relationships of the CFFT and control columns sorted according to their slenderness ratio. Both the yielding and failure loads were marked on the figures using diamond (◆) and circular (●) points, respectively (the yielding load was monitored based on strain gauges reading). It can be seen that the load-axial deflection curve of CFFT columns typically consisted of three stages. The first branch of these curves was almost linear until around 80% of f_c' and it defined the initial stiffness of the FRP-confined concrete columns. We found that the initial stiffness depended only on the concrete compressive strength regardless the slenderness ratio or the FRP tube thickness (refer to Figure 4-5). The second stage of the curve occurred with the initiation of lateral cracks as the confining pressure of the FRP tubes started to be activated. In this stage, the internal steel bars yielded and the axial stiffness of the CFFT columns was gradually reduced. With the propagation of the lateral cracks and because of the confining pressure, the load-deflection curve were charctarized by a hardening region until the failure point, which is the third branch of the curve (refer to Figure 4-5). The axial stiffness in the third branch of the curve was a function of the unconfined concrete compressive strength, FRP tube thickness, and slenderness ratio.

As it can be seen from the specimens in Figure 4-5.c and Figure 4-5.d, increasing the slenderness ratio to 16 and 20 significantly changed the hardening behavior of the load-deflection relationship, yet they had a similar initial axial stiffness as that of columns with slenderness ratio equal 4 or 8. For the specimens with the lower FRP tube thickness (120IA, 120IB, 150IA and 150IB) the CFFT columns did not show any enhancement in the

ultimate capacities after steel yielding. This indicated that, for long columns ($kl/r \geq 16$), the lower FRP tube thickness (Type I of 2.65 mm) (low confining pressure) did not enhance the ultimate capacity of the CFFT columns as a result of the fact that buckling failure load occurred before initiation of the confinement lateral pressure. On the other hand with the higher FRP tube thickness (Type II of 6.4 mm thickness), a significant enhancement in the ultimate load carrying capacity was observed even for specimens with slenderness ratio of 16 and 20.

In Figure 4-5.a, it is observed that there was a significant increase in the ultimate capacity of the CFFT cylinders compared to that of unconfined cylinders. The average increases in the ultimate capacity of the Specimens 30IA, 30IB and 30IIA over that of the unconfined cylinders were (f'_{cc}/f'_c in Table 4-2), respectively, 2.42, 1.91 and 4.11. As expected, the highest enhancement in the ultimate capacity was recorded for columns with FRP tubes of Type II (largest thickness). The increase in the strength of the CFFT columns was more pronounced for columns with lowest concrete compressive strength. For example, increasing the uniaxial concrete compressive strength by 50% (from 30 MPa to 45 MPa) (4.35 ksi and 6.525 ksi) changed the ultimate strength of the CFFT columns by 15% (from 74.2 MPa to 85.95 MPa (10.75 ksi to 12.46 ksi)). This highlighted the fact that the efficiency of the confining techniques using composite materials depended mainly on the thickness of the confining FRP tubes.

The post buckling behavior of CFFT columns is shown in Figure 4-6.a to Figure 4-6.c in terms of the load-lateral displacement relationships. For short columns with $kl/r = 8$, no lateral deformation was recorded due to axial loading, however with a higher slenderness ratio; the lateral displacement of the columns was significant indicating instability of the columns. The CFFT columns with a slenderness ratio larger than 8 started to exhibit lateral deformation tendency after load levels around 80% of the failure load. After this load level, the lateral displacement increased rapidly with a significant decrease in the ultimate capacity up to the complete instability of the column. These columns were buckled in a single curvature with a sine-function shape. More details regarding the post buckling response and lateral deformation of tested specimens are presented in the theoretical analysis section in this paper.

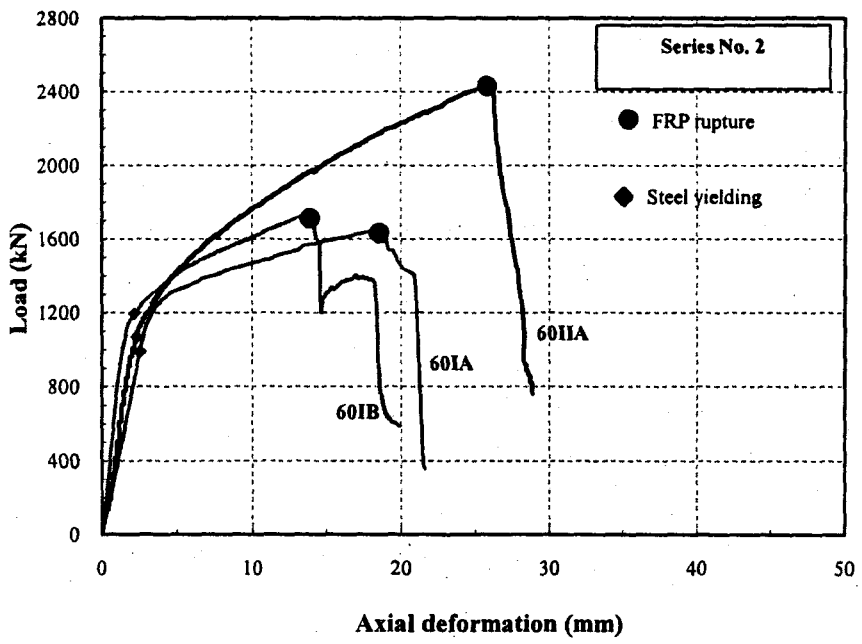

a. $kl/r = 8$

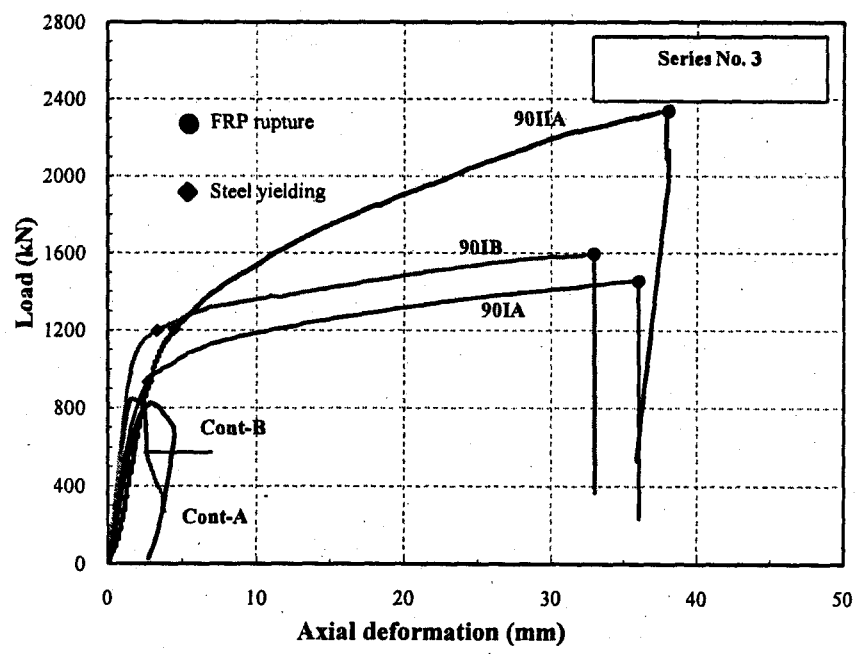

b. $kl/r = 12$

Figure 4-5 Load–axial displacement behavior of CFFT columns

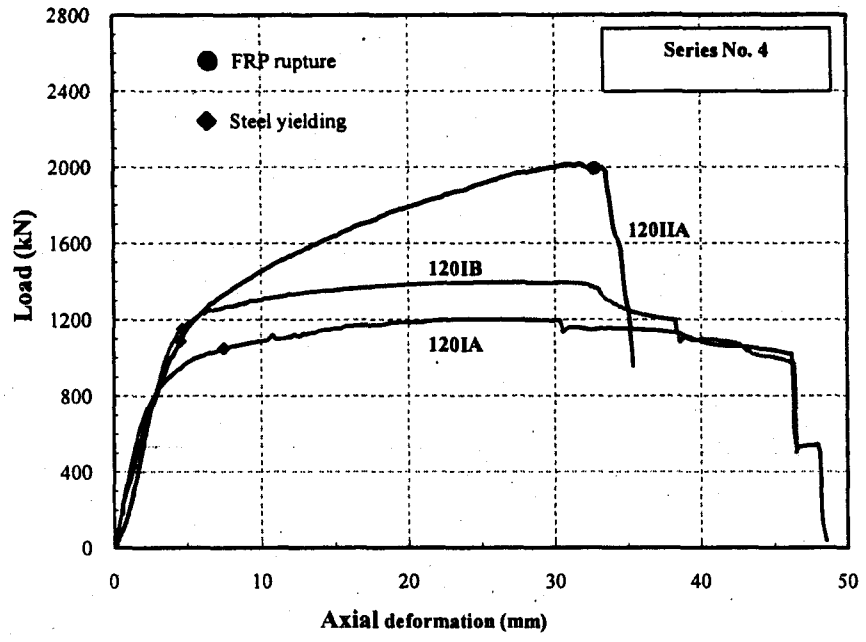

c. $kl/r = 16$

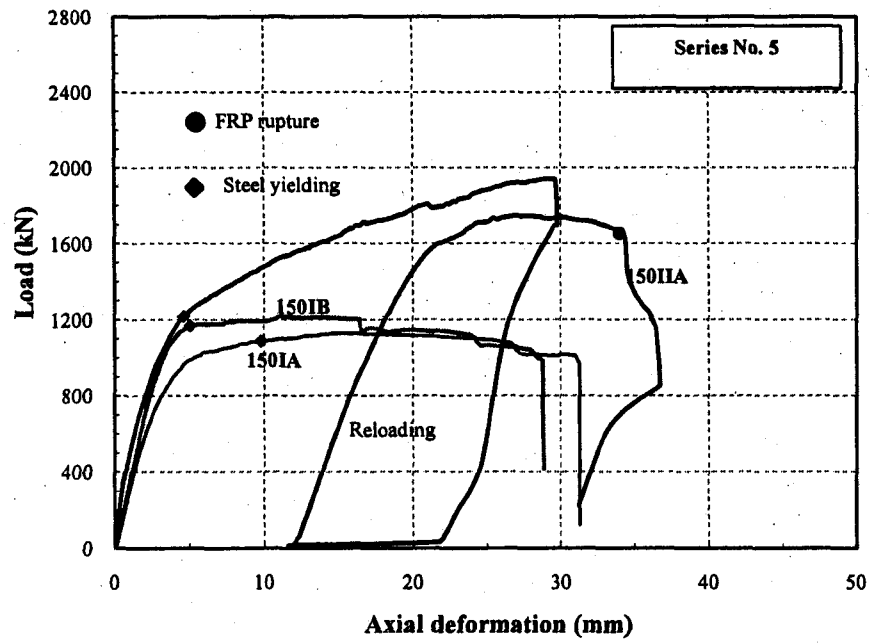

d. $kl/r = 20$

Figure 4-5 Load–axial displacement behavior of CFFT columns

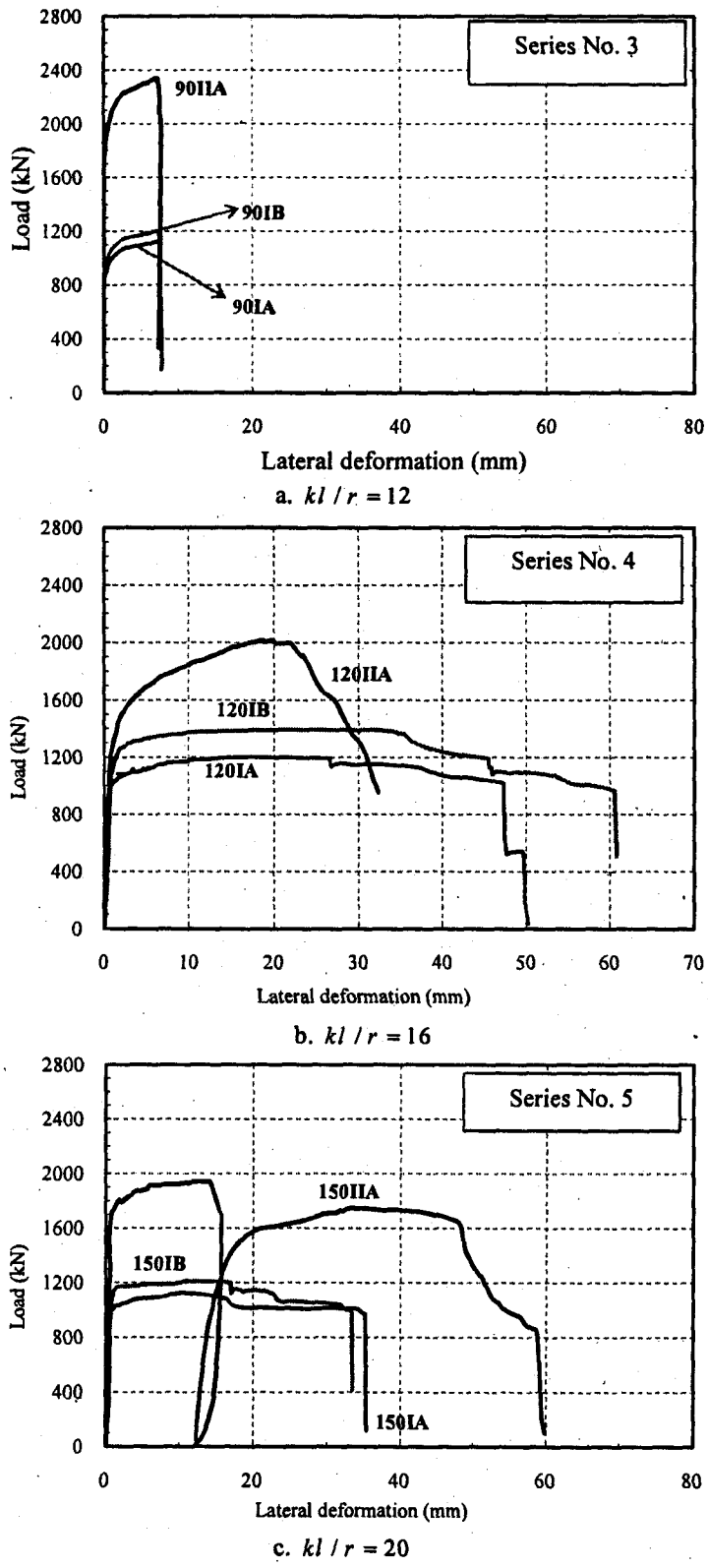

a. $kl / r = 12$

b. $kl / r = 16$

c. $kl / r = 20$

Figure 4-6 Load–lateral displacement behavior of CFFT columns

4.5.4 Effect of concrete compressive strength and FRP tube thickness

Two concrete batches representing normal strength concrete (A and B) were used in the experimental program to cast the CFFT columns. Table 4-2 shows the increase in the axial strength of all specimens in terms of the ratio f'_{cc} / f'_c. The results in Table 4-2 show that the f'_{cc} / f'_c for CFFT specimens with the concrete batch of Type B (45 MPa) (6.525 ksi) equals to 22.7%, 29.1%, 25.1%, 21.6% and 24.5% higher than those of CFFT columns with the concrete batch of Type A (30 MPa), for the same slenderness ratio. This indicated that an average reduction of 25% in the f'_{cc} / f'_c ratio was observed with the increase of the concrete compressive strength from 30 to 45 MPa, (4.35 to 6.525 ksi). Fig. 7.a shows the normalized ultimate strength-versus-unconfined compressive strength for the four slenderness ratio. As it can be seen from the figure, the increase in the axial strength of the CFFT columns was more significant for columns with lower concrete strength (30 MPa) (4.35 ksi) compared to that with higher concrete strength (45 MPa) (6.525 ksi), regardless of the slenderness ratio.

The effect of FRP lateral pressure (F_{lfrp}) on the ultimate capacity of the CFFT columns is shown in Figure 4-7.b. The results are plotted in terms of the normalized ultimate strength versus the normalized lateral confinement pressure divided by the unconfined concrete compressive strength. The FRP lateral pressure (F_{lfrp}) was calculated as follow:

$$F_{lfrp} = \frac{2t_{frp} f_{ufrp}}{D} \qquad 4\text{-}2$$

where f_{ufrp} is the ultimate failure hoop strength of the FRP tubes which resulted from the split–disk test, D and t_{frp} are the internal diameter and thickness of the FRP tubes, respectively (see Table 4-1). As shown in Figure 4-7.b, the increase in the confinement ratio resulted from the increase in the FRP tubes thickness increased the ultimate capacity of the CFFT columns.

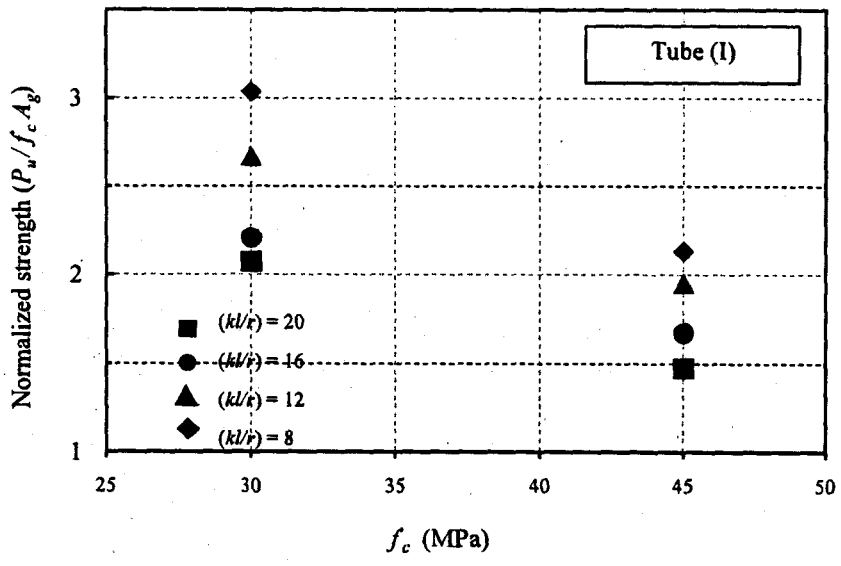

a. Effect of the concrete compressive

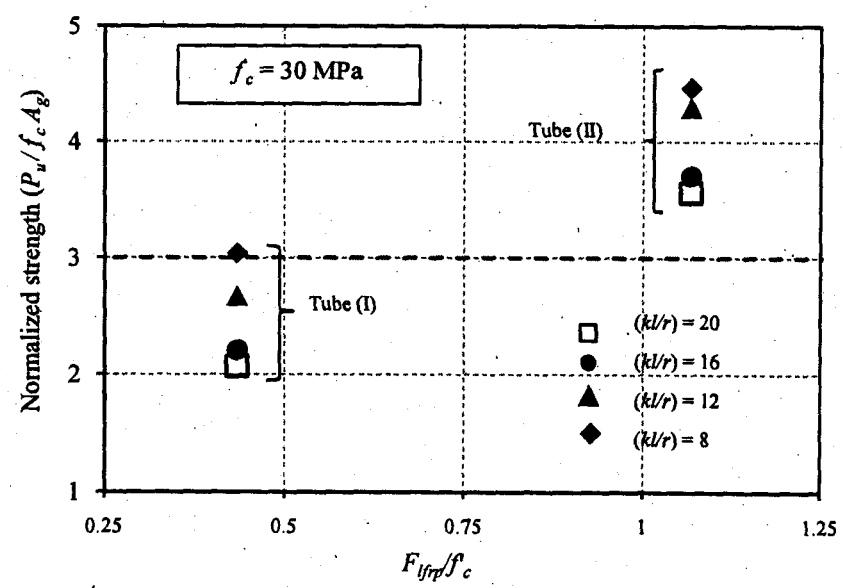

b. Effect of the confining lateral pressure

Figure 4-7 Effect of various parameters on the ultimate strength of CFFT columns

4.6 Theoretical Investigation

The main objective of this investigation is to understand the buckling and post buckling behavior of CFFT columns and to predict the critical slenderness ratio to avoid column failure instability. As a result of the experimentally observed bilinear uniaxial load-displacement relationship of CFFT columns (Figure 4-5.a to Figure 4-5.d) the instability analysis of these columns is different than RC concrete columns. The response of the column is elastoplastic distinguished by a yielding limit (f_{co}, plastic limit stress which is defined as the stress value corresponding to the yield load) and is characterized by a tangent modulus E_t in the hardening region, which is much smaller than the initial elastic modulus E_o. For such columns, one can assume that there is no damage during axial loading and the columns have unloading modulus E_u equals E_o (see Figure 4-5).

In the literature, various empirical relations have been developed to analytically model the effect of the confinement on the behavior of concrete and to find the corresponding Young's moduli values. The bilinear confinement model of Samaan et al. (1998) was verified by many researchers and showed a satisfactory accuracy to represent the uniaxial stress-strain curve of the concrete columns without internal reinforcement (De Lorenzis, and Tepfers 2003; Mohamed and Masmoudi 2009a and b). In the formula, the concrete initial tangent Young's modulus was expressed in SI units as:

$$E_{co} = 3950\sqrt{f_c'}(MPa)$$
$$E_{ct} = 245.61 f_c'^{0.2} + 1.3456\frac{E_f t_{fm}}{D}(MPa) \qquad 4\text{-}3$$

Where E_f is the modulus of elasticity in the hoop direction (note, $E_f = E_y$ as given in Table 4-1).

To account for the effect of internal reinforcement on the initial and tangent Young's modulus that are used afterwards in the stability analysis in the subsequent sections, the equivalent cross-sectional Young's moduli of the tested specimens are computed using the concrete and internal reinforcement characteristics before yielding as follow:

$$E_o = E_{co}\left[1+\rho_s\left(n-1\right)\right](MPa) \qquad 4\text{-}4$$

where E_{co} is the initial concrete Young's modulus (Equation 4-3) and ρ_s is the steel reinforcement ratio. In Equation 4-4, n indicated the steel modular ratio that is computed as E_s / E_c where E_s is the steel Young's modulus. In the hardening region of the uniaxial stress-strain curve of the CFFT (after steel yielding $n = 1$), the tangent Young's modulus of the column was determined as:

$$E_t = E_{ct}(MPa) \qquad 4\text{-}5$$

4.6.1 Buckling loads

The plastic responses of confined concrete columns mean that the critical or buckling loads of these concrete columns are significantly less than the elastic Euler buckling load. For too slender columns, it is impossible to exceed the initial yield limit before the column buckles. Thus the critical buckling load is controlled by the elastic behavior of the column (elastic Euler load with $P_E = \frac{\pi^2 E_o I}{(kl)^2}$). Thus the inelastic buckling load obviously becomes irrelevant for the design purposes. The inelastic buckling load is important in the analysis for columns that are not too slender and not too short, where they can buckle after reaching the yielding stress, f_{co}. The inelastic buckling load of confined concrete columns can be determined using two formulas (Bazant and Cedolin, 1991). The first buckling load is known as the reduced modulus load (P_r) and the second buckling formula is computed according to the tangent modulus expression (P_t). The earlier formula represents the upper inelastic buckling load while the former corresponds to the lower buckling limit. Generally, the critical buckling load (maximum applied axial load) is located between the mentioned two loads.

When the column starts to buckle due to the curvature of the deflected column, one face of the column undergoes unloading while the other face continues loading. This makes that the buckling load could remain constant (Bazant and Cedoline, 1991). The buckling

load according to this assumption is referred to it as the reduced modulus load (P_r). The reduced modulus load is computed as (Bazant and Cedoline, 1991):

$$P_r = \frac{\pi^2 E_r I}{(kl)^2}(kN) \qquad 4\text{-}6$$

where $E_r = \left[\frac{1}{2}\left(\frac{1}{\sqrt{E_u}} + \frac{1}{\sqrt{E_t}}\right)\right]^{-2}$. In this formula, it is assumed that columns buckle at a constant load level where the cross-section is subjected only to incremental compressive axial strain.

The tangent modulus load hypothesis assumes that both faces of the columns are subjected to incremental compressive strain and thus they both underwent shortening with a tangent modulus. This is quite possible as the tensile strain increment caused by the column curvature can be compensated by the incremental compressive strain caused by increasing the axial applied load and thus the axial bucking load could not remain constant. The prediction according to this assumption gives the lower or the safe limit for the critical inelastic buckling load. The column starts to buckle at the tangent modulus load according to:

$$P_t = \frac{\pi^2 E_t I}{(kl)^2}(kN) \qquad 4\text{-}7$$

The CFFT columns start to buckle at the tangent modulus load (P_t). Yet the deflected state at a load level greater than the tangent modulus load and less than the reduced modulus load is still stable. Thus the applied axial load will subsequently increase with the increase of the lateral deformation until reaching the critical load (load level somewhere between P_t and P_r) as shown in Figure 4-6. In the case that the tangent modulus load P_t is less than the yield load, this means that there is no solution for P_t and the inelastic buckling load occurs at the yield load limit.

The experimentally reported load–lateral displacement profiles of the CFFT columns shown in Figure 4-6 strongly confirm this conclusion. As seen in Figure 4-6, the

column started to buckle at a load level greater than the yield load. This load corresponds to the tangent modulus load and the applied axial load increased with the increase of the lateral deformation of the column. Taking Specimen 120IIA (Figure 4-6.b) as an example, the yield load (P_y) occurred at a load level 1153 kN (259 kips). For this particular column the tangent buckling load (Equation 4-7) is 1756.4 kN (395 kips) (case of $P_t > P_y$) and the reduced buckling load (Equation 4-6) is 4514 kN (1015 kips). The critical buckling failure load (experimental value) of this particular specimen is monitored as 2016 kN (453 kips), which is 13% larger than P_t and 45% less then P_r ($P_t < P_{max} < P_r$).

In conclusion at a load level corresponding to the tangent modulus load (P_t), the column starts to buckle; however, the deflected column is still stable and the column can carry more axial force. Note that for any load level $P_t < P < P_r$ the column is still stable. The applied axial load increases with the increase of the lateral deformation until reaching the maximum applied load that is less than the reduced modulus load. This behavior comes mainly due to the contribution of internal steel bars that provide flexural stiffness of CFFT columns. Therefore the critical buckling load satisfies the condition:

$$P_t < P_{max} \le P_r \qquad 4\text{-}8$$

The maximum critical load P_{max} as explained in Bazant and Cedoline (1991) is controlled by the type of loading; i.e. under load or displacement control as:

$$P_{max} = \begin{cases} \dfrac{2\xi}{\xi+1} P_t & \text{Under load control} \\ \dfrac{1+\xi}{2} P_t & \text{Under displacement control} \end{cases} \qquad 4\text{-}9$$

where $\xi = E_u / E_t$. Equations 6, 7 and 9 are represented schematically in Figure 4-8.a as a relationship between critical stress ratio (σ_{cr} / E_t) and slenderness ratio (λ). For specimens with a slenderness ratio 8 or 12, the failure loads for these particular columns are less than the corresponding Euler tangent loads ($P_u < P_t$). This is attributed to the mode of failure of these columns, the buckling load appeared at the yielding load level,

however the column was still stable and could carry more axial load (see Figure 4-6.a). Theoretically, the axial load had to increase until reaching the critical buckling load (p_{max} in Equation 4-9), however the rupture of FRP tube occurred at a load level that was less than the critical buckling load. For columns with a slenderness ratio 16 or 20, the column starts to buckle at a load level corresponding to P_t, while the final critical buckling load occurs at a higher load level (Equation 4-9). In conclusion, although the tangent Euler buckling load was recommended by several researchers to control the instability load of CFFT columns, it gives very conservative prediction. The critical buckling load (Equation 4-9) is more accurate than the tangent Euler load (Equation 4-7) and it is more reliable for the instability analysis especially for columns with internal longitudinal reinforcement.

4.6.2 CFFT columns strength curve

The tangent modulus load can be used as a safe limit for the design however, in fact, it gives very conservative prediction for the actual instability load value. Substituting Equations 4-2 and 4-3 in Equation 4-5 and using the confinement model of Samaan et al. (1998), one can write the governing axial stress of CFFT columns as:

$$\sigma_{cr} = \begin{cases} \sigma_t = \left(\frac{\pi}{\lambda}\right)^2 \left(245.61 f_c'^{0.2} + 1.3456 \frac{E_f t_{frp}}{D}\right)(1-\rho_s) & \text{Inelastic buckling} \\ \sigma_E = \left(\frac{\pi}{\lambda}\right)^2 \left(3950\sqrt{f_c'}\right)[1+\rho_s(n-1)] & \text{Elastic buckling} \\ f_{cc}' = f_c' + 6.0\left(\frac{2 f_{lfrp} t_{frp}}{D}\right)^{0.7} & \text{FRP tubes rupture} \end{cases} \quad 4\text{-}10$$

If the column is not too slender so that $\sigma_t > f_{co}$ then the column starts to buckle at σ_t following inelastic buckling response. For too slender columns, $\sigma_t < f_{co}$, it is impossible for a column to not buckle before reaching the yield limit f_{co}. Accordingly, there is no solution for σ_t and the column instability is controlled by the elastic buckling stress σ_E. In most of the experimental programs in the literature including the results of

this paper, columns instability of CFFT columns appeared in terms of inelastic buckling $\sigma_t > f_{co}$. Figure 4-8.b shows the design curves of CFFT columns as a relationship between the critical axial stress value and the slenderness of the column.

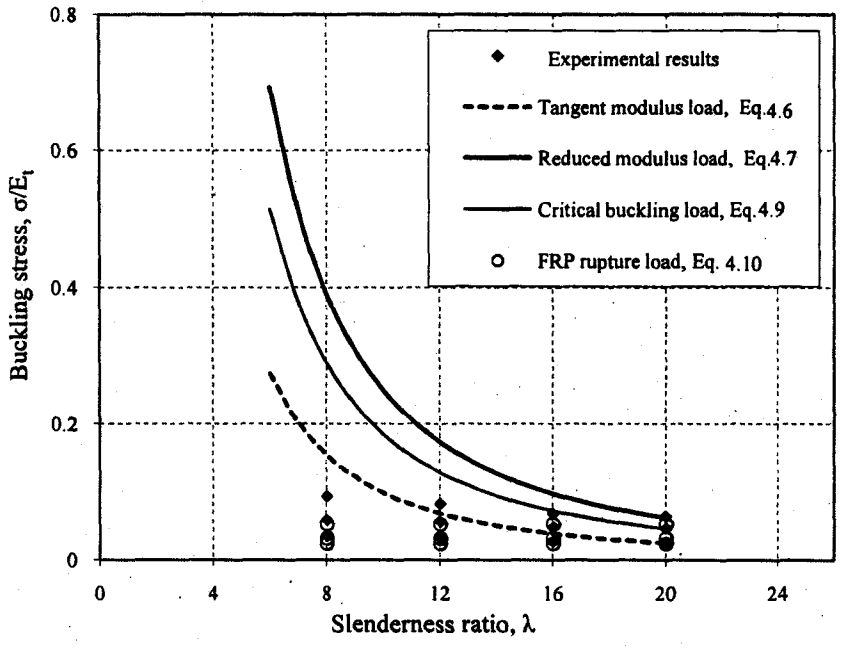

a. Verified design equation

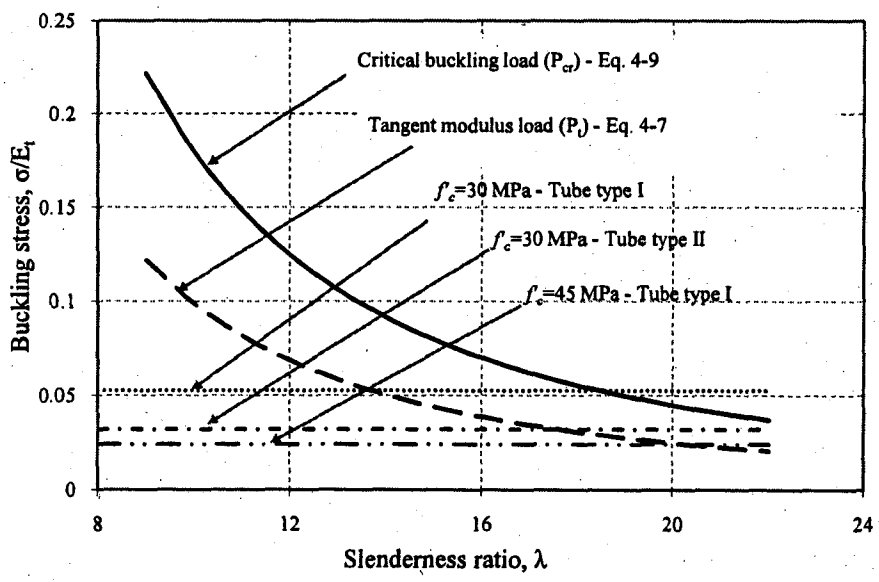

b. Design curve

Figure 4-8 Effect of the slenderness ratio on the critical buckling stress

4.6.3 Design example

In stability analysis, most of the code provisions and design guidelines limit slenderness ratios of concrete columns to prevent the buckling mode of failure. The ACI 318-08 and CSA S6-06 codes state that the effect of slenderness can be ignored for short RC columns if (kl/r) is less than 22. Figure 4-8.b, show a theoretical strength curve of confined concrete columns using both the tangent Euler formula (Equation 4-7) and the critical load formula (Equation 4-9). The horizontal limits in Figure 4-8.b indicate the ultimate strength of the short CFFT columns. It is obvious that the critical slenderness ratio (λ_{cr}) is function of both the concrete compressive strength and hoop stiffness of FRP tubes. This ratio is defined as the maximum slenderness ratio corresponding to ultimate strength of short columns (intersections of horizontal lines with buckling curves in Figure 4-8.b). In order to find a solution for λ_{cr}, one can solve Equation 4-10 with Equation 4-9 as

$$\sigma_{cr} = f'_{cc} \qquad 4\text{-}11$$

This leads to:

$$\lambda_{cr} = \frac{\pi}{S}\sqrt{\frac{E_t}{f'_{cc}}}\sqrt{\frac{2\xi}{\xi+1}} \qquad 4\text{-}12$$

Where E_t and f'_{cc} are determined from Equations 4-5 and 4-10, respectively. In Equation 4-12, S is the safety factor. The AASHTO specification use S = 2.12 to control the buckling load limit, and $\xi = E_u / E_t$. The effect of the concrete compressive strength and the lateral stiffness of the FRP tubes are shown, respectively in Fig. 9.a and 9.b. With an increase of the concrete compressive strength or decreasing the lateral stiffness of the FRP tubes, the critical slenderness ratio (Figure 4-9.a and Figure 4-9.b, respectively) increases. This indicates that the buckling behavior of CFFT columns significantly depends on the properties of FRP and concrete. From Figure 4-9, the critical slenderness ratio of the CFFT columns depends on the buckling load formula; i.e., the tangent Euler formula or the critical buckling load. The slenderness limit observed in the experimental part of this research ($\lambda = 12$) or that provided by Mirmiran et al. 2001($\lambda = 11$) is slightly less than that predicted from the theoretical analysis (Figure 4-9). This can be ascribed to the influence of the size effect and geometrical imperfections that were not yet

considered in the theoretical study. In conclusion, a slenderness limit of 12 for CFFT columns is a safe value for the design purpose. Equation 4-12 is relevant for the design purposes by dividing the predicted slenderness ratio by an appropriate factor of safety to account for the size effect and the geometric and material imperfections.

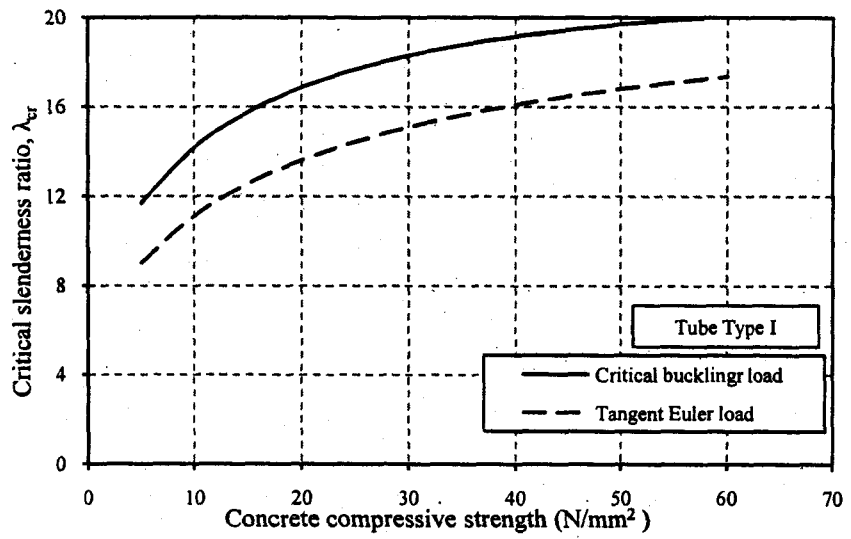

a. Effect of concrete compressive strength

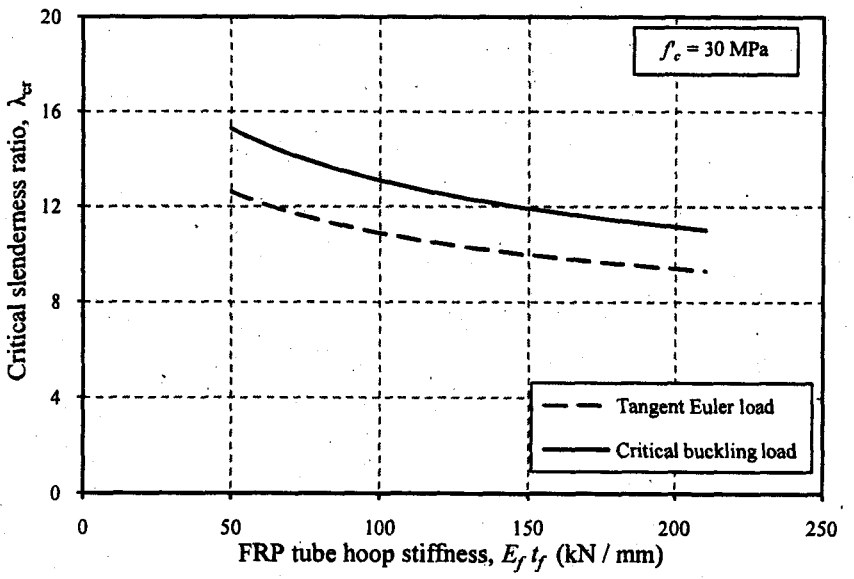

b. Effect of FRP hoop stiffness

Figure 4-9 Critical slenderness ratio

4.7 Conclusions

This paper included both experimental and theoretical investigations on the buckling responses of CFFT columns. The experimental part work included the testing of twenty two CFFT and RC columns with various slenderness ratio, FRP tube thickness and concrete compressive strength. In addition, theoretical analysis was presented to understand the post buckling behaviour of CFFT columns. Based on the specific findings of this research, the following conclusions may be drawn:

- Both the axial strength and stiffness of slender columns were increased as a result of the confining effect of the FRP tubes;
- The enhancement of the axial strength of the slender columns is more pronounced for the lower strength concrete (30 MPa (4.35 ksi)) than that for the higher strength concrete (45 MPa (6.525 ksi));
- Increasing the thickness of the GFRP tubes significantly improved the ultimate load capacity of tested specimens;
- The uniaxial compressive strength of CFFT was reduced by 13% to 23% with increasing the slenderness ratio from 2 to 20 depending on the concrete compressive strength and thickness of FRP tubes;
- A simplified formula for the limit slenderness ratio was proposed for the design purposes of CFFT columns. The predicted value according to the proposed formula agree with the observed critical slenderness ratio ($\lambda = 12$) and with the recommended value in the literature;
- It was found that the predicted slenderness limit was slightly affected by both the concrete compressive strength and FRP tube thickness, however it was reduced with increasing the thickness of the confining FRP tubes.

Chapter 5
Flexural Behaviour of Reinforced CFFT Beams

5.1 Abstract

This study presents experimental and analytical programs conducted to study the flexural behaviour of reinforced concrete-filled FRP tubes (RCFFTs) beams tested under four-point bending load. The experimental program consists of a total of ten circular-beams of a total length 2000 mm with constant diameter 213 mm, 6 RCFFT and 4 control RC beams. Experimental variables include the type of transverse reinforcements (without, spiral-steel and FRP tube), two different FRP tube thicknesses, type of internal reinforcements (steel or glass-FRP bars) and two types of concrete (30 MPa and 45 MPa). Yield and ultimate strengths, failure modes, and ductility are discussed based on measured load, deflection, and strain data. A simplified analytical method is developed to predict the yield and resisting moments corresponding to the failure modes of the tested RCFFT beams. In addition, improvement to the crack moment equation is suggested to account for the effect of confinement. In addition, this study is intended to review and verify the applicability of the North American code provisions and the available equations in the literature to predict deflection of RCFFT beams. The measured deflections and experimental values of the effective moments of inertia were analyzed and compared with those predicted by the available equations. The results of analysis indicated that the behaviour of steel or FRP-RCFFT beamrs under the flexural load was significantly different than that of control steel or FRP-RC beams. This is attributed to the confinement of the concrete core and the axial contribution of the FRP tube which in turn enhances the overall flexural behaviour and improves the tension stiffening of

RCFFT beams. Therefore, the tension stiffening predicted for steel or FRP-RCFFT beams using the conventional equations (steel or FRP-RC member) is underestimated and hence the predicted deflections are overestimated. Based on the analysis of test results of this study, the Branson's equation for the effective moment of inertia of RC structures is modified and new equations are developed to predict well the deflection of CFFT beams reinforced with steel or FRP bars.

5.2 Introduction and Background

The long-term durability of reinforced concrete structures has become a major concern for the infrastructure systems in a usable condition. One of the main factors reducing durability and service life of reinforced concrete structures is the corrosion of steel reinforcement. Thus, it is imperative to use new system that have long-term durability and require less maintenance. A solution to this challenge may be to use new materials or to implement new structural systems. In the last decade, considerable research programs have been conducted to validate the application of FRP composites in the construction industry, and recently, structural applications of FRP composites have begun to appear in different types of the concrete structures.

Recently, the application of the circular CFFT technique is new and rapidly increasing in the field of civil engineering structures. Although the beneficial effects of confinement of concrete is less in flexural as compared to axially loaded members, other advantages such as utilization of the FRP tubes as stay-in-place form work, ease of fabrication and speed of erection still makes this system attractive. The CFFT technique can be utilized successfully for different flexural structural members such as: piles; overhead sign structures; poles; bridge girders; pipes and tunnels. One of the earliest attempts to produce hybrid FRP/concrete beam elements was done by Fardis and Khalili in 1981. They simply proposed pouring concrete into FRP boxes. They also pointed out the mechanical role of FRP and concrete as follows: 1. FRP carries the tensile forces in the tension zone. 2. It provides partial confinement of concrete in the compression zone, enhancing strength and ductility. 3. It carries part of the shear force in the beam through

the two sides. 4. The concrete core provides compressive strength and rigidity and prevents local buckling of the FRP casing.

In fact, extensive research programs have been conducted to investigate the behavior of concrete columns confined with FRP sheets and FRP tubes under pure compression load. However, relatively few studies have focused on static flexural strength of concrete filled FRP tubes (Mirmiran et al. 2000; Davol et al. 2001; Fam and Rizkalla 2002; Fam and Rizkalla 2003). The flexural-axial behaviour of CFFT beam-column was investigated using a total of sixteen 2.75 m long specimens with over-reinforced and under-reinforced sections by Mirmiran et al. 2000. The tests showed that over-reinforced specimens performed superior as beam-columns. They deflected to a lesser extent; and failed at much higher axial and lateral loads, while their failure was still gradual and ductile. Mirmiran et al. 2000 concluded that the bond failure was not an issue in beam-columns. Therefore, off the-shelf tubes can be used as long as end conditions and connections are properly designed. Also, the study showed that the feasibility of concrete-filled FRP tubes as an alternative to prestressed concrete in corrosive environments encountered in Florida and elsewhere. Davol et al. 2001 conducted experimental and analytical studies on the flexural behaviour of unreinforced CFFT beams. It was concluded that the prediction of the failure mode was quite difficult, as it involved a biaxially loaded orthotropic singly curved shell.

Experimental investigation has been conducted on large-scale CFFT tubes and control hollow GFRP and steel tubes tested in bending by Fam and Rizkalla 2002. The diameter of the beams ranged from 89 to 942 mm and the spans ranged from 1.07 to 10.4 m. The study investigated the effects of concrete filling, cross-sectional configurations including tubes with a central hole, tube-in-tube with concrete filling in between, and different laminate structures of the GFRP tubes. The study demonstrated the benefits of concrete filling, and showed that a higher strength-to-weight ratio can be achieved by providing a central hole. It was concluded that the flexural behaviour was highly dependent on the stiffness and diameter-to-thickness ratio of the tube, and, to a much less extent, on the concrete strength. Test results suggested that the contribution of concrete

confinement to the flexural strength was insignificant; however, the ductility of the member was improved.

Fam and Rizkalla 2003 investigated experimentally the flexural behaviour of concrete-filled Glass-FRP tubes ranging in diameter from 90 to 626 mm, using test results of eight beams. It was found that in bending, concrete filling is more efficient for thin-walled tubes or tubes with low stiffness in the axial direction than it is for stiff or thick-walled tubes. It prevents local buckling and increases the flexural strength and stiffness. Fam and Rizkalla 2003 reported that the flexural strength can be increased either by increasing the wall thickness or the ratio of fibres in the axial direction of the tube, however, the failure mode could change to compression. The balanced reinforcement ratio is dependent on the laminate structure of the tube and generally is smaller for tubes with higher stiffness in the axial direction.

To date, only two studies have been reported in the literature on flexural behaviour of CFFT beams reinforced with longitudinal FRP or steel bars (Fam et al. 2007; Cole and Fam 2006). The experimental test results of five reinforced CFFT and two RC beams indicated that CFFT beams performed substantially better than beams with a steel spiral. Unlike CFFT with FRP rebar, CFFT with steel rebar failed in a sequential progressive manner, leading to considerable ductility and strength (Cole and Fam 2006). Also, it was concluded that the most critical parameter affecting the behaviour of steel reinforced RCFFT beams was steel reinforcement ratio: when increased, it improved stiffness, strength, and ductility. Furthermore, Cole and Fam reported that increasing the proportion of fibers in the axial direction of the tube or increasing concrete compressive strength tends to increase strength and stiffness, only after yielding of rebar. The test results of aforementioned RCFFT and control beams of Cole and Fam 2006 with new two prestressed CFFT beams were included in another study by Fam et al. 2007. It was found that the strength of control specimens was governed by crushing and spalling of concrete cover. Also, unlike spiral reinforcement, GFRP tubes confined larger concrete areas and also contributed as longitudinal reinforcement, leading to increases in flexural and shear strengths, up to 113% and 69%, respectively.

Another two experimental studies have been conducted to investigate experimentally the flexural behaviour of prestressed CFFT beams (Parvathaneni et al. 1996; Fam and Mandal 2006). The flexural strength and the behaviour of five prestressed CFFT specimens and one control steel spiral beam have been investigated experimentally by Fam and Mandal 2006. Prestressing strands were oriented in a circular pattern symmetric about the tube's longitudinal axis. The experimental parameters investigated were prestress level, laminate structures of the FRP tubes, and number of strands. Test results indicated that prestressing not only improves the strength and serviceability of the system substantially but it also activated a confinement mechanism of the concrete core restrained by the FRP tube. Fam and Mandal 2006 concluded that prestressing CFFT significantly increased their cracking strengths, initial stiffnesses, and moment capacities. The confinement effects in the compression zones of the PCFFT tested in flexure have been enhanced significantly with prestressing.

On the other hand, the shear strength of CFFT beams has been investigated experimentally by Cole 2005; Ahmad 2004. Tests on reinforced CFFT beams of different shear spans were conducted by Fam and Cole 2007. It was observed that CFFT specimens of shear span-to-depth ratios 1 and 2 failed in shear and flexural, respectively, and the shear strength of CFFT beams was higher than that of RC beams. Also, it was concluded that shear failure may occur in reinforced CFFT at shear span-to-depth ratio less than or equal to 2. Behaviour of short and deep CFFT beams has been compared experimentally to that of their slender counterparts (Ahmad et al. 2008). The test results indicated that the short and deep CFFT beams exhibited higher bending capacity than their slender counterparts, primarily due to the direct diagonal compression strut that develops in the concrete core through arching action. Also, it was concluded that shear failure is only critical for beams with shear span less than their depth (Ahmad 2004.). On the other hand, the experimental study conducted by Fam et al. 2007 indicated that composite tubes are quite effective in shear. They can effectively control diagonal tension cracking, leading to higher shear strength than beams with spiral reinforcement. They mentioned that the failure of RCFFT beams is governed by diagonal fracture of the tube.

Zhu et al. 2006 studied the feasibility of splicing techniques for unreinforced precast CFFT beams. A total of four spliced beams were tested. Three were internally spliced using grouted steel bars, grouted FRP bars, or unbounded post tensioning bars, and the fourth was spliced with FRP socket, commonly used in the piping industry. A control CFFT beam with no internal reinforcement was also tested as a reference. It was observed that the superior effect of FRP tube continuity on system performance. Although initially stiffer, none of the spliced beams tested in this program was as strong as the control specimen. Zhu et al. 2006 reported that this may be primarily attributed to the lack of continuity of the FRP tube, as well as the quality of the cement grout for dowel reinforcement. It was concluded that post tensioning proved to be efficient in improving system performance. The system may benefit from FRP continuity through either a longer and more effective socket or a threaded coupler insert or sleeve. Internal reinforcement can further increase the stiffness and strength of the connection, if grouting quality is controlled. Splicing may be improved by combining the methods tested in this program.

To date, research on CFFT has focused on the effect of static loads. However, long-term sustained loads and dynamic fatigue behavior of CFFT has received little attention. An experimental and analytical investigation was made into the flexural creep behavior of CFFT by Naguib and Mirmiran 2002a and b. It was reported that creep effects reduce the flexural stiffness of CFFT. However, ultimate strength is not significantly altered. Slow rate of loading and short-term creep at 70% of static capacity may cause premature rupture of the tube.

On the other hand, experimental investigation of cyclic behavior of a total six steel-reinforced and unreinforced CFFT beams was conducted by Shao and Mirmiran 2004 and 2005; Shao et al. 2005. The specimens were tested as simple span beam columns under constant axial loading and quasi-static reverse lateral loading in four point flexure. The study showed that concrete-filled FRP tubes can be designed with an appropriate laminate structure for a ductility level comparable to that of conventional reinforced concrete columns. It was concluded that significant ductility can stem from the fibre architecture and

interlaminar shear in the FRP tube. Also, moderate amounts of internal steel reinforcement in the range of 1–2% may further improve the cyclic behaviour of CFFT. Recently, Zhu et al. 2009 concluded that the higher load ranges may drastically reduce fatigue life of CFFT beams. Therefore, it is important to limit the load level on CFFT for a reliable and predictable member performance. Zhu et al. 2009 recommended reducing fibre orientation in angle plies with respect to the axis of the beam to improve fatigue performance of the CFFT member.

Another experimental study was conducted by Ahmad et al. 2008 to evaluate damage accumulation, stiffness degradation, fatigue life, and residual bending strength of CFFT beams. A total of eight CFFT beams with four different types of FRP tube were tested under four point bending. Test parameters included reinforcement index, fiber architecture, load range, and end restraints. It was observed that fatigue performance of CFFT beams was clearly governed by characteristics of the FRP tube and its three phases of damage growth: matrix cracking, matrix delamination, and fibre rupture. Lower reinforcement index increased stiffness degradation and damage growth, and shortened fatigue life. It was suggested that a maximum load level of 25% of the static capacity be imposed for fatigue design of CFFT. With proper design, CFFT may withstand repeated traffic loading necessary for bridge girders.

The objective of this stage of research is to evaluate the flexural behaviour of reinforced CFFT beams. New GFRP tubes were used to act as stay-in-place formwork for beams. The fibre orientations of these tubes were mainly in the hoop direction. The experimental investigation included a total of ten beam specimens, approximately 213 mm in diameter and 2.00 m in length, tested in four-point bending. In the following sections, full details about the experimental program of this study and the considered parameters are provided as well as the analysis of experimental test results and analytical investigation.

5.3 Experimental Program

5.3.1 Materials

There are four materials used in this study. These materials are FRP tubes, concrete, steel reinforcing and FRP bars. The following sections provide description of the different experimental tests conducted to evaluate the mechanical properties of the different materials. The following sections present the characteristics of these materials.

5.3.1.1 Concrete

All specimens in this study were constructed from two concrete batches (N and M) to take into consideration the effect of concrete strength on the compressive and flexural behaviour of the CFFT. The target strengths of batches N and M were intended to provide normal and medium concrete strength of 30 and 45 MPa, respectively. Both concrete batches were supplied by ready mix concrete supplier. The quantities of ingredients, used in the concrete mix are shown in Table 5-1. The maximum size of the coarse aggregates was about 20 mm and 16 mm for N and M concrete batch, respectively. Ten plain concrete cylinders (152 x 305 mm) were prepared from each concrete batch and cured under the same conditions as the test specimens. Five cylinders were tested in compression after 28 days. The 28-day average concrete compressive strength was found equal to 30 ±0.6 and 45 ±0.5 MPa for batch N and M, respectively, (Figure 5-1). The remaining five cylinders were tested in tension by performing the split cylinder test. The average tensile strength ranged from 3.0 to 3.4 MPa for batch N and was 4.1 for M batch.

Table 5-1 Mix proportion of concrete.

Batch ID	Cement		water kg/m^3	Sand kg/m^3	Aggregate kg/m^3	Air content %	W/C ratio	Super plasticizer ml/m^3	Water Reducing Admixture
	kg/m^3	Type							
N	335	Gub-SF	169	856	960	5-8%	0.5	---	350ml/100kg
M	400 435	10 SF TSF	135	680	1080	0-4%	0.32	875 ml/100kg ADVA 140	212 ml/100kg

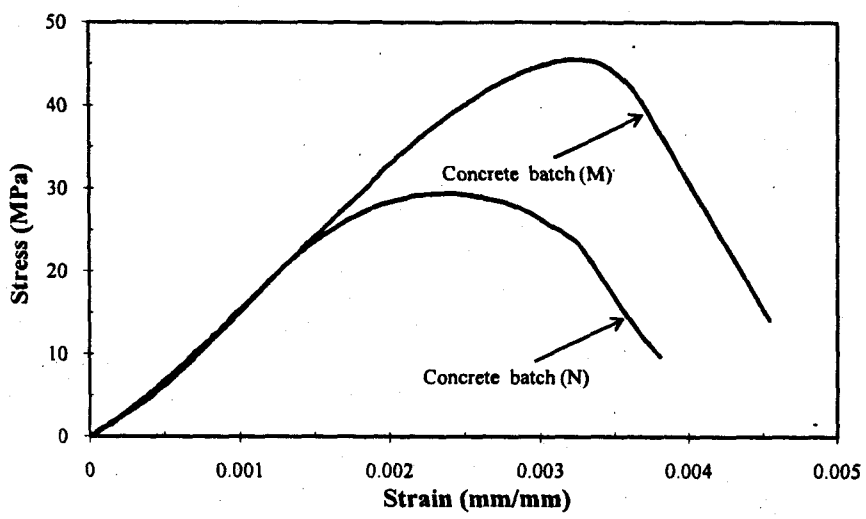

Figure 5-1 Stress-strain relationship for concrete.

5.3.1.2 Reinforcing steel

In this study, two different steel bar diameters were used to reinforce the CFFT and control specimens under flexural loads, see Figure 5-2 (a). Wire steel bars of 3.4 mm diameter were used as spiral reinforcement for the control specimens. Deformed steel bars No. 15M were used for CFFT beams. The mechanical properties of the steel bars were obtained from standard tests that were carried out according to ASTM A615/A615M-09, on five specimens for each type of the steel bars (Figure 5-2). Figure 5-3 shows the typical stress-strain curve for the different types of steel bars. The actual properties are given in Table 5-2 in terms of diameter, nominal area, yield and ultimate strength and young's modulus.

5.3.1.3 FRP bars

Sand-coated glass bars manufactured by a Canadian company [ADS Composites/Pultrall Inc., Thetford Mines, Quebec], with a fibre content of 73% in vinyl ester resin, were used. The bars were made of continuous fibres (glass) impregnated in a vinyl ester resin using the pultrusion process.

Table 5-2 Properties of reinforcing steel bars.

	Bar type		Diameter (mm)	Nominal Area (mm^2)	Yield strength (MPa)	Ultimate strength (MPa)	Modulus of elasticity (GPa)
	Size	Type					
-	Wire	Mild Steel	3.4		675	850	221
15	15M	Deformed	16.0	200	419	686	200

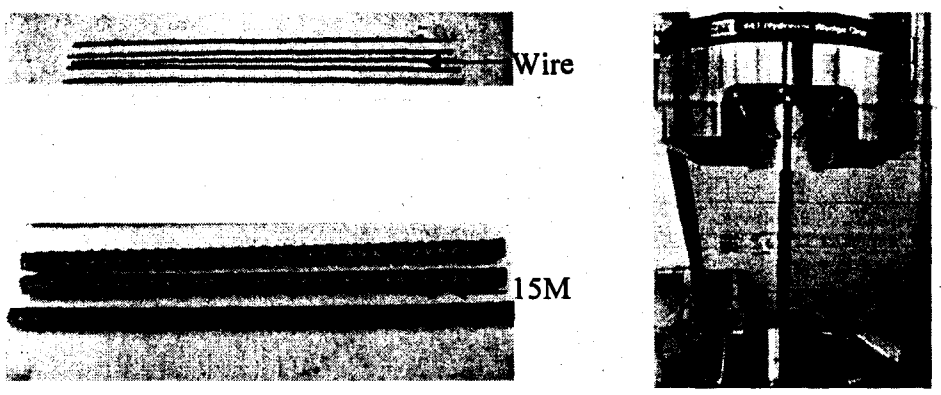

(a) Used steel reinforcing bars (b) Test set up for testing steel bars.

Figure 5-2 types of steel reinforcing bars and test set up.

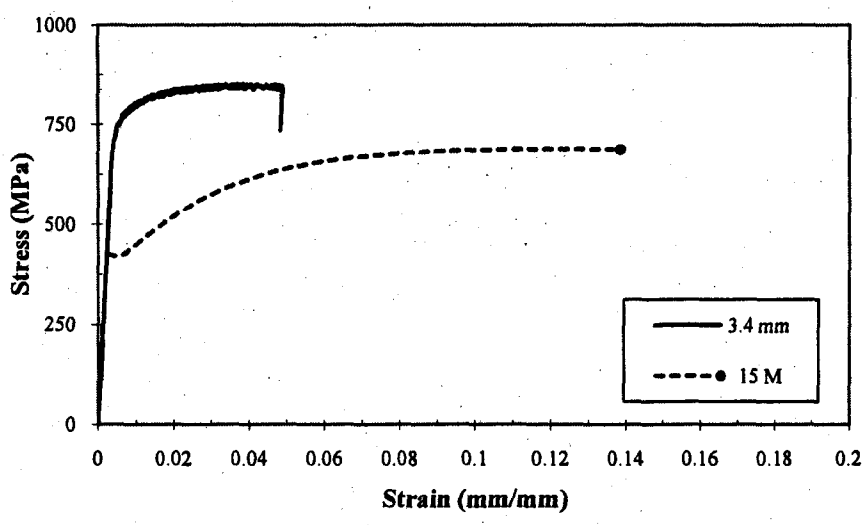

Figure 5-3 Stress-strain relationships for the steel reinforcement

The GFRP bars #5 (ϕ 15.9 mm) were used as longitudinal reinforcement for the control and CFFT beams. Figure 5-4 shows a photo of the FRP bars used in this research. The tensile properties of the FRP bars were determined by performing tensile tests on representative specimens in accordance with ACI 440.3R-04, CAN/CSA S6-00 2000, and CSA S806-02 2002. Table 5-3 presents the mechanical properties of the FRP bars.

5.3.1.4 FRP tubes

New Glass-fibre reinforced polymer (GFRP) tubes were used as structural stay in place formwork for the CFFT specimens of this study. Two different types of the GFRP tubes namely D and E were used with different thicknesses and having the same diameters. The tubes were manufactured using continuous filament winding process adopted by FRE Composites, St-Andre-d'Argenteuil, Quebec, Canada. E-glass fibre and Epoxy resin were utilized for manufacturing these tubes. The glass fibre volume fraction as provided by the manufacture was 68% ± 3%. The material properties for both the fibre and the resin, as given by the manufacture, are presented in Table 5-4.

The internal diameter for the two tubes equals 213 mm, the thickness of tube D equals 2.90 mm, while for tubes E was 6.40 mm. The thickness of tube E was almost double of tube D. Different fibre angles with respect to the longitudinal axis of the tubes were used (±60°, ±65°, ±45°, 90°). It is clear that the fibre orientations of the tubes were mainly in the hoop direction, and no fibres in the longitudinal direction. The winding angles of the tubes D were optimized for below underground pipe applications, while tubes E were designed for pipe telecommunication applications. The tubes were provided with a total length equal to 6000 mm. Figure 5-5 shows the filament wound GFRP tubes used in this study. Table 5-5 shows the details of fibre orientations, stacking sequences, thickness and internal diameter for each type of the tubes.

Table 5-3 Properties of reinforcing FRP bars.

ϕ	US size	Type	Nominal diameter (mm)	Nominal area (mm^2)	Tensile modulus of elasticity (GPa)	Ultimate tensile strength (MPa)	Ultimate strain (%)
15	#5	GFRP	15.875	198	48.2	683	1.8±0.06

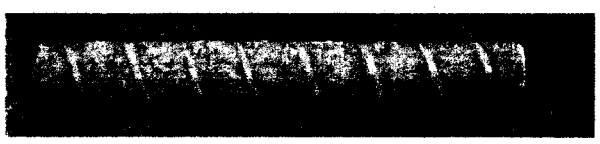

Figure 5-4 Sand coated GFRP reinforcing bars.

Figure 5-5 Filament wound GFRP tubes.

Table 5-4 Mechanical and physical properties of fibres and resin.

Glass fibres	
Linear mass (g / km)	2000
Nominal Yield (Yards / lb)	250
Tensile modulus(MPa)	80 000
Shear modulus(MPa)	30 000
Poisson's ratio	0.25
Epoxy resin	
Density (kg / m^3)	1200
Tensile modulus(MPa)	3380
Shear modulus(MPa)	1600
Poisson's ratio	0.4

Table 5-5 Dimension and details of the GFRP tubes.

Tube type	Internal diameter (mm)	Thickness (mm)	Number of layers	Stacking sequence	Weight kg/m	Length (m)
D	203	2.90	6	$[60, 90_4, 60]$	3.88	6.0
E	203	6.40	12	$[\pm 60_2, 90_2, \pm 60_2, 90_6]$	8.67	6.0

5.3.1.5 Mechanical properties of the FRP tubes

Three different experimental tests were carried out to measure the mechanical properties of the FRP tube in axial direction. The following section presents an experimental program that was conducted to determine the mechanical properties of the FRP tubes used in this study.

5.3.1.5.1 Axial tension test

For each type of FRP tubes, ten coupons cut from the untested sections were tested under uniaxial tension according to ASTM D 638-08, "Tensile properties of Plastics". The tensile coupons dimensions were prepared according the specification of the standard to provide an adequate gripping area at each end. The width of specimen at the grip length was more than that of the free length.

Figure 5-6

Figure 5-6.a shows the typical dimensions of coupon specimens for different types of FRP tubes. Tests were performed in the MTS universal testing machine under load control. The rate of loading was approximately equal to 3 to 4 kN/min. High pressure hydraulic wedge grips were used to hold the specimens in positions. The grip surfaces were deeply serrated with pattern similar to those of a coarse single-cut file, serrations about 2 mm apart and about 1.5 mm deep. The specimens were instrumented with an extensometer at the middle of the specimens. Figure 5-6.b shows the test setup and instrumentation. Failure of all specimens started with matrix cracking and was followed by fibre rupture in the longitudinal direction. Sound snapping could be heard with increasing the load, which attributed to cracking of the resin. Failure was always sudden, with a burst rupture of fibres almost always at one end of the coupons.

Figure 5-6.c presents the dominant failure mechanisms observed for coupon tension test specimens. The stress-strain relationships are presented in Figure 5-7 for the five FRP tubes, at the first stage of loading the curves were linear up to 80% of the peak load. Beyond this level the curves were nonlinear up to failure. Small load drops accompanied by the change in the stiffness were observed. This resulted from the earlier rupture of fibres and matrix cracking. The ultimate tensile stress ranged from 56 MPa to 60 MPa, while the axial strain at the peak stress ranged from 0.004 to 0.005. The initial stiffness for the different type of the tube was affected by fibre orientation of each tube. From the measured axial strains and stresses, the elastic modulus in the axial direction of the different type of the tubes was determined. The value of the elastic modulus was on average equal to 15000 MPa.

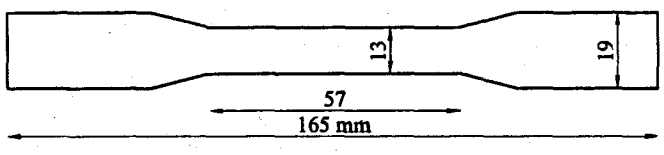

(a) Specimen dimension

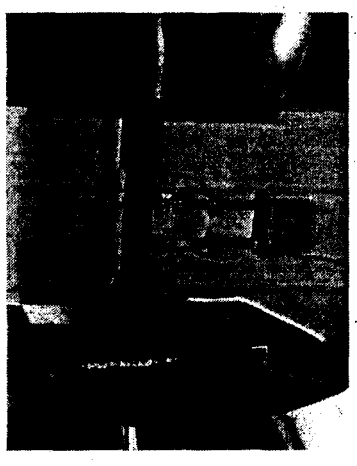

(b) Tests setup

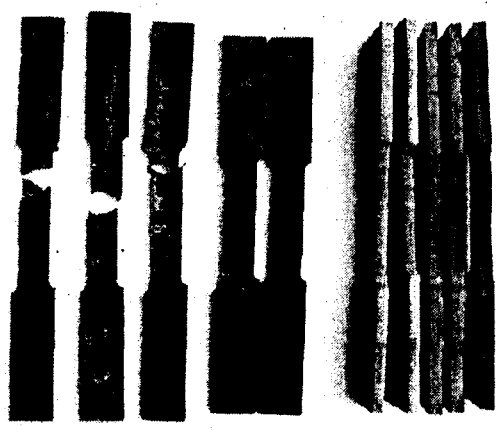

(c) Dominant failure mechanisms

Figure 5-6 Test procedures for coupon tension test.

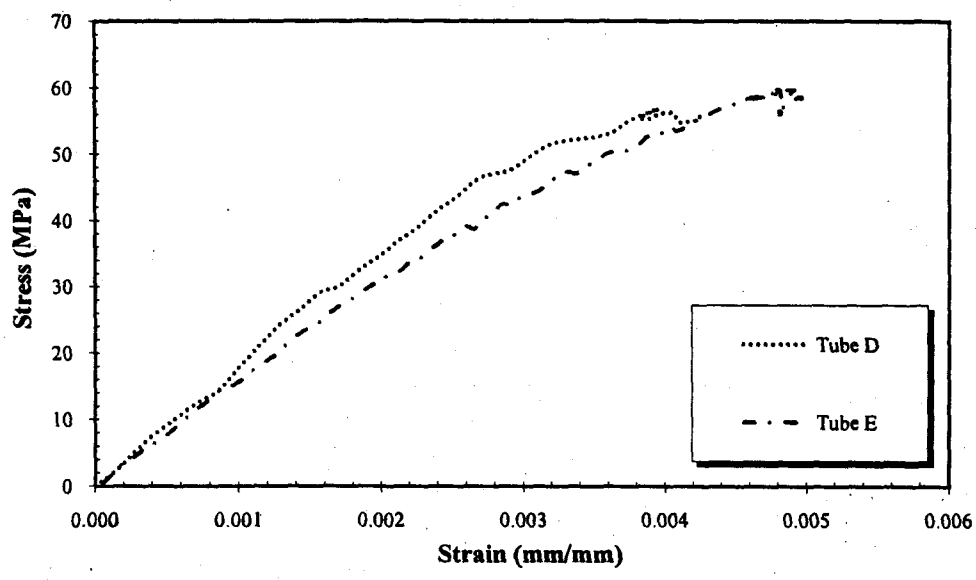

Figure 5-7 Stress-strain behaviour of the FRP tubes for the coupon tensile test.

5.3.1.5.2 Axial compression test

Uniaxial compression tests followed the ASTM D695-08. Tests were performed in the MTS universal testing machine under displacement control. The compression coupons dimensions were prepared according the specification of the standard Figure 5-8.a shows the typical dimensions of coupon specimens for different types of FRP tubes. Special steel fixtures were prepared to prevent the buckling of specimens during the test, see Figure 5-8.b. To reduce the friction between the sample and the steel fixtures, Teflon sheet was inserted between them during the test. The assembly (fixtures and sample) was placed between the jaws of the machine. The specimens were instrumented with an extensometer at the middle of the specimens. The rate of displacement was approximately equal to 0.5 mm/min. Test setup is shown in Figure 5-8. Compression coupon specimens of different tubes failed in identical manner. The failure occurred at one end of the narrow width of the specimen in the axial direction. The axial compression force produced shear stresses in the axial direction of the specimens. However, interlock or overlap was observed at the failure area between the fracture lines of the two faces. On the other hand, slight local buckling was observed for thin specimens after failure.

Figure 5-8.d shows the dominant failure mechanisms observed for coupon compression test specimens. The average stress-strain responses of coupons in compression are shown in Figure 5-9 for the five types of FRP tubes. The response is generally linear in the first stage of loading up to 80% of the peak load. After that shows nonlinear responses until reaching the peak load. The stress-strain curve of tube D presents plastic plateau after reaching the peak stress. The ultimate compression stress for tubes E and D was around 140 MPa, while the axial compression strain at the peak stress ranged from 0.025 to 0.03. The initial tangent modulus of tube D was similar to that of tube E, which approximately equal to 16000 MPa.

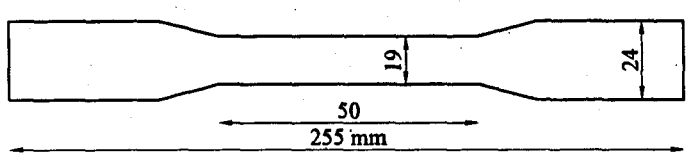

(a) Specimen dimension

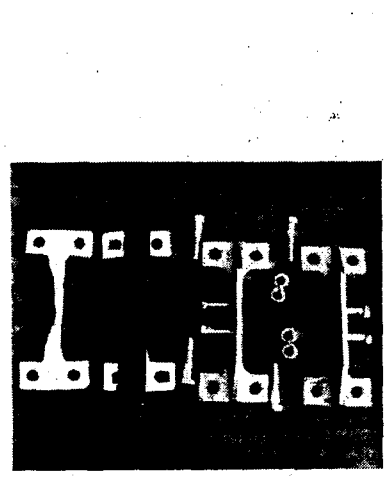

(b) Test fixture used

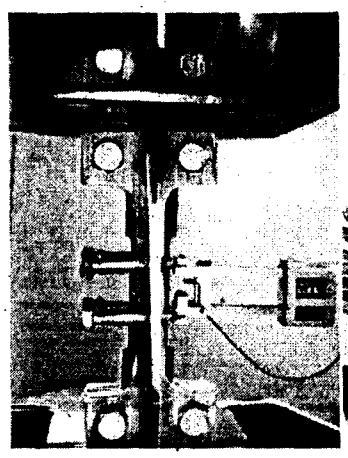

(c) Tests setup

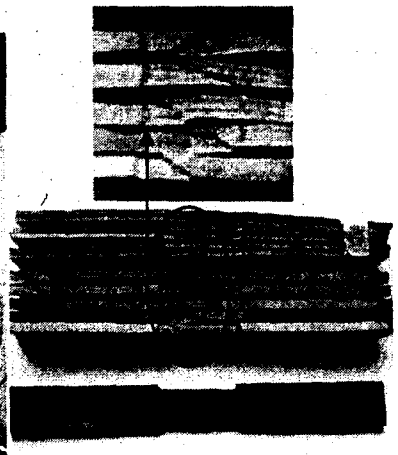

(d) Dominant failure mechanisms

Figure 5-8 Test procedures for coupon compression test.

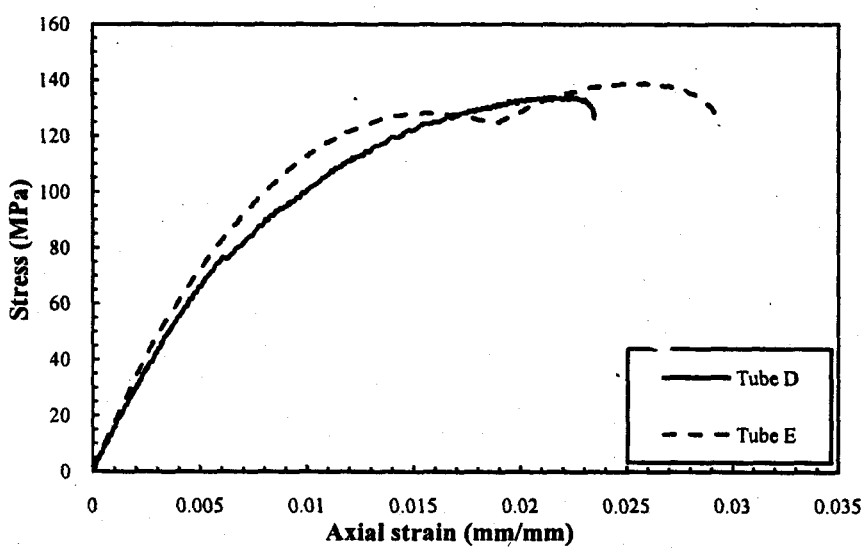

Figure 5-9 Stress-strain behaviour of the FRP tubes for the coupon compression test

5.3.2 Test specimens

The test beams were divided into two series: I and II. Series I and II were cast using concrete batch type N and M, respectively, based on Table 5-1. Each series included five beams, one conventional reinforced concrete (RC) circular beams without spiral reinforcement and one RC beam with spiral reinforcement, while the remaining three specimens were RCFFT. The specimens of each series were reinforced with steel or glass FRP bars with the same reinforcement ratio (ρ = 0.76%). Two batches of concrete were used in order to cast the beam specimens.

Table 5-6 shows the details of RC and RCFFT beams including their identification, height, diameter, type of internal reinforcements and concrete strength. The specimens were identified by codes listed in the second column of Table 5-6. The identifications CO and COS are used for control conventional RC beams without and with spiral reinforcement, respectively. The terms D or E indicate the type of the used FRP tube for the beam based on Table 5-5. The second letters indicate the type of flexural reinforcement, whereas, S or G means steel or glass FRP bars, respectively, was used for the specimen. The terms N and M are used to indicate the type of concrete used to cast the specimens based on Table 5-1.

Table 5-6: Test matrix and details of beam specimens.

	Tube type	Diameter (D=mm)	Shear reinforcement	4t/D%	Flexural reinforcement	Internal reinforcement ratio	Concrete strength (MPa)
Series No. I	CO-S-N	203	---	-	Steel bars	3.65 (6 ϕ 15)	30
	COS-S-N	203	Steel spiral	-	Steel bars		
	D-S-N	213	Tube D	4.5	Steel bars		
	D-G-N	213	Tube D	4.5	GFRP bars		
	E-G-N	213	Tube E	12.6	GFRP bars		
Series No. II	CO-G-M	203	---	-	GFRP bars	3.65 (6 No. 5)	45
	COS-G-M	203	Steel spiral	-	GFRP bars		
	D-S-M	213	Tube D	4.5	Steel bars		
	D-G-M	213	Tube D	4.5	GFRP bars		
	E-G-M	213	Tube E	12.6	GFRP bars		

The beam specimens were designed to study the effects of several parameters, and were compared to each other as follows:

1- Evaluating the contribution of FRP tubes to the flexural capacity, compared to conventional RC beams with and without steel spiral reinforcement. Specimens D-S-N and D-G-M were compared to the control specimens of Series No. I, (CO-S-N and COS-S-N) and Series No. II, (CO-G-M and COS-G-M), respectively. All the three specimens of Series No. 1 were reinforced with steel bars and, while the three specimens of Series No. 2 were reinforced with GFRP bars. The RC beams without spiral reinforcements were compared to the RCFFT specimens to determine the pure contribution of using FRP tube to the flexural capacity. On the other hand, the RC beams with spiral reinforcements were introduced to show the enhancement in the flexural capacity by using RCFFT specimens. However, the spiral reinforcement was designed to provide approximately the same stiffness in the hoop direction as compared to the stiffness of tube type D.

2- The effect of type of the internal reinforcements on the flexural performance of RCFFT beams. Steel and Glass FRP bars of the same cross sectional area (ϕ 15) were used in reinforcing concrete beams. Specimens D-S-N and D-S-M were compared to the specimen of Series No. I, (D-G-N) and specimen of Series No. II, (D-G-M), respectively. All four beam specimens were cast using the same type of the FRP tube, type D with reinforcement ratio (4t/D) equal to 4.5%.

3- The effect of the FRP tube thickness was studied through the specimens of Series No. I, (D-G-N and E-G-N), and specimens of Series No. II, (D-G-M and E-G-M). The FRP tube type E has thickness (6.40 mm), which it is almost equal to two times the thickness of the tube type D, (2.90 mm). The laminate structure of the two tubes was almost the same, however, the fibres oriented in the hoop direction at 60 and 90 degree as compared to the longitudinal axes of the tubes.

4- The effect of concrete strength by using the two types of concrete batches based on Table 5-1, to cast the FRP tubes. The three RCFFT specimens of Series No. I, (D-S-N, D-G-N and E-G-N) were made of the same materials of specimens of Series No. II, (D-S-M, D-G-M and E-G-M), except the concrete. Specimens of Series No. I and II were cast using normal (N) and medium (M) concrete strength, respectively. Two identical specimens of Series No. I and II were compared to each other to determine the effect of concrete strength on the performance of RCFFT beams.

5.3.3 Fabrication of specimens

The FRP tubes were cut to the proper length (2.00 m), as shown in Figure 5-10, using a saw and then were cleaned and dried carefully. The FRP tubes provided the formwork for beam specimens. The control specimens were prepared for vertical casting using stiff cardboard tubes. The cardboard tubes were attached with four vertical stiffeners using wood plate of 50 x 30 mm, cross section distributed at the perimeter of the tube. Reinforcement cages with different configuration were constructed from glass FRP and steel bars.

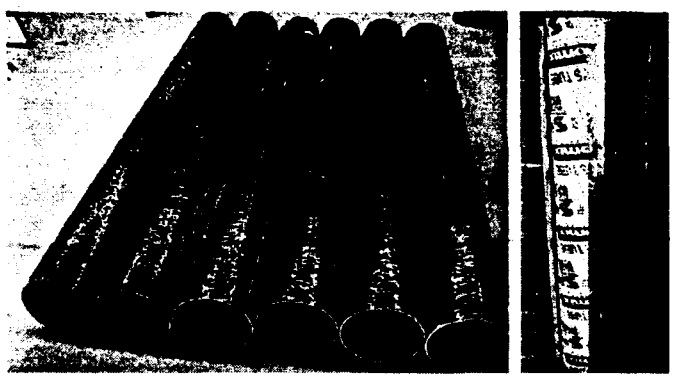

Figure 5-10 FRP and cardboard tubes for beam specimens.

The rebar cage was designed to have an outside diameter of 193 mm, allowing for 10 mm clear spacing on all perimeters of the FRP tubes, which has a 213 mm internal diameter. The cages of the RCFFT specimens had six longitudinal bars (glass FRP bars or steel bars ϕ 15). The longitudinal bars were held in its positions at equal intervals using three hoop steel stirrup (3.4 mm diameter) at the two ends and middle length of the cages. Figure 5-11 shows the typical steel and glass FRP cages which had been used to reinforce the RCFFT and control beam specimens. Two RC beams were reinforced with spiral-steel, one with longitudinal steel bars (COS-S-N), while the second with longitudinal glass FRP bars (COS-G-M). The pitch of 50.8 mm was designed to give approximately the same stiffness of the confinement for FRP tubes type D, (Fam et al. 2007). Reinforcing cages were positioned concentrically inside the tubes before casting. Figure 5-11 shows the typical steel and glass FRP cages for RC and RCFFT beam specimens. The wooden box used to brace the beam specimens vertically was similar to the formwork used for column specimens as mentioned before. Ready-mix concrete batches (N and M) were delivered to the structures laboratory and concrete was cast manually and vertically into the FRP tubes from the upper ends. The tubes were filled with concrete in four layers. Electric internal vibrator was used to consolidate the concrete and to remove air bubbles during casting after each layer. Later, after filling the tubes with the concrete, the end surfaces of the specimens were finished carefully. Top surfaces of the specimens were cured with water for two weeks after casting, to maintain a moist environment. After that, the specimens were lifted and laid horizontally sixty days up to the testing program was started.

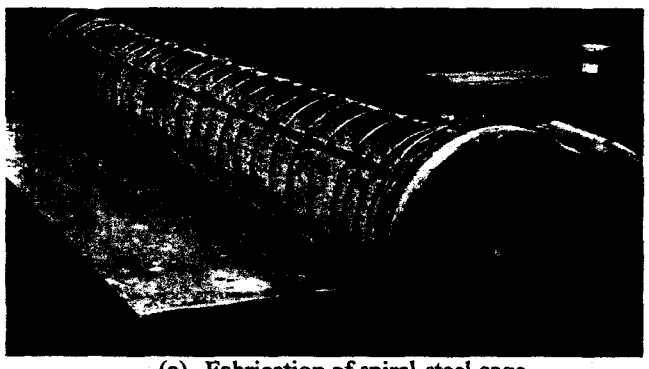

(a) Fabrication of spiral-steel cage.

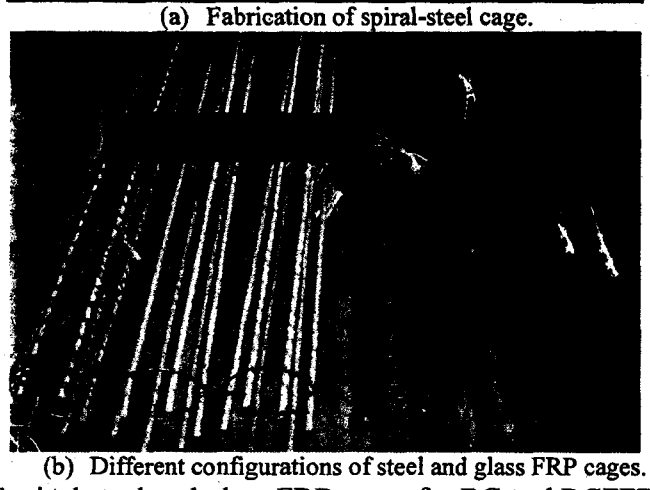

(b) Different configurations of steel and glass FRP cages.

Figure 5-11 Typical steel and glass FRP cages for RC and RCFFT beams

5.3.4 Instrumentation

To monitor the behaviour of the tested beams, the displacements, crack widths, end slip, support rotations and strains in the reinforcement and at the concrete and FRP tubes surfaces for the RC and RCFFT beam specimens, respectively, were measured using different instruments. Instrumentation of the beams included electrical resistance strain gauges for strain measurements and linear variable displacement transducers (LVDTs) for deflection and crack width measurements. Detailed description of the instrumentation is shown in Figure 5-15. Electrical resistance strain gauges produced by Kyowa Electrical Instruments Co. Ltd., Tokyo, Japan of resistance 120 ± 0.05 ohms, were attached to the reinforcing bars, concrete surface and FRP tube surface. In each beam, two electrical strain gauges of type KFG-6-120-C1-11L3M3R and gauge length 6 mm were bonded on the longitudinal reinforcing bars at mid-span to measure tensile strains. Figure 5-12 shows the instrumentation of the reinforcing bars with strain gauges before casting the

specimens. The strain gauges were glued to the reinforcing bars using M-bond 200, and covered by a waterproof coating to protect them from water and damage during casting the concrete. The wires from the strain gages were extended along the bars to one end of the tube. They were then bundled together around a hoop bar, and were taken outside through a hole cut in the tube.

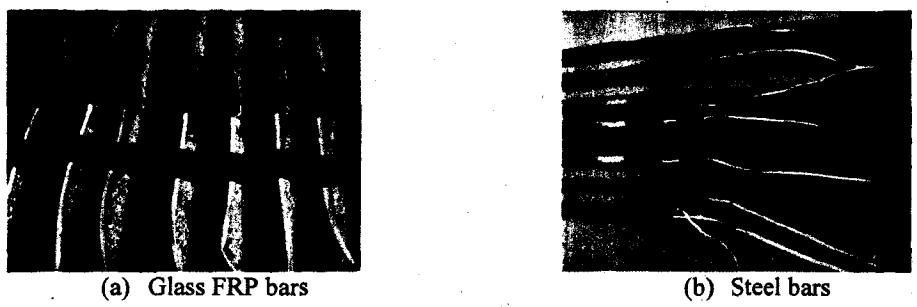

(a) Glass FRP bars (b) Steel bars

Figure 5-12 Instrumentation of the reinforcing bars with strain gauges.

In addition, two electrical strain gauges of length 67 mm were bonded on the top surface of the RC beams at mid-span to measure the concrete compressive strains. Twelve (12) electrical resistance strain gauges (KFG-6-120-C1-11L3M3R) were affixed to the outside surface of each tube at its mid-span section. Six were in the hoop direction, while the other six were in the longitudinal direction. The strain gages were distributed evenly around the section at 60° angles. In additional, three strain gauges, in a rosette pattern, were fixed to the out surface of the FRP tubes to measure the hoop, diagonal and longitudinal strains at the mid-height of the beam specimens, at the middle of the shear span, at the two different sides of the beams. The GFRP tubes' surfaces were sanded to remove the protective UV coating before installation of strain gauges. The deflections were measured using three LVDTs at the mid-span and at each quarter-span to monitor the deflection profile along the beams. Two high-accuracy LVDTs (± 0.001 mm) were installed at the mid-span to measure the crack width. Also, one LVDT was attached at each support, to measure beam end rotations. In addition, two high-accuracy LVDTs (± 0.001 mm) were installed at the end of the beams to measure the slip between concrete core and FRP tube.

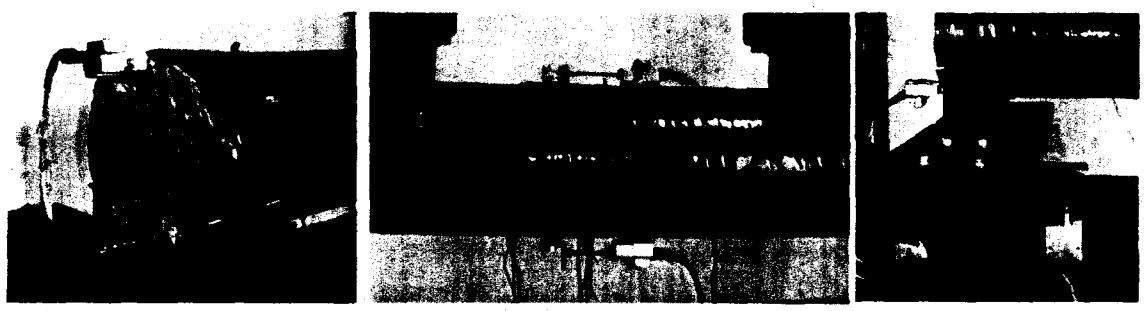

(a) End slippage (b) Crack width at mid span (c) Support rotation

Figure 5-13 Different types of instrumentation for the beam specimens.

5.3.5 Test setup

The structural steel testing frame, shown in Figure 5-14, was used for the testing of the beam specimens. The frame consisted of four large I-section columns (W12) and connected by horizontal I-section beams (W18). Each of the columns was bolted to the ground stiff-concrete floor with 32 mm threaded rods. A hydraulic actuator with a capacity of 500 kN was held in the middle of the frame from an upper horizontal I-section beam (W18).

Figure 5-14 Steel frame of the test setup

The specimens were tested in four-point bending over a simply supported clear span of 1920 mm, see Figure 5-15. The load was transferred from the actuator to the tested beam at two points through a steel spreader I-beam applied on the round surface of the beams through curved loading plates on one-third diameter of the beam. A roller support was obtained by placing a steel cylinder between two steel flat plates. A pin support was obtained by using specially adapted steel I-beam. The upper plate of the I-beam had spherical groove and the plate was supported on the web plate which had a spherical end to house the plate and allow the rotation. Curved steel plated were connected at the top of the pin and roller supports, to cradle the beams against side movement, see Figure 5-16. At each of the tested beam, the roller and pin support were rested on rigid steel I-beam which was secured on the concrete floor. During the test, the load was monotonically applied at a stroke controlled rate of 0.8 mm/minute using a 500 kN closed-loop MTS actuator. The applied load was measured by the internal load cell on the actuator. The MTS actuator, strain gauges and LVDTs were connected by two 20 channels Data Acquisition System and the data were recorded every second during the test.

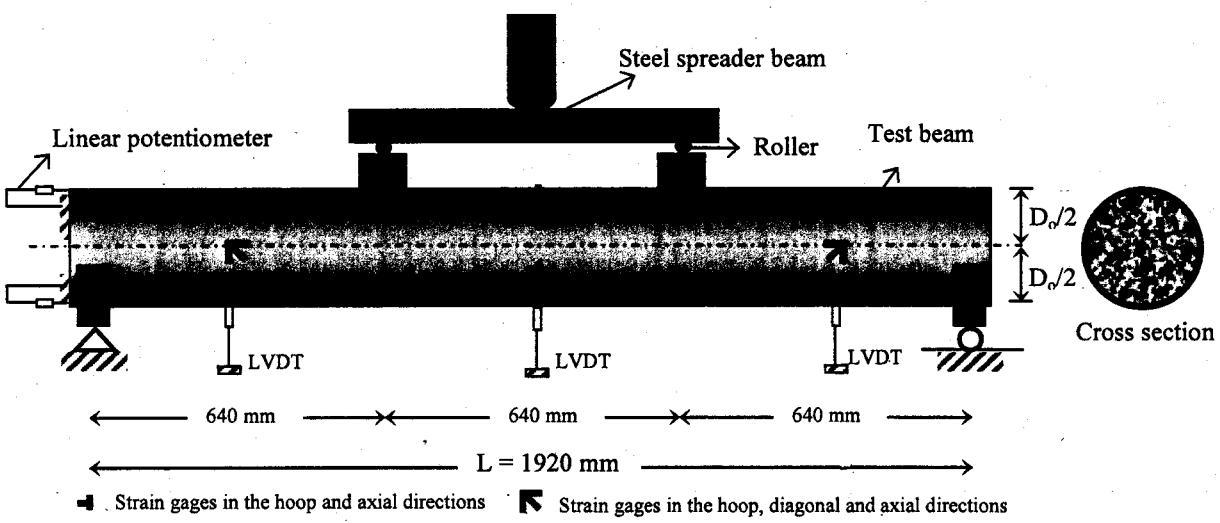

Figure 5-15 Schematic of test setup for RCFFT and control beams

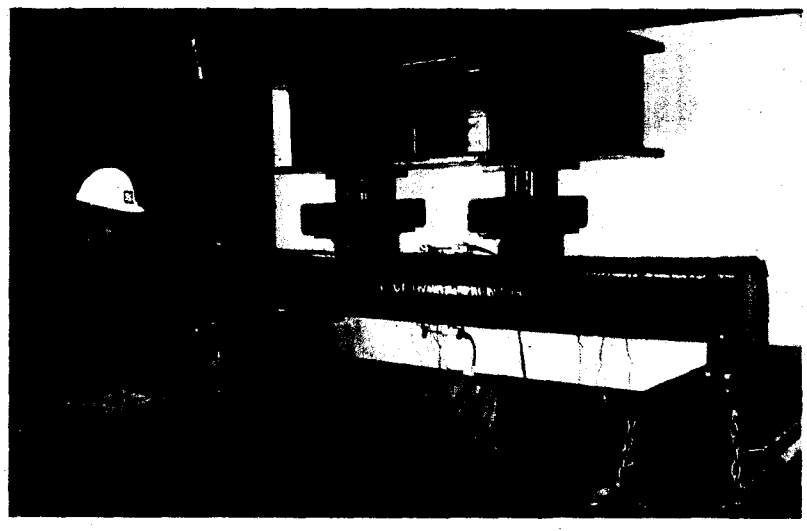

(a) Front view for the test setup

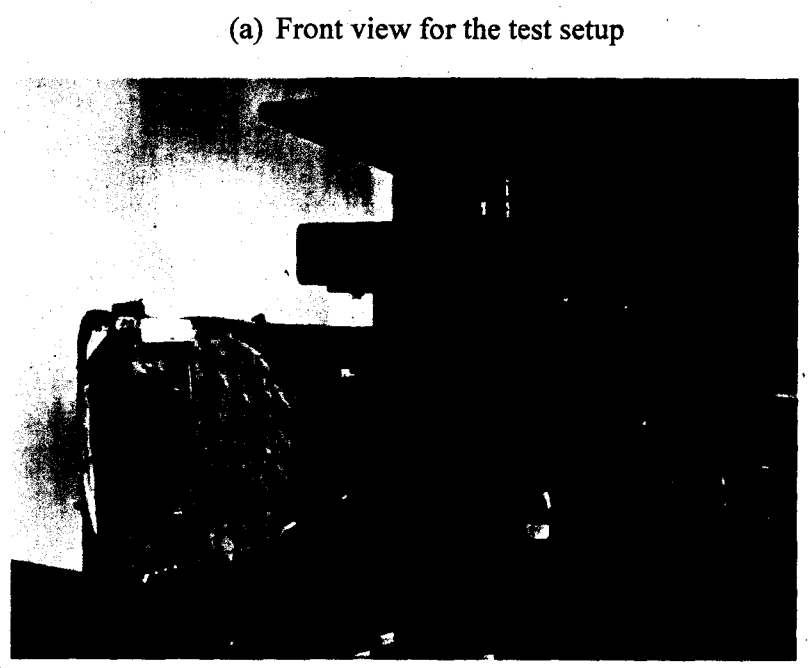

(b) Side view for the test setup

Figure 5-16 Overview for the test setup.

5.4 Test Results and Discussions

A total of 10 circular reinforced concrete beams were tested to failure under four point bending loads. The ten beams divided into two series. All the beams were reinforced longitudinally with steel bars or glass FRP bars of the same reinforcement ratio. Each series included one beam without transverse reinforcement, one beam with steel spiral reinforcement as shear reinforcement and three beams reinforced transversally with two different types of the FRP tubes. The test variables considered in this phase were the type of longitudinal reinforcements and the thickness of the FRP tubes as well as the concrete compressive strength. The test results of the 10 beams are presented in the following subsections in terms of general and flexural behaviour.

5.4.1 General behaviour

All the six RCFFT beams of this phase failed in flexure due to the tensile rupture of FRP tubes and reinforcing bars at the tension side. While the four reinforced concrete beams without and with steel spiral reinforcement failed in shear and shear compression, respectively. A summary of the beam test results is presented in Table 5-7. The applied load at flexural cracking, the yield load, the ultimate load, the mid-span deflection and end support rotation at ultimate load, the maximum strain in the longitudinal bars, FRP tubes and concrete, and the failure modes are given in Table 5-7. It should be noted that each beam was symmetrically loaded with two concentrated loads and consequently, the applied load is the sum of the two concentrated loads.

5.4.2 Cracking and yield loads

Flexural cracks were initiated in the region of constant moment between the two concentrated loads. Table 5-7 gives the applied load at the initiation of flexural cracking for each tested beam. Figure 5-17 show the moment- curvature relationships for the RC and RCFFT beams of Series 1 and 2. In Figure 5-17 (a) and (b) the curvatures are calculated using the top and bottom longitudinal strains measured on the surface of the FRP tube.

The corresponding curvature of the section, Ψ, which is the slope of the strain profile, is calculated as:

$$\Psi = \frac{\varepsilon_b - \varepsilon_t}{D} \qquad 5\text{-}1$$

where ε_b and ε_t are the tensile and compressive strains of the bottom and top fibre of the tube.

Figure 5-17 shows that the first cracking in the concrete occurs at a relatively low load level, compared to the ultimate load. The cracking load ranged between 11.99 and 12.14 kN for the RC beams and ranged between 15.90 and 19.88 kN for the RCFFT beams of Series No. I. These values are approximately 7.50 to 11.68% of the ultimate load. On the other hand, the cracking loads for specimens of Series No. II ranged between 13.25 and 13.75 kN for the RC beams and ranged between 15.90 and 22.37 kN for the RCFFT beams. These values are approximately 7.50 to 17% of the ultimate load. It can be noticed from Table 5-7 that in the two series of test beams, there is a difference in the flexural cracking load. For each series, the beam reinforced transversely with FRP tube cracked at a load higher than that of the beam reinforced with steel spiral reinforcement or without.

The average cracking loads of beams reinforced with steel spiral reinforcement or without are 88.5 and 80% that of the beams reinforced with FRP tubes for specimens of Series No. 1 and 2, respectively. This difference in the flexural cracking load may be attributed to the positive contribution of the FRP tubes to increase the axial stiffness of the beam as compared with steel spiral reinforcement beams. Also, for each series, the RCFFT beams reinforced with steel bars cracked at a load higher than that of the RCFFT beams reinforced with FRP bars. The average cracking load of RCFFT beams reinforced with steel bars is 81% that of the RCFFT beams reinforced with FRP bars. This difference in the flexural cracking load may be attributed to the difference in the axial stiffness of the longitudinal reinforcement. Table 5-7 gives the yield load for the RC and RCFFT beams reinforced with steel bars of Series No. 1 and 2. The yield load for RC beams without and with steel spiral reinforcement (CO-S-N and COS-S-N) occurred at 75 and 54% of the ultimate load, respectively, and the corresponding value for the RCFFT beams (D-S-N and D-S-M) are 50 and 52%, respectively. The yield load for the

beam reinforced with FRP tube Type D (D-S-N) yielded at load higher than that of the beam reinforced with steel spiral reinforcement (COS-S-N) which, in turn, had a higher yield load of the beam without transverse reinforcement (CO-S-N). The yield load for the beam reinforced with steel spiral reinforcement (COS-S-N) is 70% that of the beam reinforced with FRP tube Type D (D-S-N) and the corresponding value for the beam without transverse reinforcement (CO-S-N) is 66%. On the other hand, the yield load for the RCFFT beam constructed from concrete Type M (D-S-M) yielded at load 7.5% higher than that of the RCFFT beam constructed from concrete Type N.

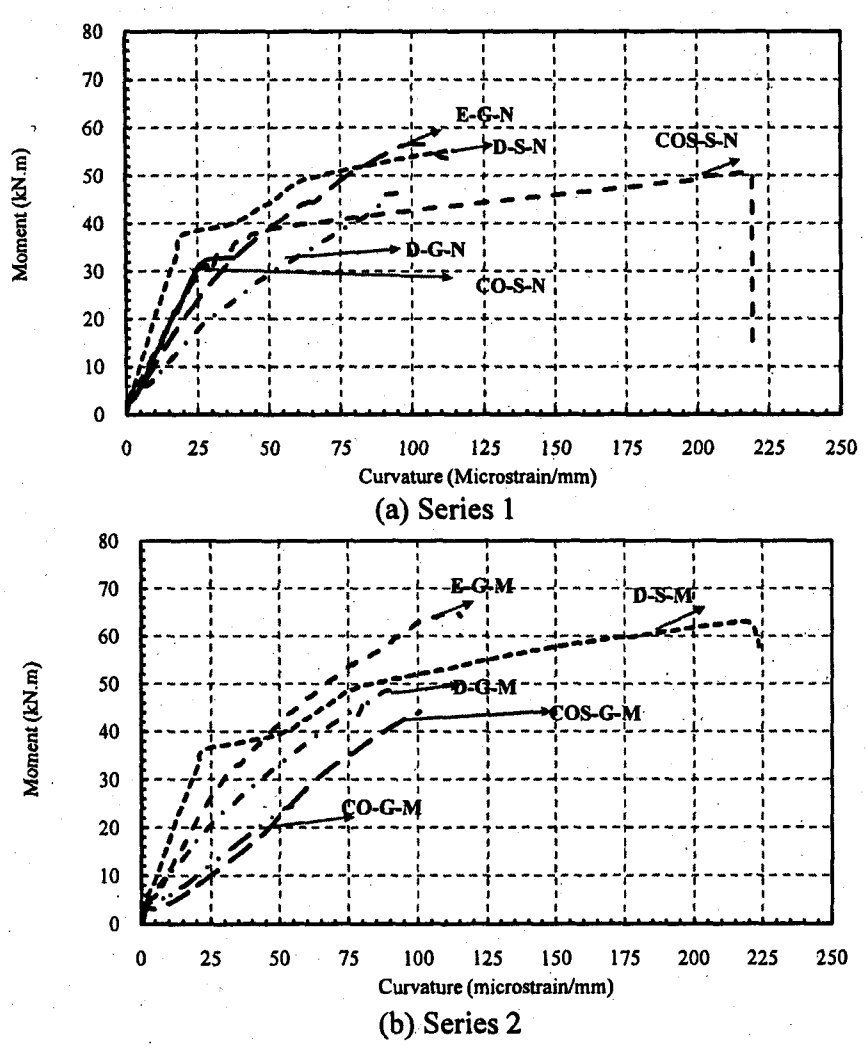

Figure 5-17 Moment-curvature relationships for RC and RCFFT beams

Table 5-7 Test results of RC and RCFFT beams

	Specimen ID	Load (kN)			Moment (kN.m)			Curvature ($\mu\varepsilon$/mm)		Comp strain* ($\mu\varepsilon$)	Rotation of support* (deg.)	Deflection* (mm)	Failure mode**	Ductility (kN.m)
		Crack	Yield	Max	Crack	Yield	Max	Crack	Max					
Series No. 1	CO-S-N	11.99	77.7	102.65	3.84	24.86	32.85		35	2633	0.85	11.99	DT	0.78
	COS-S-N	12.14	82.5	152.97	4.88	26.40	48.95	1.00	216	3959	9.75	136.25	SC	17.75
	D-S-N	19.88	116.3	236.71	6.36	37.21	75.75		112	15516	9.70	124.91	FL	32.40
	D-G-N	15.90	---	144.79	5.09	---	46.33	3.01	93	6017	3.20	43.13	FL	5.78
	E-G-N	17.34	---	177.14	5.55	---	56.68	2.02	100	6479	2.70	38.68	FL	8.77
Series No. 2	CO-G-M	13.25	---	77.10	4.24	---	24.67	1.65	54	2628	1.45	24.33	DT	1.09
	COS-G-M	13.75	---	139.22	4.40		44.55	2.4	100	3124	3.60	57.47	SC	5.53
	D-G-M	15.90	---	151.66	5.09	---	48.53	3.04	86	5415	2.95	45.14	FL	5.92
	E-G-M	19.50	---	202.44	6.24	---	64.78	1.71	110	7009	2.55	43.75	FL	9.76
	D-S-M	22.37	125	237.00	7.16	40	75.84	1.52	217	10629	5.95	126.69	FL	34

*The experimental results at ultimate load; **DT = diagonal tension failure; SC = shear compression failure; FL = flexural failure.

5.4.3 Load-deflection response

Deflections of all beams were measured using linear variable displacement transducers (LVDTs) and recorded using a data acquisition system. The applied load versus mid-span deflection relationships of the ten beams are presented through Figure 5-18to Figure 5-26. Table 5-7 gives also the mid-span deflection at the ultimate load for each beam. The mid-span deflection at failure ranged between 11.99 mm and 136.25 mm, corresponding to a deflection-to-clear span ratio of 1/155 and 1/14, respectively. In this section, the load-deflection curves for the 10 beams are presented in different groups to show the effect of individual parameters on flexural behaviour of RC and RCFFT beams. Figure 5-18and Figure 5-19 show the effect of the contribution of FRP tubes to the load-deflection behaviour as compared to conventional RC beams with and without steel spiral reinforcement.

The influence of the confinement using steel spiral or FRP tubes of the three beams of Series No. 1 (CO-S-N, COS-S-N and D-S-N) that reinforced internally with steel bars is shown in Figure 5-18. The load-deflection was bilinear for the two beams COS-S-N and D-S-N, and linear for beam CO-S-N. Note that, the elastic-plastic behaviour of the steel-reinforced beams (COS-S-N and D-S-N) and their eventual failure at large deflection. Also, Figure 5-18 shows the brittle failure of the beam which had no transverse reinforcement (Cont-1). The figure indicates that the beam confined by FRP tube (D-S-N) experienced lower deflection, higher stiffness and superior strength (55% higher) than the beam reinforced with a steel spiral. The initial stiffness and the stiffness after yielding of Specimen D-S-N was approximately 61 and 49%, respectively, higher than that of the beam reinforced with a steel spiral, COS-S-N. This is attributed to the contribution of the helical fibres of the FRP tubes to provide shear and flexural resistance to the beam, and to confine a much larger concrete cross-sectional area than steel spiral.

The most important difference that can be observed is the ductility of the tested beams. Table 5-7 presents the ductility of the 10 beams as measured by the energy absorption. Energy absorption is one of the important deformational characteristics of concrete structure to determine the ductility of the structure. The energy absorption was

determined as the area under the load-deflection curve. The integration of the area under the load-displacement was performed numerically from the experimental data of the load versus displacement along the whole load history. Table 5-7 presents the ductility of the 10 beams. D-S-N exhibited great ductility, with sequential failure and residual strength at very large deflection (125 mm). As indicated in Table 5-7, the ductility index of D-S-N is 82% higher than that of COS-S-N. This result is consistent with the test results as discussed in previous studies by (Fam et al. 2007; Cole and Fam 2006).

The influence of the confinement using steel spiral or FRP tubes of the three beams of Series No. 2 (CO-G-M, COS-G-M and D-G-M) that reinforced internally with GFRP bars is shown in Figure 5-19. The load-deflection responses are almost linear up to the failure. The figure indicates that the beam confined by FRP tube (D-G-M) experienced lower deflection, higher ductility, higher stiffness and superior strength (9% higher) than the beam reinforced with a steel spiral (COS-G-M).

The first part of the load plot up to flexural cracking was similar for the three beams representing the behaviour of the uncracked beam utilizing the gross moment of inertia of the concrete cross-section. The second part, post-cracking up to failure, represents the cracked beam with reduced moment of inertia. In this part, the flexural stiffness of the tested beams was dependent on the type of the transverse reinforcement. For the three beams, the post-cracking flexural stiffness for the beam reinforced with FRP tube (D-G-M) is 60% higher than that of beam reinforced with and without steel spiral reinforcement, (COS-G-M and CO-G-M). Also, the figure indicated that the post-cracking flexural stiffness for the beam CO-G-M up to failure was similar to that of beam COS-G-M. From Figure 5-18and Figure 5-19, it can be concluded that the overall improvement achieved for the beam confined with FRP tube even reinforced with steel or GFRP bars are similar in terms of deflection, strength and stiffness.

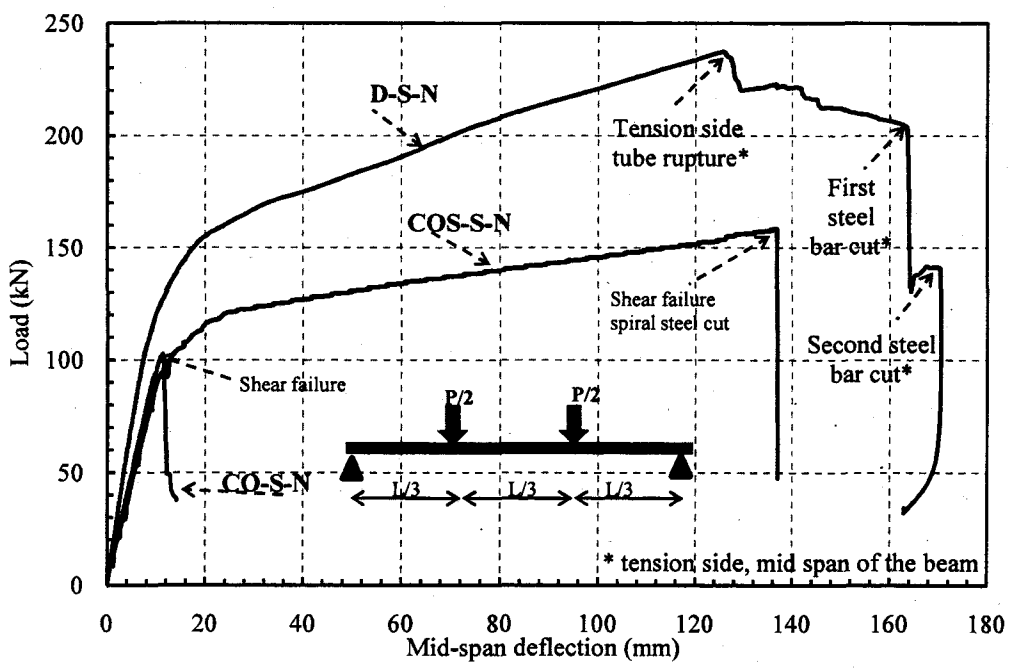

Figure 5-18 Load–deflection curves for Specimens (CO-S-N, COS-S-N and D-S-N)

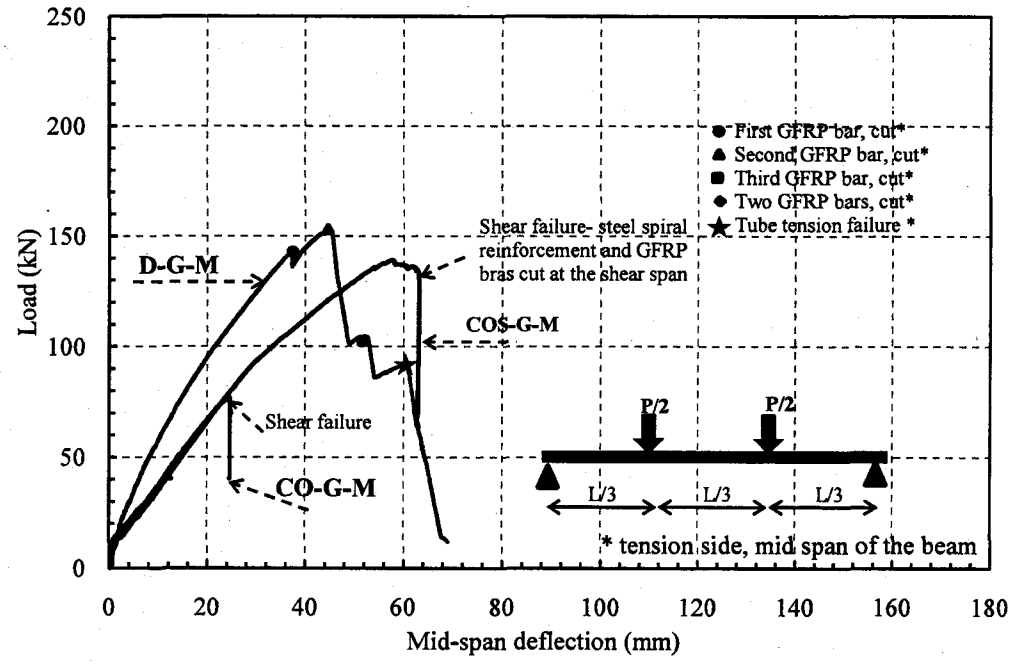

Figure 5-19 Load–deflection curves for Specimens (CO-G-M, COS-G-N and D-G-M)

Figure 5-20 and Figure 5-21 present the effect of type of the internal reinforcements on the flexural performance of RCFFT beams. Steel and Glass FRP bars of the same cross sectional area were used in reinforcing concrete beams. The load-deflection curves for Specimens D-S-N and D-S-M were compared to the specimen of Series No. 1, (D-G-N) in Figure 5-20 and specimen of Series No. 2, (D-G-M) in Figure 5-21, respectively. All the four beam specimens were cast using the same type of the FRP tube, Type D with reinforcement ratio (4t/D) equal to 4.5%. Since FRP reinforcing bars are linear-elastic to failure when loaded in tension and fail in a brittle manner, a ductile steel-like failure does not occur in FRP-reinforced concrete beams. Figure 5-20 and Figure 5-21 show the elastic-plastic behaviour of the steel-reinforced beams (D-S-N and D-S-M) and their eventual failure at larger deflection as compared with the elastic behaviour of FRP-reinforced beams (D-G-N and D-G-M). The behaviour of FRP reinforced CFFT beams showed no yielding as compared with the steel reinforced CFFT beam. The figures indicate that the beam reinforced with steel bars (D-S-N and D-S-M) experienced lower deflection, higher stiffness and 64 and 57% higher strength than the RCFFT beam reinforced with FRP bars (D-G-N and D-G-M), respectively. On the other hand, the most important significant behaviour is the difference in the ductility between the steel-RCFFT beams and glass FR-RCFFT beams. As indicated in Table 5-7, the ductility indices of D-S-N and D-S-M are 5.6 and 5.7 times the ductility indices of D-G-N and D-G-M, respectively.

For the four beams, the post-cracking flexural stiffness for the beam reinforced with steel bars is higher than that of RCFFT beam reinforced with glass FRP bars. This result reflects the effect of the modulus of elasticity of the reinforcing bars on the post-cracking flexural stiffness as the four RCFFT beams had the same reinforcement ratio. The average ratio between the post-cracking flexural stiffness of the steel-RCFFT beams and the glass FRP-RCFFT beams was approximately 3.9. This ratio was approximately the same as the ratio of the modulus of elasticity of steel to that of glass FRP bars as it was 4.1. Consequently, it can be concluded that the post-cracking flexural stiffness of the FRP-RCFFT beams to that of steel-RCFFT beams is the same as the ratio of the axial stiffness of FRP reinforcing bars to the axial stiffness of steel bars.

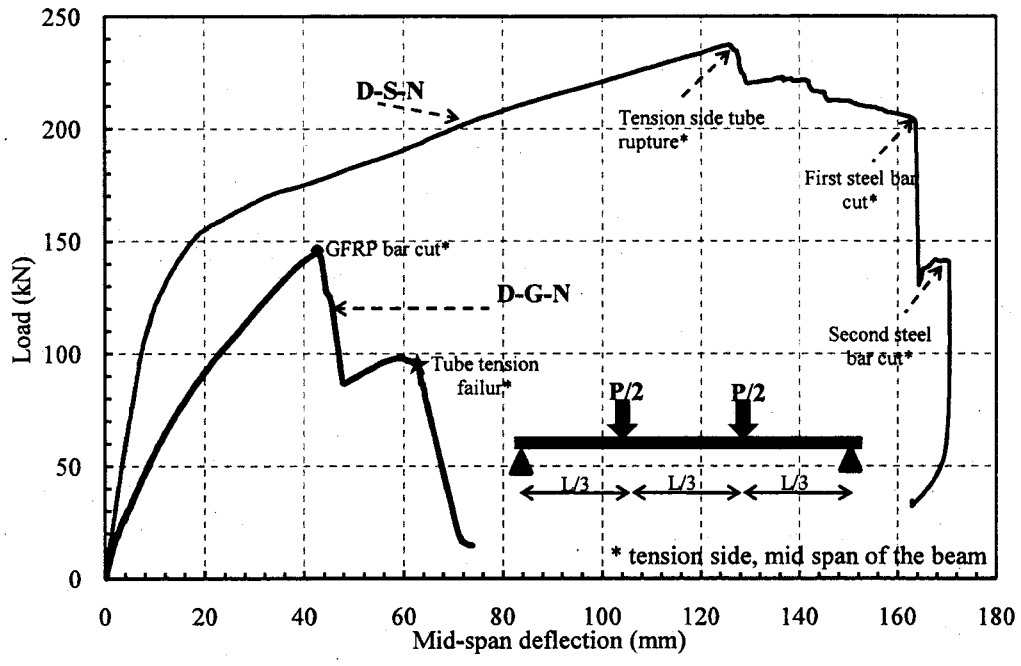

Figure 5-20 Load–deflection curves for Specimens (D-S-N and D-G-N)

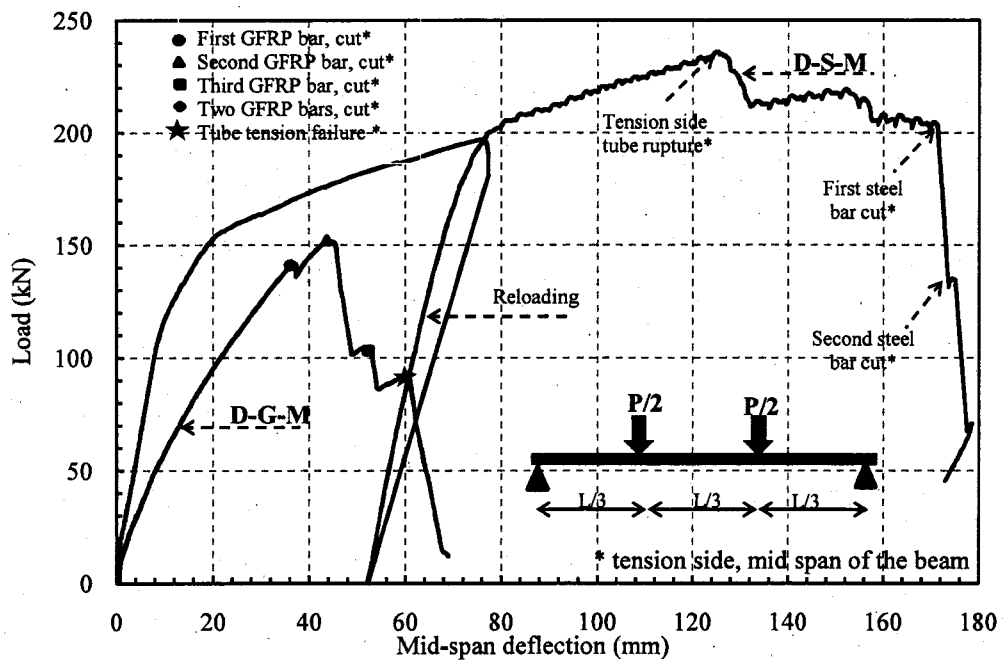

Figure 5-21 Load–deflection curves for Specimens (D-S-M and D-G-M)

Figure 5-22 and Figure 5-23 present the effect of the FRP tube thickness through the test results of specimens of Series No. 1, (D-G-N and E-G-N), and specimens of Series No. 2, (D-G-M and E-G-M), respectively. The four beams had identical reinforcement ratio of the GFRP bars. The FRP tube Type E has thickness (6.40 mm), which it is equal to 2.2 times the thickness of the tube type D, (2.90 mm). The laminate structure of the two tubes was almost the same, however, the fibres oriented in the hoop direction at 60 and 90 degree as compared to the longitudinal axis of the tube. The load-deflection plots for the four beams exhibited similar characteristics. The figures indicate that the beams constructed from the tube Type E (E-G-N and E-G-M) experienced 22.3 and 33.3% higher strength than that of beam constructed from the tube Type D (D-G-N and D-G-M). Also, the RCFFT Beams of tube Type E showed lower deflection than that beams of tube Type D, at all load levels. Table 5-7 shows that the ductility indices of E-G-N and E-G-M are 52 and 64% higher than that of D-G-N and D-G-M.

For the four beams, the post-cracking flexural stiffness for the RCFFT beams constructed from tube Type E is higher than that of RCFFT beams constructed from tube Type D. This result reflects the effect of the axial stiffness of the FRP tubes on the post-cracking flexural stiffness of the RCFFT beams. The average ratio between the post-cracking flexural stiffness of the RCFFT beams constructed from tubes Type E and Type D was approximately 1.85. This ratio was approximately the same as the ratio of the axial modulus of elasticity of the FRP tube multiplied by the FRP tube thickness (for tube Type E, $(E_x t_{FRP})_E$ to that of tube Type D, $(E_x t_{FRP})_D$ as it was 1.90.

The influence of the concrete strength on the load-deflection responses of the three beams of Series 1, (D-S-N, D-G-N and E-G-N) and the three beams of Series 2 (D-S-M, D-G-M and E-G-M) that contained identical internal reinforcement ratio of steel or FRP bars and constructed from the FRP tubes Type D or E is shown in Figure 5-25, Figure 5-26 and Figure 5-27. Two identical specimens of Series 1 and 2 were compared to each other to determine the effect of concrete strength on the performance of RCFFT beams. Specimens of Series 1 and 2 were cast using normal (N) and medium (M) concrete strength, respectively.

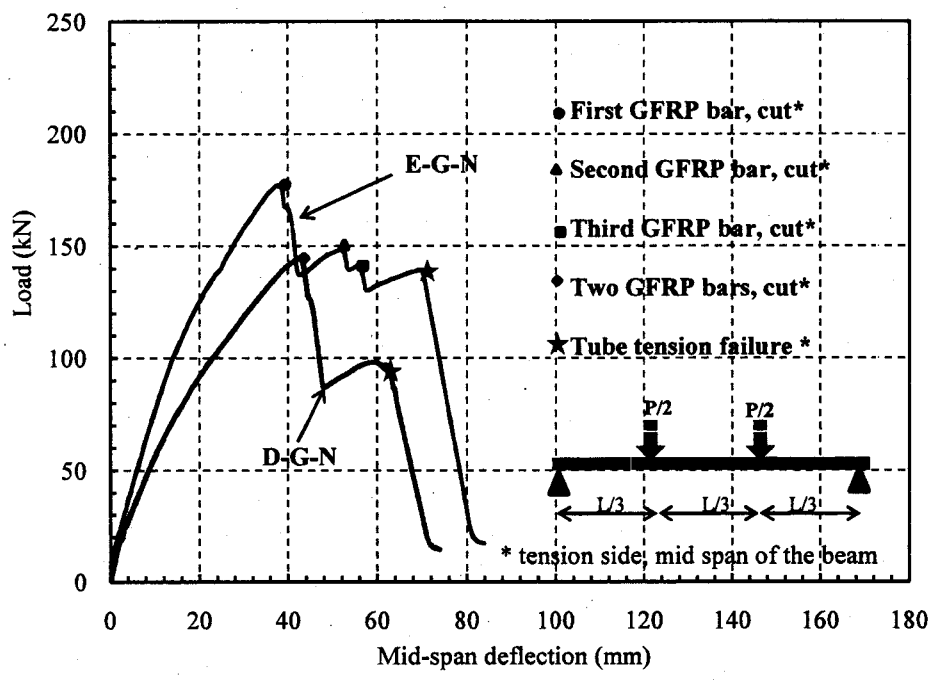

Figure 5-22 Load–deflection curves for Specimens (D-G-N and E-G-N)

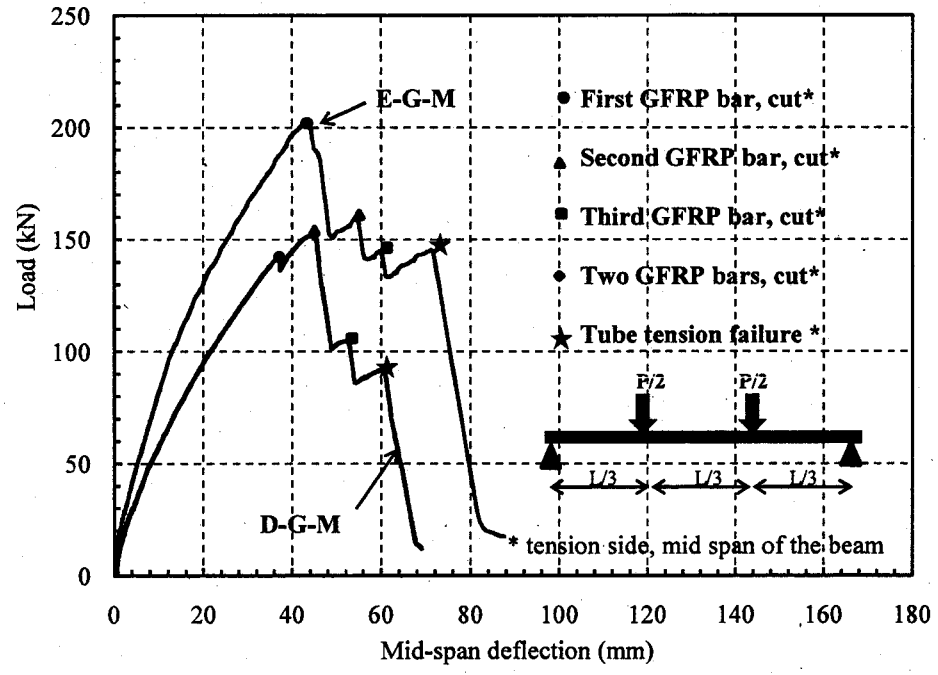

Figure 5-23 Load–deflection curves for Specimens (D-G-M and E-G-M)

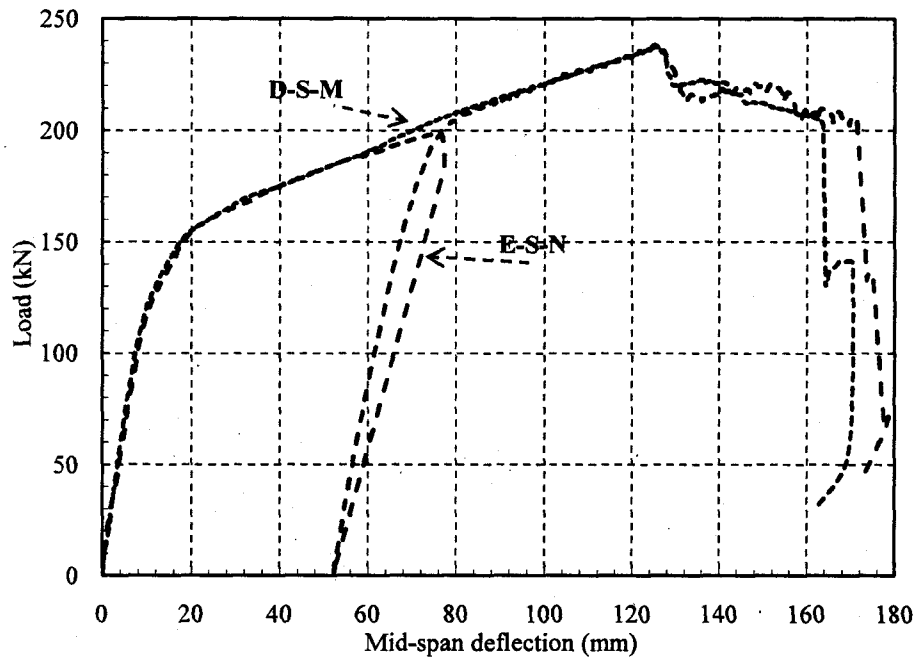

Figure 5-24 Load–deflection curves for Specimens (D-S-N and E-S-M)

The three figures indicated that, for the three RCFFT beams constructed from concrete Type N (30 MPa), the initial and post-cracking flexural stiffness were similar to that of the three RCFFT beams constructed from concrete Type N (45 MPa). Figure 5-24 indicates that the beam reinforced with steel bars (D-S-M) does not have gain in the strength as compared with beam D-S-N. Also, Figure 5-25 indicates that the increase in the flexural strength for beams reinforced with GFRP bars is not significant with increasing the concrete strength from 30 MPa (Specimen D-G-N) to 45 MPa (Specimen D-G-M), Specimen D-G-M having only 4.8% higher strength. Figure 5-26 indicates that the RCFFT beam E-G-M experienced 14% higher strength that that of RCFFT beam E-G-M. It can be concluded that the flexural behaviour of the six RCFFT beams tested in this study were not significantly affected with increasing the concrete strength from 30 MPa to 45 MPa. This is attributed to two factors First, the six RCFFT beams failed in flexure due to the tensile rupture of the FRP tube and FRP bras or steel bars at the tension side of the beam. Second, the FRP tubes confined the concrete core of the beams, as evident from the final failure mode the concrete core inside the FRP tube at the compression side did not experienced crushes or spalls as compared with failure mode of the steel-spiral beams.

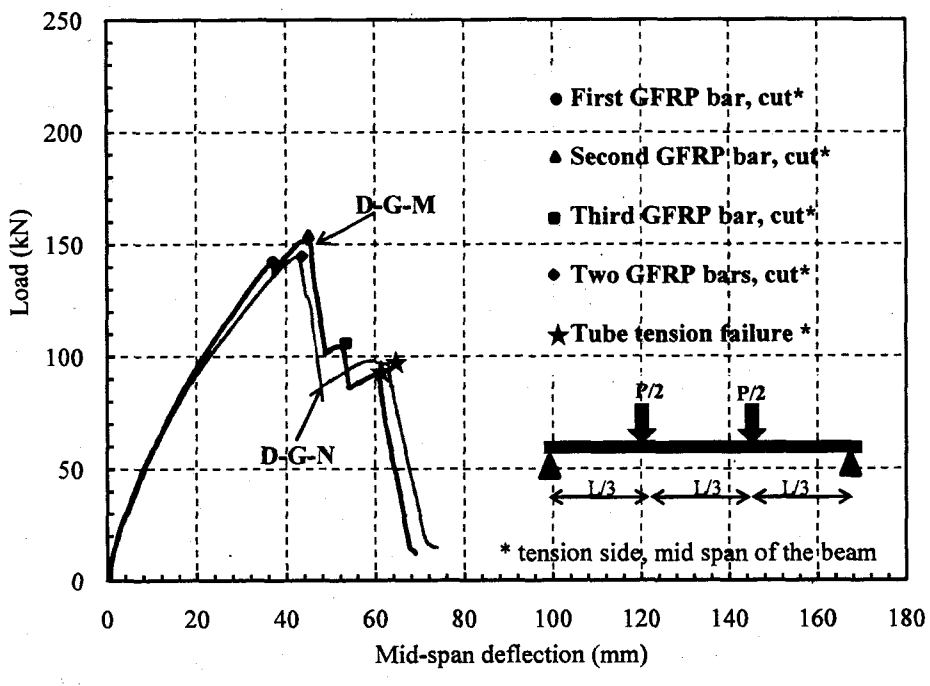

Figure 5-25 Load–deflection curves for Specimens (D-G-N and D-G-M)

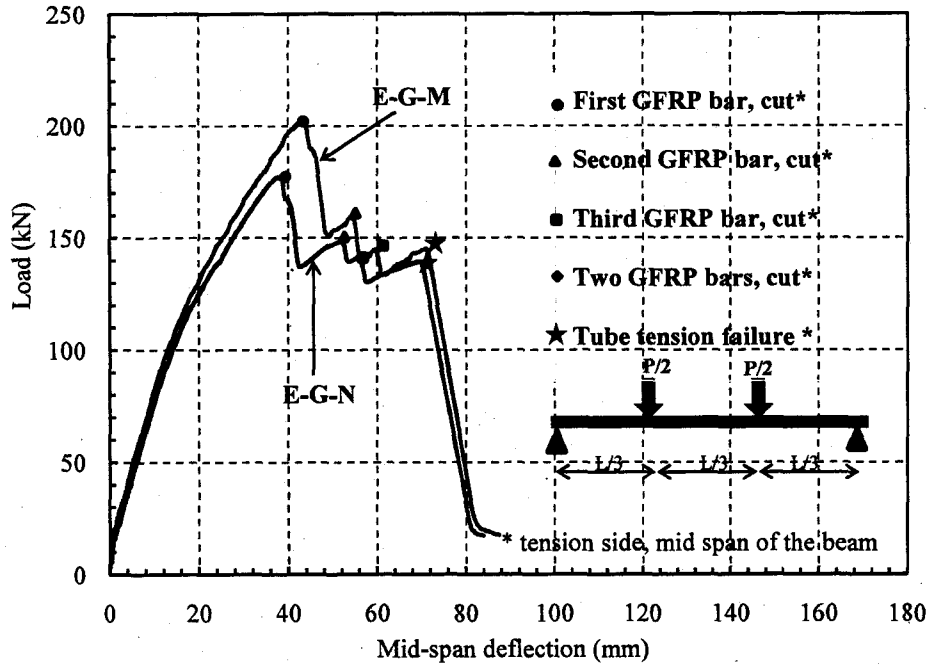

Figure 5-26 Load–deflection curves for Specimens (E-G-N and E-G-M)

5.4.4 Load-strain relationships

5.4.4.1 The flexural longitudinal compression and tension strains

Figure 5-27 and Figure 5-28 show the measured mid-span strains in the reinforcements (steel and FRP bars) at the tension side as well as in the concrete and FRP tubes at the compression side versus the applied load for the tested beams of Series 1 and 2, respectively. Also, Table 5-7 gives the measured mid-span strains in the reinforcement and concrete at the ultimate load for each beam. The maximum compression strains at failure were 2633 and 2628 micro-strain for the RC beams with no transverse reinforcements, CO-S-N and CO-G-M, respectively. These values are less than the ultimate useable strain of the 3000 micro-strain, indicating that no flexural compression failure had occurred at the onset of shear failure. On the other hand, the maximum compression strains at failure were 3959 and 3224 micro-strain for the steel spiral beams, COS-S-N and COS-G-M, respectively. These values are higher than the ultimate useable strain, indicating that the shear failure occurred accompanied with flexural compression failure. In addition, the maximum measured compression strain for the steel-RCFFT beams in the FRP tube at the compression side were 15516 and 10629 micro-strain for D-S-N and D-S-M, respectively, these values present 70 and 50% of the ultimate strains of the FRP tubes. While the corresponding values for the glass FRP-RCFFT beams ranged from 5415 to 4064 micro-strain which are quite below (76% to 81% less) the ultimate strains of the FRP tubes. This indicated that no compression flexural failure had occurred for the steel and FRP-RCFFT beams at the onset of tensile flexural failure.

For the steel-RCFFT beams, the maximum measured tensile strains in the steel bars on average ranged from 15000 to 15500 micro-strains. These values approximately are the same value of the ultimate tensile strain of the steel bars obtained from the standard tensile tests (Figure 3.3). This indicates that the steel-RCFFT beam failed at onset of flexural tensile failure, whereas the FRP tube strain at the compression side were quite below the ultimate FRP tube strain. It should be pointed out that the two strain gauges bonded on the steel bars of the steel-RCFFT beams malfunctioned before failure and consequently, no steel strain readings were recorded up to the failure. Figure 5-27 shows that the steel strains of D-S-N occurred at higher loads levels than that of COS-S-N,

during the all load stages, this attributed to the confinement effect and flexural tensile strength of the FRP tubes.

For the FRP-RCFFT beams, it can be noted that after cracking, the compression strains of FRP tubes and tension strains of FRP bars vary almost linearly with the increased load up to failure. Also, for the steel-RCFFT beams, the load-compression strains relationships of the FRP tubes after cracking are bilinear up to failure, where the bend point occurred on the curve after yielding stages. Also, the load-tension strain curves of the steel bars present elastic-plastic responses up to failure.

It can be noticed from Figure 5-27 and Figure 5-28 that the increase in the thickness of the FRP tube (from tube D to E) decreased significantly both the compression and tension strains of the FRP tubes and FRP bars, respectively, that measured at the same load level. The similar behaviour was observed, as using the steel bars instead of FRP bars decreased significantly the compression and tension strains measured at the same load level. Also, the increase in the concrete compressive strength from 30 to 40 MPa decreased slightly both the compression and tension strains of the FRP tubes as well as FRP and steel bars.

Figure 5-29 and Figure 5-30 show the strain distribution and the neutral axis at mid-span section for the RC and RCFFT beams of Series 1 and 2, respectively, at five stages of the ultimate load level (25, 50, 75, 90 and 100%). For the RC beams, strain distribution remains linear up to failure. Also, for the RCFFT beams up to 50% of the ultimate load, the strain distribution remains approximately linear, however, beyond that level, RCFFT beams begin to exhibit non-linear strain distribution. The figures indicate that the highest tensile and compressive strains are observed for the steel-RCFFT beams, D-S-N and D-S-M. It appears from these figures that that the neutral axis is located within a region of 0.25 to 0.35.

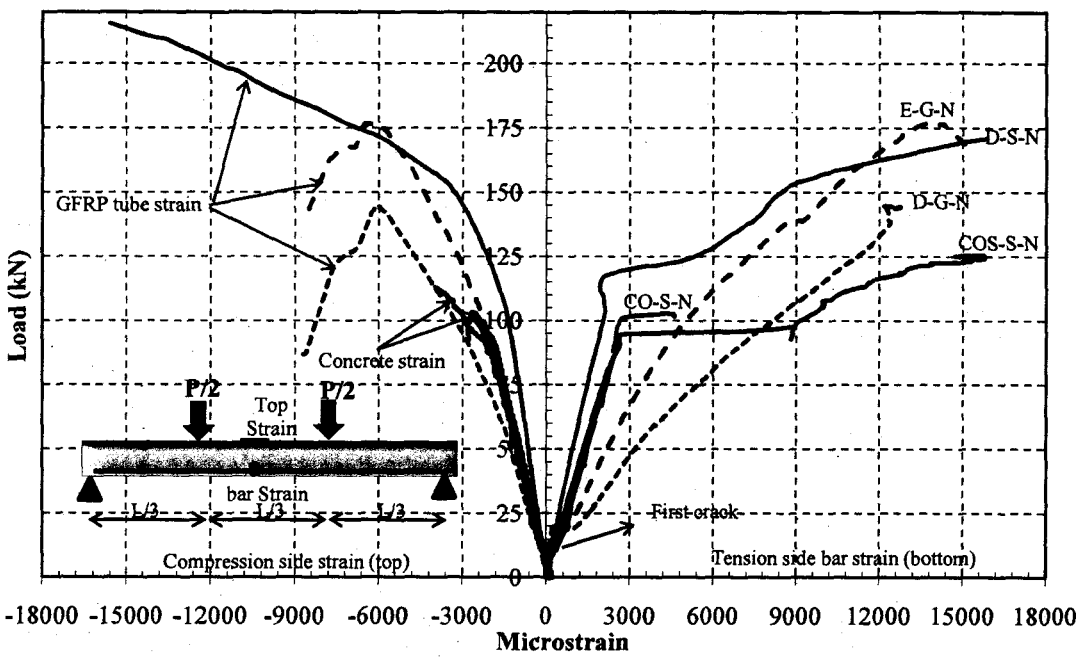

Figure 5-27 Load-flexural compression and tension relationships (Series 1)

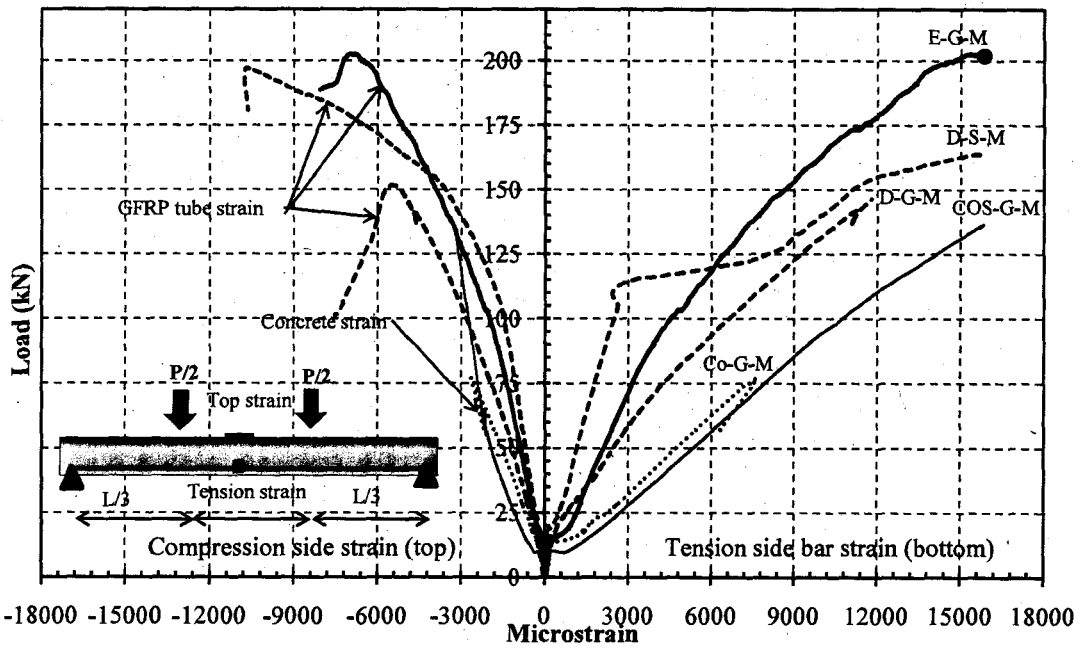

Figure 5-28 Load-flexural compression and tension relationships (Series 2)

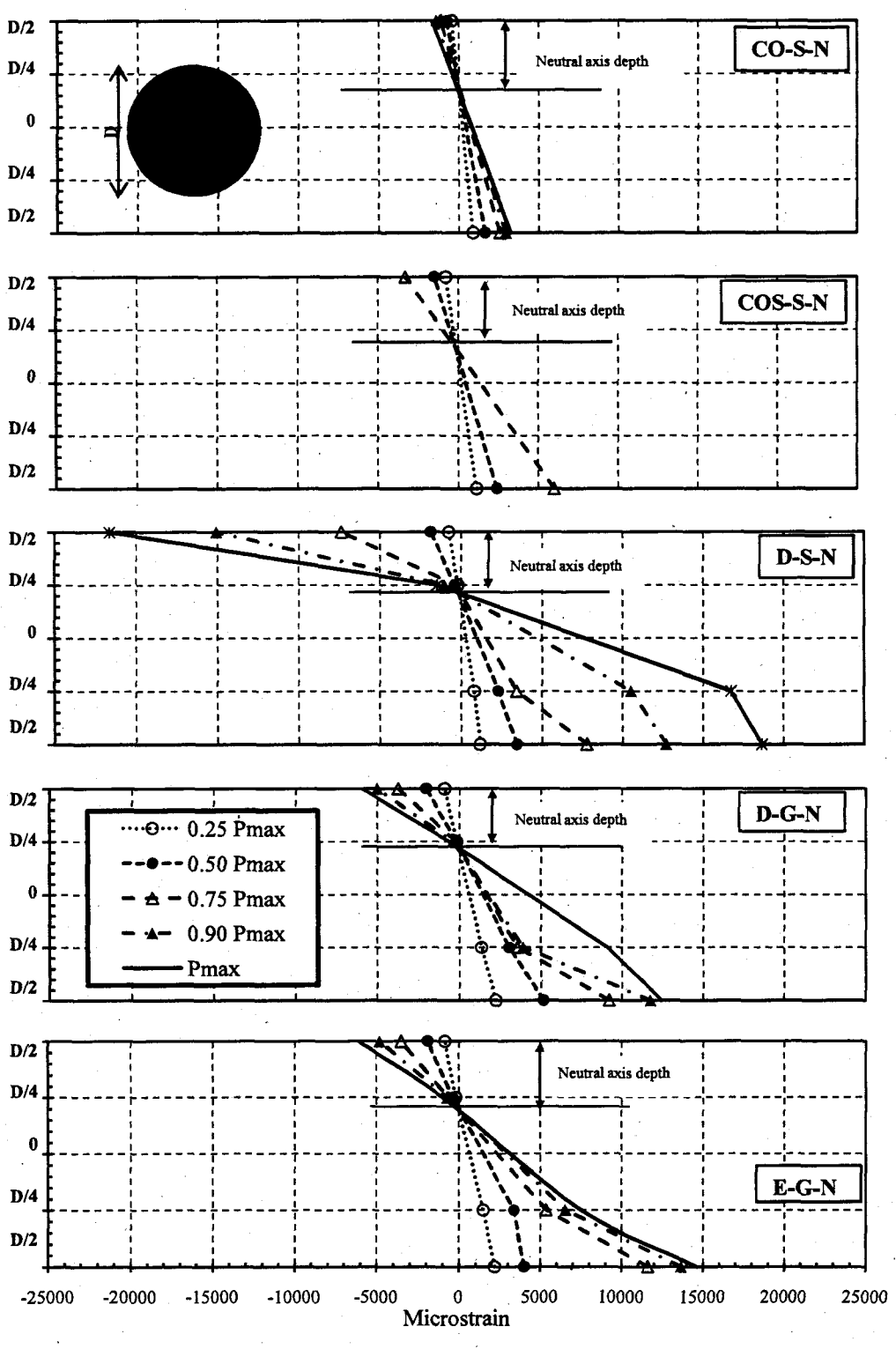

Figure 5-29 Strain profile at mid-span section of control and CFFT beams (Series No. 1)

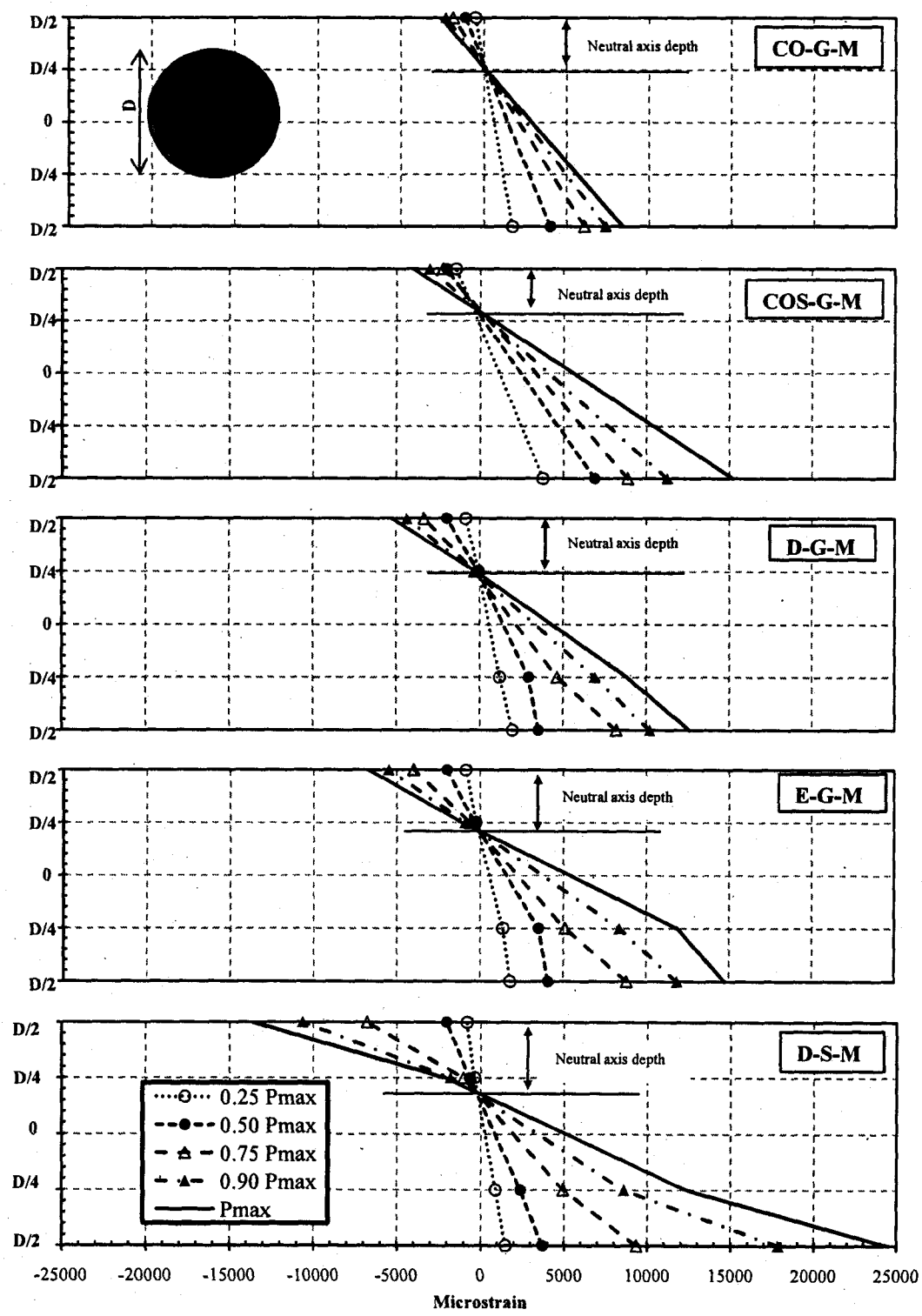

Figure 5-30 Strain profile at mid-span section of control and CFFT beams (Series No. 2)

5.4.4.2 The flexural hoop strain response

Figure 5-31 and Figure 5-32 show the measured mid-span hoop strains in the FRP tubes with strain gage locations marked in the legend versus the applied load for the tested beams of Series 1 and 2, respectively. The hoop strains were measured at four different levels through the depth of the beams. The hoop strains No. 1 and 4 were located at the bottom and top surface of the beams, respectively, while hoop strains No. 2 and 3 were located at the D/4 from the bottom and top surface of the beams, respectively. For the six RCFFT beams, the figures indicate that lateral compressive strains develop on the tension side of the beams (strain gauge No. 1), this attributed to the tensile strain of the beam in the longitudinal direction which in turn develop compression strain in the hoop direction due to the Poisson's ratio effect of the tube.

Also, the figures indicated that the hoop strains 2 and 3 develop tensile strain (positive), the maximum measured lateral strains at these locations on average ranged from 500 to 1000 micro-strains. However, these values are quit below the FRP hoop strain of the FRP tubes used in this study. This reflects the insignificant confinement effect of the FRP tube in flexure at the middle zone of the beam. On the other hand, the figures indicate that lateral tensile strains develop on the compression side of the beams (strain gauge No.4). The figures show that the lateral strain at this location increased excessively as the load increased, the load-strain curves were almost bilinear. The maximum measured strains at ultimate on average ranged from 2000 to 4000 micro-strains. This indicates that the confinement effect of the FRP tube become more activation as the load increase.

In fact, The FRP tube lateral and longitudinal strains at the mid-span at the tension and compression side of the beam presents a bi-axially loaded case. Whereas, the tension side is under tensile and compressive strains in the axial and hoop direction, respectively, while the compression side is under compressive and tensile strains in the axial and hoop direction, respectively.

5.4.4.3 The shear strain rosette response

Figure 5-33 and Figure 5-34 show strain gauges measurements taken on the concrete and FRP tubes surfaces of RC and RCFFT beams, respectively, of Series 1 and 2. H, I and V represent the horizontal, diagonal and vertical strains measurements at mid-depth of the mid-shear span of the beams. The strain rosette (three strain gauges H, I and V) was recorded at the right and left hand of the mid-shear span of the beams.

The figures indicate that the vertical strains develop tensile strain (positive), the maximum measured vertical strains on average ranged from 100 to 400 micro-strains, except the vertical strains of steel-RCFFT beams reached on average to 500 micro-strains. However, these values are quit below as compared with the axial or hoop strain of the FRP tubes. This reflects the insignificant confinement effect of the FRP tube in shear at the mid-span of the beam. On the other hand, it is obvious that the horizontal strains are approximately coinciding with diagonal strains up to failure. The maximum measured horizontal and diagonal strains for RCFFT beams on average ranged from 1500 to 2500 micro-strains. For the control specimens, the horizontal and diagonal strains increased progressively after yielding or cracking for the steel-RC and FRP-RC beams, respectively. This indicates vulnerability of the beam to shear failure as it was evident from the final failure modes for the RC beams (shear failure). The figures also show that for all RCFFT beams of Series 1 and 2 the mid-span flexural strains (referee to Figure 5-27 Figure 5-28) are higher than the measured shear strain rosette in the three directions (H, I and V). This indicates that the tested RCFFT beams of this study were flexure-critical rather shear-critical, as it was evident from the failure modes for all RCFFT beam, flexural failure. It can be noticed from Figure 5-33 and Figure 5-34 that the increase in the thickness of the FRP tube (from tube D to E) decreased both the horizontal and diagonal strains that measured at the same load level. The similar behaviour was observed, as using the steel bars instead of FRP bars decreased the horizontal and diagonal strains measured at the same load level. Also, the increase in the concrete compressive strength from 30 to 40 MPa decreased slightly the horizontal and diagonal strains of the FRP tubes as well as FRP and steel bars.

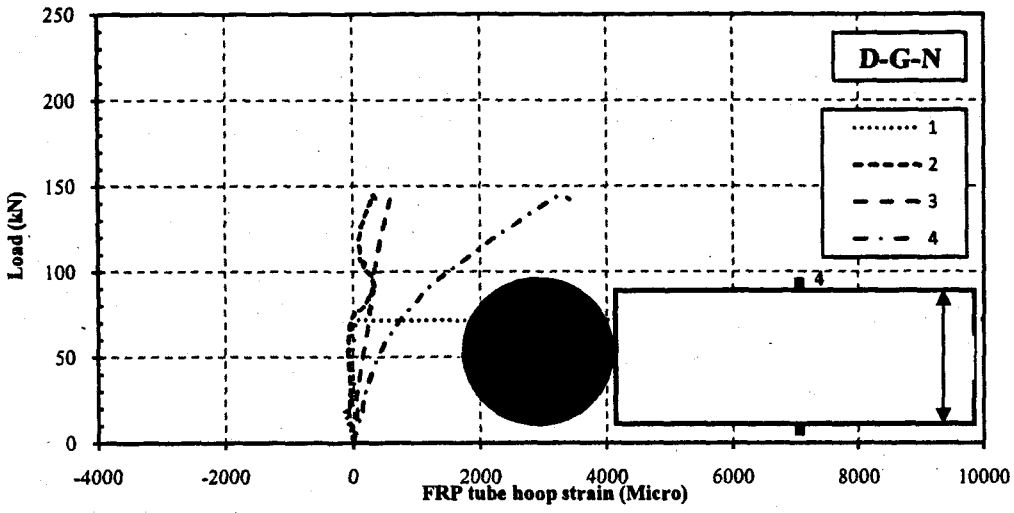

Figure 5-31 Mid-span hoop strain of reinforced CFFT beams (Series No. 1)

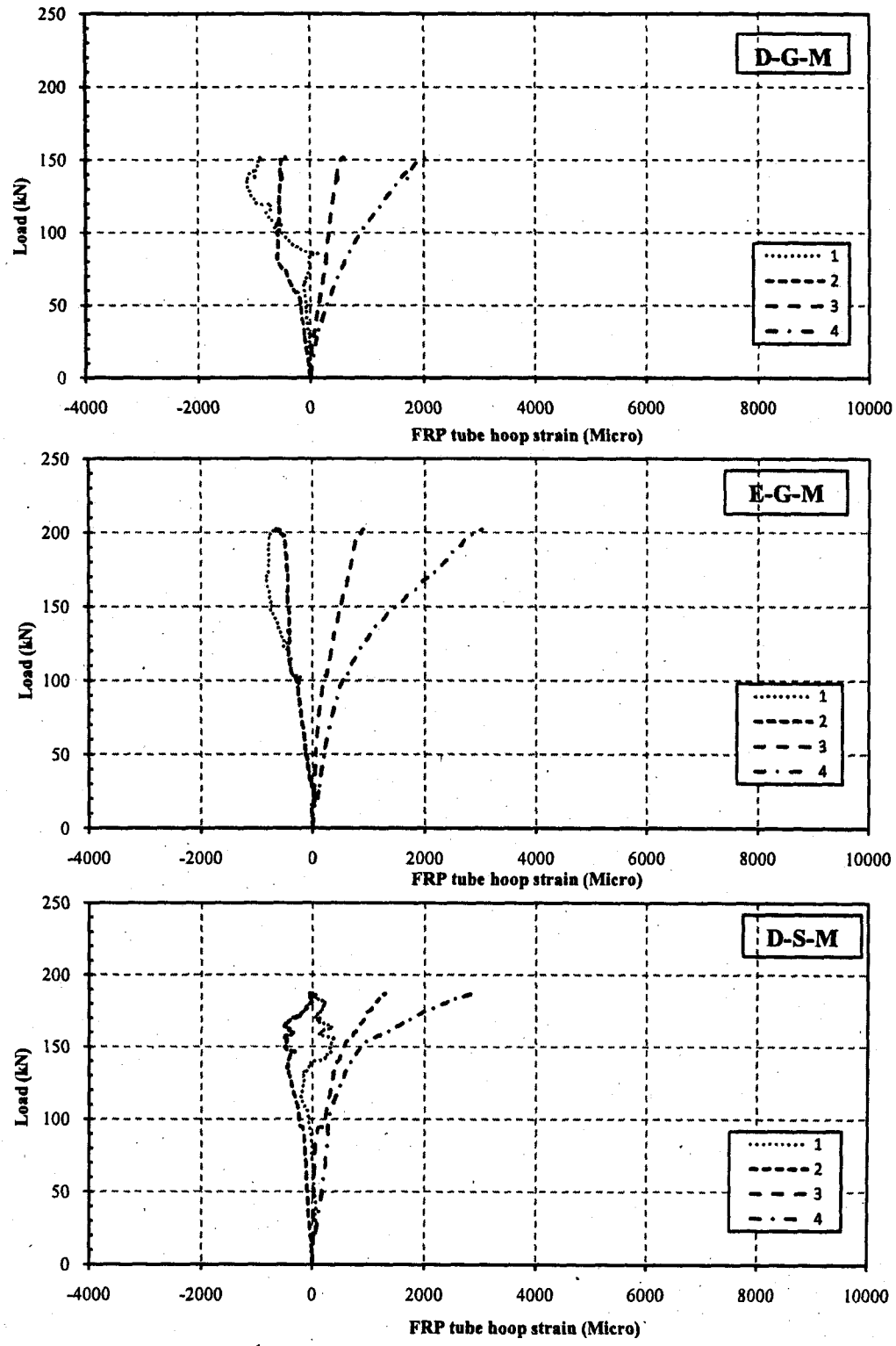

Figure 5-32 Mid-span hoop strain of reinforced CFFT beams (Series No. 2)

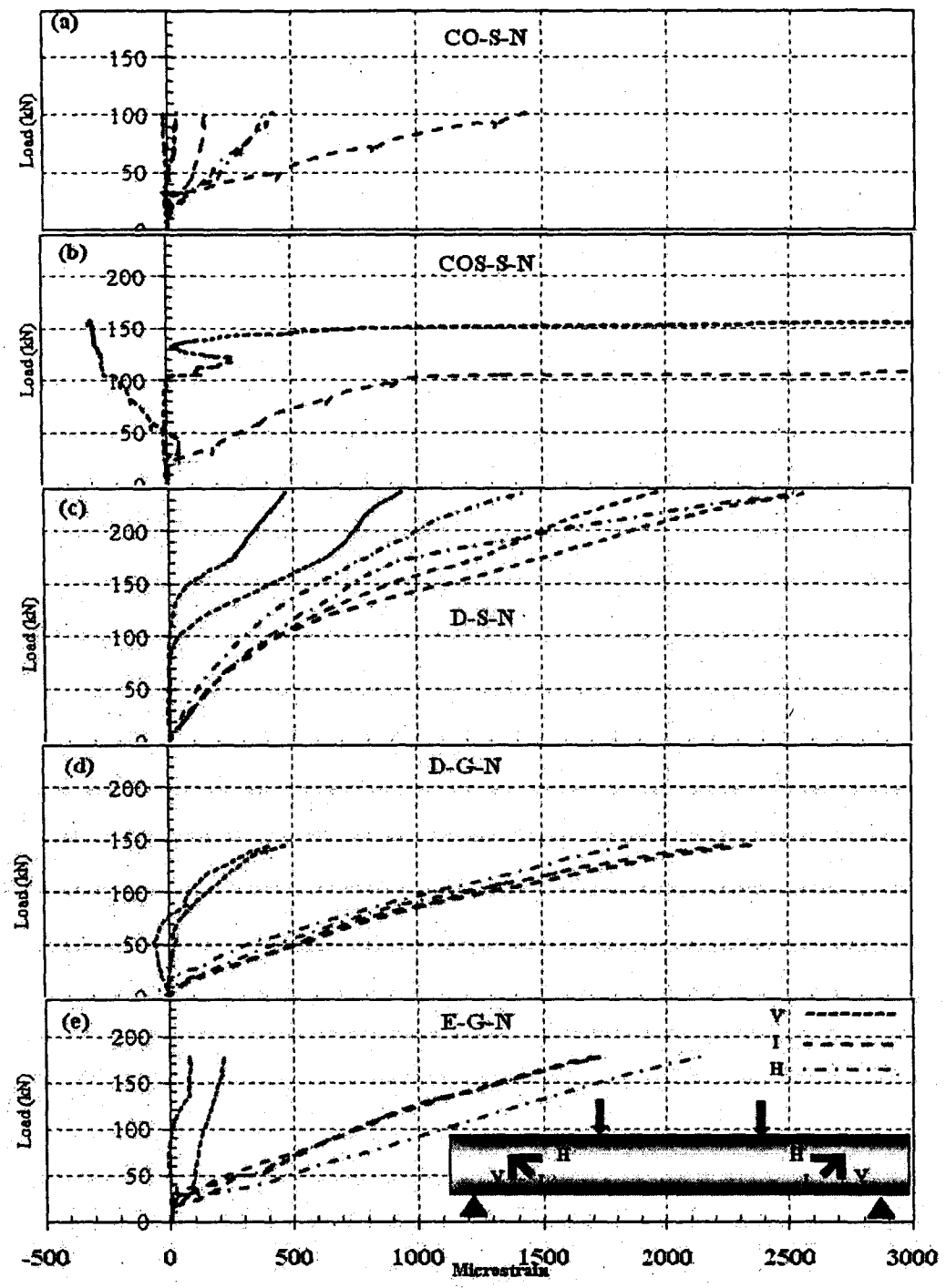

Figure 5-33 load-strain rosette relationships at mid-height of tested beams (Series 1)

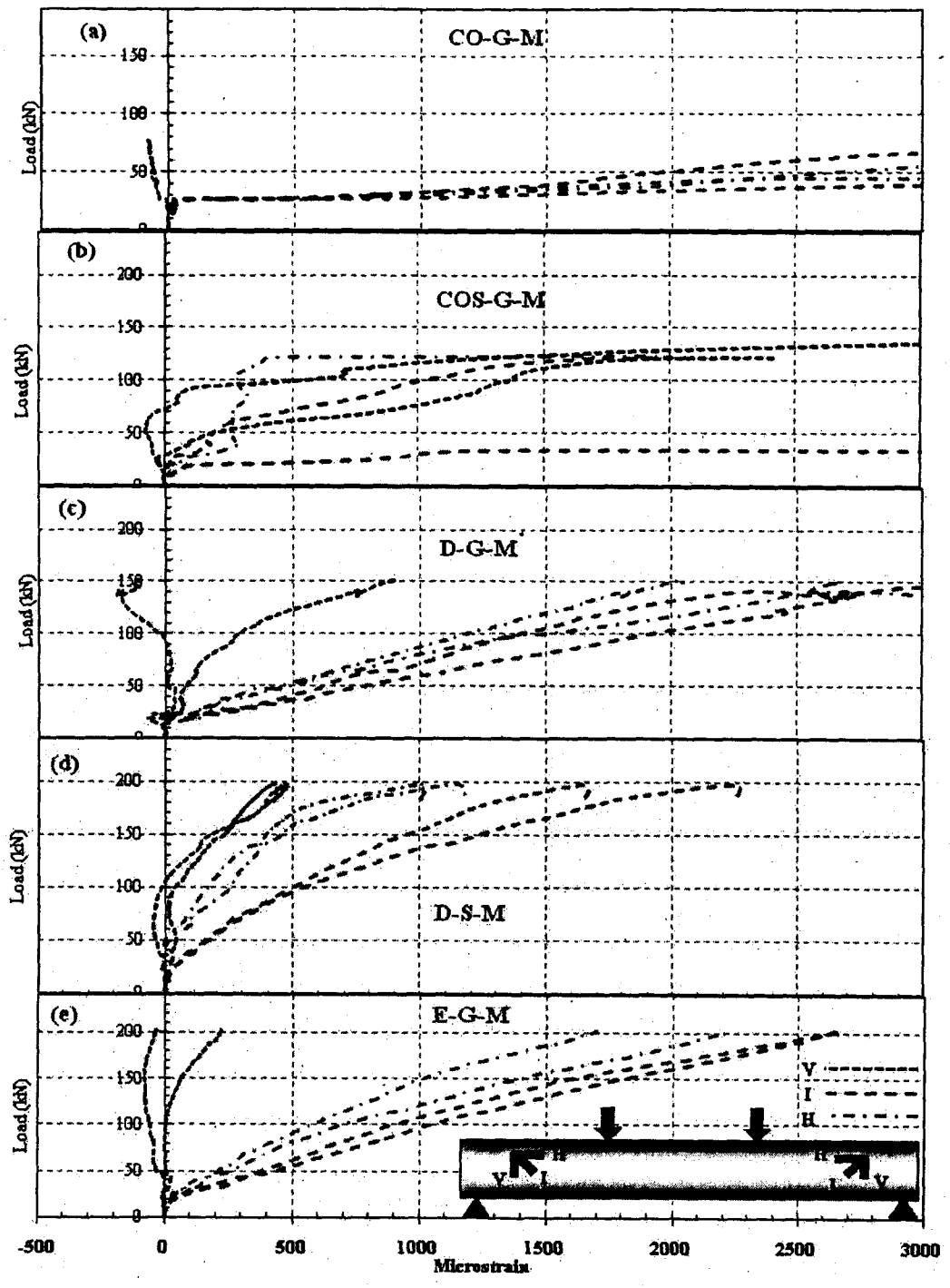

Figure 5-34 load-strain rosette relationships at mid-height of tested beams (Series 2)

5.4.5 Failure modes and crack patterns

Figure 5-35 to Figure 5-44 present the different finale failure modes, core concrete crack patterns and mid-span FRP rupture pattern in tension for the RC and RCFFT beams. Also, Figure 5-45 shows the load-end rotation relationships of RC and CFFT beams, while Figure 5-46 presents the load-concrete end slippages of reinforced RCFFT Beams.

All six tested RCFFT beams of this study failed in flexural at the mid-span of the beams. The failure occurred due to the tensile rupture of FRP tubes accompanied with tensile rupture of steel or FRP bars at the tension side of the beams. However, diagonal tension failure at the shear span and shear compression failure were the final failure modes for the RC control beams without and with spiral steel, respectively.

Figure 5-35 and Figure 5-36 show the failure modes of RC steel beam (Co-S-N) and FRP beam (CO-G-M), respectively, that without steel spiral. Similar characteristics of crack patterns were observed for the two beams. Crack formation was initiated in the flexural span between the two concentrated loads where the flexural stress is highest and shear stress is zero. The cracks were vertical perpendicular to the direction of the maximum principle tensile stress induced by pure bending, see Figure 5-35 (c) and Figure 5-36(a). As load increased, additional flexural cracks opened within the shear span. However, because of the dominance of the shear stresses, the cracks became progressively more inclined and propagated towards the load points leading finally to diagonal tension failure, see Figure 5-35 (b) and Figure 5-36 (b). The main diagonal tension cracks are characterized by joining the loading point at the top and support. Despite the CO-G-M constructed from concrete Type M (45 MPa) that has higher compressive strength than that of CO-S-N, the shear strength (failure load) of CO-G-M was lower than that of CO-S-N. This attributed to the difference in the type of internal reinforcements, however beam CO-S-N reinforced with steel bars that have higher tensile stiffness than FRP bars which were used for beam CO-G-M. A maximum end rotation of 0.85^{o} and 1.45^{o} were captured for CO-S-N and CO-G-M, respectively, see Figure 5-45 (a) and (b). On the other hand, the maximum recorded deflections at failure at the mid-span were 11.99 and 24.33 mm, for CO-S-N and CO-G-M, respectively.

a- Overview of deflected shape at failure

b- Shear-span crack pattern

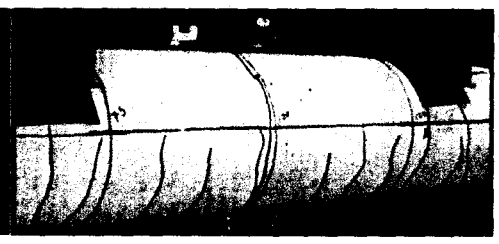

c- Mid-span crack pattern

Figure 5-35 Failure mode and concrete crack pattern of RC beam CO-S-N

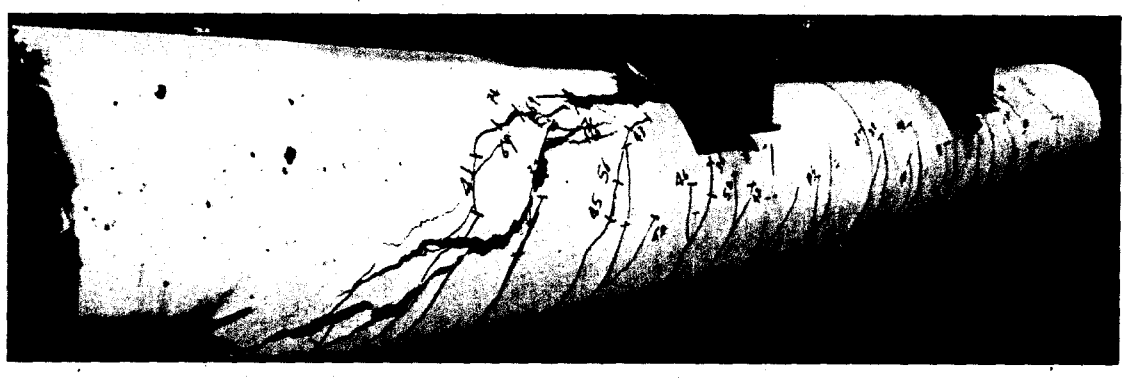

a- Overview of deflected shape at failure

b- Shear-span crack pattern

Figure 5-36 Failure mode and concrete crack pattern of RC beam CO-G-M

Figure 5-37and Figure 5-38 show the failure modes of RC steel beam (COS-S-N) and FRP beam (COS-G-M), respectively, that reinforced with steel spiral. In the early stages of loading, flexural were observed in the region of pure bending as the applied load increased. With a further increase of load, additional flexural cracks were developed in the mid-span, and new flexural cracks formed on the shear span. As the load increased, inclined cracks started within the beam web, almost half way of between the loading and support points. At the final stage of loading, the width of the flexural and inclined cracks at the mid-span and at the shear span, respectively, became more significant and flexural compression cracks formed at the top surface of the beam between the two points of loading. At 95% of the ultimate loading, an excessive concrete crushing occurred significantly at the top surface for beam COS-S-N, near to the two points of loading, see Figure 5-37 (c). On the other hand, for beam COS-S-N, a secondary concrete splitting failure occurred within the shear span at level of the longitudinal reinforcement. The splitting occurred immediately after formation of critical diagonal shear crack. The finale failure mode for the two beams was shear accompanied with crushing of the concrete. The concrete crushing for beam COS-G-M was limited to the surrounding area at the two point of loading, while it was extended over the total surface area between the two concentrated loads for beam COS-S-N. It is of interest to mention that, at failure the steel spiral was cut at the mid-height of the mid-shear span for the two beams. Also, rupture of the FRP bars was observed after the test through the main diagonal tension crack for beam COS-G-M.

Figure 5-39 to Figure 5-44 show the different failure modes of steel and FRP-RCFFT beams. Flexural failure was the final failure mode for all CFFT beams of Series 1 and 2 with different character. Failure occurred by tensile rupture of FRP tube at mid-span accompanied with tensile rupture of FRP or steel bars. Crack patterns of the concrete core were examined by removing the FRP tube after failure. At the early stage of loading, no cracks or anything could be observed rather than the deflection at the mid-span for all the RCFFT beams. As the load increased, white patches and flexural transverse visible matrix cracking was observed on the outer layer of the FRP tube after 40% of the ultimate load in the tension side of the beam between the two concentrated loads.

a- Overview of deflected shape at failure

b- Shear-span crack pattern c- Mid-span crack pattern (compression failure)

Figure 5-37 Failure mode and concrete crack pattern of RC beam COS-S-N

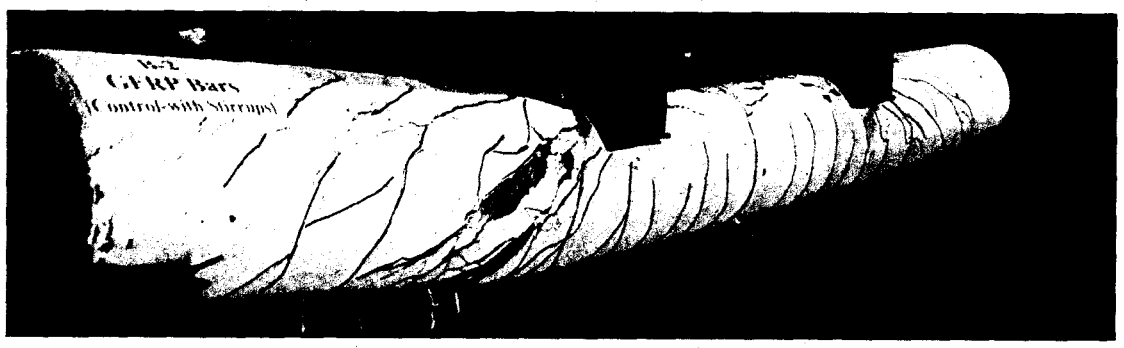

a- Overview of deflected shape at failure

b- Shear-span crack pattern

Figure 5-38 Failure mode and concrete crack pattern of RC beam COS-G-M

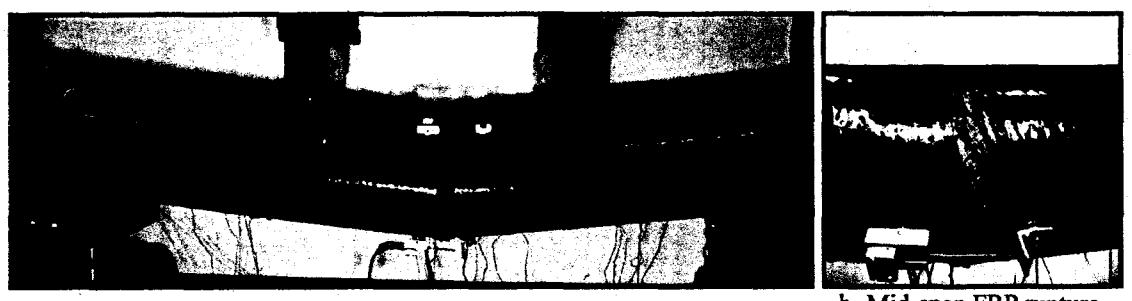

a- Overview of deflected shape at failure

b- Mid-span FRP rupture pattern in tension

c- Beam core concrete crack pattern

d- Mid-span core concrete crack pattern

Figure 5-39 Failure mode and concrete core crack pattern of RCFFT beam D-G-N

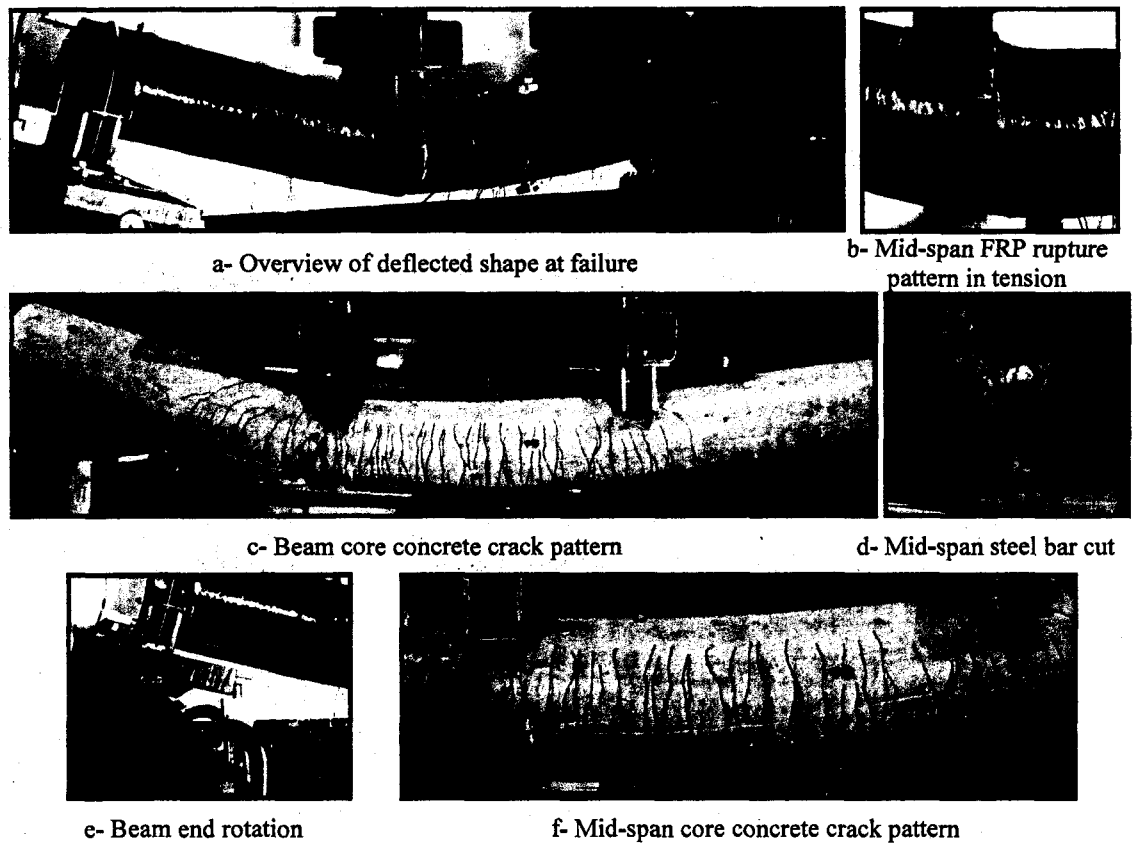

a- Overview of deflected shape at failure

b- Mid-span FRP rupture pattern in tension

c- Beam core concrete crack pattern

d- Mid-span steel bar cut

e- Beam end rotation

f- Mid-span core concrete crack pattern

Figure 5-40 Failure mode and concrete core crack pattern of RCFFT beam D-S-N

Figure 5-40 and Figure 5-42 show the failure modes of the steel-RCFFT beams (D-S-N and D-S-M). The failure was gradual and ductile. At the end of the plastic stage, necking of FRP tube was visible along with matrix delamination at the bottom of the beam in the mid-span region. The flexural failure started by the tensile rupture of the GFRP tube in the maximum tension moment zone. The FRP tube rupture occurred under the concentrated load which was near from the hinge support of the beam as shown in Figure 5-40 (a) and (b) for D-S-N, and Figure 5-42 (a) and (d) for D-S-M. The rupture occurred beyond the yield of the tension steel bars and at the end of the plastic stage with a drop in the flexural load. After that, the deflection increased significantly combined with a reduction in the load carrying capacity. However, the complete failure occurred after the first and second cut of the steel bars in the tension side with noticeable buckling at the compression side; see Figure 5-40 (d) and Figure 5-42 (d).

The crack patterns of the concrete core and D-S-M are presented in Figure 5-40 (c) and (f) for D-S-N and Figure 5-42 (b) for D-S-M. The figures indicate that uniform and excessive flexural cracks were developed at the mid-span of the beam between the two points of loading, also, the cracks propagated up to mid-depth of the beam at failure. It is of interest to mention that no crushing occurred for the concrete at the maximum compression moment zone. The major flexural crack was formed at the same location of FRP tube and steel bars rupture. On the other hand, limited flexural-shear cracks were observed at the shear-span located at the hinge support under the concentrated load for the two beams. The flexural cracks were seemingly wider and more dominant than that the limited flexural-shear cracks. Figure 5-40 (d) show the beam end rotation at the hinge support for D-S-N, while Figure 5-42 (c) show the beam ends rotation at the hinge and roller supports of D-S-M. The rotations at the ultimate were 9.70° and 5.95° for beams D-S-N and D-S-M, respectively.

On the other hand, the flexure failure of the FRP-RCFFT beams started by tensile rupture of the longitudinal GFRP rebars followed by tensile rupture of the FRP tube. The failure was gradual and progressive. It was also noted that local buckling of the tube occurred at the top zone of the beam at the mid span prior to the failure. In addition,

white patches were observed forming hoop cracks at the surrounding area of the GFRP tubes during the plastic stages of the loading, especially at tension side of the tube. After finishing the test, the GFRP tubes were removed for all beams to check the crack pattern of the concrete core. However, it was evident that no crushing occurred for the concrete at the maximum compression moment zone. On the other hand, uniform flexural cracks were observed in the flexural span between the two concentrated loads, where the bending stress is high and shear stress is zero. The numbers of the flexural cracks were not significant as compared with the crack patters for the steel-RCFFT. Also, no shear cracks were observed for these beams. On the other hand, the rotations at the ultimate for the FRP-RCFFT beams (ranged from 2.7 ° to 3.2 °) were quite below the recorded rotations for the steel-RCFFT beams.

The applied load versus end-rotation plot (Figure 5-45) follows the same trend as the load-deflection curves for all RCFFT beams. The stiffer the longitudinal reinforcement in the specimen, the higher the slope of the load versus end-rotation plot. For all tested beams and at the same level of applied load, the beam reinforced with glass FRP bars experienced higher rotation than the beam reinforced with steel bars. This result indicates the effect of the modulus of elasticity of the reinforcing bars on the end-rotation of the beam. Similar to the effect of the modules of elasticity of the reinforcing bars, Figure 5-45 (a) and (b) indicate that the higher the FRP tube thickness (Type E), the smaller the end rotation. Figure 5-46 show the load-concrete end slippages of RCFFT beams of Series 1 and 2. The end slippages between the FRP tube and concrete core were measured at the top and bottom surfaces at the hinge support of the beams. The figure indicates that no significant slippage or relative movement occurred between the tube and the concrete core at the end surfaces for all the RCFFT beams.

Finally, from comparing the failure modes of RC beams and RCFFT beams test in this study it can be concluded that, using FRP tubes changed the mode failure from shear and compression-shear to the onset flexural failure. This is attributed to the multidirectional contributions of the FRP tube, where longitudinal fibres contribute in flexure, while circumferential fibres provide confinement and shear resistance.

a- Overview of deflected shape at failure

b- Mid-span FRP rupture pattern in tension

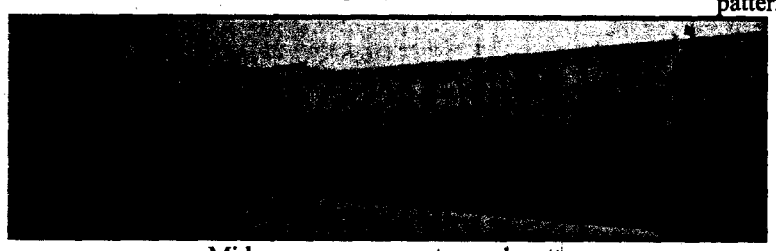

c- Mid-span core concrete crack pattern

Figure 5-41 Failure mode and concrete core crack pattern of RCFFT beam D-G-M

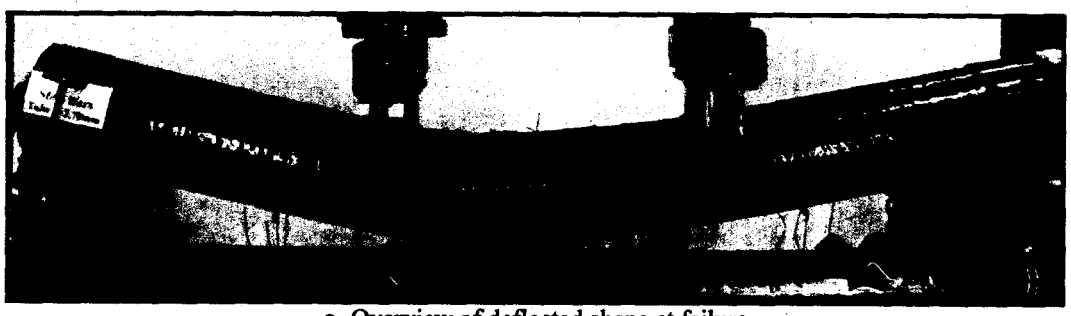

a- Overview of deflected shape at failure

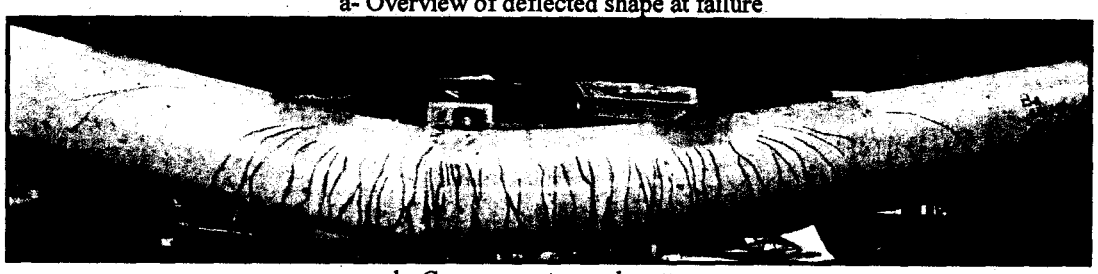

b- Core concrete crack pattern

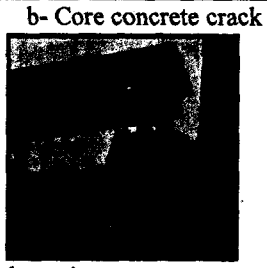

c- Beam end rotation

d- Mid-span FRP rupture

Figure 5-42 Failure mode and concrete core crack pattern of RCFFT beam D-S-M

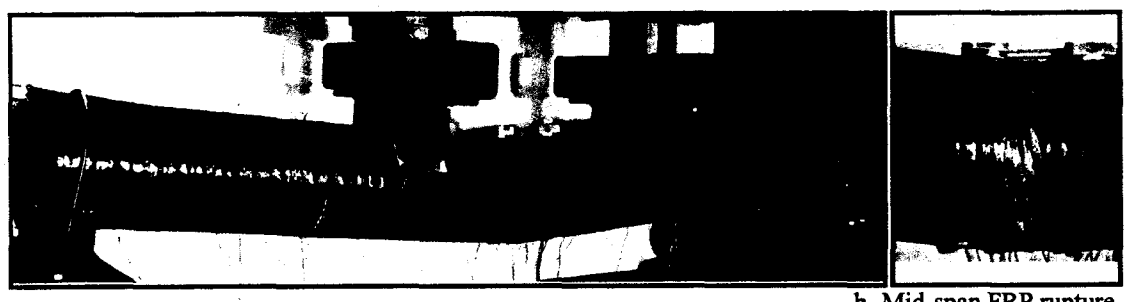

a- Overview of deflected shape at failure

b- Mid-span FRP rupture pattern in tension

c- Mid-span core concrete crack pattern

d- Mid-span FRP tube rupture at tension

Figure 5-43 Failure mode and concrete core crack pattern of RCFFT beam E-G-N

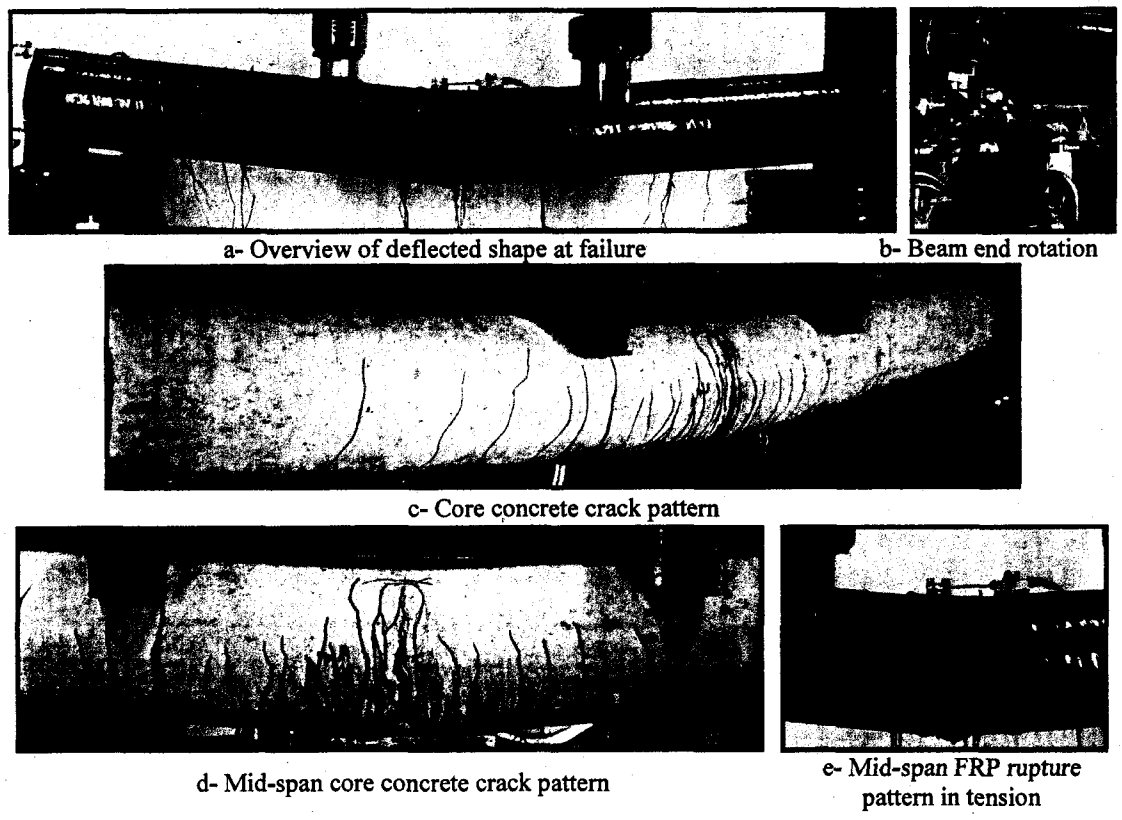

a- Overview of deflected shape at failure

b- Beam end rotation

c- Core concrete crack pattern

d- Mid-span core concrete crack pattern

e- Mid-span FRP rupture pattern in tension

Figure 5-44 Failure mode and concrete core crack pattern of RCFFT beam E-G-M

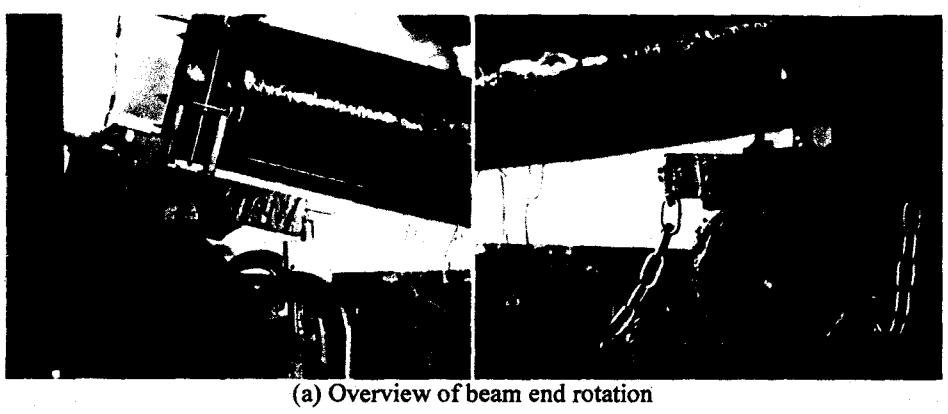

(a) Overview of beam end rotation

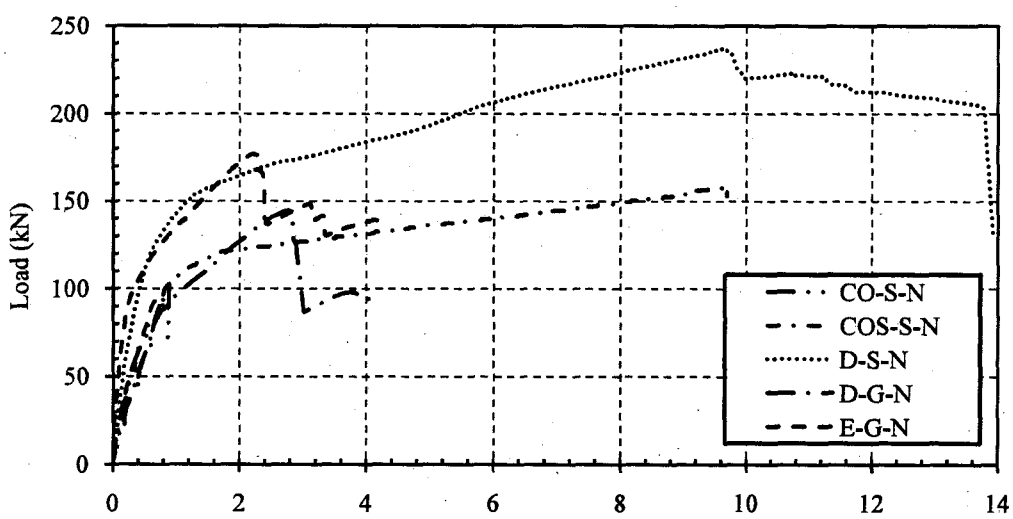

(b) Series No. 1

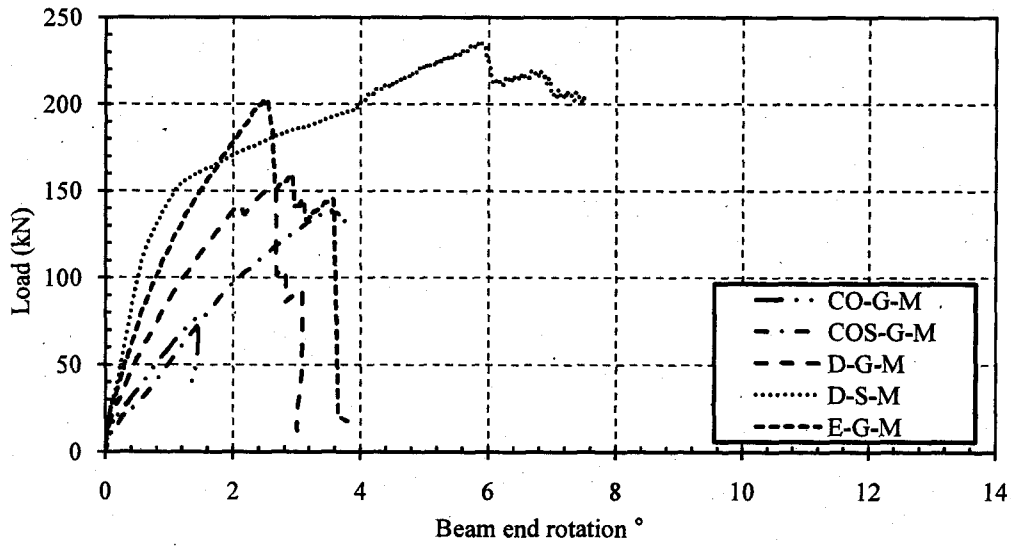

(c) Series No. 2

Figure 5-45 Load-end rotations of RC and CFFT beams

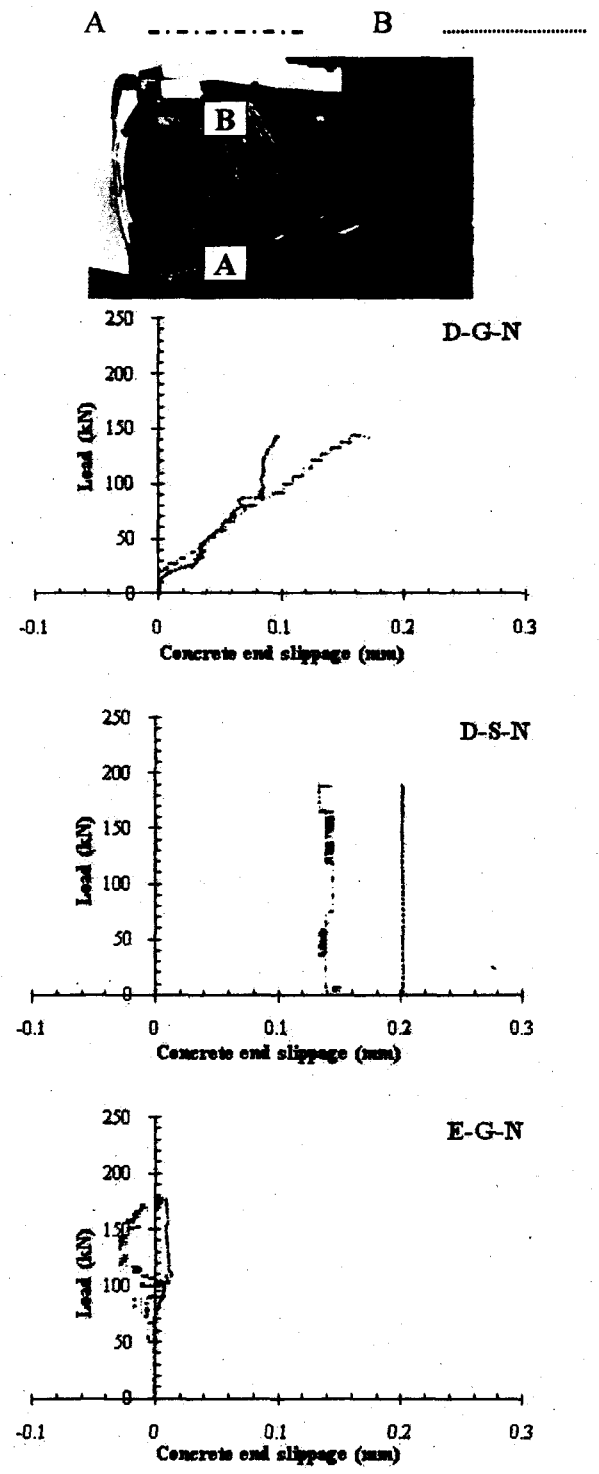

Figure 5-46 Load-concrete end slippages of reinforced RCFFT Beams

5.5 Effect of Test Parameters on Flexural Strength and Ductility

The objective of this phase of research program was to evaluate the FRP tube contribution to the flexural strength of concrete beams reinforced with steel or FRP bars. The objective was accomplished as the shear failure was avoided, and all RCFFT beams failed in flexural. The ultimate flexural strength and the ductility as measured by the energy absorption, of the tested beams, including the effect of the test variables, are discussed in the following sections.

5.5.1 Effect of type of transverse reinforcement

The influence of the confinement using steel spiral or FRP tubes on the flexural strength and ductility of the tested beams is shown in Figure 5-47 and Figure 5-48, respectively. The test results of the three beams of Series No. 1 and the three beams of Series No. 2 that reinforced internally with steel bars and FRP bars, respectively, are presented in these figures. The GFRP tube has increased the ultimate strength significantly and also improved the energy absorption capacity. This is attributed to two important aspects: The tube has a reinforcing effect in the longitudinal direction, which is not provided by the steel spirals, and also has a confining effect on the concrete core that is more effective than the steel spirals because the tube is located at the outermost surface and thus confines a larger concrete area, (this result is in a good a agreement with the test results conducted Fam and Mandal 2006). The figures indicate that the increase in the flexural strength and energy absorption for the steel-RCFFT beams are 55% and 82%, respectively, higher than the beam reinforced with a steel spiral for specimens of Series No. 1. On the other hand, the increase in the flexural strength and energy absorption for the FRP-RCFFT beams are 9 and 7%, respectively, higher than the beam reinforced with a steel spiral for specimens of Series No. 2. It can be observed that the improvement in the strength and energy absorption is not clear for beam reinforced with glass FRP bars, which may be attributed to the low modulus of elasticity of the glass FRP bars compared to steel bars. However, for the two series, using FRP tubes changed the mode of failure from shear (beam with and without steel-spiral) to flexural failure.

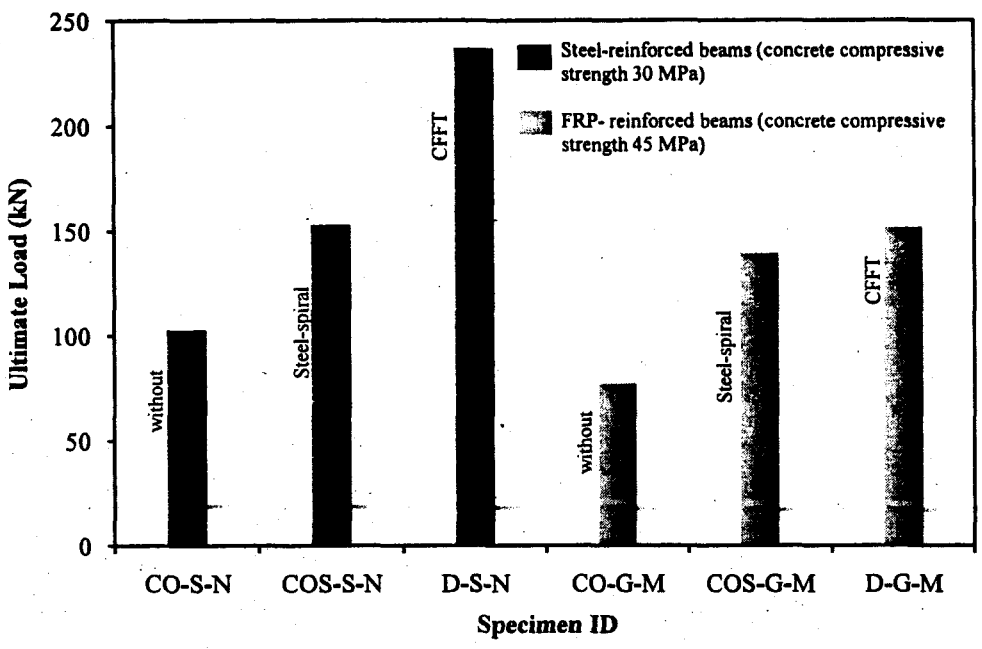

Figure 5-47 Effect of type of transverse reinforcement on the flexural strength

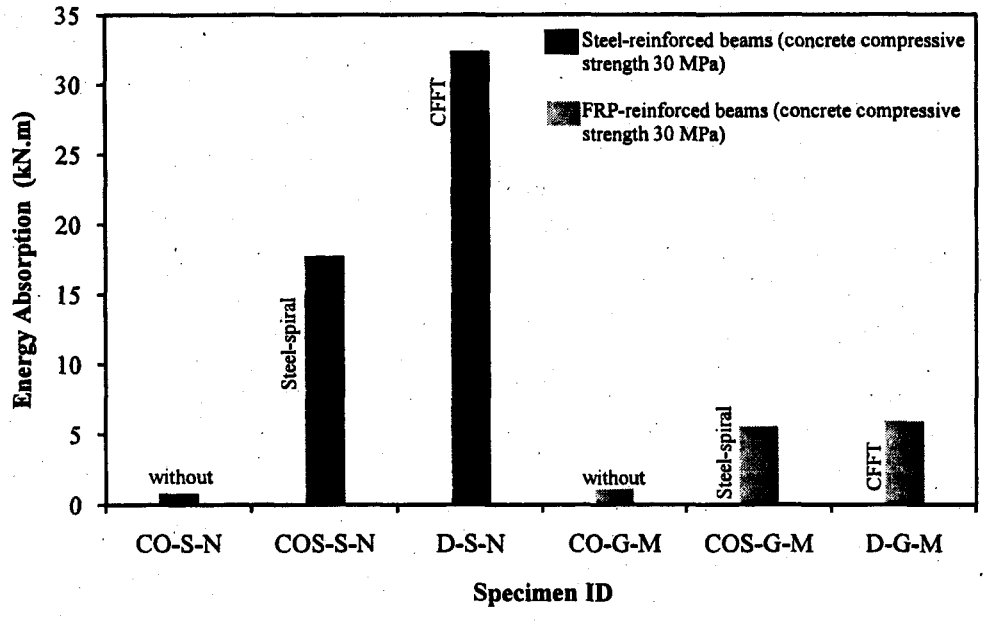

Figure 5-48 Effect of type of transverse reinforcement on the energy absorption

5.5.2 Effect of type of longitudinal reinforcing bars

Figure 5-49 and Figure 5-50 present the effect of type of the internal reinforcements on the flexural strength and energy absorption of tested RCFFT beams of Series No. 1 and 2. The vertical axis in Figure 5-49 and Figure 5-50 represents the flexural strength and the energy absorption, respectively, while the horizontal axis represents the effect of the type of longitudinal reinforcement as measured by the Young's modulus. Steel and Glass FRP bars of the same cross sectional area were used in reinforcing CFFT beams. Figure 5-49 shows that the ratio of the strength of FRP-RCFFT beams to that of steel-RCFFT beams was 60%. This ratio approximately equals the cube root of axial stiffness ratio between glass and steel bars $\sqrt[3]{\rho_{fl} E_{fl} / \rho_{sl} E_{sl}}$ (the corresponding beam had the same reinforcement ratio). This result is consistent with the test results conducted by El-Sayed et al. 2006 on reinforced concrete beams without stirrups and reinforced in the longitudinal direction with glass FRP, carbon FRP and steel bars. The increase in the flexural strength for steel-RCCFTs beams is attributed to the difference in the Young's modulus between the steel and GFRP bars. On the other hand, Figure 5-50 shows that the energy absorption of the RCFFT beams reinforced with steel bars on average are 460% higher than that of beams reinforced with GFRP bars. This is attributed to the elastic-plastic behaviour of the steel bars as compared with the linear elastic behaviour of FRP bars. This result reflects the effect of the modulus of elasticity of the reinforcing bars on the flexural strength as well as the ductility of the RCFFT beams.

5.5.3 Effect of reinforcement ratio of FRP tubes

The effect of FRP tube reinforcement ratio on the flexural strength and energy absorption is presented in Figure 5-51 and Figure 5-52, respectively for the four tested RCFFT beams. The horizontal axis in Figure 5-51 and Figure 5-52 represents the FRP tube reinforcement ratio as measured by the area of the tube divided by the area of the concrete core, $4t_{FRP}/D$. The four beams had identical reinforcement ratio of the GFRP bars, while the FRP tube reinforcement ratios ranged from 6 to 13%. It can be noticed that the flexural strength and energy absorption increased as the FRP tube reinforcement ratio was increased by using tube Type E instead of tube Type D.

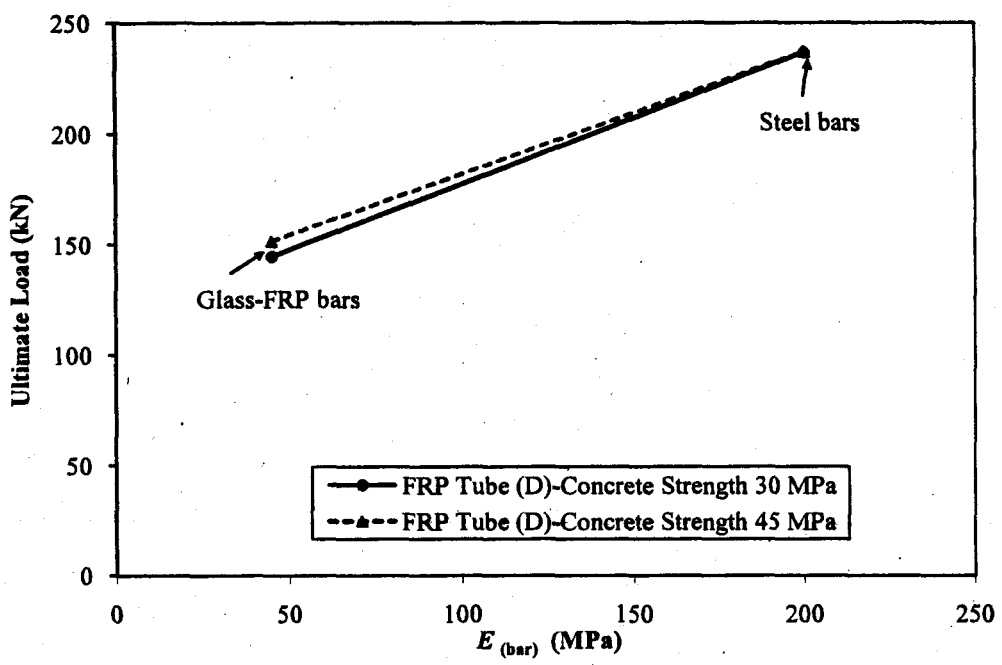

Figure 5-49 Experimental flexural strength versus Young's modulus of bars

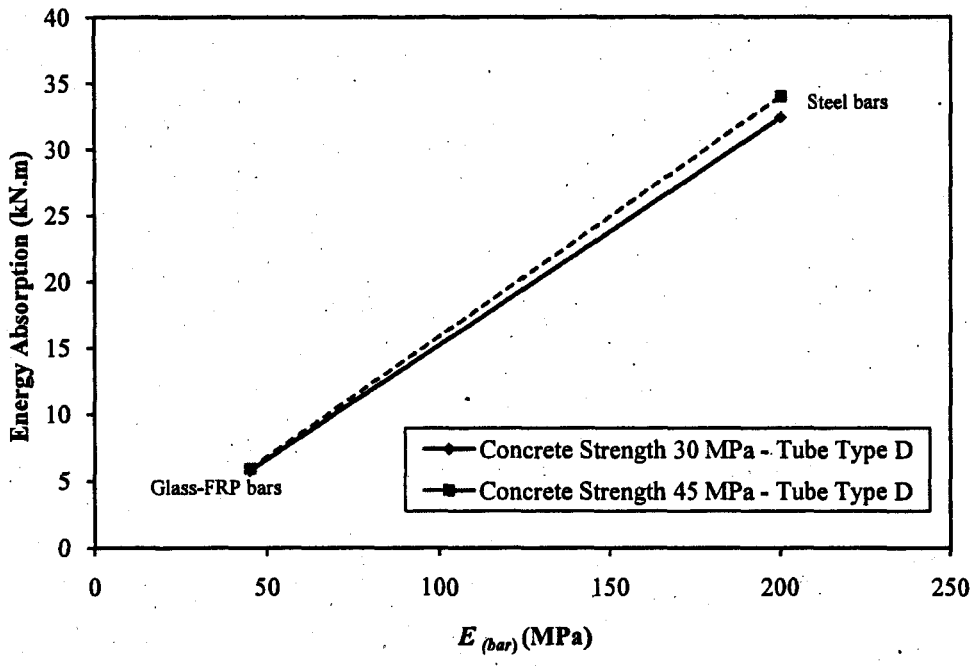

Figure 5-50 Energy absorption versus Young's modulus of bars

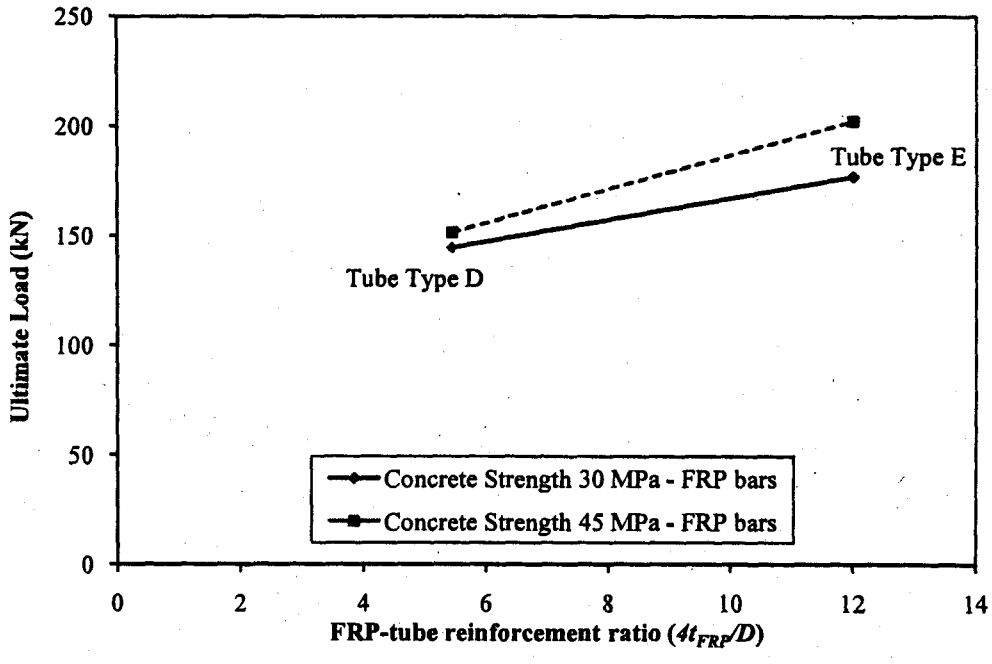

Figure 5-51 Experimental flexural strength versus FRP-tube reinforcement ratio

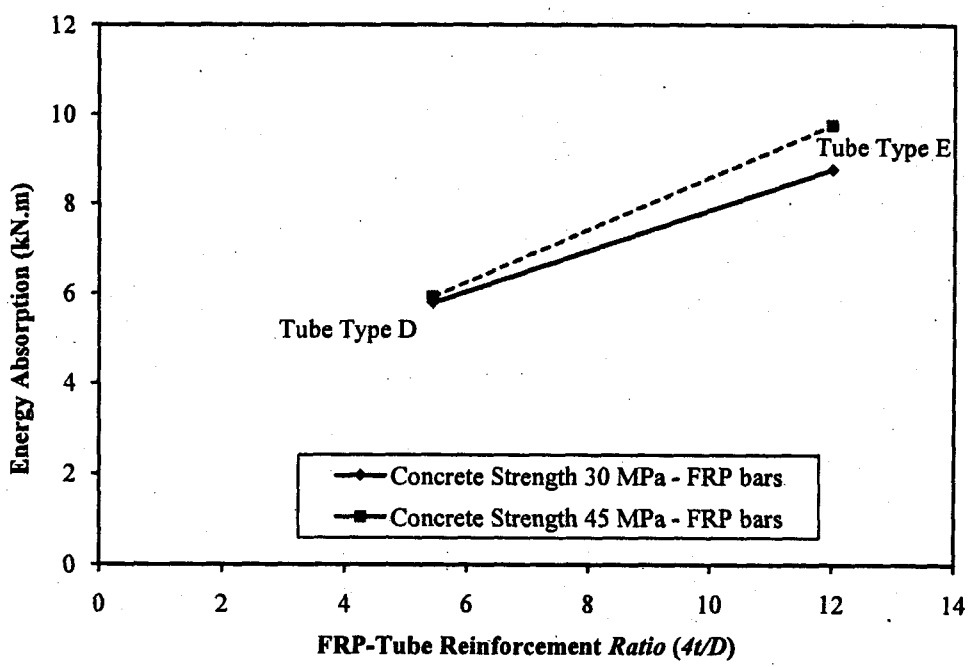

Figure 5-52 Energy absorption versus FRP-tube reinforcement ratio

The FRP tube Type E has thickness (6.40 mm), which it is equal to 2.2 times the thickness of the tube type D, (2.90 mm). Figure 5-51 shows that increasing the FRP tube reinforcement ratio by 120% (from 5.44 to 13%) increased the flexural strength and the energy absorption on average by 20 and 58%. It is clear that the increase in the flexural strength (20%) is not significant as compared by the increase in the FRP tube reinforcement ratio (120%). This is attributed to the increase in the flexural strength is mainly resulted from the contribution of the increase in the thickness of the FRP tubes in the tension side of the beams. While the increase in the thickness of the FRP tubes in middle zone and compression side is attributed to increase the shear and compressive strengths of the beams. This was evidence as no crushing and shear failure occurred for all the RCFFT beams compared to steel-spiral RC beams. On the other hand, it is found that the average ratio of the experimental flexural strength is equal to the 3.5 root of the axial stiffness ratio (axial modulus of elasticity multiplied by the FRP tube thickness) between the two tubes, $\sqrt[3.5]{(E_{fl}t_{FRP})_{tube\,No.2}/(E_{fl}t_{FRP})_{tube\,No.1}}$, where tube No.1 has smaller thickness than tube No. 2.

5.5.4 Effect of concrete compressive strength

The influence of the concrete strength on the flexural strength and energy absorption of the RCFFT beams is shown in Figure 5-53 and Figure 5-54, respectively. The figures indicate that the increase in the flexural strength and energy absorption is not significant as compared with the increase in the concrete compressive strength 50% (from 30 to 45 MPa) for the tested RCFFT beams of series No. 1 and 2. Figure 5-53 and Figure 5-54 indicate that the increases in the flexural strength and energy absorption are limited to 4 and 3% respectively, for the beams reinforced with steel bars and cast in FRP tube Type D, with increasing the concrete compressive strength from 30 to 45 MPa. The corresponding values for the beams reinforced with FRP bars and cast in FRP tube Type E are 14 and 11%. It can be concluded that the flexural behaviour of the six RCFFT beams tested in this study were not significantly affected with increasing the concrete strength from 30 MPa to 45 MPa.

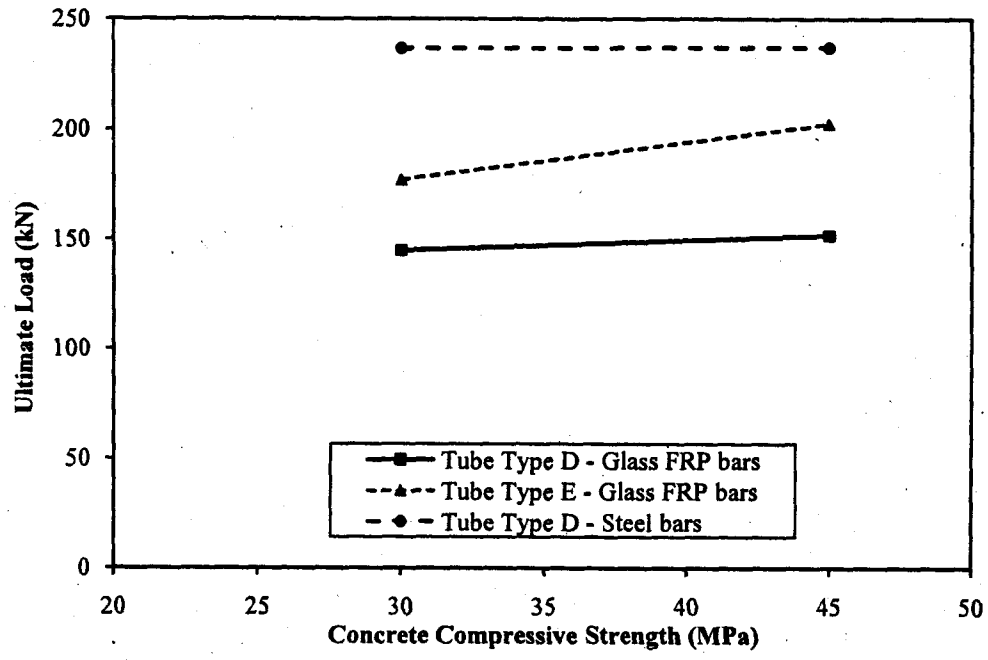

Figure 5-53 Experimental flexural strength versus concrete compressive strength

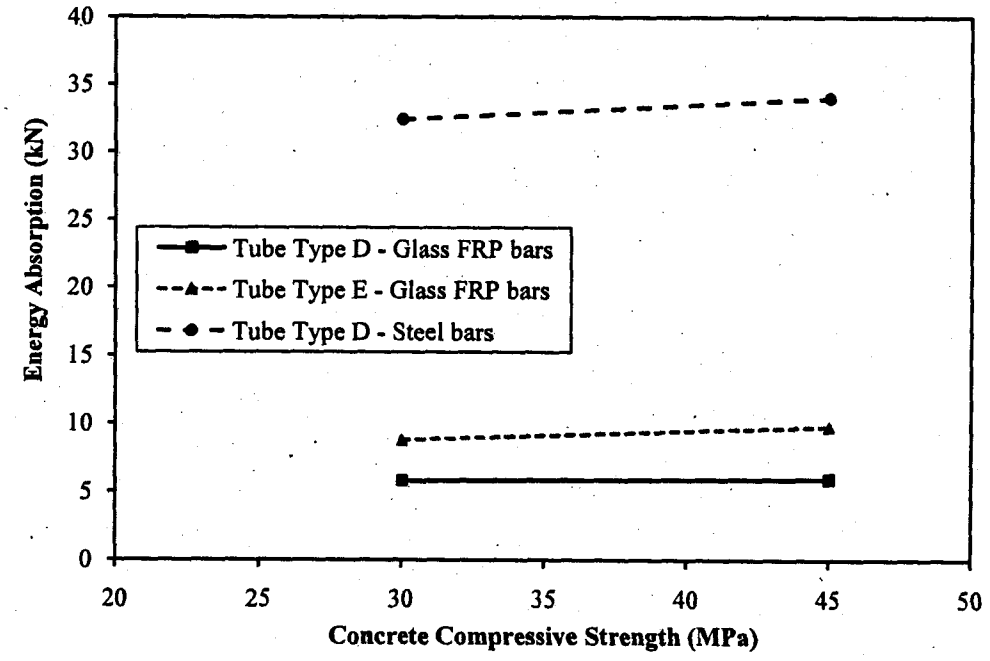

Figure 5-54 Energy absorption versus concrete compressive strength

5.6 Theoretical Analysis

Concrete structures are conventionally reinforced with steel bars. For structures subjected to aggressive environments (e.g. de-icing salts in bridges, marine structures, etc.), combinations of moisture, temperature and chlorides may results in a corrosion of reinforcing steel, leading to the deterioration of concrete and loss of serviceability. The corrosion problem of steel rebar is the greatest factor limiting the life expectancy of reinforced concrete structures. In the last decade, considerable research programs have been conducted to validate the application of FRP composites in the construction industry, and recently, structural applications of FRP composites have begun to appear in different types of the concrete structures. Recently, the application of the circular RCFFT beams technique is new and rapidly increasing in the field of civil engineering structures. The FRP tube provides a lightweight permanent formwork for fresh concrete, acts as a noncorrosive reinforcement, reinforcement in the tension side, confinement of the concrete in the compression side, shear reinforcement and protect the internal reinforcement and concrete core from the aggressive environments. In fact, extensive research programs have been conducted to investigate the behavior of concrete beams reinforced with FRP or steel reinforcement that have rectangular cross section. In addition, all the codes and guidelines provide flexural design provisions and equations for the reinforced concrete beams based on they have rectangular cross section. This is resulted from the common practical use of the rectangular reinforced concrete beams in civil engineering structures. Circular axi-symmetric flexural members are desirable in certain applications, including concrete piles, pier columns, utility and light poles, highway overhead sign structures, and fender piles. (Mandal 2004; Karbhari 2000; Fam et al. 2007). One of the main objectives of this study is to validate, and/or modify the current design approaches for flexural for RCFFT beams.

Due to the lack of flexural design provisions for RCFFT beams reinforced with steel or FRP bars, the flexural strength behaviors are analyzed using the simplified analytical method and the available flexural design equations specified in North American codes and guidelines (ACI and Canadian standards) for calculating crack, yield

and ultimate moment and deflection. The results of analysis are compared to the experimental values. In addition, this part presents a modification to the available existing design provisions and proposes new flexural design equations which are concerned with evaluating the FRP tube confinement contribution to the flexural resistance of CFFT beams reinforced longitudinally with steel or FRP bars.

5.6.1 Cracking moment of RCFFT beams

The cracking moment capacities M_{cr} of test RCFFT beams are estimated using Equation 5-2, and considering elastic theory based on the gross section properties commonly employed in structural design

$$M_{cr} = \frac{f_r I_g}{y_t} \qquad 5\text{-}2$$

where f_r modulus of rupture of concrete; I_g moment of inertia of gross section and y_t distance of the extreme tension fibre from the neutral axis.

The moment of inertia for concrete, bars and FRP tube are considered in this study in estimating the moment of inertia of gross section of test RCFFT beams. The gross moment of inertia is calculated using the following equation:

$$I_g = I_{Concrete} + (n-1)I_{Bars} + n_{tube} I_{Tube} \qquad 5\text{-}3$$

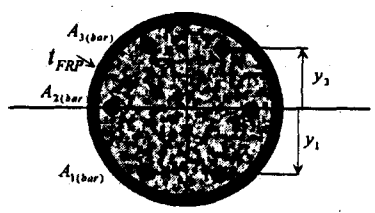

Figure 5-55 The Typical cross section of the RCFFT beams

The modular ratio, $n = E_s / E_c$ for steel RCFFT beams, $n = E_f / E_c$ for FRP-RCFFT beams, and $n_{tube} = E_{t(axial)} / E_c$ for FRP tube, where E_c is the concrete Young's modulus

$E_c = 5000\sqrt{f_c'}$, E_s and E_f are the steel and FRP bars Young's modulus, respectively, and $E_{t(axial)}$ is the modulus of elasticity of the FRP tube in the axial direction.

$$I_{Concrete} = \frac{\pi (D)^4}{64} \qquad 5\text{-}4$$

$$I_{Tube} = \pi (D_o/2)^3 t_{FRP} \qquad 5\text{-}5$$

where, $D_o = D + t_{FRP}$, D and t_{FRP} are the internal diameter and thickness of FRP tube, respectively.

$$I_{Bar} = \sum_{i=1}^{n} 2A_{i(bar)} y_i^2 \qquad 5\text{-}6$$

where $A_{i(Bar)} = A_1, A_2, A_3, \ldots\ldots A_n$ and $y_i = y_1, y_2, y_3, \ldots\ldots y_n$

where n is the number of internal rebar rows, $A_{i(Bar)}$ and y_i are the cross section area of one bar in each row and its distance from the centerline of the cross section, respectively.

The ACI building code (ACI 318-08) and design guidelines (ACI 440.1R-06) for reinforced concrete structures with steel and FRP bars, respectively, use Equation 5-7 to predict the modulus of rupture of concrete. Also, the same equation is provided by the Canadian code for Design and Construction of Building Components with FRP (CAN-CSA S806-02) (CSA standard A23.3). On the other hand, the Canadian Highway Bridge Design Code provides (CAN-CSA S6-06) Equation 5-8 to predict the modulus of rupture of concrete.

$$f_r = k\lambda\sqrt{f_c'} \qquad k = 0.62 \qquad 5\text{-}7$$

$$f_r = k\lambda\sqrt{f_c'} \qquad k = 0.40 \qquad 5\text{-}8$$

where $\lambda = 1.0$ for normal-weight concrete

The predicted cracking moments M_{cr} were compared to the experimental values as given in Table 5-8, for the test RCFFT beams reinforced with steel and GFRP bars. It can be noticed that the experimental cracking moments ($M_{cr(exp)}$) are higher than that the

predicted values($M_{cr(pred)}$). This is evident from Table 5-8, as the mean values of $M_{cr(exp)}/M_{cr(pred)}$ were 1.55 and 2.32 using Equations 5-7 and 5-8, respectively. This indicates that the RCFFT beams have higher cracking strength than that conventional RC beams. The increase in the cracking moment is attributed to the improvement in the flexural tensile strength of the beams which was resulted from the confinement of the concrete core inside the FRP tube and the contribution of the FRP tube in the tension side to the flexural capacity. In addition, casting the concrete in the FRP tube eliminates the initial cracks after the initial setting of the beams and restrained the expansion of concrete during curing, which might have induced a state of chemical prestressing of the concrete. This result is consistent with the test results as reported by Fam 2000. The test results are used to modify the coefficient k of Equation 5-7 or 5-8 to correlate the experimental results with the theoretical results. As indicated in Table 5-8, the mean and standard deviation values of $M_{cr(exp)}/M_{cr(pred)}$ were 0.99 and 0.03, respectively, using the modified Equation 5-9 based on $k = 0.94$.

$$f_r = k\sqrt{f_c'} \qquad k = 0.94 \qquad \text{5-9}$$

On the other hand, the flexural behaviours of CFFT beams were investigated by Fam 2000 by testing CFFT beams with small and large diameters. The test results indicated that with $k = 1.00$ the ACI equation predicted well the experimental values. The proposed value for k by Fam 2000 (1.0) is slightly higher than the proposed value (0.94) of the present study. The increase in the k value is attributed to the difference in the fibre orientation in the axial direction for the used FRP tubes. Whereas, the FRP tubes which had been used by Fam 2000 included fibre in the axial directions much higher than that used in the present study, which in turn increased the cracking moment; this indicate that the value of k can be described based on the stiffness of the FRP tube in the hoop and axial directions. More research studies are required in this area to study the effect of fibre orientation of FRP tubes on the cracking moment behaviour of CFFT beams.

Table 5-8 Experimental and predicted cracking moment for test RCFFT beams

	Crack Moment, M_{cr} (kN.m)					$M_{cr(exp)}/M_{cr(pred)}$			
	Experimental	ACI 318-08, ACI 440.1R-06, CSA S806-02	CSA S6-06	Fam 2000	Proposed equation Eq 5.2	ACI 318-08, ACI 440.1R-06, CSA S806-02	CAN-CSA S6-06	Fam 2000	Proposed equation Eq 5.2
D-S-N	6.75	4.40	2.93	7.34	6.9	1.53	2.30	0.92	0.98
D-G-N	5.09	3.32	2.21	5.54	5.2	1.53	2.30	0.92	0.98
E-G-N	5.55	3.40	2.26	5.67	5.33	1.63	2.46	0.98	1.04
D-G-M	5.82	3.89	2.59	6.48	6.09	1.50	2.25	0.90	0.96
E-G-M	6.24	3.96	2.64	6.60	6.21	1.58	2.36	0.94	1.00
D-S-M	7.53	4.9	3.31	8.29	7.79	1.54	2.27	0.91	0.97
Average						1.55	2.32	0.93	0.99
SD						0.05	0.07	0.19	0.03

5.6.2 Theoretical development for yield and ultimate moment of test RCFFT beams

Three types of flexural failure (tension, balanced and compression-controlled section) of a RC beam can be expected depending on the percentage of the reinforcement ratio used in the section. In beam designed as tension-controlled sections, the FRP-reinforced concrete beams are manifested by the rupture of bars in the tensile zone of the beam. In the case of steel-reinforced concrete beams, the tension failure mode is indicated by steel yielding, which leads to either the secondary compression failure of concrete or the rupture of steel in tension. The test results of this study showed that the complete failure of the tested steel and FRP-RCFFT beams occurred due to the rupture of FRP and steel bars, respectively. Since, the rupture of steel or FRP bars in tension is highly unlikely, except in cases of highly under-reinforced beam sections. This indicates that the tested steel and FRP-RCFFT beams could be considered as under-reinforced beam sections. On the other hand, the experimental observations discussed earlier (5.4.4.2) indicate that the FRP tubes confine the concrete core on the compression side of the tested RCFFT beams. This is evident from Figure 5-31 and Figure 5-32 where the load-hoop strain response on the compression side of the specimens is an indication of confinement. The figures

indicated that the maximum measured hoop strains on the compression side on average ranged from 2000 to 4000 micro-strains. The change from the initial to the second slope indicates initiation of confinement and the slope of the second line is an indication of the level of confinement. On the other hand, the values of the hoop strains indicate that concrete in the compression zone of reinforced CFFT experiences an intermediate level of confinement as compared to the CFFT columns under pure compression load. This result is consistent with the test results as reported by Cole and Fam 2006; Fam and Rizkalla 2002; Davol et al. 2001; Fam 2000. In this case, it is quite clear that the FRP tubes were activated to confine the concrete in compression as a result of making the RCFFT beams reach a substantially higher load level than that of RC beams, (without tube). In this case the concrete compressive stress and strain at ultimate should be higher than that the corresponding values of unconfined concrete and less than the corresponding values of full confined concrete, or it can be expressed as follows:

$$f_c' \le f_{cu} \le f_{cc}' \qquad 5\text{-}10$$

$$\varepsilon_c' \le \varepsilon_{cu} \le \varepsilon_{cc}' \qquad 5\text{-}11$$

Where f_c' and f_{cc}' are the ultimate unconfined and confined concrete compressive strength under pure axial load, respectively, f_{cu} is the partially confined concrete compressive strength of the tested CFFT beams under flexural load at ultimate load. ε_c' , ε_{cc}' and ε_{cu} are the strain values at the aforementioned corresponding strength values, respectively.

In fact, the analysis of a circular cross section is more complex than that of a rectangular one. The stresses, which are variable over the section depth, are also distributed along an area of variable width. In addition, the bars are usually disturbed throughout the depth and the FRP tube is continuous around the perimeter, such that the cross-sectional area of reinforcement at any given depth is more difficult to calculate than in conventional RC sections. On the other hand, whereas the tested RCFFT beams are under-reinforced (tension-controlled section) and the concrete core is under partial confinement condition, therefore the analysis becomes more complex unlike the conventional steel RC design. Since the FRP reinforcement does not yield in case of FRP-RCFFT beams and the secondary compression failure of concrete does not occur up to the rupture of steel in

tension for the tested steel-RCFFT beams, the ultimate confined compressive strain and stress cannot be reached in the concrete ($\varepsilon_{cu} < \varepsilon'_{cc}$; $f_{cu} < f'_{cc}$). Therefore the equivalent rectangular stress block is not easy to assume.

In this section, simplified analytical method is developed to predict the yield and resisting moments corresponding to the failure modes of the tested RCFFT beams. The analysis of the two series of tested RCFFT beams were conducted according to the equations derived from linear elastic analysis, and assuming Bernoulli's theory (plane section remains plane). The flexural analysis procedure was straightforward. The parts of the FRP tube above and below the neutral axis are considered effective in resisting compression and tension forces, respectively. However, in tension the concrete is assumed not to contribute to the internal forces after cracking. Figure 5-56 shows the cross section of the circular RCFFT beam that was used in the analysis, where the neutral axis is located within the cross-section at a depth c. The following sections provide a detailed description of the theoretical analysis, including different scenarios of stress and strain distribution, along with formulation of essential equations.

Referring to the equivalent stress and strain distribution diagram shown in Figure 5-56, the internal tensile forces in the FRP tube and steel or FRP bars, T, can be expressed respectively, as follows:

$$T_{tube} = \frac{1}{2} E_{tx} \varepsilon_{Bottom} (D_o - c) t_{FRP} \qquad 5\text{-}12$$

$$T_{bar1} = A_{b1} E_b \varepsilon_{b1} \qquad 5\text{-}13$$

$$T_{bar2} = A_{b2} E_b \varepsilon_{b2} \qquad 5\text{-}14$$

With reference to Figure 5-56 the strains ε_{Bottom} and ε_{b2} can be computed in terms of ε_{b1} as follows:

$$\varepsilon_{Bottom} = \varepsilon_{b1} \left(\frac{D_o - c}{D_o - c - d} \right) \qquad 5\text{-}15$$

$$\varepsilon_{b2} = \varepsilon_{b1} \left(\frac{0.50 D_o - c}{D_o - c - d} \right) \qquad 5\text{-}16$$

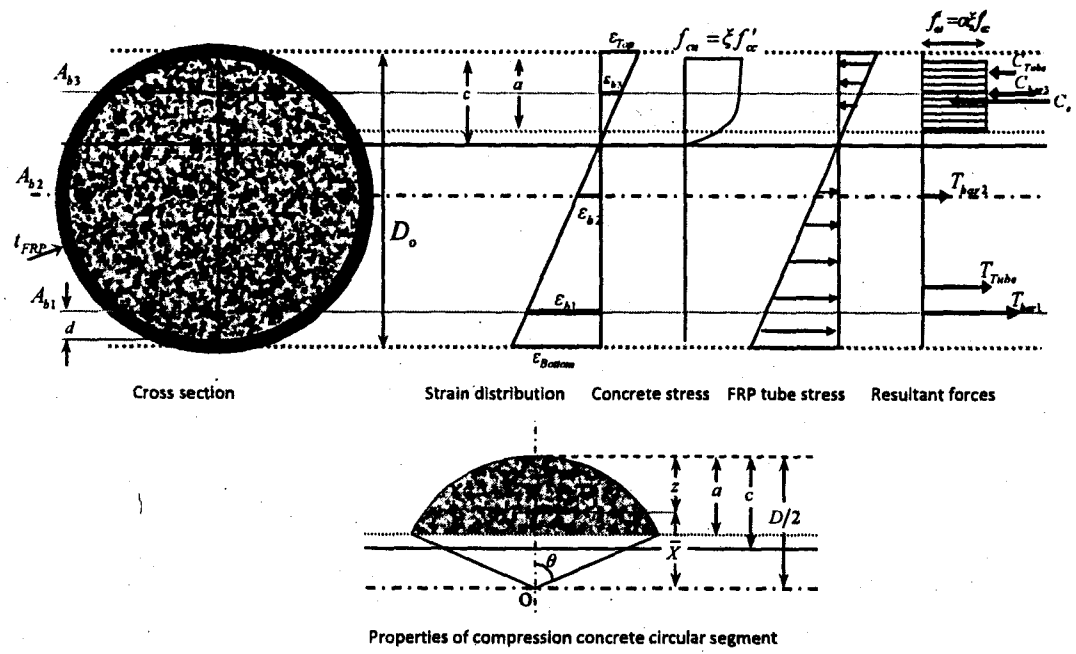

Figure 5-56 Details of RCFFT beam cross section and its strain and stress profiles

Referring to the equivalent stress and strain distribution diagram shown in Figure 5-56, the internal compression forces in the FRP tube and steel or FRP bars, C, can be expressed as follows:

$$C_{tube} = \frac{1}{2} c\, E_{tc}\, \varepsilon_{Top}\, t_{FRP} \qquad 5\text{-}17$$

$$C_{bar3} = A_{b3}\, E_b\, \varepsilon_{b3} \qquad 5\text{-}18$$

With reference to Figure 5-56 the strains ε_{Top} and ε_{b1} can be computed in terms of ε_{b1} as follows:

$$\varepsilon_{Top} = \varepsilon_{b1}\left(\frac{c}{D_o - c - d}\right) \qquad 5\text{-}19$$

$$\varepsilon_{b3} = \varepsilon_{b1}\left(\frac{c-d}{D_o - c - d}\right) \qquad 5\text{-}20$$

The internal compression force in the concrete block at the top can be calculated based on an equivalent stress distribution assuming a rectangular stress block with a depth equal to some fraction of the neutral axis depth, where $a = \beta c$, and a magnitude

equal to some fraction of the concrete compressive strength, $f_{cu}^{e} = \alpha f_{cu}$, (CSA standard A23.3). α is the ratio of the assumed uniform stress in the rectangular compression block (f_{cu}^{e}) to the maximum partially confined concrete compressive strength (f_{cu}), given by

$$\alpha = 0.85 - 0.0015 f_c' \geq 0.6 \qquad 5\text{-}21$$

β is the ratio of the depth of the rectangular compression block (a) to the depth to the neutral axis (c), given by

$$\beta = 0.97 - 0.0015 f_c' \geq 0.6 \qquad 5\text{-}22$$

With reference to Figure 5-56 the area of compression segment can be computed as follows:

$$\text{Area of compression concrete segment} = 0.25 D^2 (\theta - \sin\theta \cos\theta) \qquad 5\text{-}23$$

where $\cos\theta = (1 - 2a/D)$

Location of centroid of compression segment $\overline{x}$ (from the core center 0):

$$\overline{x} = \frac{1}{3} \frac{(D \sin^3\theta)}{(\theta - \sin\theta \cos\theta)} \qquad 5\text{-}24$$

$$z = 0.50 D_0 - \overline{x} \qquad 5\text{-}25$$

where z is the location of centroid of compression segment from the top layer

Hence, the internal compression force in the concrete block can be expressed as follows:

$$C_c = \alpha f_{cu} \text{ x Area of concrete compression segment} \qquad 5\text{-}26$$

It is assumed that the ratio of the partially confined concrete compressive strength f_{cu}, to the confined concrete compressive strength f_{cc}' equal to ξ or can be expressed as follows:

$$C_c = \alpha f_{cu} \text{ x Area of concrete compression segment} \qquad 5\text{-}27$$

$$f_{cu} = \xi f_{cc}' \qquad 0.0 < \xi < 1.0 \qquad 5\text{-}28$$

Substituting Equation 5-28 in Equation 5-26 can lead to

$$C_c = \alpha \xi f'_{cc} \text{ x Area of concrete compression segment} \quad 5\text{-}29$$

The value of ξ presents the level of confinement gained from the interaction between FRP tube and concrete core of RCFFT beam under flexural load. Also, this value (ξ) depends on different parameters such as thickness and fibre orientation of FRP tubes, type and reinforcement ratio of internal rebars and concrete compressive strength. Strength of confined concrete f'_{cc} is related to its unconfined concrete strength and the confinement pressure from the FRP tubes. The f'_{cc} values can be presented by any model of the available confinement models in the literature, in this study the proposed confinement model Equation 5-30, of Mohamed and Masmoudi 2010 is used.

$$f'_{cc} = f'_c \left[0.7 + 2.7 \left(\frac{f_{lFRP}}{f'_c} \right)^{0.7} \right] \quad 5\text{-}30$$

$$f_{lFRP} = \frac{2t_{FRP} f_{FRPu}}{D_o} \quad 5\text{-}31$$

Where f_{lFRP} and f_{FRPu} are the FRP lateral pressure and the ultimate hoop tensile strength of the FRP tubes, respectively.

Therefore, the nominal moment strength of the beam can be determined by taking the moment of tensile and compression stress resultants of tube and bars about the compression stress resultant in concrete.

$$M_{theo} = T_{bar1}(D-d-z) + T_{bar2}\left(\frac{D}{2}-z\right) + T_{tube}\left(\frac{2(D-c)}{3}+c-z\right) \quad 5\text{-}32$$
$$-C_{bar3}(z-d) - C_{tube}\left(z-\frac{c}{3}\right)$$

In fact, in the aforementioned equations there are three unknowns: strains, neutral axis depth c and ξ. As a result, the design procedure is iterative. Since the RCFFT beams of this study failed in tension due to mainly the rupture of bars and also,

observation of the failure mode indicates no compression crushing occurred at the top surface of the concrete. Hence, the analytical procedure is performed by assuming a given strain value (ε_{b1}) at the level of the bottom row of steel or FRP bars for the steel or FRP-RCFFT beams, respectively, corresponding to the required load level, (yield or ultimate). For FRP- RCFFT beams, it is assumed $\varepsilon_{b1} = \varepsilon_{Fu}$, for determining the ultimate moment, where ε_{Fu} is the ultimate strain of the FRP bars. For the steel-RCFFT beams, it is assumed $\varepsilon_{b1} = \varepsilon_y$, for determining the yield moment, where ε_y is the yield strain of the steel bars and for determining the ultimate moment, the steel tensile stress is taken as the ultimate strength f_u. On the other hand, flexural analysis of CFFT beam suggest that the neutral axis is located within a region of 0.25~0.4D, (Ahmad et al. 2005 a and b; Qasrawi and Fam 2008). Therefore, the analytical procedure for the RCFFT beams is performed by assuming the neutral axis depth (c) equal to ηD, where η is taken in range between 0.25 to 0.40. The strain values for bars, tube and concrete at any level are determined based on the assumption of a linear strain distribution along the depth of the beam between the extreme compression fibres and the tensile FRP tube reinforcement. The moment capacities of the RCFFT beams are determined for all values of η. Then the experimental bending moments of RCFFT beams are compared with the theoretical. Then, the optimum value of η is obtained to correlate the theoretical with experimental bending moments for the steel and FRP-RCFFT beams. Figure 5-57.a shows the variation $M_{u(exp)}/M_{u(theo)}$ for the FRP-RCFFT beams. Figure 5-57.b shows the variation $M_{y(exp)}/M_{y(theo)}$ and $M_{u(exp)}/M_{u(theo)}$ for the steel-RCFFT beams. In Table 5-9 the ratios of $M_{u(exp)}/M_{u(theo)}$, $M_{y(exp)}/M_{y(theo)}$, Average and Standard Deviation are provided for the different values of η. The interpretation of these numbers is as follows: If the $M_{u(exp)}/M_{u(theo)}$ is greater than one, the equations are conservative, the theory underestimates the actual capacity of the beams. Conversely, if $M_{u(exp)}/M_{u(theo)}$ is less than one the results are unconservative.

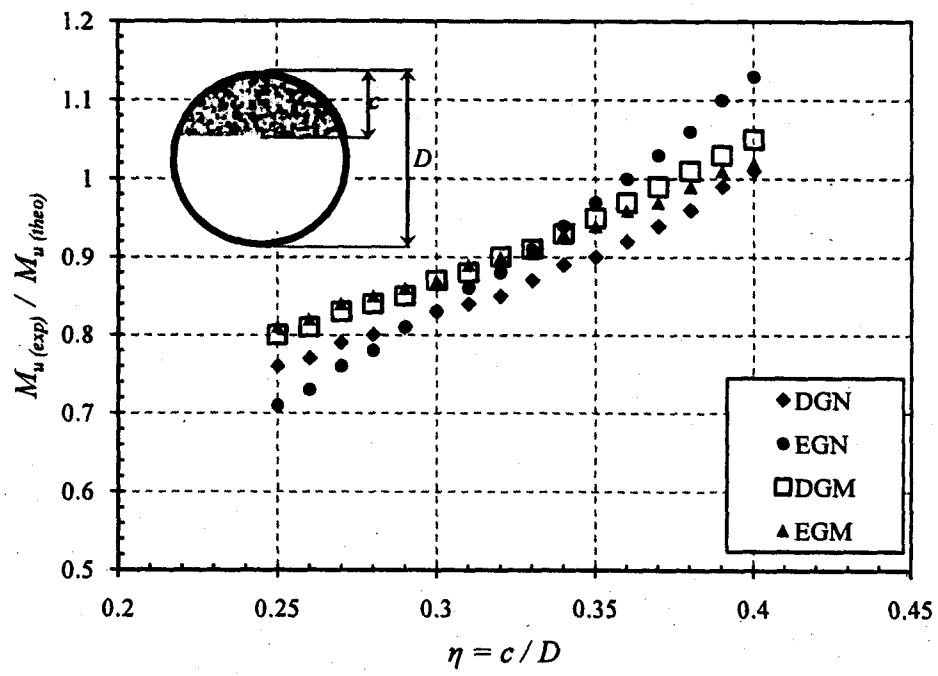

(a) FRP-RCFFT beams

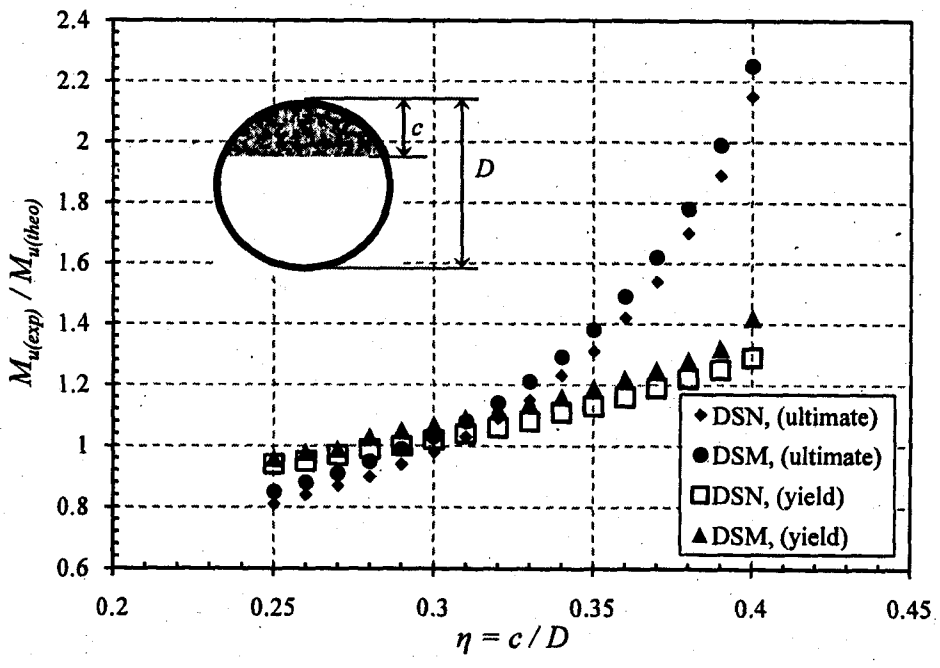

(b) Steel-RCFFT beam

Figure 5-57 The experimental to theoretical monument ratio versus the neutral axis depth ratio

Table 5-9 The theoretical results of moment capacities, η and ξ values

Specimen ID	$\eta = c/D$															
	0.25	0.26	0.27	0.28	0.29	0.30	0.31	0.32	0.33	0.34	0.35	0.36	0.37	0.38	0.39	0.40
	FRP-RCFFT Beams															
	$M_{u(exp)}/M_{u(theo)}$															
D-G-N	0.76	0.77	0.79	0.80	0.81	0.83	0.84	0.85	0.87	0.89	0.90	0.92	0.94	0.96	0.99	1.01
E-G-N	0.71	0.73	0.76	0.78	0.81	0.83	0.86	0.88	0.91	0.94	0.97	1.00	1.03	1.06	1.10	1.13
D-G-M	0.80	0.81	0.83	0.84	0.85	0.87	0.88	0.90	0.91	0.93	0.95	0.97	0.99	1.01	1.03	1.05
E-G-M	0.81	0.82	0.84	0.85	0.86	0.87	0.89	0.90	0.91	0.93	0.94	0.96	0.97	0.99	1.01	1.02
Average	0.77	0.78	0.81	0.82	0.83	0.85	0.87	0.88	0.90	0.92	0.94	0.96	0.98	1.01	1.03	1.05
SD	0.05	0.04	0.04	0.03	0.03	0.02	0.02	0.02	0.02	0.02	0.03	0.03	0.04	0.04	0.05	0.05
	$\xi = f_{cu}/f'_{cc}$ $\quad 0.0 < \xi < 1.0$															
D-G-N	1.22	1.13	1.04	0.96	0.89	0.82	0.76	0.70	0.65	0.60	0.55	0.50	0.46	0.42	0.38	0.34
E-G-N	1.16	1.08	1.00	0.94	0.88	0.82	0.77	0.72	0.68	0.63	0.59	0.55	0.52	0.48	0.45	0.42
D-G-M	1.01	0.94	0.88	0.82	0.76	0.71	0.66	0.62	0.57	0.53	0.50	0.46	0.43	0.39	0.36	0.33
E-G-M	0.98	0.91	0.85	0.79	0.74	0.70	0.65	0.61	0.57	0.54	0.50	0.47	0.44	0.41	0.38	0.35
Average	1.09	1.02	0.94	0.88	0.82	0.76	0.71	0.66	0.62	0.58	0.54	0.50	0.46	0.43	0.39	0.36
SD	0.10	0.09	0.08	0.07	0.07	0.06	0.06	0.05	0.05	0.04	0.04	0.04	0.03	0.03	0.03	0.04
	Steel-RCFFT Beams															
	1- Ultimate moment $\quad M_{u(exp)}/M_{u(theo)}$															
D-S-N	0.81	0.84	0.87	0.90	0.94	0.98	1.03	1.09	1.15	1.23	1.31	1.42	1.54	1.70	1.89	2.15
D-S-M	0.85	0.88	0.91	0.95	0.99	1.03	1.08	1.14	1.21	1.29	1.38	1.49	1.62	1.78	1.99	2.25
Average	0.83	0.86	0.89	0.93	0.97	1.01	1.06	1.12	1.18	1.26	1.35	1.46	1.58	1.74	1.94	2.20
SD	0.03	0.03	0.03	0.04	0.04	0.04	0.04	0.04	0.04	0.04	0.05	0.05	0.06	0.06	0.07	0.07
	$\xi = f_{cu}/f'_{cc}$ $\quad 0.0 < \xi < 1.0$															
D-S-N	1.82	1.58	1.36	1.15	0.97	0.79	0.62	0.47	0.32	0.18	0.05	-0.07	-0.19	-0.31	-0.43	-0.54
D-S-M	1.91	1.66	1.43	1.21	1.01	0.83	0.66	0.49	0.34	0.19	0.06	-0.08	-0.20	-0.33	-0.45	-0.56
Average	1.86	1.62	1.39	1.18	0.99	0.81	0.64	0.48	0.33	0.19	0.05	-0.08	-0.20	-0.32	-0.44	-0.55
SD	0.05	0.04	0.03	0.03	0.02	0.02	0.02	0.01	0.01	0.00	0.00	0.00	0.00	0.01	0.01	0.01
	2- Yield moment $\quad M_{y(exp)}/M_{y(theo)}$															
D-S-N	0.94	0.95	0.97	0.99	1.00	1.02	1.04	1.06	1.08	1.11	1.13	1.16	1.19	1.22	1.25	1.29
D-S-M	0.96	0.98	0.99	1.03	1.05	1.07	1.09	1.12	1.14	1.16	1.19	1.22	1.25	1.28	1.32	1.42
Average	0.95	0.97	0.98	1.01	1.03	1.05	1.07	1.09	1.11	1.14	1.16	1.19	1.22	1.25	1.28	1.36
SD	0.02	0.02	0.01	0.03	0.04	0.04	0.04	0.04	0.04	0.04	0.04	0.04	0.04	0.04	0.04	0.09
	$\xi = f_{cu}/f'_{cc}$ $\quad 0.0 < \xi < 1.0$															
D-S-N	0.80	0.73	0.68	0.63	0.58	0.53	0.49	0.45	0.42	0.38	0.35	0.32	0.29	0.27	0.24	0.22
D-S-M	0.84	0.77	0.71	0.66	0.61	0.56	0.52	0.48	0.44	0.40	0.37	0.34	0.31	0.28	0.25	0.23
Average	0.82	0.75	0.69	0.65	0.59	0.55	0.50	0.46	0.43	0.38	0.35	0.33	0.30	0.28	0.25	0.22
SD	0.02	0.02	0.02	0.02	0.01	0.01	0.01	0.01	0.01	0.01	0.01	0.01	0.01	0.01	0.01	0.01

Equating the compressive and tensile forces Equation 5-33, and taking into account Equation 5-12 to Equation 5-29, the values of ξ are determined for the different values of η as shown in Table 5-9.

$$T_{bar1} + T_{bar2} + T_{tube} = C_c + C_{bar3} + C_{tube} \quad 5\text{-}33$$

Table 5-9 shows that a strong correlation is observed between the theoretical predictions and the test results for the ultimate moment capacity of FRP-RCFFT beams when the values of η are in the range 0.35 to 0.40. The corresponding $M_{u(exp)}/M_{u(theo)}$ ratios and ξ values are on average in the range 0.94 ± 0.03 to 1.05 ± 0.05 and 0.50 ± 0.04 to 0.36 ± 0.04, respectively. For the steel-RCFFT beams the experimental test results at ultimate are close to the theoretical predictions when the values of η are in the range 0.30 to 0.33. The corresponding $M_{u(exp)}/M_{u(theo)}$ ratios and ξ values are on average in the range 1.01 ± 0.04 to 1.06 ± 0.04 and 0.81 ± 0.04 to 0.64 ± 0.04, respectively. On the other hand, the $M_{y(exp)}/M_{y(theo)}$ ratios are correlated on average in the range 0.97 ± 0.01 to 1.09 ± 0.04 when the values of η are in the range 0.28 to 0.33.

The neutral axis depth is a function of the reinforcement ratio in the cross-section and the varying stiffness of the reinforcing bars (steel or FRP Bars) under increased strain. Under-reinforced and over-reinforced section conditions, with respect to the balanced condition, will result in different calculations to determine the neutral axis depth at ultimate failure load. Based on the statistical analysis of the test results and theoretical predictions of the moment capacities, two empirical equations are introduced based on the reinforcement index ψ of the tested RCFFT beams for determining the ratio (η) of the neutral axis depth (c) to the concrete core depth (D) depth as follows:

For under-reinforced FRP-RCFFT beams cross section condition:

$$\eta = c/D = 0.39 - 0.001\psi \quad 5\text{-}34$$

For under-reinforced steel-RCFFT beams cross section condition:

$$\eta = c/D = 0.33 - 0.0033\psi \quad 5\text{-}35$$

$$\psi = \rho_{tube}\frac{F_{u,tube}}{f'_c} + \rho_{bar}\frac{F_{u,bar}}{f'_c} \quad 5\text{-}36$$

where $F_{u,tube}$ is the ultimate tensile strength of the FRP tube in the axial direction; $F_{u,bar}$ is the ultimate tensile strength of internal reinforcement (steel or FRP bars).

The FRP tube reinforcement ratio ρ_{tube} is the ratio of the cross-sectional area of the GFRP tube to the cross sectional area of the concrete core, and is given by:

$$\rho_{tube} = \frac{4t_{FRP}}{D} \qquad 5\text{-}37$$

The internal bars reinforcement ratio, ρ_{bar} is defined as the ratio of the area of all the internal reinforcing bars $A_{bar,total}$, to the area of the concrete core, and is given by:

$$\rho_{bar} = \frac{A_{bar,total}}{\pi D^2/4} \qquad 5\text{-}38$$

It is interesting to mention that the concrete compressive strengths f_{cu} at ultimate for the FRP-RCFFT beams are on average 45% the confined concrete compressive strength f'_{cc}, also the corresponding values for the steel-RCFFT beams at yield load level and ultimate are approximately equal to 65%. These results confirm that the FRP tubes partially confined the concrete core of the tested RCFFT beams. Also, the steel-RCFFT beams are reached to a higher level of the confinement than the FRP-RCFFT beams at ultimate. This is attributed to the increase in the load carrying capacities of the steel-RCFFT beams as compared to the FRP-RCFFT beams, which in turn allow for higher activation of the FRP tube to confine the concrete core of the beams.

The previous traditional procedures were found to be acceptable for predicting the ultimate and yield moments capacities of the under-reinforced FRP or steel-RCFFT beams cross section condition, refer to Figure 5-58. The accuracy of the theoretical analysis procedures pertains good agreement with measured values. The strain at the bottom steel or FRP bars is used as a reference and the neutral axis depth ratio is determined using the two empirical equations. They are simple to use and provide prediction than the analytical model available in the literature. However, more studies are needed to verify the predictive equations of the neutral axis depth ratio, concrete compressive stress and strain at ultimate for FRP or steel-RCFFT beams with the under and over- reinforced cross section condition.

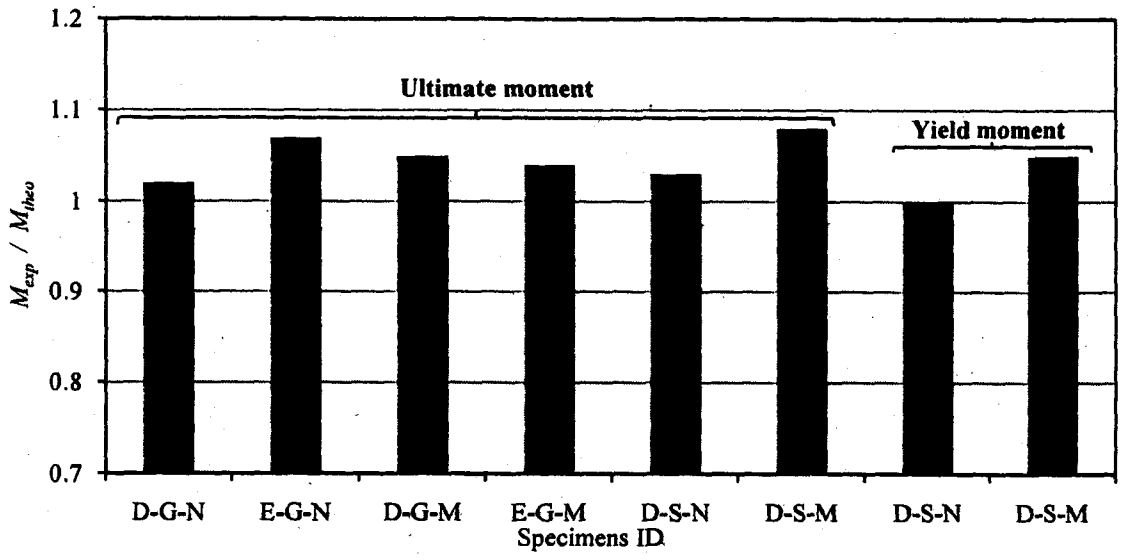

Figure 5-58 The experimental to the theoretical moment capacities of RCFFT beams

5.6.3 Defection calculation of steel and FRP-RCFFT beams

This study evaluates the deflection behaviour of simply supported normal-strength concrete RCFFT beams subjected to four-point monotonic loading and reinforced with steel or GFRP bars. In the following section, it can be considered the first attempt to develop design equations for predicting the load-deflection curve of RCFFT beams. This study is intended to review and verify the applicability of the North American code provisions and the available equations in the literature to predict deflection of RCFFT beams. The Branson's equation for the effective moment of inertia of RC structures is modified and new equations are developed to predict deflection of CFFT beams reinforced with steel or FRP bars. However, it should be noted that these equations were developed based on the limited test data of this study. The equations might be revised when more data and research works becomes available.

Unlike steel or FRP-RC structures, RCFFT members can exhibit additional flexural capacity in the post-yielding or cracking stages. This is attributed to the contribution of FRP tube in confining the concrete core and acting as flexural reinforcement in the axial directions. This makes the existing models of the FRP or steel-RC inapplicable in case of RCFFT members. Therefore, some analytical models using a computer program have

been developed to predict the flexural behaviour, the moment-curvature and the load-deflection of CFFT (Qasrawi and Fam 2008; Fam and Son 2008; Mandal and Fam 2006; Cole and Fam 2006; Cole 2005; Mandal 2004). These models are based on strain compatibility, internal force equilibrium, and material constitutive relationships. The forces within the CFFT cross-section are calculated by analytically integrating the stresses over the area for each individual material. Also, these models accounts for the slight non-linearity of the FRP tube arising from progressive laminate failure and concrete non-linearity. Despite of these analytical models predict well the flexural behaviour of the CFFT beams, however it is not easy to use because it is based on a computer program and require some sophisticated calculation procedures. Up to date, no simplified method had been validated to evaluate the deflections of CFFT elements. Accordingly, there is still a demand for simplified and more convenient procedures for predicting the flexural-deflection behaviour of CFFT beams.

5.6.3.1 Review of deflection formulas for steel and FRP-RC members

The flexural component of the deflection for simply-supported RCFFT beam of span L subjected to four point bending loads can be calculated with the usual deflection Equation 5-39 derived from linear elastic analysis as follows:

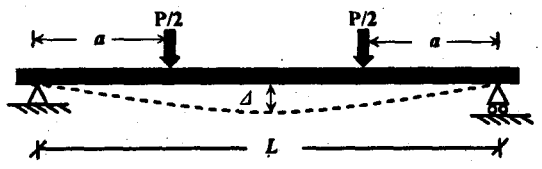

Figure 5-59 Deflected shape of simply supported beam subjected to two equal concentrated loads

$$\Delta = \frac{Pa}{48E_cI_e}(3L^2 - 4a^2) \qquad 5\text{-}39$$

Where P is the total applied load divided into two concentrated loads each applied at distance a from the support, E_c is the modulus of elasticity of concrete and I_e if the effective moment of inertia of the beam cross section. The moment of inertia, in addition

to the modulus of elasticity, determines the stiffness of the flexural members. At the pre-cracking stage ($M_a \leq M_{cr}$), the applied moment M_a is less than the cracking moment M_{cr}. This stage is characterized by the elastic behaviour and no cracks can be initiated in concrete. Accordingly, the effective moment of inertia may be considered equivalent to the moment of inertia of the transformed uncracked section I_g.

After cracking ($M_a \geq M_{cr}$), the North American codes, the ACI building code: ACI 318-08 and the Canadian Concrete Design Standard: CSA A23.3-04, and elsewhere (SAA 2001), deflection calculation of flexural members is mainly based on using the average effective moment of inertia, I_e, given by the well-known equation developed by Branson in 1965, (Branson 1977).

$$I_e = \left[\frac{M_{cr}}{M_a}\right]^m I_g + \left[1 - \left(\frac{M_{cr}}{M_a}\right)^m\right] I_{cr} \leq I_g \qquad 5\text{-}40$$

where I_{cr} = moment of inertia of the fully cracked transformed cross section and the power m equals to 3.

The average effective moment of inertia, I_e, Equation 5-20 is based on semi-empirical considerations, and despite some doubt about its applicability to steel-reinforced concrete members subjected to different loading and boundary conditions, it has yielded satisfactory results in most practical applications over the years. According to this equation and with increasing the load on the beam, I_e is gradually degraded from I_g to I_{cr}, dependent on the ratio of cracking moment M_{cr} to the applied moment M_a.

Extensive research works have consistently demonstrated that the Branson's equation does not predict deflection well for both RC beams having low reinforcement ratios and FRP reinforced concrete beams (Rafi and Nadjai 2009; Bischoff and Scanlon 2007; Gilbert 2006; Mota et al. 2006; Bischoff 2005; Toutanji and Deng 2003; Bischoff 2005; Yost et al. 2003; Abdalla 2002; Toutanji and Saafi 2000; Alsayed et al. 2000; Gilbert 1999; Masmoudi et al. 1998; Benmokrane, Chaallal and Masmoudi 1996). On the other hand, it has been derived that the Branson's equation does not address post-yielding deflection for FRP-strengthened RC beams (Charkas et al. 2003; El-Mihilmy and Tedesco 2000).

The first attempt had been introduced by Benmokrane, Chaallal and Masmoudi in 1996 to improve the performance of the Branson's equation. Two factors (α and β) were developed through a comprehensive experimental program on FRP-RC beams to modify the Branson's equation, as given by

$$I_e = \left[\frac{M_{cr}}{M_a}\right]^3 \frac{I_g}{\beta} + \alpha I_{cr}\left[1-\left(\frac{M_{cr}}{M_a}\right)^3\right] \le I_g \qquad 5\text{-}41$$

where α and β are equal to 0.84 and 7, respectively.

Masmoudi, Thériault and Benmokrane 1998 continued to investigate experimentally the deflection behaviour of FRP-RC beams, and then they introduced a new modification the Branson's equation, as given by

$$I_e = \beta\left[\frac{M_{cr}}{M_a}\right]^3 I_g + \left[1-\left(\frac{M_{cr}}{M_a}\right)^3\right] I_{cr} \le I_g \qquad 5\text{-}42$$

where β is a reduction coefficient equal to 0.6.

In 2000, Toutanji and Saafi showed that the order of the Branson's equation depends on both the modulus of elasticity of FRP, as well as the reinforcement ratio. Accordingly, Toutanji and Saafi (2000) recommended the following equation for deflection calculation of FRP-RC beams:

$$I_e = \left[\frac{M_{cr}}{M_a}\right]^m I_g + \left[1-\left(\frac{M_{cr}}{M_a}\right)^m\right] I_{cr} \le I_g \qquad 5\text{-}43$$

where

$$\text{For} \quad \frac{E_{FRP}}{Es}\rho_{FRP} < 0.3 \qquad m = 6 - 10\frac{E_{FRP}}{Es}\rho_{FRP}$$

$$\text{For} \quad \frac{E_{FRP}}{Es}\rho_{FRP} \ge 0.3 \qquad m = 3.0$$

where E_{FRP} is the modulus of elasticity of GFRP bar, E_s Es is the modulus of elasticity of steel, and ρ_{FRP} is the GFRP longitudinal reinforcement ratio in percentage.

In 2001, a new form of the effective moment of inertia I_e, was introduced in the ISIS Design Manual M03-01 The new equation is different in form as compared to the Branson's equation, as given by

$$I_e = \frac{I_T I_{cr}}{I_{cr} + \left[1 - 0.5\left(\frac{M_{cr}}{M_a}\right)^2\right]\left(I_g - I_{cr}\right)} \leq I_g \qquad 5\text{-}44$$

where I_T = uncracked moment of inertia of the section transformed to concrete.

The ACI committee (ACI 440.1R-03) has proposed a modified expression for the effective moment of inertia of the Branson's equation for RC beams reinforced with FRP bars.

$$I_e = \left[\frac{M_{cr}}{M_a}\right]^3 \beta I_g + \left[1 - \left(\frac{M_{cr}}{M_a}\right)^3\right] I_{cr} \leq I_g \qquad 5\text{-}45$$

The factor β is a reduction coefficient related to the reduced tension stiffening exhibited by FRP-reinforced members, given by

$$\beta = \alpha\left(\frac{E_F}{E_S} + 1\right) \leq 1.0$$

where α= bond dependent coefficient (until more data become available, α=0.5); E_F and E_s are the modulus of elasticity of the FRP and steel reinforcements, respectively.

Recently, research has demonstrated that the degree of tension stiffening is affected by the amount and stiffness of the flexural reinforcement (Toutanji and Saafi 2000; Yost et al. 2003). Based on an evaluation of experimental results from several studies, the ACI committee (ACI 440.1R-06) has proposed the following simple relationship for β_d

$$I_e = \left[\frac{M_{cr}}{M_a}\right]^3 \beta_d I_g + \left[1 - \left(\frac{M_{cr}}{M_a}\right)^3\right] I_{cr} \leq I_g \qquad 5\text{-}46$$

where $\beta_d = \frac{1}{5}\left(\frac{\rho}{\rho_b}\right) \leq 1.0$

where ρ and ρ_b are the actual and balanced reinforcement ratio, respectively.

5.6.3.2 Evaluation of moment of inertia equations for deflection prediction of RCFFT beams

The values of the experimental moment of inertia I_{exp} for the tested RCFFT beams are determined based on the laboratory-measured applied loads P_{exp} and the corresponding center-span deflections Δ_{exp} using the following equation:

$$I_{exp} = \frac{P_{exp} a}{48 E_c \Delta_{exp}} (3L^2 - 4a^2) \qquad 5\text{-}47$$

The values of the cracking moments M_{cr} and gross moment of inertia I_g for the tested beams are calculated using the previous Equations 5-2 and 5-3, respectively. Also, the transformed cracked-section moment of inertia I_{cr} is determined using the proposed Equations 5-34 and 5-35 for the neutral axis depth ratio, taking into account the contribution of the internal reinforcing bars and the FRP tube in the tension and compression sides.

A comparison of the experimental I_e/I_g values, which were computed using the recorded deflection data and those predicted using the Branson's equation (ACI 318-08), has been plotted in Figure 5-60.a and Figure 5-60.b, versus M_a/M_{cr} for the tested steel-RCFFT beams, DSN and DSM, respectively. It can be seen that Branson's equation gives a response that is obviously too less stiff of these beams. On the other hand, Figure 5-61 presents experimental and theoretical predictions of I_e/I_g versus M_a/M_{cr} relationships for the four tested FRP-RCFFT beams, DGN, EGN, DGM and EGM. The theoretical predictions of I_e are determined using five selected equations for FRP-RC beams, which are presented in the previous section, ACI 318-08 (Branson's equation); ACI 440.1R-06; ISIS 2001; Masmoudi et al. 1998; Benmokran et al. 1996.

It has been observed that all the aforementioned equations does not predict deflection well of the FRP-RCFFT beams. All the former equations had been modified to account for the nature of the FRP reinforcement that exhibited larger deformation than the steel reinforcement. However, in case of steel or FRP-RCFFT members, the behaviour under the flexural load is significantly different than that of steel or FRP RC

members. Again, this is attributed to the confinement of the concrete core and the axial contribution of the FRP tube which in turn enhance the overall flexural behaviour and improve the tension stiffening of RCFFT beams. Therefore, the tension stiffening predicted for steel or FRP-RCFFT beams using the former equations (steel or FRP-RC member) is underestimated and hence the predicted deflections are overestimated. In the following section, the Branson's equation will be modified to account for the tension stiffening of the steel and FRP-RCFFT beams. The basic form of the effective moment of inertia equation should remain as close to the original Branson's equation as possible, because it is easy to use and designers is familiar with it, (Al-Sayed et al. 2000).

5.6.3.3 Modified Branson's equation for steel-RCFFT beams

It can be seen from Figure 5-60 (a) and (b) that the experimental I_e/I_g versus M_a/M_{cr} relationship is divided into four stages: (a) pre-cracking; (b) cracking; (c) post-yielding (d) post-cracking.

(a) Pre-cracking stage ($M_a \le M_{cr}$)

This stage is characterized with its elastic behaviour since no cracks initiated in concrete yet. Accordingly, the effective moment of inertia I_e can be considered equal to I_g.

(b) Cracking stage $M_{cr} \le M_a \le M_y$

At the beginning of this stage, the first crack initiated and the concrete in the tensile side cracks suddenly. The effective moment of inertia degraded rapidly but it is still higher than the cracking moment of inertia I_{cr}, due to tension stiffening effect. As it is evident from Figure 19.a and b, where the experimental I_e/I_g curve is at the upper side from the horizontal line I_{cr}/I_g. Based on the experimental data obtained for this stage, it was found that the basic form of the effective moment of inertia of Branson's equation could be predicted well the experimental I_e/I_g, if the power m is considered to be equal to 0.6, as follows:

$$I_e = \left[\frac{M_{cr}}{M_a}\right]^{0.6} I_g + \left[1 - \left(\frac{M_{cr}}{M_a}\right)^{0.6}\right] I_{cr} \le I_g \qquad 5\text{-}48$$

(b) Post-cracking stage $M_y \le M_a \le 0.85M_u$

While conventionally reinforced concrete beams at this stage are considered to have reached ultimate load limit, steel-RCFFT beam exhibited significantly additional load capacity. The increase in the load carrying capacity after yielding depends on the steel reinforcement ratio, FRP tube strength and stiffness in the axial and hoop direction. The ratio between the ultimate moment and the yield moment M_u/M_y for the tested steel-RCFFT beams of this study, DSN and DSM is on average equal to 2. The same ratio for reinforced concrete beams strengthened with FRP can be achieved. However, the ratio between the ultimate moment and the yield moment M_u/M_y for a conventionally singly reinforced section with f'_c less than 35 MPa and reinforcement ratio less than 0.02 is approximately 1.06 (El-Mihilmy and Tedesco 2000; Park and Pauley 1975). This confirms that the significant contribution of the FRP tube to increase the strength and improve the flexural behaviour of steel- RCFFT beams in the post-yielding as well as in the post cracking stages. It is observed that the effective moment of inertia I_e degraded linearly and become lower than the cracking moment of inertia I_{cr}. Since the Branson's equation is based on I_e should be higher than I_{cr}. Therefore, the Branson's equation will not be valid for this stage, and an alternative procedure for calculation deflection should be developed.

New proposed equation for the effective moment of inertia I_e, is suggested based on the regression analysis of the experimental data of I_e/I_g versus M_a/M_{cr} for this stage, as follows:

$$I_e = I_g\left(1.5-0.15\frac{M_a}{M_{cr}}\right) \qquad 5\text{-}49$$

Figure 5-60 shows that the predictions of I_e/I_g in the cracking stages ($M_{cr} \le M_a \le M_y$) using the modified Branson's Equation 5-48 and in the post cracking stages ($M_y \le M_a \le 0.85M_u$) using the new proposed Equation 5-49 are in a good agreement with the experimental values.

5.6.3.4 Modified Branson's equation for FRP-RCFFT beams

Figure 5-61 shows that the effective moment of inertia degraded gradually but it is still higher than the cracking moment of inertia I_{cr}, up to the failure of the beams. However, it is observed that the original Branson's equation with the power m=3 underestimate the effective moment of inertia for four RCFFT beams reinforced with GFRP bars. In addition, the experimental and theoretical curves are parallel. This means that the exponent m should be less than 3. The experimental test results for the four FRP-RCFFT beams that confined with two different types of FRP tubes (D and E) show that the effect of FRP tube parameters should be incorporated in the exponent m. Based on the experimental data obtained in this study, a modified expression for the moment of inertia of simply supported CFFT beams reinforced with GFRP rebars is introduced. To keep the form of the Branson's equation with minimum modification, however, the incorporation of the effect of FRP tube parameters and the properties of concrete used in the order m are included, as follows:

(a) Pre-cracking stage ($M_a \le M_{cr}$)

$$I_e = I_g \tag{5-50}$$

(b) Cracking stage ($M_a \ge M_{cr}$)

$$I_e = \left[\frac{M_{cr}}{M_a}\right]^m I_g + \left[1 - \left(\frac{M_{cr}}{M_a}\right)^m\right] I_{cr} \le I_g \tag{5-51}$$

$$m = 1.70 - 0.35\beta_t \tag{5-52}$$

$$\beta_t = \rho_{tube} \frac{(f_c'/E_c)}{(f_t/E_t)} \tag{5-53}$$

where β_t is defined as the strength-reinforcement index of the FRP tube and concrete.

Validation of the modified above equation with the present test data of the four FRP-RCFFT beams confirmed its accuracy to predict the effective moment of inertia, refer to Figure 5-61.

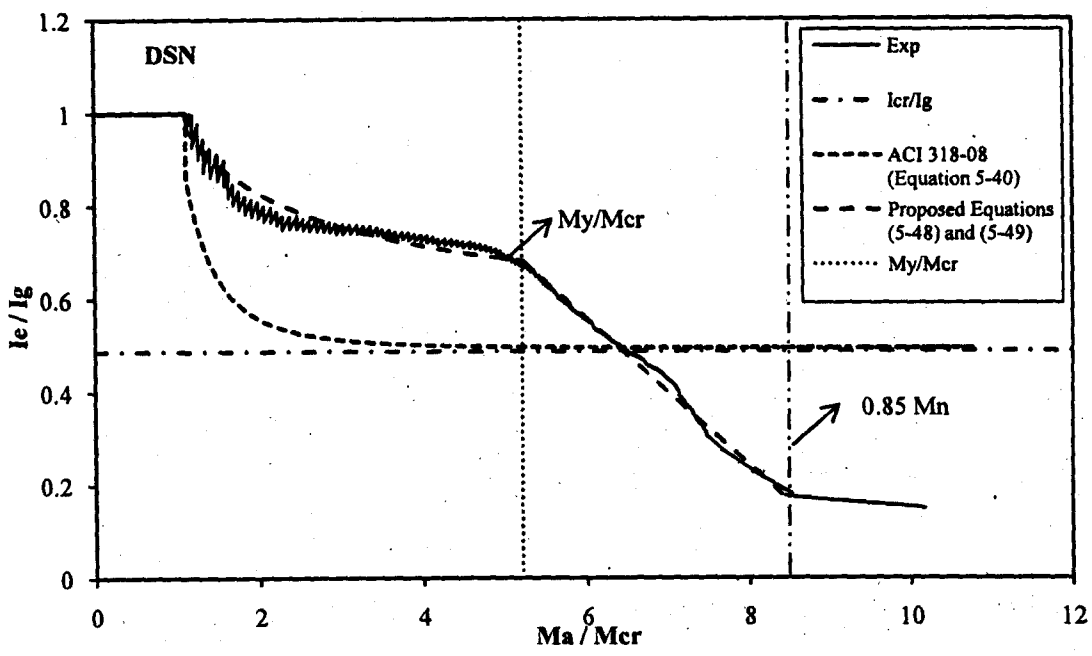

(a) Steel-RCFFT beam (DSN)

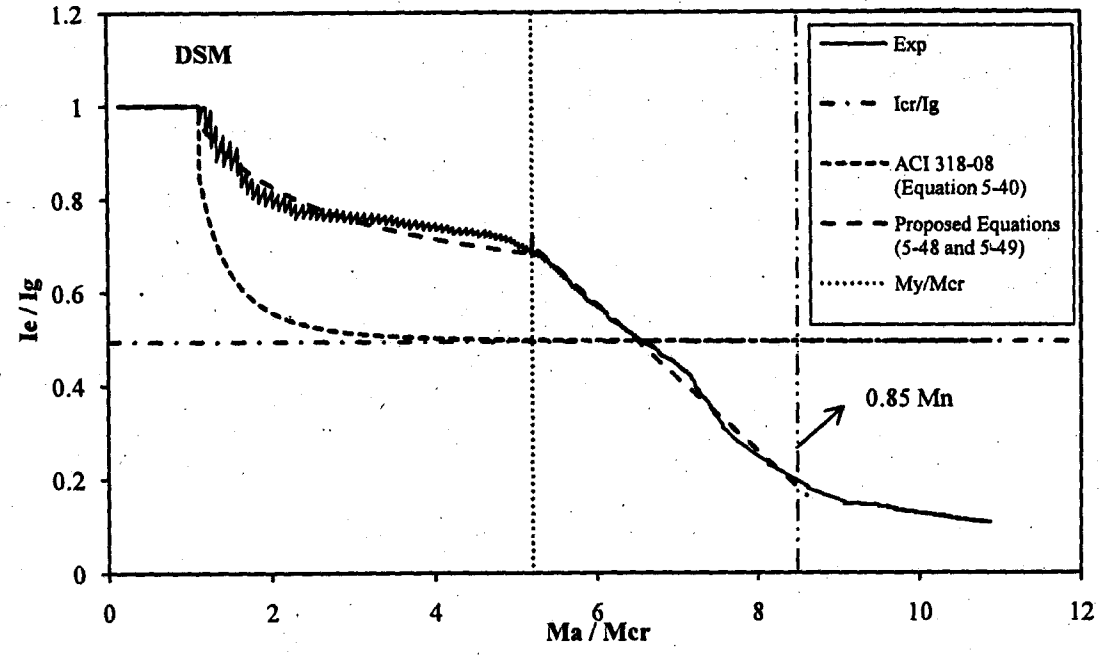

(b) Steel-RCFFT beam (DSM)

Figure 5-60 Effective to gross moment of inertia versus M_a / M_{cr}, (Steel-RCFFT beams)

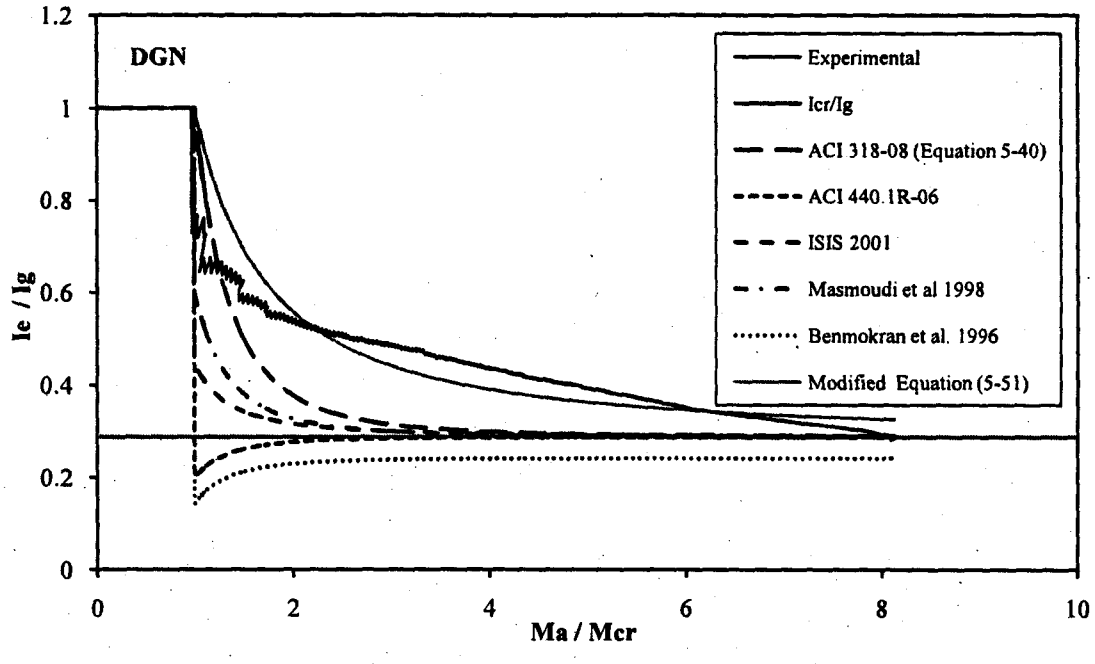

(a) FRP-RCFFT beam (DGN)

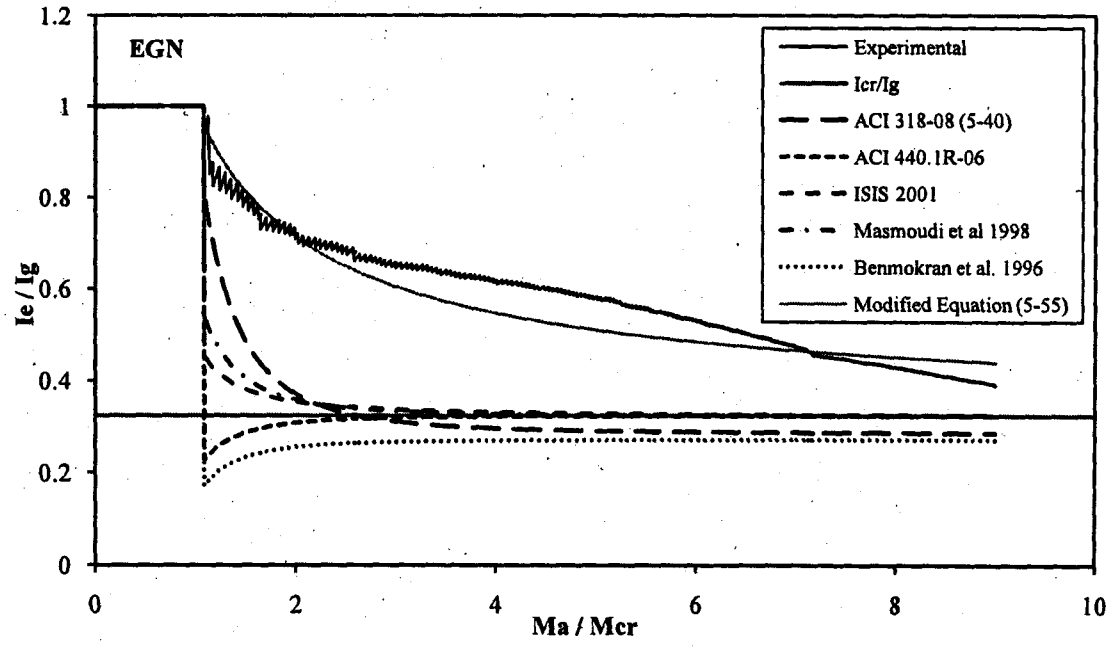

(b) FRP-RCFFT beam (EGN)

Figure 5-61 Effective to gross moment of inertia versus M_a / M_{cr}, (FRP-RCFFT beams)

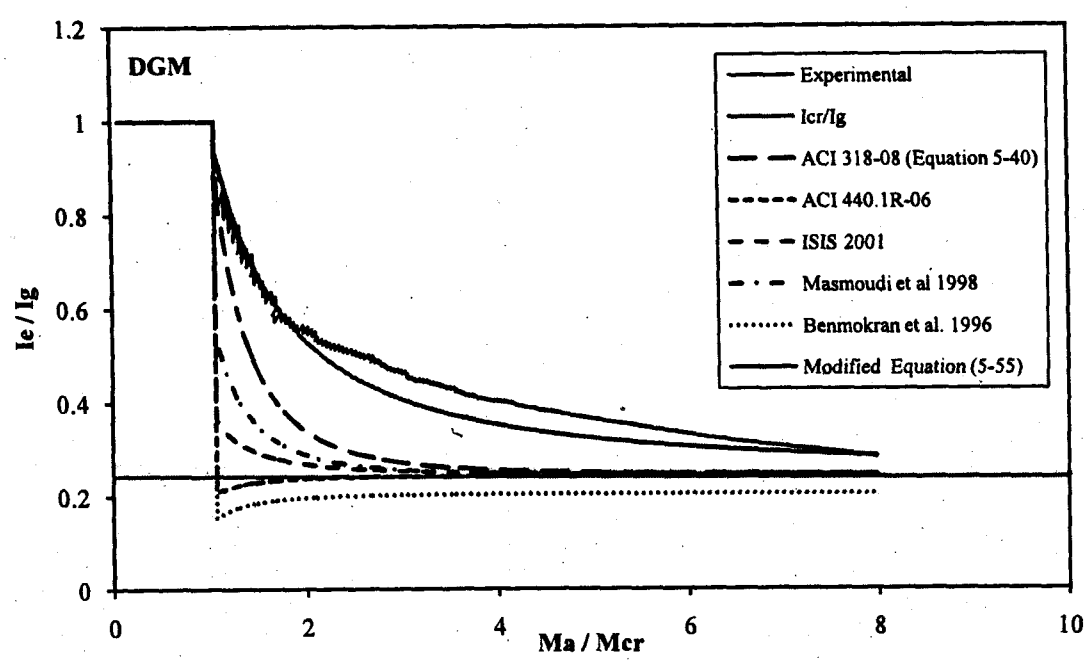

(c) FRP-RCFFT beam (DGM)

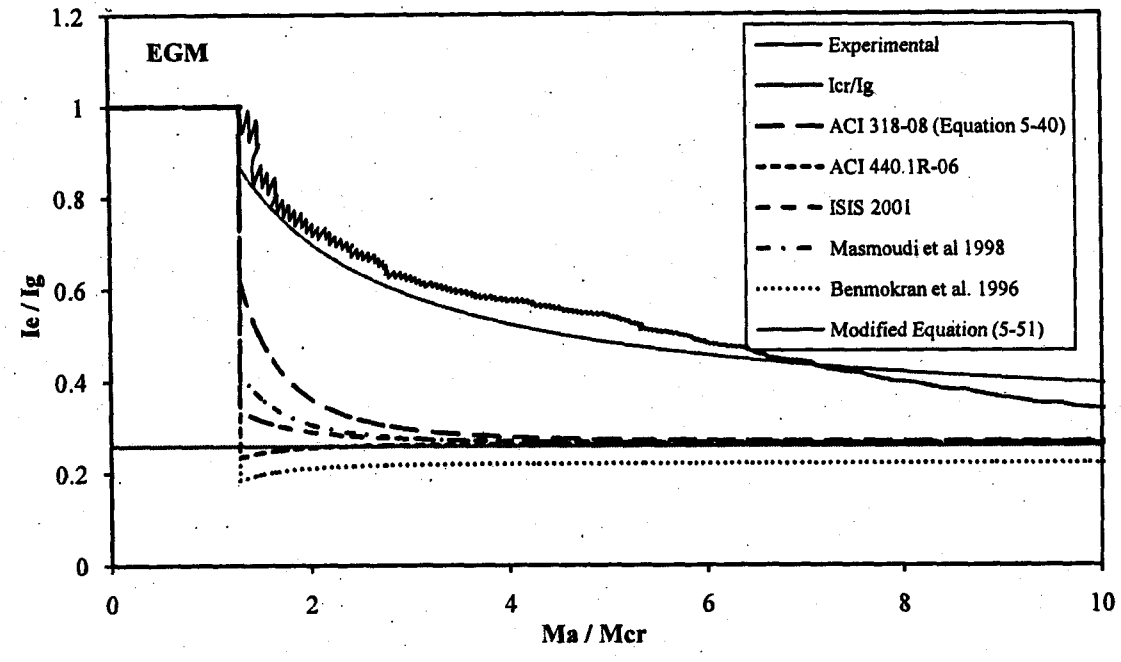

(d) FRP-RCFFT beam (EGM)

Figure 5-61 Effective to gross moment of inertia versus M_a / M_{cr}, (FRP-RCFFT beams)

5.6.3.5 Proposed equation for FRP-RCFFT beams

New proposed equation for the effective moment of inertia I_e, is suggested based on the analysis of the experimental data I_e/I_{cr} versus M_a/M_{cr} for CFFT beams reinforced with GFRP bars. Figure 5-62 shows the experimental test results for ratio of I_e/I_{cr} versus the ratio of M_a/M_{cr} for the four FRP-RCFFT beams. The curves are plotted in the cracking stage, where $M_a/M_{cr} \geq 1.0$. The regression analysis which was performed on these results suggests that the effective moment of inertia can be taken as follows:

a) Pre-cracking stage ($M_a \leq M_{cr}$)

$$I_e = I_g \qquad 5\text{-}54$$

(b) Cracking stage ($M_a \geq M_{cr}$)

$$I_e = \alpha_t I_{cr}\left(\frac{M_{cr}}{M_a}\right)^{0.4} \qquad 5\text{-}55$$

$$\alpha_t = 0.65\beta_t + 1.76 \qquad 5\text{-}56$$

where β_t is the same as given before in Equation 5-53

In the above suggested equation, the effective moment of inertia I_e is dependent on the ratio of the M_{cr}/M_a, the transformed cracked-section moment of inertia I_{cr}, and β_t as defined before. Figure 5-62 shows the value of the theoretical I_e/I_{cr} determined using the new equation (Equation 5-55) versus M_a/M_{cr} besides the experimental values. It can be seen that the I_e/I_{cr} predictions values up to the failure load are quite close to the recorded data.

5.6.3.6 Experimental verification of the modified and proposed equations

A comparison between experimental moment-mid-span deflection curves obtained in this study for the steel-RCFFT beams and those predicted by the modified Branson's Equation 5-48 and the new proposed Equation 5-49 is presented in Figure 5-63 (a and b). The moment-defection relationship is plotted up to 0.85 of the ultimate moment of the beams. The curves show that there is a good agreement between the experimental and the predicted values through the cracking and post-cracking stages. The equations are capable to predict

the deflection of steel-CFFT beams of this study in the different loading stages accounting to the pre-yielding, yielding and post yielding stages. On the other hand, Figure 5-63 (c, d, e and f) provides a comparison between the measured moments versus instantaneous deflection response at mid-span of each of the FRP-RCFFT beam with the calculated responses obtained using the modified Branson's Equation 5-51 and the new proposed Equation 5-55. For the four beams, the two equations provide a good agreement with the test results over the fall moment-deflection response. The two equations account to the change in the concrete compressive strength and the stiffness of the FRP tubes. However, in all cases, the new Equation 5-55 provides a much closer agreement with the measured deflection than the modified equation.

The effective moment of inertia of the RCFFT beams under flexural load tested in this study can be considered the first attempt in worldwide. The Branson's equation is modified to account for the increase in the tension stiffening of RCFFT beams and new equations are proposed to predict the effective moment of inertia. However, due to the relatively limited number of test specimens, the field data are still need more experimental investigations to enhance and improve the suggested modifications and the new proposed equations of this study.

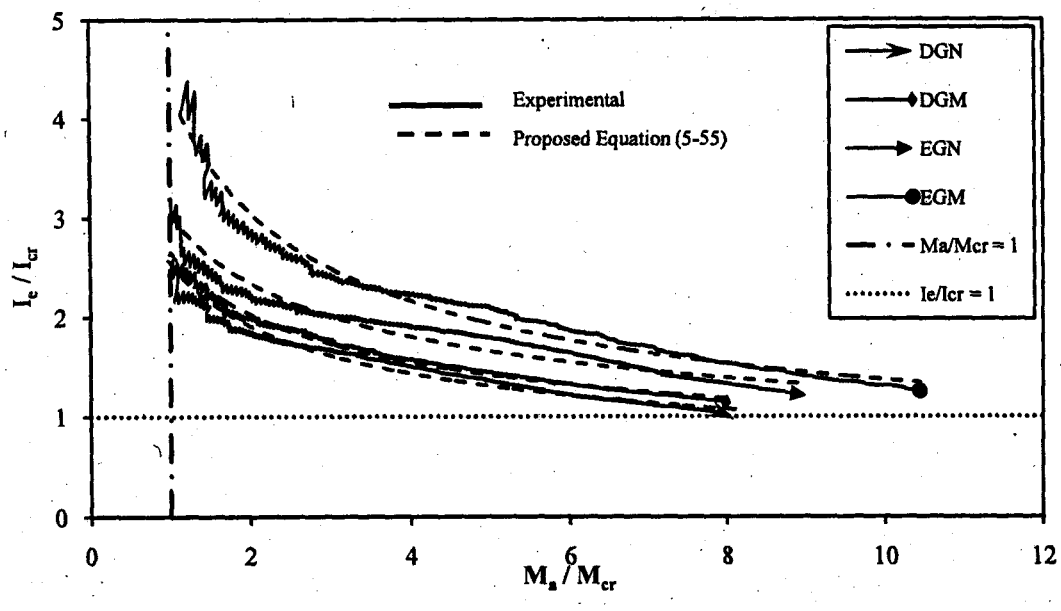

Figure 5-62 Effective to cracking moment of inertia versus M_a/M_{cr}, (FRP-RCFFT beams)

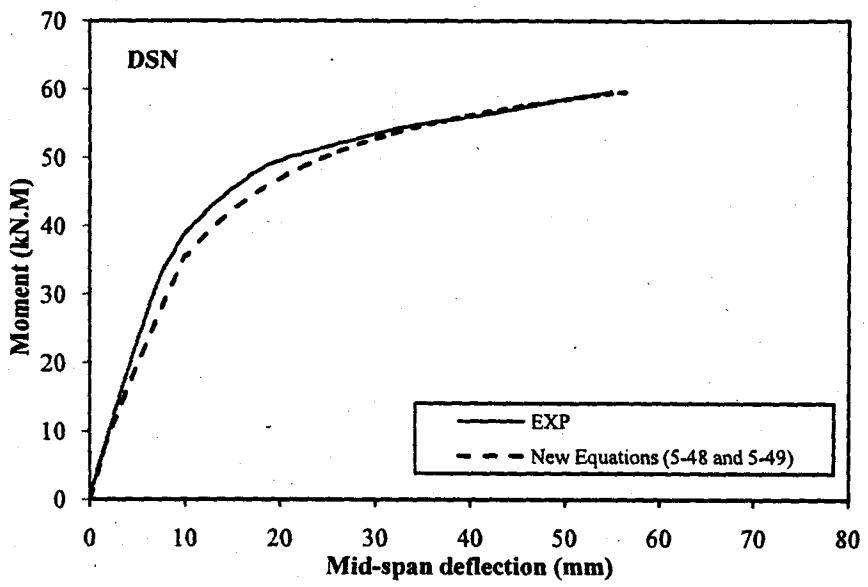

(a) Steel-RCFFT beam (DSN)

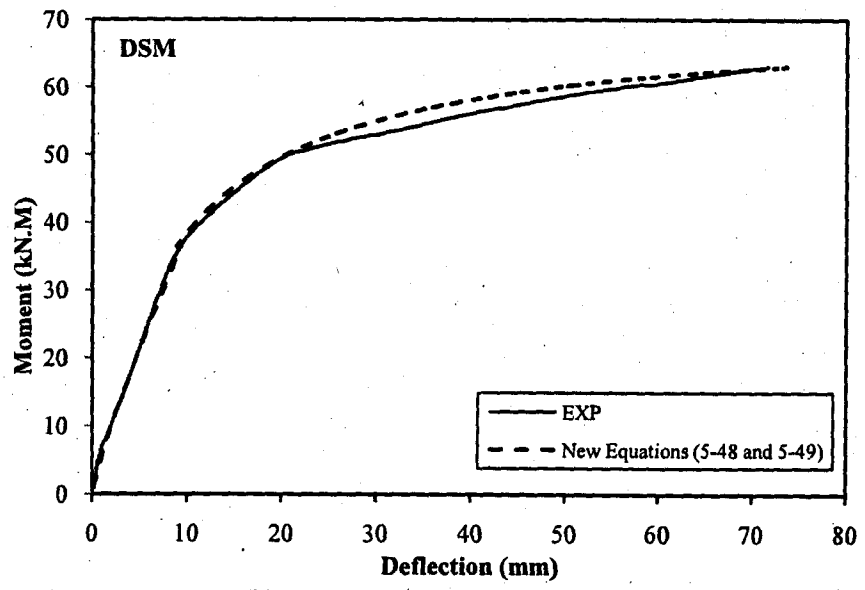

(b) Steel-RCFFT beam (DSM)

Figure 5-63 Mid-span moment versus deflection measurements and predictions

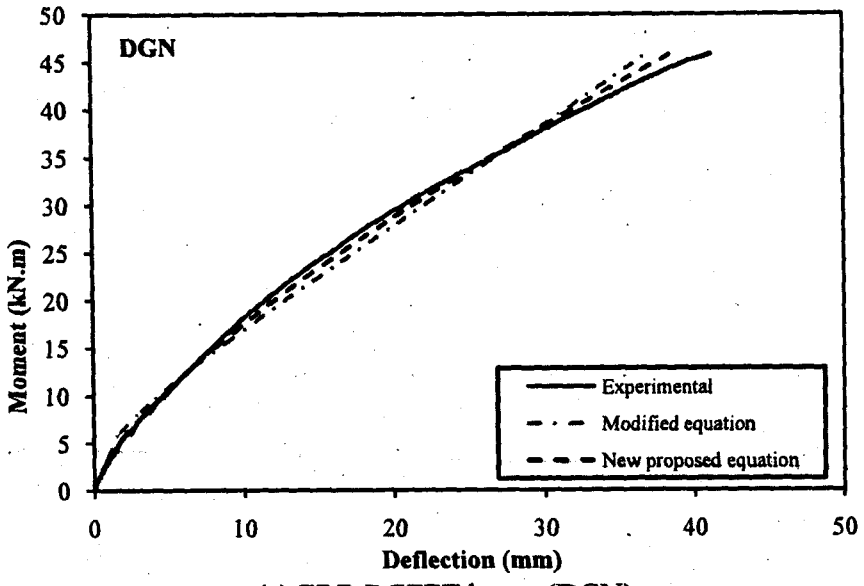

(c) FRP-RCFFT beam (DGN)

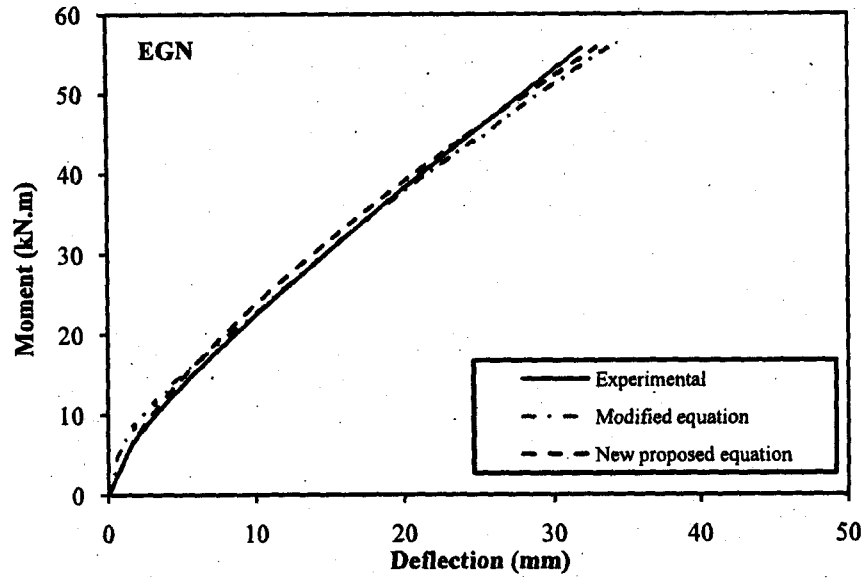

(d) FRP-RCFFT beam (EGN)

Figure 5-63 Mid-span moment versus deflection measurements and predictions

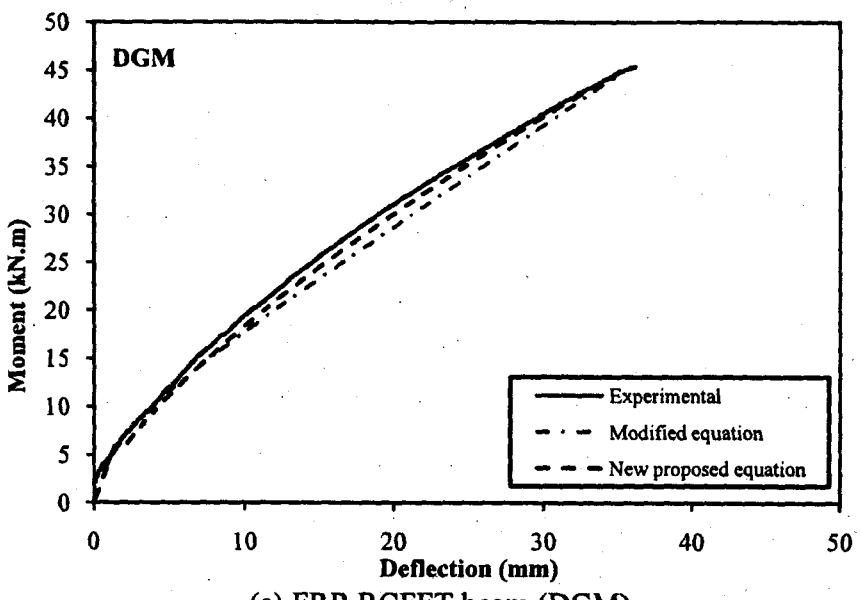

(e) FRP-RCFFT beam (DGM)

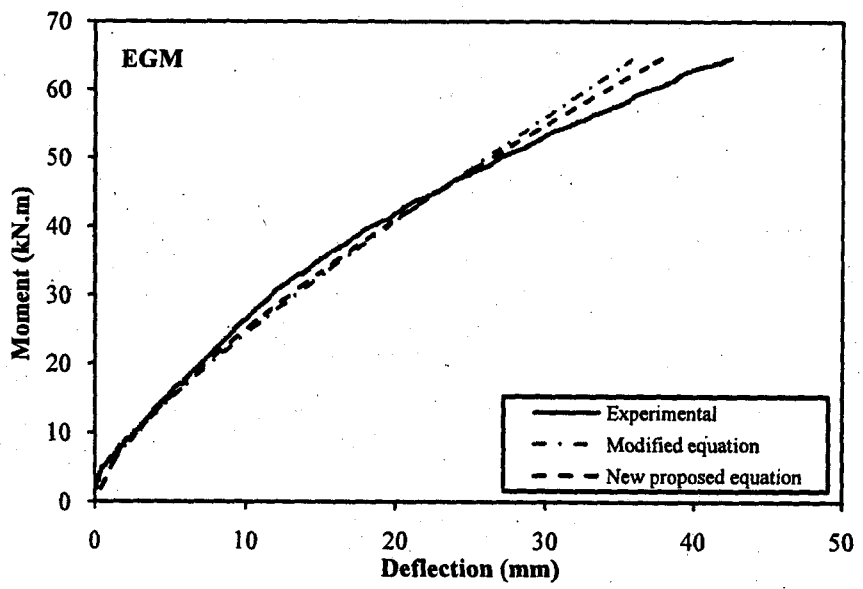

(f) FRP-RCFFT beam (EGM)

Figure 5-63 Mid-span moment versus deflection measurements and predictions

5.7 Conclusions

1. All the CFFT beams tested to failure in this study, failed in flexure. However, diagonal tension failure at the shear span and shear compression failure were the final failure modes for the RC control beams without and with spiral steel, respectively.
2. The experimental test results indicated that the beams confined by FRP tubes experienced lower deflection, higher cracking load level, higher ductility, higher stiffness and superior strength than the beam reinforced with a spiral-steel.
3. From the load-flexural hoop strain curves at the mid-span of the tested beams, it was confirmed that the FRP tubes were activated to confine the concrete core of the beam.
4. It was found that the confinement provided by the FRP tubes improved the tension stiffening of the tested beams.
5. For normal and medium strength concrete, the test results indicated that the ratio of the strength of FRP-RCFFT beams to that of steel-RCFFT beams was 60%. This ratio approximately equals the cube root of axial stiffness ratio between glass FRP and steel bars $\sqrt[3]{\rho_{fl} E_{fl} / \rho_{sl} E_{sl}}$.
6. It was observed that the effect of two types of concrete considered in this study on the flexural behaviour of tested CFFT beams was insignificant. It was observed that the strength, deflection and ductility of the CFFT beams were affected significantly by the axial stiffness of the FRP tubes.
7. The equations provided by ACI 318-08 code and ACI 440.1R-06 design guidelines for reinforced concrete structures with steel and FRP bars, respectively, and both CAN-CSA S806-02-CSA standard A23.3 and CAN-CSA S6-06 codes underestimated the modulus of rupture of RCFFT beams.
8. The conventional beam theory can be used for the analysis and design of the CFFT beams, assuming that the bond between the tube and the concrete is fully developed. The traditional procedures were found to be acceptable for predicting the ultimate and yield moments capacities of the under-reinforced FRP or steel-

RCFFT beams cross section condition. The accuracy of the theoretical analysis procedures pertained good agreement with measured values

9. The experimental results of tested RCFFT beams in four point loading bending with varying properties revealed that the current conventional or modified models available in the literature, codes (ACI 318-08; CSA A23.3-04; SAA 2001) and design guidelines (ACI 440.1R-06; ISIS 2001) for predicting the effective moment of inertia of beams reinforced by steel or FRP bars, respectively, over-estimates the deflections in these beams and therefore it needs to be revised.
10. It was observed that, in case of steel or FRP-RCFFT members, the behaviour under the flexural load was significantly different than that of steel or FRP RC members.
11. New proposed equations and a proposed modification to the equations of effective moment of inertia were presented for steel and FRP-RCFFT beams. The modification is based on experimental findings, which represent the potential of empirical and semi-empirical formulations. The proposed equations were used to calculate the effective moment of inertia of the tested RCFFT beams, which in turn used to calculate the moment-deflection response. The calculated effective moment of inertia and the moment-deflection response were compared to the experimental ones. It was observed that the proposed equations gave accurate predictions over the range of variables tested parameters to affect the moment-deflection response.

Chapter 6

Behavior of Concrete-Filled FRP Tubes Columns under Eccentric Loads

6.1 Abstract

Recently, Concrete filled fibre-reinforced polymers (FRP) tube columns (CFFT) have gained approval in civil engineering for different structural applications, such as precast piles, girders, and pier columns. A lot of the experimental and analytical research studies have been conducted to understand the behavior of CFFT under axial load. However, studying concrete columns under eccentric loading are very important for practical applications. This study experimentally investigated the performance of the CFFT columns under eccentric loads. The experimental program was conducted on five unconfined concrete cylinders, two confined CFFT cylinders (152 x 305 mm), five CFFT columns and two control steel spiral reinforcement concrete columns (152 x 912 mm). The internal diameter of the GFRP tubes which were used in this investigation was 152 mm, the tube thicknesses was 2.85 mm, the fibre orientation mainly in the hoop direction (±60 degree). The composite FRP tubes are fabricated using the filament winding technique; E-glass fibre and Epoxy resin are utilized for manufacturing these tubes. The CFFT columns loaded with different eccentricity 15, 30, 45 and 60 mm from the center of the columns. The results indicated that the ultimate load capacity, failure mode, axial and lateral deformation of the CFFT affected by the eccentric loading. Test results of the stress-strain, load-deformation behavior, and the final failure modes were presented.

6.2 Introduction

Actually, the applications of the concrete-filled FRP tube columns in the field of civil engineering structure has become adapted for different structural applications, such as utility pole, precast piles, girders, and pier columns, (Fam et al. 2003a and b; Mohamed and Masmoudi 2007). Also FRP composite materials have recently been used as internal reinforcement for beams, slabs and pavements Masmoudi et al. 1998. Moreover it is used as external reinforcement for rehabilitation and strengthening different structures. Several experimental and analytical investigations were conducted to study the behaviors of the CFFT columns. However, most of the research studies were concentrated on the behavior of CFFT tubes under uniaxial or flexural load. In fact, structural concrete columns under axial loads exhibited to eccentric load. This occurs for the edge and corner columns in the residential or office building and opened garages. Also the designed axially loaded columns are suffered from the eccentricity due to unintentional load eccentricities, possible construction error, lateral deformation and buckling phenomenon. Also, there are many columns are intended to carry an eccentric load. Therefore, it is important to understand the behavior of the CFFT columns under eccentric load. The benefits of CFFT columns include protective jacket, flexural and shear reinforcements, confinements, durability, formwork and corrosion resistance. At the beginning of 1970s, the plastic pipes (PVC) were suggested to confine the concrete (Kurt 1978). However FRP composites have been proposed for confinement of concrete since the early 1980's. The concept of concrete filled FRP tube columns was introduced by Fardis and Khalili 1981. The general process used to manufacture FRP tubes is one of placing and retaining fiber reinforcements in the direction needed to provide the hoop and axial strength. It can be done by pultrusion, filament winding, centrifugal casting or resin infusion. In the filament winding process, the placement of the primary fibre-glass reinforcement is tightly controlled and can be oriented in either a hoop or axial direction or anywhere in between as needed to develop the necessary strength properties in the hoop or axial direction..

The objective of this study is to examine the behavior of CFFT columns under concentric and eccentric loading. Five unconfined cylinders, two confined CFFT

cylinders, five CFFT columns and two control steel spiral reinforcement concrete columns were cast and tested under concentric and eccentric loading. The CFFT columns were loaded with different eccentricity 15, 30, 45 and 60 mm from the center of the columns. Experimental data on strength, lateral and axial deformations and failure modes were obtained for each column.

6.3 Experimental Program

6.3.1 Materials

6.3.1.1 GFRP tubes

All specimens constructed from the same type of the glass fibre-reinforced polymers (GFRP) tubes. The internal diameter of the tubes is equal to 152 mm. The GFRP tubes were fabricated using filament winding technique; E-glass fibre and Epoxy resin were used for manufacturing these tubes. The GFRP tubes consist of four (±60°) layers oriented in the hoop direction with respect to the longitudinal axis of the tubes, the total thickness is 2.85 mm. The split-disk test and coupon tensile test were performed according to ASTM D-2290-08 and ASTM D 638-08 standard, respectively, on five specimens of the tube. The Young's modulus in the longitudinal and hoop directions is 8787 and 20860 MPa, respectively. Figure 6-1 shows the average stress-strain relationship for the split-disk test, the load-strain curve for the split-disk test was linear up to failure for all specimens. Figure 6-2 presents the axial tensile stress-strain responses for the average results obtained from the five specimens for the coupon tests.

6.3.1.2 Concrete

All specimens were constructed from the same concrete batch using a ready mix concrete supplier. The concrete mixture was intended to provide 30 MPa a concrete compressive strength. The average concrete strength at 28-days testing of all cylinders was found to be 30 ± 1 MPa.

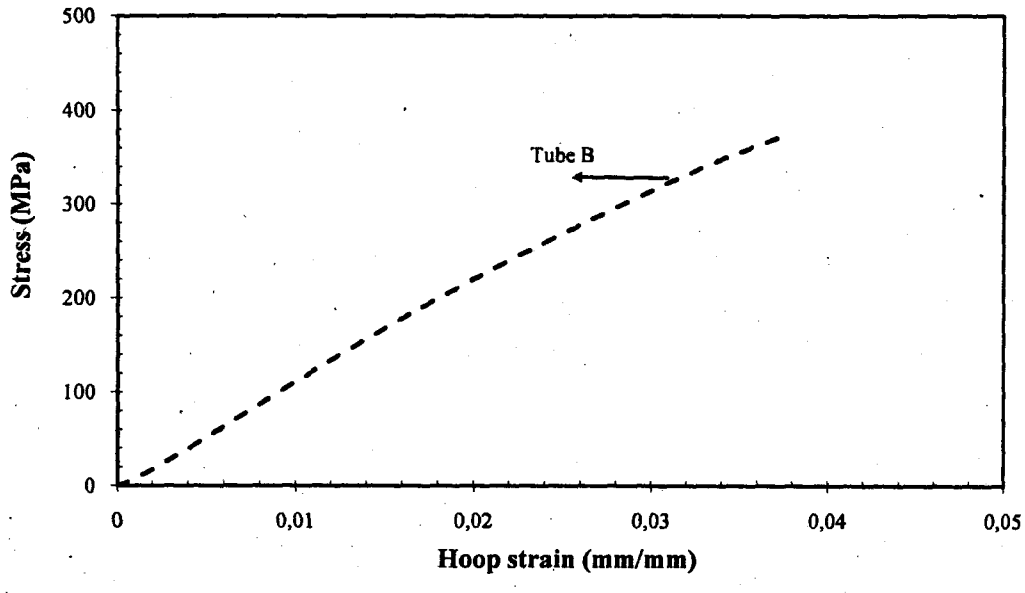

Figure 6-1 stress-strain curve for the split-disk

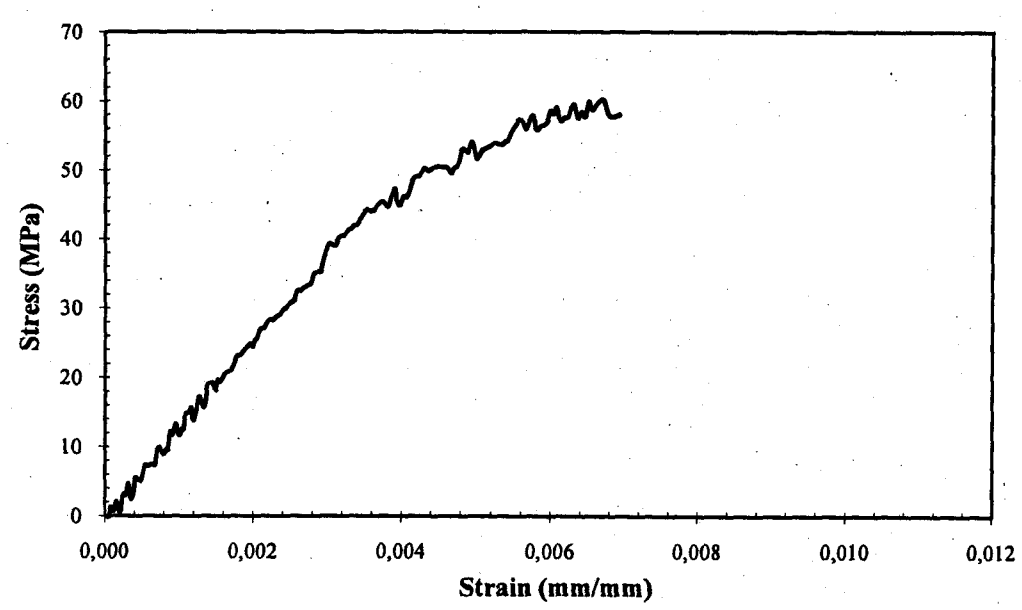

Figure 6-2 Stress-strain curve for coupon tensile test

6.3.2 Reinforcing steel

In this study, two different steel bar diameters were used to reinforce the CFFT and control specimens. Mild steel bars of 3.4 mm diameter were used as spiral reinforcement for the control specimens. Deformed steel bars No. 10M were used as a longitudinal reinforcement for CFFT and control columns. The mechanical properties of the steel bars were obtained from standard tests that were carried out according to ASTM A615/A615M-09, on five specimens for each type of the steel bars. Figure 6-3 shows the typical stress-strain curve for different type of the steel bars. The actual properties are given in Table 6-1 in terms of diameter, nominal area, yield and ultimate strength and young's modulus.

Table 6-1 Properties of reinforcing steel bars.

Φ	Bar type		Diameter (mm)	Nominal Area (mm^2)	Yield strength (MPa)	Ultimate strength (MPa)	Modulus of elasticity (GPa)
	Size	Type					
-	Wire	Mild Steel	3.4		675	850	221
10	10M	Deformed	11.3	100	460	575	200

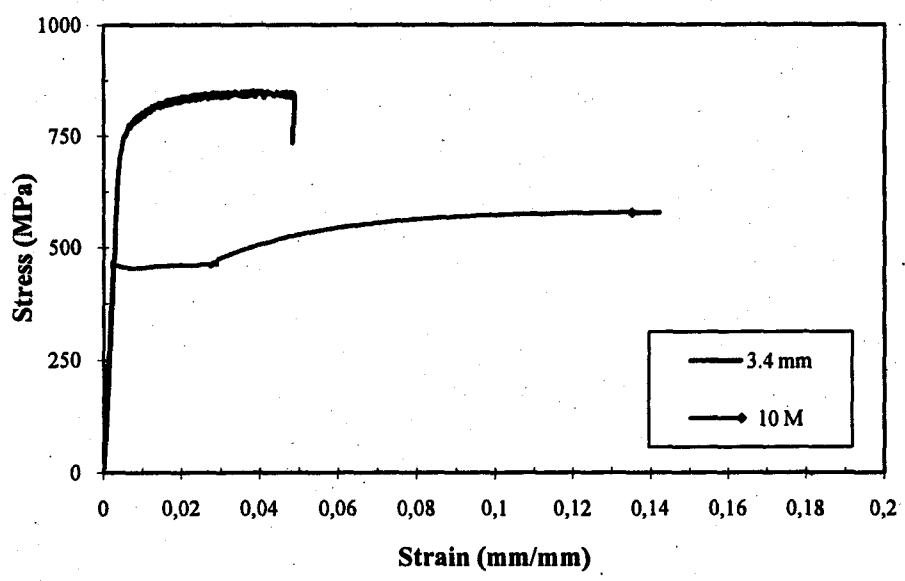

Figure 6-3 Stress-strain relationships for the steel reinforcement

6.3.3 Test matrix and specimen preparation

Test matrix and details of the CFFT columns are presented in Table 6-2. The CFFT specimens were identified by codes listed in the second column of Table 6-2. The first number from the left presents the height of specimen in (cm), and the last number if exist, it indicates the eccentricity value of the specimen measured from the center in (mm).

The experimental program for this study includes five unconfined concrete cylinders and two confined CFFT cylinders (152 x 305 mm), were subjected to concentric load to obtain the unconfined and confined concrete compressive strength. One CFFT column (152 x 912 mm) was tested under concentric load; also four CFFT columns (152 x 912 mm) were subjected to variable eccentric load, (15, 30, 45 and 60 mm). The percentage of the GFRP reinforcement ratio ($4t_{FRP}/D$) is equal to 7.50, where t_{FRP} is the thickness of the GFRP tube. The CFFT columns were internally reinforced with six deformed steel longitudinal bars 10M. The bars were distributed uniformly inside the cross section of the GFRP tube. The distance between the bars and the tubes was 8 mm. A concrete cover of 10 mm was provided between the ends of the longitudinal steel bars and the top and bottom surfaces of the specimens to avoid the stress concentration at the steel bars area.

Finally, the last two specimens (series No. 4) were spirally steel reinforced concrete columns. These specimens prepared to be as a control to obtain the ultimate load capacity under the concentric load. The specimens were reinforced with 6 longitudinal deformed steel bars No. 10M. Also; mild steel bar of diameter 3.4 mm was used for the spiral reinforcement. The pitch equals to 50.6 mm of the spiral was designed to give approximately the same stiffness of the confinement for the GFRP tube. All specimens were cast with concrete in a vertical position. This was performed by fixing the GFRP tubes specimens in a vertical position inside the wooden box formwork. Two holes were drilled at the top and bottom of the wooden box to fix each specimen vertically. Also the bottom surface area of the wooden box was attached with a horizontal wood plate to prevent the leakage of the concrete, see Figure 6-4.

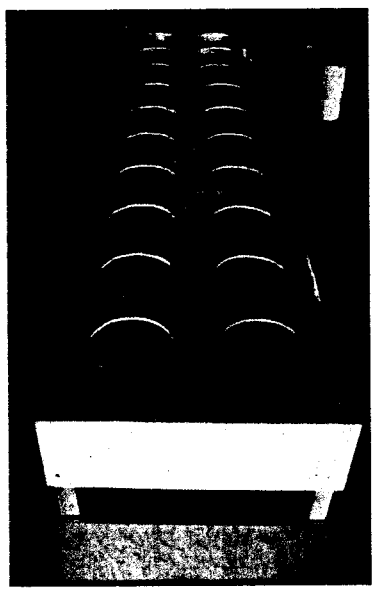

(a) Wooden box.

(b) Fixing tube vertically.

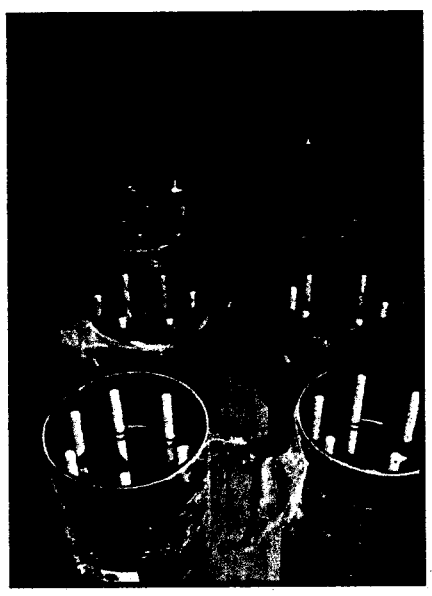

(c) Fixing cages inside tubes.

(d) Casting.

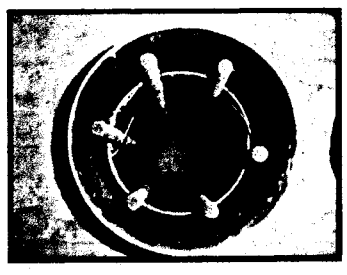

(e) Overview for cages inside tube

Figure 6-4 Formwork and casting procedures

Table 6-2 Details of specimens and summary of test matrix

Series No.	Specimen ID	Height (mm)	Eccentricity (e= mm)	Internal reinforcement	No of specimen	Loading pattern	Type of confinement
1	Cylinder	305	-	----	5	Concentric	Plain concrete
2	CFFT Cylinder	305	-	----	2	Concentric	GFRP Tube
	B90SN0	912	0	6 No. 10	2	Concentric	GFRP Tube
	B90SN15	912	15	6 No. 10	1	Eccentric	GFRP Tube
3	B90SN30	912	30	6 No. 10	1	Eccentric	GFRP Tube
	B90SN45	912	45	6 No. 10	1	Eccentric	GFRP Tube
	B90SN60	912	60	6 No. 10	1	Eccentric	GFRP Tube
4	Ctrl-1	912	0	6 No. 10	2	Concentric	Steel Spiral

6.3.4 Test setup

The concentrically and eccentrically loaded CFFT and control specimens were tested under monotonically increasing axial compressive loading condition. All specimens were prepared before the test by a thin layer of the high strength sulphur capping on the top and bottom surfaces to insure the uniform stress distribution during the test. Steel collars (4.0 mm thickness and 60.0 mm width) were attached to the ends of the specimens to prevent premature failure at these locations.

For eccentrically CFFT columns, the load was applied with specific eccentricities using specially designed two rigid steel end cap and roller bearing assembly. The two rigid steel end caps were designed and fabricated from high strength steel plates and semicircular section of thicknesses 30 mm and 5 mm, respectively. The steel plates and semicircular section were welled together with outward radiating stiffeners of thickness equal to 25 mm. The CFFT specimens were tested under four variable eccentric loads. Therefore, four lines holes were drilled at the top and bottom surfaces of the steel plate of the two caps at distance 15, 30, 45, 60 mm from the center of specimen's position to fix the roller steel rod. The caps sections were placed over the two ends of the CFFT specimens and clamped together 15 mm high strength steel bolts. The rigid steel caps details and test setup for concentrically and eccentrically loaded CFFT are shown in

Figure 6-5. The specimens were tested using a 6,000 kN capacity FORNEY machine located at Construction Facilities Laboratory of Department of Civil Engineering, University of Sherbrooke, was used to apply the compression load on specimens. The specimens were setup vertically at the center of loading plates of the machine. The FORNEY machine, strain gauges and LVDTs were connected by a 20 channels Data Acquisition System. The loading rate range was 2.0 to 2.50 kN/s during the test by manually controlling the loading rate of the hydraulic pump.

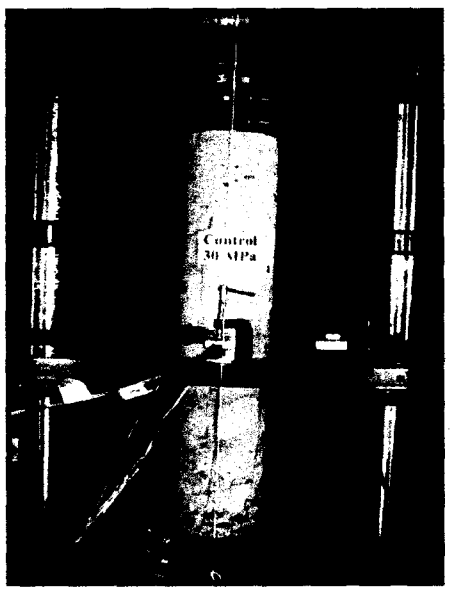

a. Overview for test setup with CFFT specimens under eccentric axial load

b. Overview for test setup with CFFT specimens under eccentric axial load

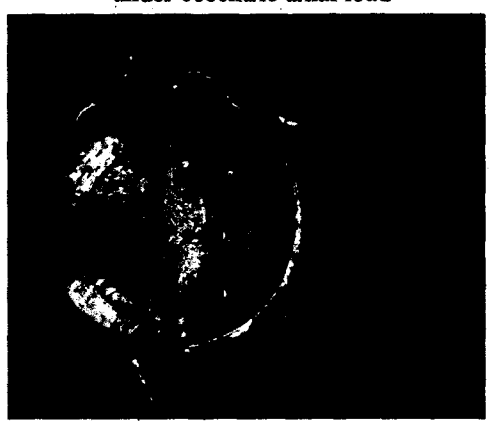

c. Plane for rigid-steel frame

d. Front view for rigid-steel frame.

Figure 6-5 Test set up for eccentric axial load

6.4 Test Results and Discussion

The load carrying capacity of eccentrically loaded columns was reduced due to the presence of the moment resulting from the applied load with eccentricity. The peak loads (P_r), moment at peak load (M_r), and corresponding horizontal displacements at the mid-height of the columns (Δ^*_h), also the maximum axial and horizontal deformations (Δ_v) and (Δ_h), respectively, and the confined concrete compressive strength to the unconfined concrete compressive strength ratio (f'_{cc}/f'_c) are given in Table 6-3. The table also includes concentrically loaded CFFT and RC columns of the same materials (B90SN0 and Ctrl-1, respectively) as a reference to emphasize the effect of load eccentricity on the behaviour of the column. The total maximum moment M_r at mid-height for eccentrically columns is composed of the primary moment, based on the initial eccentricity, and the secondary moment due to the lateral deflection at failure at mid-height.

Table 6-3 Test results for the eccentrically and concentrically loaded CFFT columns

Specimen ID	P_r (kN)	P_y (kN)	Δ_h (mm) Max	Δ_v (mm) Maxi	$(\Delta^*_h + e)$ (mm)	M_r (kN.m)	(f'_{cc}/f'_c)
B90SN0	1595	965	73.70	32.05	73.70	0	2.93
B90SN15	825.0	717	81.00	28.33	31.00	25.51	1.51
B90SN30	620.0	521	117.0	39.10	45.5	28.00	1.14
B90SN45	466.0	412	97.00	43.2	60.00	27.84	0.85
B90SN60	367.0	326	118.00	50.00	73.00	26.72	0.67
Ctrl-1	822.0	805	2.00	4.40	2.00	0	---

6.4.1 Axial and lateral strain behaviour

Figure 6-6 to Figure 6-9 show the load-axial and lateral strain curves for eccentrically loaded columns (B90SN15, B90SN30, B90SN45 and B90SN60). The axial and lateral strains were measured at the tension and compression sides of the mid-height of the columns. The recorded negative (–) and positive (+) results are plotted in the left and right hands of the figures. The strain gauges at the two sides failed due to matrix cracking

before reaching the ultimate load. However, the dash lines on Figure 6-6 to Figure 6-9 present the damage of the strain gauges. The axial strain of the eccentrically loaded columns at the compression side showed negative values at all load levels. However, at the first stages of loading, the axial strain at the tension side showed negative and zero values, after that the strain values were become positive up to failure. On the other hand, the load-axial and lateral strain curves for all eccentrically loaded columns at the two sides showed linear response up to the yield load level. At the yielding load level, the axial strain were varied on average from (–0.003 to –0.0035) and (+0.0012 to +0.0016), at the compression and tension sides, respectively. The Load–axial strain curves at the compression and tension sides showed plateau response after reaching the yielding stage. However, beyond the peak load level, the load–lateral strain curves at the compression and tension sides exhibited descending with nonlinear response up to the failure. Also, the lateral strain in the compression and tension side showed positive and negative strain values, respectively, up to failure. In general, the stress-strain responses of the CFFT columns under eccentric loads softening beyond the peak load level.

6.4.2 Load–strain relationship of internal reinforcements

The axial strains of the two longitudinal steel bars were recorded using two strain gauges at the tension side of the eccentrically loaded columns. Figure 6-10 (a to d) show the load–strain relationships for these internal longitudinal reinforcements for Specimens B90SN15, B90SN30, B90SN45 and B90SN60, respectively. The figures present the elastic–plastic behaviour, whereas the curves show linear response at the initial stages of loading up to the yield load. After yielding the strain increased progressively showing plateau response up to the failure of the specimen. A transition curve connected the linear and plateau parts of the load–strain relationships. For all specimens, the yield load occurred at close value to the peak load at an average strain equal to 0.0015.

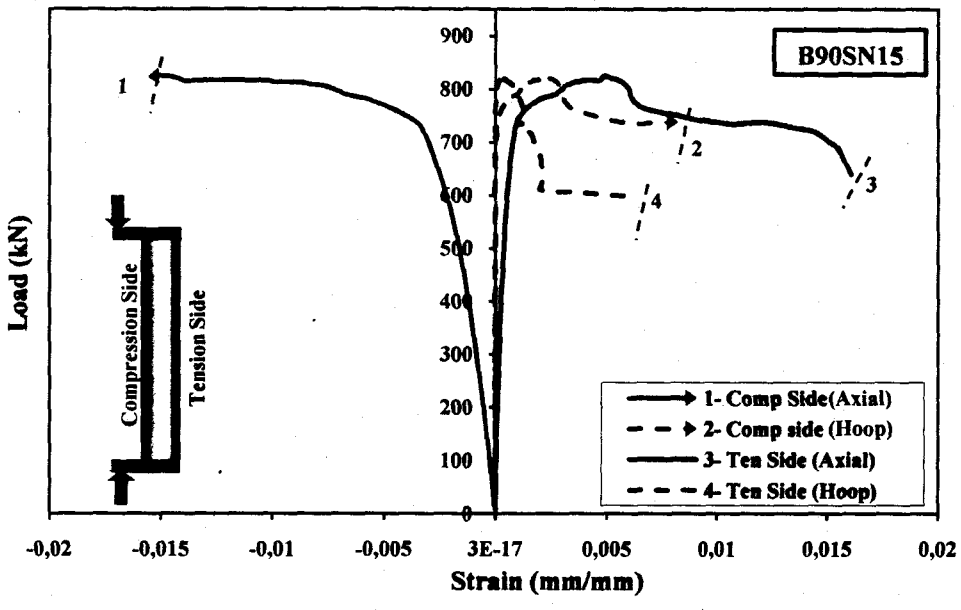

Figure 6-6 Load–axial and lateral strains relationships of Specimen B90SN15

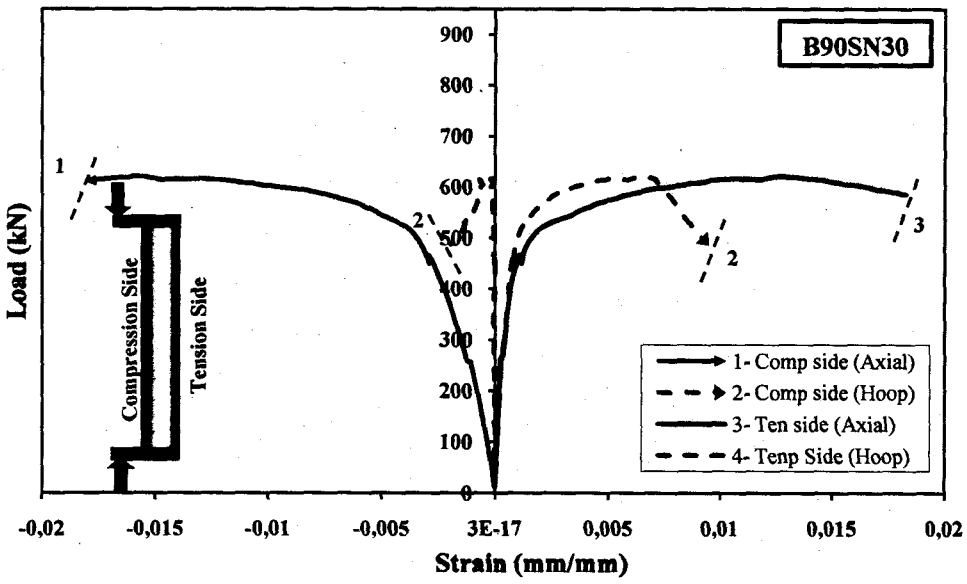

Figure 6-7. Load–axial and lateral strains relationships of Specimen B90SN30

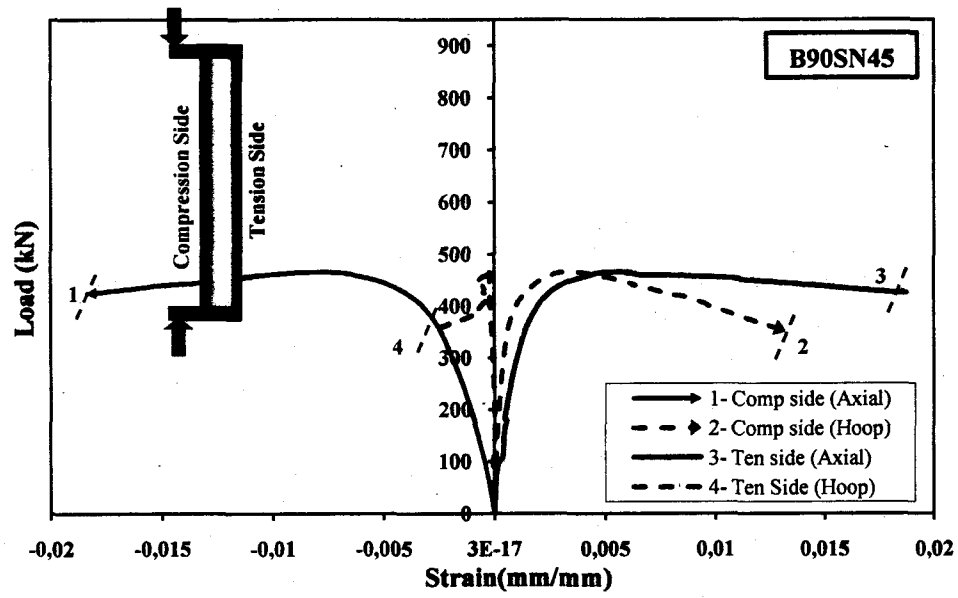

Figure 6-8 Load–axial and lateral strains relationships of Specimen B90SN45

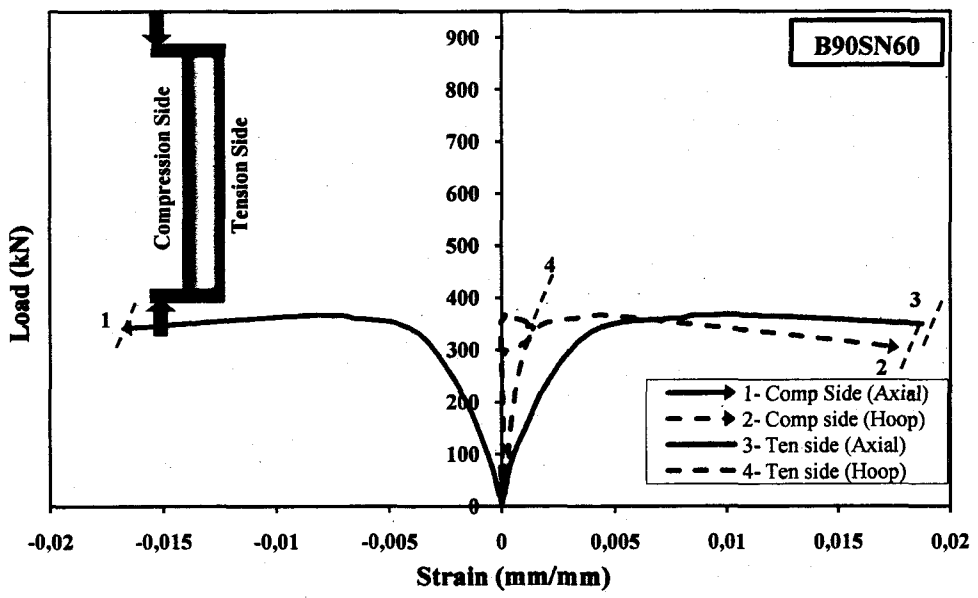

Figure 6-9 Load–axial and lateral strains relationships of Specimen B90SN60

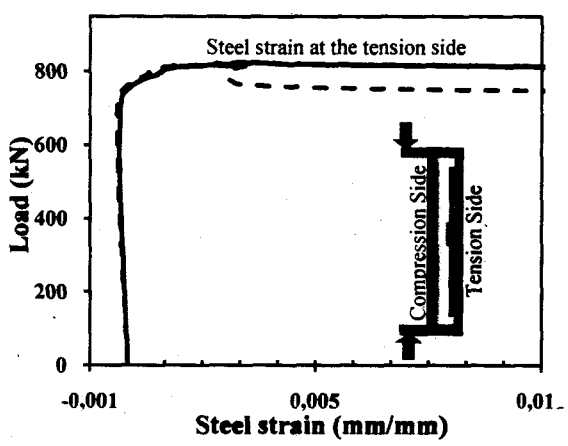

(a) Specimen B90SN15

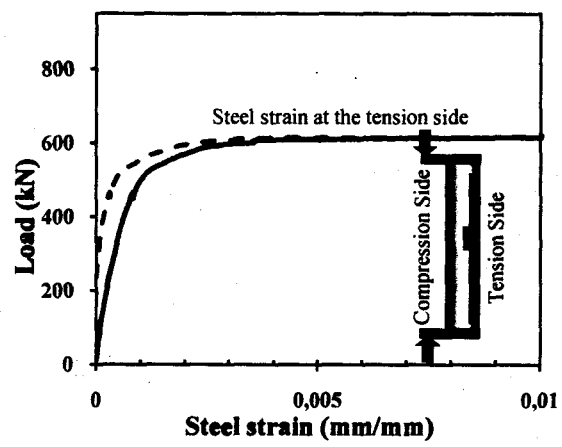

(b) Specimen B90SN30

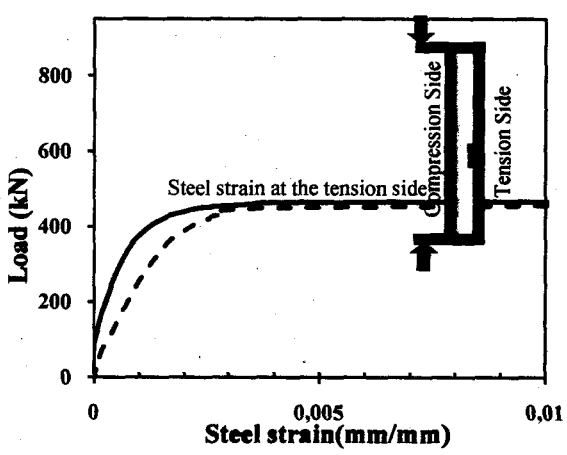

(c) Specimen B90SN45

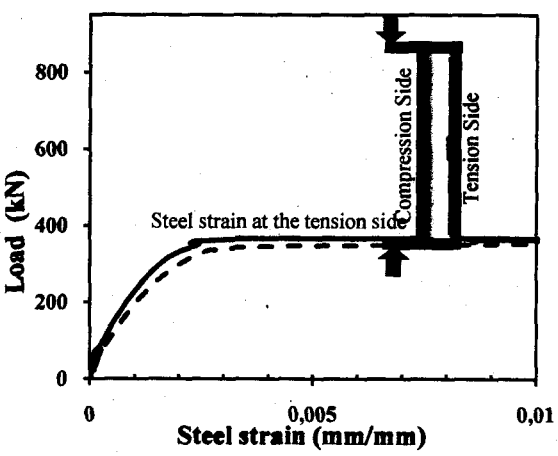

(d) Specimen B90SN60

Figure 6-10 Load–strain relationships of internal steel reinforcements (tension–side)

6.4.3 Axial and horizontal deformation

The load–axial and horizontal deflection curves of eccentrically loaded columns are shown in Figure 6-11 and Figure 6-12, respectively. The figures also include concentrically loaded column to emphasize the effect of load eccentricity on the behaviour of the column. All the columns showed similar behaviour under the eccentric

loading. The initial behaviour shown in the axial load-shortening of the eccentrically loaded columns was almost linear up to yielding of the longitudinal steel bars and before reaching the peak load level. On the other hand, the axial and horizontal load–deflection curves show that before reaching the peak load, the load increased at a constant rate and the horizontal deflection increased at a very slow rate as compared to the increase in the axial deformation. It was probably because the effect of the eccentric load had not been fully developed at this stage. When the maximum load was reached, the lateral deflection began to increase progressively.

The effect of the eccentricity is clearly recognizable by comparing the behaviours of the columns with zero eccentricity value (Specimen B90SN0) versus different values of the eccentricity (15, 30, 45 and 60 mm for specimens B90SN15, B90SN30, B90SN45 and B90SN60, respectively), as shown in Figure 6-11 and Figure 6-12. The initial tangent modulus for the eccentrically loaded CFFT columns decreased with increasing the eccentricity values. On the other hand, beyond the peak loads, the load-axial and horizontal deflection curves for these specimens are nonlinear and presenting softening response. This response is opposite to the response of the concentrically column which presented hardening behaviour. It is of interest to mention that, from Figure 6-11, the peak loads (825. 620, 466, 367 kN) of specimens B90SN15, B90SN30, B90SN45 and B90SN60, respectively, occurred approximately at the same value of the axial deformation (7.50 mm). The axial and horizontal deformation of the eccentrically columns increased gradually with load increase up to the peak load, after that the deformation increased progressively with decreasing the load.

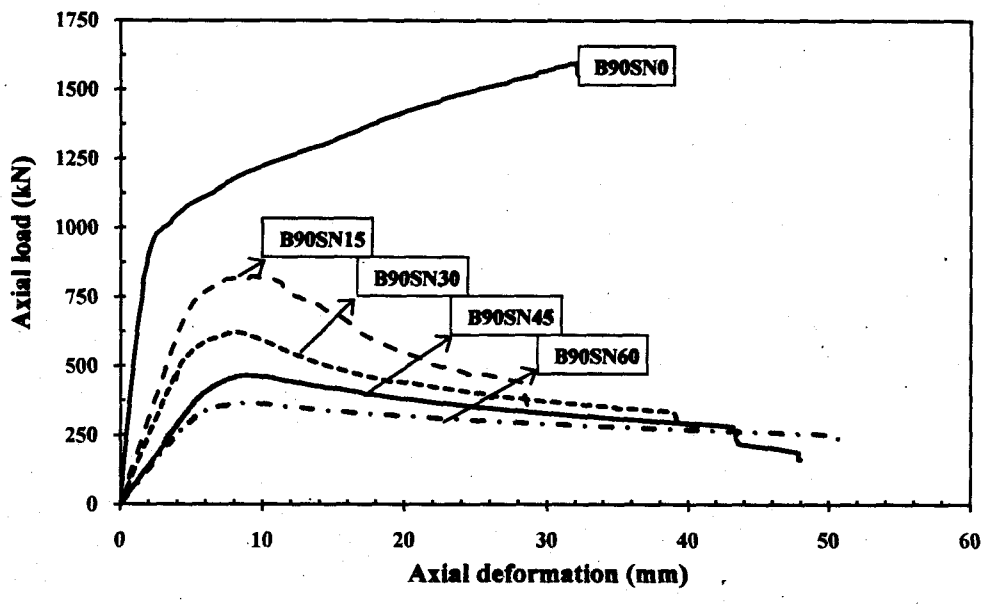

Figure 6-11 Load-axial deformation relationships for the eccentrically and concentrically loaded CFFT columns

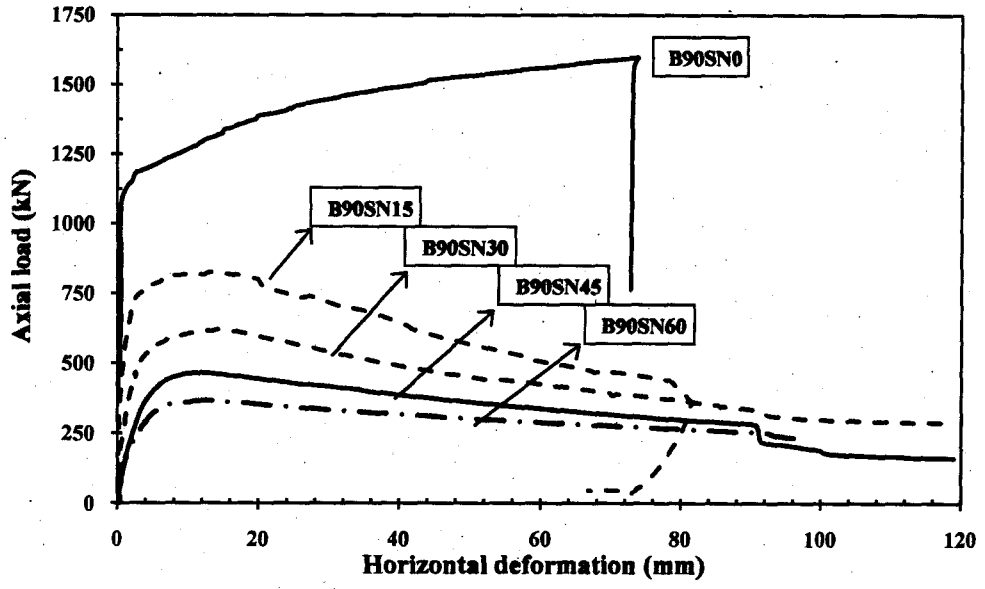

Figure 6-12 Load-horizontal deformation relationships for the eccentrically and concentrically loaded CFFT columns

6.4.4 Failure modes

Figure 6-13.a shows the failure mode for the three types of the CFFT cylinder specimens of Series No. 2. All specimens failed due to the rupture of the fibre in the hoop direction at the ultimate hoop stress resulting from the dilation of the concrete. As shown in Figure 6-13.a, the rupture cracks in the FRP tubes were propagated along the longitudinal vertical axis of the column indicating that these tubes were failed when the lateral strain values were exceeded the ultimate strain values of GFRP materials. The failure crack was a zigzag line normal to the direction of the fibres in the hoop direction. Low sounds heard during the early-to-middle stages of loading were referred to the dilation, micro-cracking of concrete and offset of the aggregate. At higher levels of loading; sounds were heard clearly due to rupture of the fibres in the GFRP tubes. The ultimate failure was very explosive for specimens of tube A, and the rupture of the GFRP tubes was followed by concrete crushing. The concrete fell out from the tube in a crushed state immediately after failure especially for tube A.

For CFFT columns tested under concentric load, the failure modes were a combination of rupture of the GFRP tubes and local buckling of internal steel bars at the column mid-height (see Figure 6-13.b). Typical failure was generally observed by the rupture of the tubes between one end and the mid-height of the specimen. Figure 6-13.b shows the rupture of the GFRP tubes is recognized by a zigzag line. This indicates that the helical fibres of the tubes failed in tension because of the hoop stresses developed by the concrete core that provided an effective confinement. On the other hand, for all specimens after reaching the unconfined concrete compressive strength, cracking of concrete could be heard. Significant white patches and transverse cracks were observed through the middle zone of the specimens at 70–90% of the ultimate load. Yet the CFFT columns have not buckled and it can be represented as short columns. Distortions of the cross section and outward bulging of the tube occurred near the mid height of the columns for all specimens before the failure. This mode of failure arisen from lateral expansion of the concrete core and the local buckling of the internal steel bars. On the other hand, sound snapping was heard even after stopping the test and removal of the

specimens from the setup. This continued until the stored energy in the hoop direction and the interaction between fibre and the prestressed concrete core was released..

The failure of the control specimen started by vertical cracks at the bottom region of the column distributed uniformly around the hoop direction. The failure mode was typical for unconfined concrete columns. It characterized by concrete compression with concrete cover splitting. The failure mode was taken place once the internal steel bars were yielded. Figure 6-13.c show the failure modes of the RC control columns.

Figure 6-13.d shows the overview of the final failure mode for the four eccentrically loaded CFFT columns tested in this study. The failure was generally marked by a ductile failure. As the peak load was reached, horizontal flexural cracks propagated quickly through the tension side. Significant decrease in the ultimate load capacity was observed for all eccentrically specimens as compared with the ultimate load capacity of concentrically loaded CFFT columns. Excessive horizontal deformation at the mid height of the CFFT columns was observed beyond the peak load. The final failure mode for the eccentrically loaded CFFT columns was permanent with a single curvature in the direction of the tension side as shown in Figure 6-13.e. Beyond the peak load, the failure was marked by the rupture of FRP tube at the tension side in the axial direction for all specimens. On the other hand, minor local buckling in the compression side for the FRP tubes at the mid height occurred for Specimen B90SN60 due to the increases in the lateral deformations; see Figure 6-13.l.

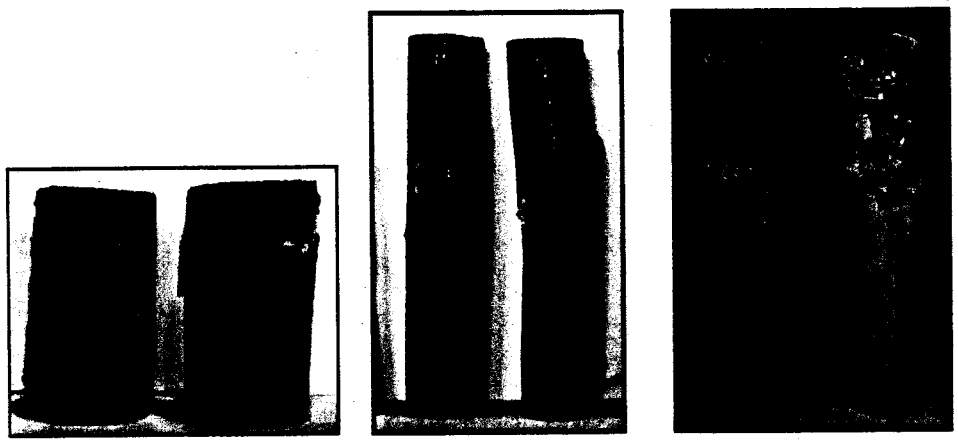

a. CFFT-Cylinders b. B90SN0 c. Control

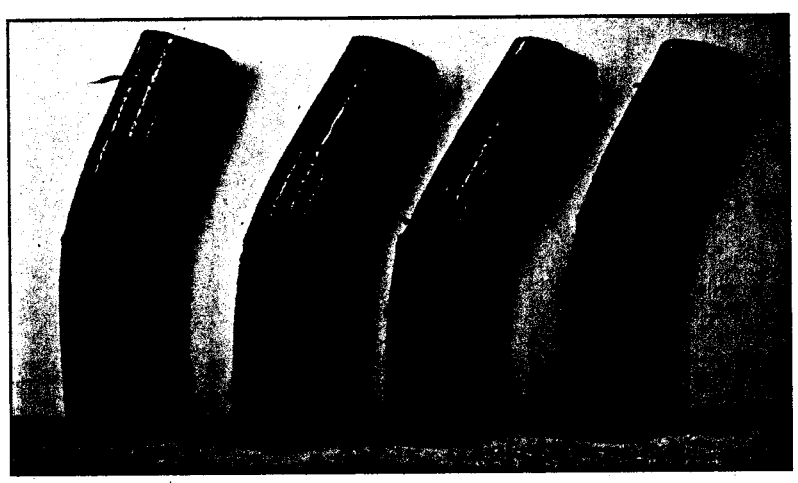

d. Deformed shape of eccentriclly-loaded CFFT after test

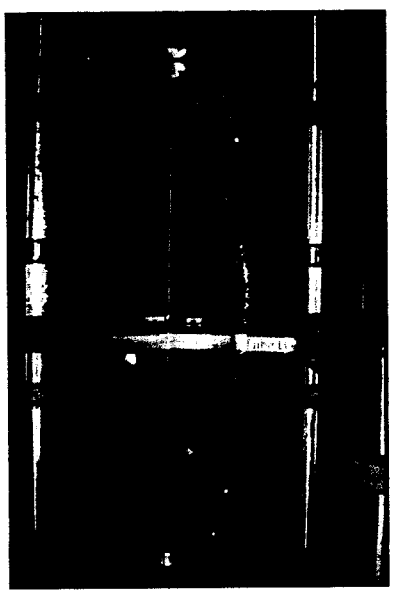

e. B90SN45

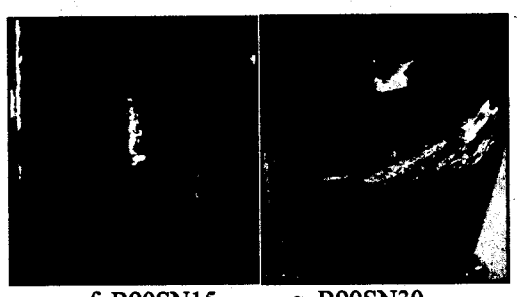

f. B90SN15 g. B90SN30

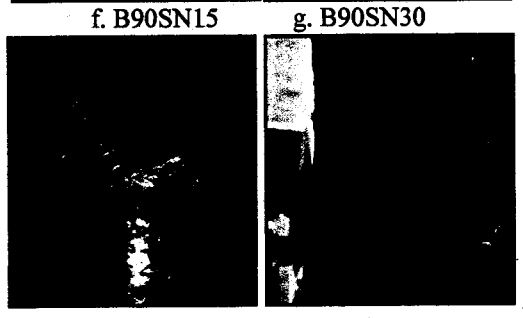

j. B90SN45 l. B90SN60

Figure 6-13 Failure modes of eccentrically loaded CFFT column specimens

6.4.5 Interaction diagram

The load carrying capacity of eccentrically loaded columns was reduced due to the presence of the moment resulting from the applied load with eccentricity. Therefore the mid-height moments induced in the specimen consisted of two components, described by Equation below:

$$M_r = P_r(\Delta_h^* + e) \qquad 6\text{-}1$$

where M_r = the total moment at the mid-height; P_r = the maximum applied axial load to the specimen; (e) are the eccentricity at which the axial load was applied; and (Δ_h^*) the horizontal deflection at the mid-height at the maximum load level. Table 6-3 shows the different values of the M_r, P_r and Δ_h^* for Specimens B90SN0, B90SN15, B90SN30, B90SN45 and B90SN60.

Figure 6-14 shows the relationship between the eccentricity value and the axial load on the CFFT columns. The ultimate load capacity for Specimens B90SN15, B90SN30, B90SN45 and B90SN60, decreased 48, 61, 70 and 77%, respectively as compared to the ultimate load capacity of Specimen B90SN0. The experimental results were used to establish interaction diagram for the CFFT columns, see Figure 6-15. The curve is of a similar shape to that which can be expected for a typical reinforced concrete column. It is clear that the maximum benefit of using GFRP tubes as a confinement mechanism occurs when the section subjected to pure axial loads. Also, the figure reflects clearly the transition from tension to compression failure through the balanced point. However, in the region of the curve with increasing axial load and moment, specimens B90SN45 and B90SN60 failed mainly by tensile yielding steel bars and rupture of the FRP tube on the tension side. Specimens B90SN30 presents the balanced point on the curve. Above the balanced point, at which the curve reverses direction, increasing axial load and decreasing the total moment which resulted from decreasing the eccentricity (e). Specimen B90SN0 failed in compression, while Specimen B90SN15 failed in compression and tension by crushing of the concrete at the compression side and rupture of the FRP tube in the axial direction at the tension side, respectively.

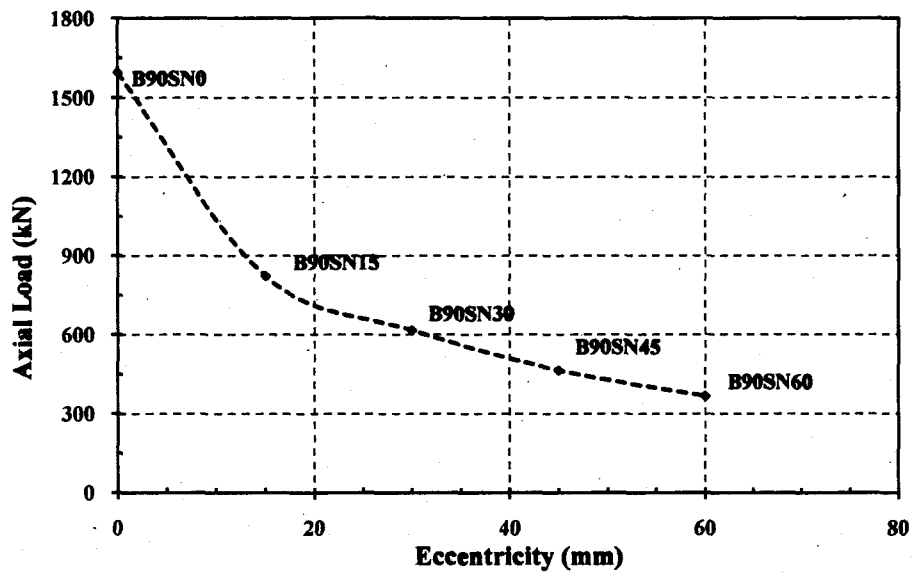

Figure 6-14 Load-eccentricity relationships

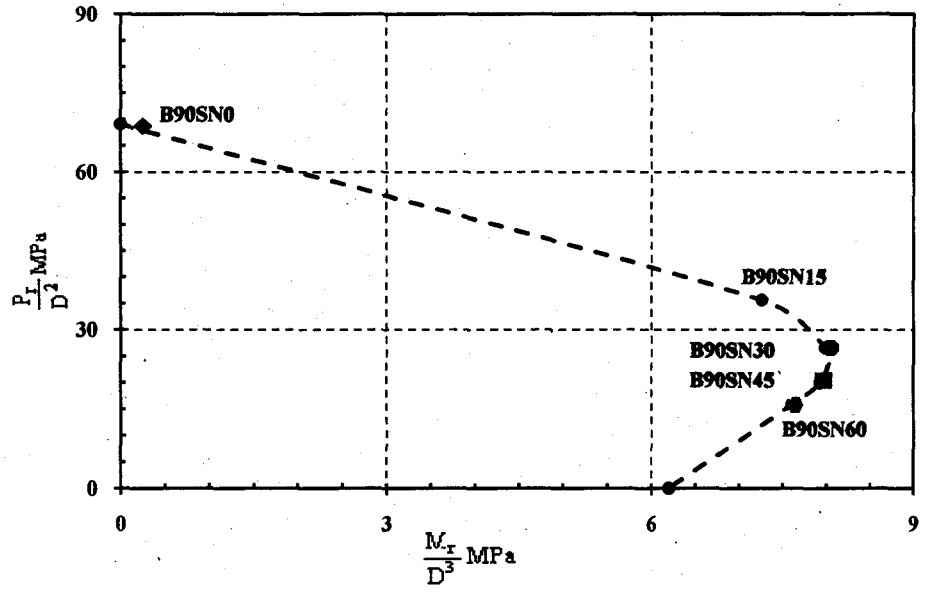

Figure 6-15 Experimentally interaction diagram for CFFT columns

6.5 CONCLUSIONS

The behaviors of internally reinforced CFFT columns under different eccentric load values were presented. The behavior of the concrete filled GFRP tubes is significantly affected by the eccentric load. The confinement provided by the GFRP tubes improves both the load-carrying capacity and the ductility of the concrete columns under concentric load. The following general conclusions can be drawn based on the experimental research work presented in this study:

1. The behaviour of CFFT columns under eccentric loads is completely different as compared to those tested columns under concentric loads.
2. The load carrying capacities of CFFT columns under load eccentricities, e/D from 0.10, 0.2, 0.3 and 0.4 were reduced by 48, 61, 71 and 77%, respectively, as compared to the load carrying capacity of the same CFFT column under concentric load.
3. The axial and lateral deformations were increased progressively with increasing the eccentricity values.
4. The stress-strain curve of the CFFT columns under eccentric loads is nonlinear and exhibited softening after peak load. However, the slope of the descending region of the stress-strain relationship is steeper for columns with higher eccentric value.
5. The failure mode of the CFFT columns is dependent on the type of loading. For the short columns, the rupture of the FRP tube tubes in the hoop direction and local buckling of internal steel bars are the dominant in case concentric. While the combination of tensile rupture in the axial direction and excessive axial and lateral deformations are the dominant in case eccentric loading.

Chapter 7
Assessment of Confinement Models for Concrete Confined with FRP Tubes

7.1 Abstract

The application of fiber-reinforced polymers (FRP) tubes for the confinement and reinforcing the axial structure members (columns, piles, and pier bridges) is rapidly gaining acceptance in the civil engineering community. A research program is currently being carried out at the laboratories of the Department of Civil Engineering, University of Sherbrooke. The objective of that program is to investigate and evaluates the compressive behavior of the concrete-filled FRP tubes (CFFT) columns. The FRP tubes benefits are in confinement, protective jackets, providing shear or/and flexural reinforcement and permanent formwork. This paper presents the experimental and analytical results of axially loaded CFFT cylinders. Twelve plain concrete cylinders and twelve CFFT cylinders (152 x 305 mm) were tested under uniaxial load. New filament wound GFRP tubes manufactured from glass fiber and epoxy resin were used as structural stay in place form work for the CFFT specimens. The fiber orientations of the tubes were mainly in the hoop direction. The FRP tubes used have constant internal diameters 152 mm. The parameters used in this investigation include the effect of laminate thickness of FRP tubes and unconfined concrete strength. The final failure modes, stress-strain behavior are presented for all specimens. Different FRP-confined models for prediction the ultimate strength of CFFT have been reviewed. A comparison between the experimental results and those predicted by the selected models is presented.

7.2 Introduction

In general, fiber reinforced polymer (FRP) composite materials have recently been used as internal or external reinforcement in the field of civil engineering constructions. It is used as internal reinforcement for beams, slabs and pavements Also it is used as external reinforcement for rehabilitation and strengthening different structures (Spadea et al. 2000; Almusallam and Al-Salloum 2001; Lam and Teng 2003). However, in recent year, the application of concrete-filled FRP composites tubes (CFFT) for different structural applications piles, column, girder, bridge piers have been studied and investigated (Karbhari et al. 2000; Fam et al. 2003a; Mohamed and Masmoudi 2009a). The benefits of CFFT cylinders include protective jacket, flexural and shear reinforcements, confinements, durability, formwork and corrosion resistance (Mohamed and Masmoudi 2008a, b and c). The general process used to manufacture FRP tubes is one of placing and retaining fiber reinforcements in the direction needed to provide the hoop and axial strength. It can be done by pultrusion, filament winding, centrifugal casting or resin infusion. In the filament winding process, the placement of the primary fiber-glass reinforcement is tightly controlled and can be oriented in either a hoop or axial direction or anywhere in between as needed to develop the necessary strength properties in the hoop or axial direction. Confinements of the concrete are produced by the reaction of FRP tubes normal to the hoop direction for structure members under uniaxial loads. So that the fiber layers in the hoop direction activated to provide the confinement of the concrete. The axial layer is not economic in case of CFFT cylinders. However the earlier local buckling of the axial layer is more expected under compression load on the CFFT cylinders. Kaynak et al. 2005 conducted a split-disk tests for specimens produced with five different winding angle to investigate processing parameters of continues FRP tubes produced by filament winding technique. The results indicate that both hoop tensile strength and hoop tensile modulus of elasticity depended strongly on the fiber direction of specimens. Specimens having 90° and ±65° had much higher values compared to the ones having ±45°, ±25° and 0°.

The aim of the present study is assessment of the performance of the existing FRP-confined models for predicting the ultimate strength of specimens tested in this study. The research mainly focuses on the experimental and analytical work concerning small-scale axially loaded concrete cylinders, confined with glass FRP tubes. The assessment has based on the prediction of the ultimate axial strength of the CFFT specimens, rather than on its strain or whole stress-strain relationships.

7.3 Review of Strength Models of FRP- Confined Concrete

In recent years, a number of experimental studies on the confined concrete by FRP sheets or FRP tubes have been carried out and several empirical models to describe its behavior have been proposed. In addition, a number of the analytical models were devolved as an extension of the model by Mander et al. 1988, for steel confined concrete. Fourteen selected models will be briefly presented, and their predictions will be compared and evaluated to the experimental test results of this study. In the presentation and discussion of the different confinement models provided by the different researchers, a uniform set of parameters, which may be different from the original ones, has been adopted for consistency. Table 7-1 presents a synopsis of the expressions provided by each author for the calculation of the maximum compressive strength (f'_{cc}) for the FRP-confined concrete cylinders of circular cross section.

In the following expressions, (f_l) represents the lateral confining pressure exerted by the FRP tubes on the concrete core. The FRP tube has an internal diameter and wall thickness equal to (D) and (t_{FRP}), respectively. (E_f) and (f_u) are the elastic modulus and ultimate tensile strength of the FRP tubes in the circumferential direction. The ultimate lateral confining pressure (f_l) is calculated by assuming that the concrete will fail when the FRP tube reaches its failure stress. Thus, using equilibrium of forces, an expression can be obtained giving the lateral confining pressure at ultimate

Table 7-1 Existing confining models for FRP-confined concrete

Model	Equations	
Richart et al. 1929*	$f'_{cc} = f'_c\left[1+4.1\frac{f_l}{f'_c}\right]$	7-1
Fardis and Khalili 1981+	$f'_{cc} = f'_c\left[1+2.05\frac{f_l}{f'_c}\right]$	7-2
Mander et al. 1988*, Spoelstra and Monti 1999 (Exact)‡	$f'_{cc} = f'_c\left[2.254\sqrt{1+7.94\frac{f_l}{f'_c}}-2\frac{f_l}{f'_c}-1.254\right]$	7-3
Cusson and Paultre 1995‡	$f'_{cc} = f'_c\left[1+2.1\left(\frac{f_l}{f'_c}\right)^{0.7}\right]$	7-4
Pliakoutas and Mortazavi 1997‡	$f'_{cc} = f'_c\left[1.125+2.5\frac{f_l}{f'_c}\right] \quad 2\frac{f_l}{f'_c}\geq 0.1$	7-5
	$f'_{cc} = f'_c\left[1+5\frac{f_l}{f'_c}\right] \quad 2\frac{f_l}{f'_{co}}\leq 0.1$	7-6
Karbhari and Gao 1997 [19]‡	$f'_{cc} = f'_c\left[1+3.1v_c\frac{2t}{D}\frac{E_f}{E_c}+2\frac{f_l t}{Df'_c}\right]$	7-7
Samaan et al. 1998 [20]+	$f'_{cc} = f'_c\left[1+6.0\frac{f_l^{0.7}}{f'_c}\right]$	7-8
Spoelstra and Monti 1999 (Approximate)‡	$f'_{cc} = f'_c\left[0.2+3.0\left(\frac{f_l}{f'_c}\right)^{0.5}\right]$	7-9
Saafi et al. 1999+	$f'_{cc} = f'_c\left[1+2.2\left(\frac{f_l}{f'_c}\right)^{0.84}\right]$	7-10
Miyauchi et al.1999‡	$f'_{cc} = f'_c\left[1+2.98\frac{f_l}{f'_c}\right]$	7-11
Toutanji revised 1999‡	$f'_{cc} = f'_c\left[1+2.3\left(\frac{f_l}{f'_c}\right)^{0.85}\right]$	7-12
Theriailt and Neale 2000‡ Lam and Teng 2002‡, Wu et al. 2002‡	$f'_{cc} = f'_c\left[1+2.0\frac{f_l}{f'_c}\right]$	7-13
Becque et al. 2003+	$f'_{cc} = f'_c+6\left((f_l)^{-0.3}\right)f_l$	7-14
Mandal et al. 2005†	$f'_{cc} = f'_c\left[0.0017\left(\frac{2E_f tf_u}{Df'_c}\right)^2+0.0232\left(\frac{2E_f tf_u}{Df'_c}\right)+1\right]$	7-15

* Steel-based confinement models, ‡FRP wrapping-based confinement models,
+ FRP tubes-based confinement models and † FRP wrapping and tubes-based confinement models

$$f_l = \frac{2 f_u t_{FRP}}{D} \qquad 7\text{-}16$$

In 1929's, the first attempt was developed to model the steel confined concrete by Richart, Grandtzaeg and Brown, where the confined concrete strength (f'_{cc}) was taken as a function of the unconfined concrete strength (f'_c) and the confining pressure at ultimate, (f_l)

$$f'_{cc} = f'_c \left[1 + k_1 \frac{f_l}{f'_c} \right] \qquad 7\text{-}17$$

The value of the coefficient (k_1) was obtained as an average value (4.1) from the test results on concrete confined with steel ties. Fardis and Khalili 1981 were the first who developed a confinement model for the FRP-encased concrete in compression based on the steel confined model of Richart et al. 1929. Most of the existing strength models for the FRP confined concrete were developed takes the form of Equation 7-17. However, the new values of the coefficient (k_1) were obtained from the test results on the concrete cylinders confined by FRP sheets or tubes, (Pliakoutas and Mortazavi 1997; Samaan et al. 1998; Miyauchi et al.1999; Spoelstra and Monti 1999).

Equation 7-18 represents the second form for the FRP confined concrete, showing a nonlinear relationship between the increase in the concrete strength and the confinement ratio f_l / f'_c , Cusson and Paultre 1995. It was based on the experimental test results which indicated that the lateral confinement was less effective at higher levels of the confining pressure.

$$f'_{cc} = f'_c \left[1 + k_1 \left(\frac{f_l}{f'_c} \right)^{m_1} \right] \qquad 7\text{-}18$$

This equation was then checked by a number of researchers who suggested different values of the k_1 and m_1 values, (Samaan et al. 1998, Miyauchi et al.1999; Spoelstra and Monti 1999; and Toutanji 1999), as shown in Table 7-1. On the other hand, a simple confined model of Lam and Teng 2002 has been developed based on a large test

database assembled from an extensive survey of existing studies. The study showed that the ultimate strength of the confined concrete depends little on the unconfined concrete, size, length-to-diameter ratio of the test specimens and FRP type, but depends significantly on the accuracy of the actual value of the hoop tensile strength of the FRP. The presented model (Theriailt and Neale 2000, Lam and Teng 2002, Wu et al. 2002) as shown in Table 7-1, Equation 7-13 was found approximately identically similar to the model provided by Fardis and Khalili 1981.

7.4 Experimental Work

Table 7-3 presents a total of twelve CFFT cylinders of two different concrete compressive strengths and three different thicknesses of the FRP tubes were selected to evaluate the performance and contrast the different approaches taken by the selected confinement models. The test matrix is consisted from two groups; the specimens are identified as shown in Table 7-2. The first letter indicates the tube type used from Table 3-1, the first number indicates the unconfined concrete compressive strength and the second number presents the replicates of the specimens. The cross section diameter for all specimens is 152 mm. The test specimens are classified for two groups. The first group included six CFFT cylinders cast from concrete batch No. 1 (f_c' =45 MPa), two cylinders where cut from GFRP tube type A, B and C which are different in the thicknesses. The percentages of the GFRP reinforcement ratio ($4t_{FRP}/D$) are equal to 6.97, 7.5 and 13.15 for tube A, B and C, respectively, where (t_{FRP}) is the thickness of the GFRP tube. However, the specimens of group No. 2 are similar to specimens of group No. 1 except the concrete used from batch No. 2 (f_c' =45 MPa).

More details regarding the mechanical characteristics and material properties of the FRP tubes, concrete compressive strength and test setup can be found in (Chapter 3).

Table 7-2 Test matrix and specimens details

Data Set No.	ID	Tube	4t/D %	*D/t*	*H* (mm)	*H/D*	Number of specimens
1	A-30-1 A-30-2	A	6.97	58	305	2	2
	B-30-1 B-30-2	B	6.97	58			2
	C-30-1 C-30-2	C	16.8	24			2
2	A-45-1 A-45-2	A	6.97	58	305	2	2
	B-45-1 B-45-2	B	6.97	58			2
	C-45-1 C-45-2	C	16.8	24			2

The average ratios of confined to unconfined concrete strength (f'_{cc} / f'_c) were 2.42, 2.7, and 4.11 for CFFT cylinders casted in tubes A, B and C, respectively, with concrete patch No. 1. As expected, significant enhancement of the strength as well as the ductility for the CFFT cylinders was achieved by increasing the thickness of FRP tubes. The maximum confined concrete strength was observed for specimen C-30-2 reaching up to 128 MPa. The average confined concrete strength (f'_{cc}) for A-45 is exceeds that of specimen A-30, by 15 %. However, this increase is not significant when compared to the strength increase between confined and unconfined concrete specimens, which is equal to 50 %. In addition, the (f'_{cc} / f'_c) ratio for A-45 and A-30 is equal to 1.90 and 2.42, respectively, which further show that the ultimate strength of the confined concrete is mainly dependent on the stiffness of the GFRP tubes, and more is effective for normal concrete strength.

More details regarding the test results in terms of stress-strain relationships, confined concrete compressive strength and the failure modes can be found in (Chapter 3).

Table 7-3 Experimental test results

Data set	ID	H (mm)	Tube type	f_c' (MPa)	f_{cc}' (MPa)	$\frac{f_{cc}'}{f_c'}$	P_{Max} (kN)	Failure mode
(1)	A-30-1	305	A	30	74.40	2.48	1350	Tube rupture
	A-30-2	305	A	30	71.00	2.37	1283	Tube rupture
	B-30-1	305	B	30	81.88	2.73	1490	Tube rupture
	B-30-2	305	B	30	80.00	2.67	1450	Tube rupture
	C-30-1	305	C	30	119.1	4.00	2160	Tube rupture
	C-30-2	305	C	30	128.0	4.23	2302	Tube rupture
(2)	A-45-1	305	A	45	89.40	1.98	1620	Tube rupture
	A-45-2	305	A	45	82.50	1.82	1502	Tube rupture
	B-45-1	305	B	45	101.7	2.26	1930	Tube rupture
	B-45-2	305	B	45	103.5	2.30	1805	Tube rupture
	C-45-1	305	C	45	142.6	3.17	2525	Tube rupture
	C-45-2	305	C	45	148.5	3.30	2410	Tube rupture

7.5 Assessment of Selected FRP-Confined Models

In this section, the theoretical confined concrete strength (f_{cc}'), the ratio of the theoretical confined concrete strength to the unconfined concrete compressive strength (f_{cc}'/f_c'), and the experimental confined concrete compressive strength divided by the theoretical confined concrete compressive strength (f_{cc}'/f_c') are presented and compared in Table 7-4, for the selected confined models of this study.

The confining pressure f_l was calculated based on the ultimate hoop tensile strength, f_u which it is equal to the value obtained from the split disk test results. If the ratios of the experimental to theoretical (f_{cc}'/f_c') being higher than unit value, this indicates to a conservative predictions, whereas the ratios are lower than the unit value, this indicates to non conservative predictions of the models.

The statistical performance of each model was assessed by both data sets 1 and 2, as shown in Table 7-5. The statistical values were presented in the form of the average (mean), standard deviation and coefficient of variation values for the ratios of the experimental confined concrete compressive strength to the theoretical confined concrete compressive strength for each data set calculated by each model. The standard deviation is a measure of the dispersion of a data set. A low standard deviation indicates that the data points tend to be very close to the same value (the mean), while high standard deviation indicates that the data are "spread out" over a large range of values. The coefficient of variation is defined as the ratio of the standard deviation to the mean. The accuracy of the models has been also quantitatively evaluated computing the average absolute deviation as follows:

$$AAD = \frac{1}{N}\sum_{i}^{N}\left(x_i - \bar{x}\right) \qquad 7\text{-}19$$

where N = total number of specimens for each data set which equal to six, x_i is the ratio of the experimental confined concrete compressive strength to the theoretical confined concrete compressive strength relative to the i_{th} data point and $\bar{x}$ is the average value of the six point for each data set.

As shown in Table 7-4 and Table 7-5, it is observed that some of the models give close predictions values of the experimental test results for data set 1 and 2, but others do not. It was found that the Richart et al. model's which was originally created for steel-confined concrete significantly overestimate the ultimate confined strength for CFFT specimens of both data set 1 and 2. On the other hand, the predictions values for data set 1, obtained by Mander et al.'s and Spoelstra and Monti (Exact) model's are very close to the experimental results, while the predictions values for data set 2, are unconservative, whereas the average value for six specimens is 0.95. Also, the prediction values obtained by Miyauchi et al.'s model are close to the experimental results, whereas the average value for data set 1 and 2 are 1.06 and 1.08, respectively. On the other hand, Mandal et al.'s model is the only model which gave the predictions values over conservative for both data set 1 and 2.

Table 7-4 Performance of selected confined models and compression with test data

Data set (1)	Theoretical values		Experimenta\Theoretical	Data set (2)	Theoretical values		Experimental\ Theoretical
	f'_{cc}	f'_{cc}/f'_{co}	f'_{cc}/f'_{cc}		f'_{cc}	f'_{cc}/f'_{co}	f'_{cc}/f'_{cc}
Richart et al. 1929							
A-30-1	79.32	2.64	0.94	A-45-1	94.32	2.10	0.94
A-30-2	79.32	2.64	0.90	A-45-2	94.32	2.10	0.91
B-30-1	86.89	2.90	0.94	B-45-1	101.89	2.26	0.93
B-30-2	86.89	2.90	0.92	B-45-2	101.89	2.26	1.02
C-30-1	164.64	5.49	0.73	C-45-1	179.64	3.99	0.79
C-30-2	164.64	5.49	0.77	C-45-2	179.64	3.99	0.83
Fardis and Khalili 1981							
A-30-1	54.66	1.82	1.36	A-45-1	69.66	1.55	1.28
A-30-2	54.66	1.82	1.30	A-45-2	69.66	1.55	1.23
B-30-1	58.44	1.95	1.40	B-45-1	73.44	1.63	1.29
B-30-2	58.44	1.95	1.37	B-45-2	73.44	1.63	1.41
C-30-1	97.32	3.24	1.23	C-45-1	112.32	2.50	1.27
C-30-2	97.32	3.24	1.30	C-45-2	112.32	2.50	1.32
Mander et al. 1988, Spoelstra and Monti 1999 (Exact)							
A-30-1	76.63	2.55	0.97	A-45-1	98.74	2.19	0.90
A-30-2	76.63	2.55	0.93	A-45-2	98.74	2.19	0.87
B-30-1	80.79	2.69	1.01	B-45-1	104.17	2.31	0.91
B-30-2	80.79	2.69	0.99	B-45-2	104.17	2.31	0.99
C-30-1	107.21	3.57	1.12	C-45-1	142.28	3.16	1.00
C-30-2	107.21	3.57	1.18	C-45-2	142.28	3.16	1.04
Cusson and Paultre 1995							
A-30-1	63.23	2.11	1.18	A-45-1	82.53	1.83	1.08
A-30-2	63.23	2.11	1.12	A-45-2	82.53	1.83	1.04
B-30-1	66.72	2.22	1.23	B-45-1	86.47	1.92	1.09
B-30-2	66.72	2.22	1.20	B-45-2	86.47	1.92	1.20
C-30-1	97.12	3.24	1.24	C-45-1	120.80	2.68	1.18
C-30-2	97.12	3.24	1.31	C-45-2	120.80	2.68	1.23
Pliakoutas and Mortazavi 1997							
A-30-1	63.82	2.13	1.17	A-45-1	80.70	1.79	1.10
A-30-2	63.82	2.13	1.11	A-45-2	80.70	1.79	1.06
B-30-1	68.44	2.28	1.20	B-45-1	85.31	1.90	1.11
B-30-2	68.44	2.28	1.17	B-45-2	85.31	1.90	1.21
C-30-1	115.85	3.86	1.04	C-45-1	132.73	2.95	1.07
C-30-2	115.85	3.86	1.10	C-45-2	132.73	2.95	1.12

Table 7-4 Performance of selected confined models and compression with test data (cont)

Data set (1)	Theoretical values		Experimenta\Theoretical	Data set (2)	Theoretical values		Experimental\ Theoretical
	f'_{cc}	f'_{cc}/f'_{co}	f'_{cc}/f'_{cc}		f'_{cc}	f'_{cc}/f'_{co}	f'_{cc}/f'_{cc}
Karbhari and Gao 1997							
A-30-1	58.45	1.95	1.27	A-45-1	74.99	1.67	1.19
A30-2	58.45	1.95	1.22	A-45-2	74.99	1.67	1.14
B-30-1	62.21	2.07	1.32	B-45-1	78.95	1.75	1.20
B-30-2	62.21	2.07	1.29	B-45-2	78.95	1.75	1.31
C-30-1	98.16	3.27	1.22	C-45-1	116.85	2.60	1.22
C-30-2	98.16	3.27	1.29	C-45-2	116.85	2.60	1.27
Samaan et al. 1998							
A-30-1	64.22	2.14	1.16	A-45-1	79.22	1.76	1.12
A-30-2	64.22	2.14	1.11	A-45-2	79.22	1.76	1.08
B-30-1	67.82	2.26	1.21	B-45-1	82.82	1.84	1.14
B-30-2	67.82	2.26	1.18	B-45-2	82.82	1.84	1.25
C-30-1	99.12	3.30	1.21	C-45-1	114.12	2.54	1.25
C-30-2	99.12	3.30	1.28	C-45-2	114.12	2.54	1.30
Spoelstra and Monti 1999 (Approximate)							
A-30-1	60.34	2.01	1.23	A-45-1	78.80	1.75	1.13
A-30-2	60.34	2.01	1.18	A-45-2	78.80	1.75	1.09
B-30-1	64.36	2.15	1.27	B-45-1	83.96	1.87	1.13
B-30-2	64.36	2.15	1.24	B-45-2	83.96	1.87	1.23
C-30-1	95.78	3.19	1.25	C-45-1	124.33	2.76	1.15
C-30-2	95.78	3.19	1.32	C-45-2	124.33	2.76	1.19
Saafi et al. 1999							
A-30-1	62.99	2.10	1.18	A-45-1	78.80	1.75	1.13
A-30-2	62.99	2.10	1.13	A-45-2	78.80	1.75	1.09
B-30-1	67.21	2.24	1.22	B-45-1	83.96	1.87	1.13
B-30-2	67.21	2.24	1.19	B-45-2	83.96	1.87	1.23
C-30-1	100.16	3.34	1.20	C-45-1	124.33	2.76	1.15
C-30-2	100.16	3.34	1.27	C-45-2	124.33	2.76	1.19
Miyauchi et al.1999							
A-30-1	65.85	2.19	1.13	A-45-1	80.85	1.80	1.10
A-30-2	65.85	2.19	1.08	A-45-2	80.85	1.80	1.06
B-30-1	71.35	2.38	1.15	B-45-1	86.35	1.92	1.09
B-30-2	71.35	2.38	1.12	B-45-2	86.35	1.92	1.20
C-30-1	127.86	4.26	0.94	C-45-1	142.86	3.17	1.00
C-30-2	127.86	4.26	0.99	C-45-2	142.86	3.17	1.04

Table 7-4 Performance of selected confined models and compression with test data (cont)

Data set (1)	Theoretical values		Experimenta\Theoretical	Data set (2)	Theoretical values		Experimental\ Theoretical
	f'_{cc}	f'_{cc}/f'_{co}	f'_{cc}/f'_{cc}		f'_{cc}	f'_{cc}/f'_{co}	f'_{cc}/f'_{cc}
Toutanji revised 1999							
A-30-1	61.73	2.06	1.21	A-45-1	78.72	1.75	1.13
A-30-2	61.73	2.06	1.15	A-45-2	78.72	1.75	1.09
B-30-1	65.83	2.19	1.24	B-45-1	83.07	1.85	1.14
B-30-2	65.83	2.19	1.22	B-45-2	83.07	1.85	1.25
C-30-1	104.51	3.48	1.15	C-45-1	124.19	2.76	1.15
C-30-2	104.51	3.48	1.21	C-45-2	124.19	2.76	1.20
Theriailt and Neale 2000, Lam and Teng 2002, Wu et al. 2002							
A-30-1	54.06	1.80	1.38	A-45-1	69.06	1.53	1.29
A-30-2	54.06	1.80	1.32	A-45-2	69.06	1.53	1.24
B-30-1	57.75	1.93	1.42	B-45-1	72.75	1.62	1.30
B-30-2	57.75	1.93	1.39	B-45-2	72.75	1.62	1.42
C-30-1	95.68	3.19	1.25	C-45-1	110.68	2.46	1.29
C-30-2	95.68	3.19	1.33	C-45-2	110.68	2.46	1.34
Becque et al. 2003							
A-30-1	64.22	2.14	1.16	A-45-1	79.22	1.76	1.12
A30-2	64.22	2.14	1.11	A-45-2	79.22	1.76	1.08
B-30-1	67.82	2.26	1.21	B-45-1	82.82	1.84	1.14
B-30-2	67.82	2.26	1.18	B-45-2	82.82	1.84	1.25
C-30-1	99.12	3.30	1.21	C-45-1	114.12	2.54	1.25
C-30-2	99.12	3.30	1.28	C-45-2	114.12	2.54	1.30
Mandal et al. 2005							
A-30-1	39.28	1.31	1.89	A-45-1	53.11	1.18	1.68
A-30-2	39.28	1.31	1.81	A-45-2	53.11	1.18	1.61
B-30-1	41.46	1.38	1.98	B-45-1	54.88	1.22	1.72
B-30-2	41.46	1.38	1.93	B-45-2	54.88	1.22	1.89
C-30-1	82.13	2.74	1.46	C-45-1	85.75	1.91	1.66
C-30-2	82.13	2.74	1.55	C-45-2	85.75	1.91	1.73

The average prediction values for both data set 1 and 2 obtained by Fardis and Khalili's, Theriailt and Neale's, Lam and Teng's, and Wu et al.'s models are approximately equal to 1.30, which means that it is in safe side and conservative. On the other hand, the eight remaining models of Cusson and Paultre, Pliakoutas and Mortazavi , Karbhari and Gao, Samaan et al. Spoelstra and Monti 1999 (Approximate), Saafi et al. , Toutanji revised and Becque et al give very similar predictions which are conservative and show the

experimental to the theoretical ultimate confined strength ratios ranged from 1.10 to 1.25. They also show the best statistical performance when assessed using either data set 1 or 2. In general, it is observed that the predictions values of the different models for data of set (1) are more conservatively than that of data of set (2). However, the unconfined concrete compressive strength of data set (1) is lower than that of data set (2).

Table 7-5 Statistical performance of strength model for CFFT specimens

Model	Test –to-Theoretical f'_{cc}							
	Data Set (1) (f'_{co} =30 MPa)				Data Set (2) (f'_{co} =45 MPa)			
	M	SD	CV	AAD	M	SD	CV	AAD
Richart et al. 1929	0.86	9.30	10.70	0.078	0.90	8.10	8.97	0.061
Fardis and Khalili 1981	1.32	6.10	4.59	0.049	1.29	6.20	4.77	0.044
Mander et al. 1988, Spoelstra and Monti 1999 (Exact)	1.03	9.70	9.38	0.078	0.95	7.00	7.36	0.061
Cusson and Paultre 1995	1.21	6.10	5.05	0.045	1.13	7.70	6.75	0.066
Pliakoutas and Mortazavi 1997	1.13	5.90	5.26	0.048	1.11	5.40	4.83	0.035
Karbhari and Gao 1997	1.26	4.00	3.17	0.032	1.22	6.10	5.01	0.046
Samaan et al. 1998	1.19	5.80	4.87	0.042	1.19	8.80	7.36	0.076
Spoelstra and Monti 1999 (Approximate)	1.25	4.80	3.84	0.032	1.15	5.30	4.58	0.041
Saafi et al. 1999	1.19	4.50	3.78	0.030	1.15	5.30	4.58	0.041
Miyauchi et al.1999	1.06	8.50	7.92	0.069	1.08	6.90	6.34	0.050
Toutanji revised 1999	1.19	3.90	3.21	0.031	1.15	5.60	4.81	0.042
Theriailt and Neale 2000, Lam and Teng 2002, Wu et al. 2002	1.34	5.90	4.40	0.048	1.31	6.30	4.78	0.046
Becque et al. 2003	1.19	5.80	4.87	0.042	1.19	8.80	7.36	0.076
Mandal et al. 2005	1.77	21.5	12.15	0.178	1.71	9.50	5.51	0.065

M: Mean, SD: Standard Deviation (%), CV: Coefficient of Variation (%), AAD: The Average Absolute Deviation.

7.6 Conclusions

This paper has presented an experimental and theoretical study on the compressive strength of the CFFT cylinders. Existing strength model for FRP-confined concrete have been reviewed and compared with the experimental results. The following conclusions can be deduced from the study:

1. The ultimate strength of the CFFT is mainly dependent on the stiffness of the GFRP tubes, and it is more effective for normal than medium concrete strength.
2. The initial dilation ratios for all specimens appear to be the same having a value approximately equals to Poisson's ratio for the unconfined concrete, the peak dilation values depend on the confinement level of the GFRP tubes.
3. The study shows that the FRP tensile properties were obtained from ring split-disk test are conservatively to predict the ultimate confined concrete strength of the CFFT cylinders.
4. It has been found that the steel-based models are not safe to predict the behaviour of the CFFT cylinders.
5. Some of the existing models have found to be overestimate, while the others predict the confined strength close to the experimental results in the safe side. These models can be used with appropriate reduction factors for the ultimate strength design of the CFFT applications.

Chapter 8
Summary and Conclusions

8.1 Summary

The current study has investigated the behaviour of concrete filled-FRP tubes (CFFT) columns and beams. The study included experimental and analytical investigations. In the experimental program, the CFFT columns were reinforced internally with steel bars, while the CFFT beams were reinforced with steel or GFRP bars. New filament-wound FRP tubes were used as stay-in-place form works for the columns and beams. Normal and medium-strength concrete were used to cast the columns and beams.

The experimental program included a total of thirty seven columns (short and long) and ten beams tested to failure. The columns were tested using concentric and eccentric loading conditions. The beams were tested under four point bending. The test results provided priceless information on the behaviour of reinforced CFFT columns and beams.

As regards short CFFT columns, the test results of experimental investigation combined with other reported data in the literature were evaluated using regression analysis and a number of comparisons. These analyses were used to evaluate the validity of the confinement models and design equations of the three North America, ACI 440.2R-08, CSA S6-06 and CSA S806-02 guidelines. Simple nonlinear empirical model for confined ultimate strength of CFFT has been proposed. The proposed model, used in conjunction with reduction factor can be employed for the ultimate confined strength. In addition, step-by-step design equations were proposed to predict the factored ultimate load resistance of the CFFT columns.

As regards slender CFFT columns, CFFT columns of different heights, 305, 608, 912, 1216 and 1520 mm were tested under uniaxial compression load. The effect of three parameters and their interactions on the buckling behavior were investigated; namely, the FRP tube thickness, concrete compressive strength, and slenderness ratio. The theoretical study is then introduced to verify the accuracy of existing critical buckling load formulas. The analysis indented to understand the effect of the slenderness ratio on the critical buckling load of axially loaded CFFT columns. This involved introducing buckling formulas of CFFT columns, strength curve and design example for these CFFT columns.

As regards CFFT beams, the experimental investigation included a total of ten beam specimens, approximately 213 mm in diameter and 2.00 m in length, tested in four-point bending. Six RCFFT beams and four conventional reinforced concrete (RC) circular beams with and without spiral reinforcement were cast in the experimental program to extend the data base for RCFFT beams. Glass FRP bars and conventional steel bars were used in reinforcing concrete beams. Five of the test beams were constructed using normal strength concrete (30 MPa), and five beams using medium strength concrete (45 MPa). The analytical investigation included analysis of the tested RCFFT using the conventional beam theory to predict the yield and ultimate strengths. In addition, the moment-deflection responses and the effective moments of intertie of the tested RCFFT beams were analyzed using different available equations in the literature, codes (ACI 318-08; CSA A23.3-04; SAA 2001) and design guidelines (ACI 440.1R-06; ISIS 2001). The results obtained from each analysis were compared to the corresponding experimental results. Based on the results of this comparison and the experimental finding, a proposed modification to the existed design equations for predicting the effective moment of inertia was presented.

8.2 Conclusions

The following general conclusions can be drawn based on the experimental and analytical research work presented in this dissertation:

8.2.1 Reinforced CFFT columns

8.2.1.1 Short CFFT columns under concentric loading

6. The experimental test results of this study indicated that the confinement provided by the GFRP tubes improved both the load-carrying capacities and the ductility of the columns.
7. The stress-strain responses in the axial and lateral directions of reinforced and unreinforced CFFT columns are bilinear. The first slope of the response depends basically on the concrete core, while the second slope depends mainly on the hoop stiffness of the FRP tube.
8. The longitudinal steel bars provide significant dowel action, which delays the dilation of concrete core inside CFFT, thereby improving the ductility of CFFT columns.
9. The modes of failure of the short CFFT specimens were characterized mainly by FRP tubes rupture in the hoop direction.
10. The load-carrying capacities of the CFFT are considerably higher than the conventional RC columns. The strength enhancement is depended of the stiffness of the FRP tube in the hoop direction. Whereas, increasing the thickness of the GFRP tubes significantly improved the ultimate load capacities of tested specimens.
11. The test results indicated that the yield load of CFFT columns occurred at level approximately equal to 60% of the ultimate load.
12. Limiting f_{LFRP} to be $\leq f_c'$ by CSA S6-06, and limiting FRP hoop tensile strength to 0.004 its elastic modulus E_{FRP} by CSA S806-02 leads to a conservative prediction for confined concrete compressive strength.
13. The CSA S6-06 and CSA S806-02 confinement models showed conservative predictions, while the ACI was slightly less conservative (when the reduction factors were used for the three codes).
14. The confinement models calibrated for steel-confined concrete are not applicable to CFFT.

15. The design guidelines of the ACI 440.2R-08, CSA S6-06 and CSA S806-02 overestimate the factored axial load capacity of the reinforced and unreinforced CFFT columns, whereas the ACI predictions were the least conservative.
16. The code design equations for factored axial load capacity must deal with the cracking or yielding load level of the FRP-confined columns.
17. For concrete strength up to 60MPa confined model is proposed

$$f_{cc}^{'} = f_{c}^{'}\left[0.7 + 2.7\left(\frac{f_{lFRP}}{f_{c}^{'}}\right)^{0.7}\right]$$

18. Based on the test results of the reinforced and unreinforced CFFT columns in this study with other reported data in the literature, the following expression is proposed for the factored ultimate load capacity:

- Reinforced CFFT columns

$$P_r = 0.85\phi k_{cr}\left[k_{cc}f_{cc}^{'}(A_g - A_s) + f_y A_s\right]$$

- Unreinforced CFFT columns

$$P_r = 0.80\phi k_{cr}\left[k_{cc}f_{cc}^{'}A_g\right]$$

where,

a. k_{cc} is a new factor introduced to account for the in-place-strength of CFFT columns to CFFT cylinder strength,($f_{cc(column)}^{'}/f_{cc(cylinder)}^{'}$). k_{cc} is taken 0.80 and 0.75 for the reinforced and unreinforced CFFT columns, respectively.
b. New product ($k_{cr} = 0.6$) is proposed to account for the initiation of the steel yielding and concrete cracking for the FRP-confined columns.
c. The product value of 0.85 or 0.80 is introduced as a strength reduction factor for unexpected eccentricities for the reinforced and unreinforced CFFT columns, respectively.

8.2.1.2 Slender CFFT columns under concentric loading

19. Both the axial strength and stiffness after yielding of slender columns were increased as a result of the confining effect of the FRP tubes;
20. The level of confinement effectiveness for CFTT specimens featuring similar FRP volumetric ratio (and therefore same cross-sectional area), decreases as the slenderness ratio increases. Because for the slender columns the failure occurs due to buckling instability before attaining the full confinement.
21. The enhancement of the axial strength of the slender columns is more pronounced for the lower strength concrete (30 MPa) than that for the higher strength concrete (45 MPa).
22. Increasing the thickness of the GFRP tubes significantly improved the ultimate load capacities of tested slender CFFT columns.
23. The modes of failure of the slender CFFT specimens were characterized mainly by buckling instability.
24. The uniaxial compressive strength of CFFT was reduced by 13% to 23% with increasing the slenderness ratio from 12 to 20 depending on the concrete compressive strength and thickness of FRP tubes.
25. Simplified formula for the limit slenderness ratio was proposed for the design purposes of CFFT columns. The predicted value according to the proposed formula agree with the observed critical slenderness ratio ($\lambda = 12$) and with the recommended value in the literature.
26. It was found that the predicted slenderness limit slightly affected by both the concrete compressive strength and FRP tube thickness, however it was reduced with increasing the thickness of the confining FRP tubes.

8.2.1.3 Short CFFT columns under eccentric loading

27. The behaviour of CFFT columns under eccentric loads is completely different as compared to those tested columns under concentric loads.
28. The load carrying capacities of CFFT columns under load eccentricities, e/D from 0.10, 0.2, 0.3 and 0.4 were reduced by 48, 61, 71 and 77%, respectively, as

compared to the load carrying capacities of the same CFFT columns under concentric load.

29. The axial and lateral deformations were increased progressively with increasing the eccentricity values.
30. The stress-strain curve of the CFFT columns under eccentric loads is nonlinear and exhibited softening after peak load. However, the slope of the descending region of the stress-strain relationship is steeper for columns with higher eccentric value.
31. The failure mode of the CFFT columns is dependent on the type of loading. For the short columns, the rupture of the FRP tube tubes in the hoop direction and local buckling of internal steel bars are the dominant in case concentric. While the combination of tensile rupture in the axial direction and excessive axial and lateral deformations are the dominant in case eccentric loading.

8.2.2 Reinforced CFFT beams

32. All the CFFT beams tested to failure in this study, failed in flexural. The prevailing flexural mode of failure was the tensile rupture of the FRP tube in the longitudinal direction with ruptures the reinforcing bars in the tension side. However, diagonal tension failure at the shear span and shear compression failure were the final failure modes for the RC control beams without and with spiral steel, respectively. This indicted that the FRP tube changed the mode of failure from shear to flexural failure. All the CFFT beams reinforced with steel or FRP bars exhibited progressive and sequential failure manner, leading to a remarkable pseudo-ductile behaviour.
33. The experimental test results indicated that the beams confined by FRP tubes experienced lower deflection, higher cracking load level, higher ductility, higher stiffness and superior strength than the beam reinforced with a spiral-steel.
34. From the load-flexural hoop strain curves at the mid-span of the tested beams, it was confirmed that the FRP tubes were activated to confine the concrete core of

the beam. The steel-RCFFT beams experienced higher level of confinements than the FRP-RCFFT beams.

35. It was found that the confinement provided by the FRP tubes improved the tension stiffening of the tested beams, which in turn increased the effective moment of inertia of the tested beam after cracking as compared to the conventional RC beams.
36. For normal and medium strength concrete, the test results indicated that the ratio of the strength of FRP-RCFFT beams to that of steel-RCFFT beams was 60%. This ratio approximately equals the cube root of axial stiffness ratio between glass FRP and steel bars $\sqrt[3]{\rho_{fl} E_{fl} / \rho_{sl} E_{sl}}$. On the other hand, the ductility of reinforced CFFT beams depends significantly on the type of the internal reinforcement. The ductility of steel-RCFFT beams is substantially higher than that of FRP-RCFFT beams.
37. It was observed that the effect of two types of concrete considered in this study on the flexural behaviour of tested CFFT beams was insignificant. It was observed that the strength, deflection and ductility of the CFFT beams were affected significantly by the axial stiffness of the FRP tubes. On the other hand, it was found that the average ratio of the experimental flexural strength was equal to the 3.5 root of the axial stiffness ratio (axial modulus of elasticity multiplied by the FRP tube thickness) between the two tubes, $\sqrt[3.5]{(E_{fl} t_{FRP})_{tube\,No.2} / (E_{fl} t_{FRP})_{tube\,No.1}}$, where tube No.1 has smaller thickness.
38. The equations provided by ACI 318-08 code and ACI 440.1R-06 design guidelines for reinforced concrete structures with steel and FRP bars, respectively, and both CAN-CSA S806-02-CSA standard A23.3 and CAN-CSA S6-06 codes underestimated the modulus of rupture of RCFFT beams. The test results indicated that the cracking moment of CFFT beams was occurred at a higher load level than that of RC beams. Based on the test results a modification to the code and design guidelines equations was suggested for predicting the modulus of rupture of RCFFT beams.

39. The conventional beam theory can be used for the analysis and design of the CFFT beams, assuming that the bond between the tube and the concrete is fully developed. The traditional procedures were found to be acceptable for predicting the ultimate and yield moments capacities of the under-reinforced FRP or steel-RCFFT beams cross section condition. The accuracy of the theoretical analysis procedures pertained good agreement with measured values. The strain at the bottom steel or FRP bars was used as a reference and the neutral axis depth ratio was determined using two new proposed empirical equations.
40. The experimental results of tested RCFFT beams in four point loading bending with varying properties revealed that the current conventional or modified models available in the literature, codes (ACI 318-08; CSA A23.3-04; SAA 2001) and design guidelines (ACI 440.1R-06; ISIS 2001) for predicting the effective moment of inertia of beams reinforced by steel or FRP bars, respectively, over-estimates the deflections in these beams and therefore it needs to be revised.
41. For reinforced CFFT beams, the transition between gross and cracked section properties is gradually. The basic cubic parabolic form of the Branson equation is a poor mathematical shape for predicting the change in stiffness of steel or FRP-RCFFT beams. The loss in stiffness for CFFT beams is much less than that for companion steel or FRP-reinforced sections. As such, the intended nonlinear transition between gross and cracked section properties does not occur for RCFFT beams in the same way as for steel or FRP-reinforced flexural not confined members.
42. It was observed that, in case of steel or FRP-RCFFT members, the behaviour under the flexural load was significantly different than that of steel or FRP RC members. This attributed to the confinement of the concrete core and the axial contribution of the FRP tube which in turn enhance the overall flexural behaviour and improve the tension stiffening of RCFFT beams. Therefore, the tension stiffening predicted for steel or FRP-RCFFT beams using the available equations (steel or FRP-RC member) is underestimated and hence the predicted deflections are overestimated.

43. The current form of I_e, as recommended in North American codes and design guidelines, underestimate this parameter for steel and FRP reinforced concrete beams confined with glass-FRP tubes.
44. For steel and GFRP-RCFFT beams, the transition between gross and cracked section properties is much more gradual than that of conventional RC beams.
45. For GFRP-RCFFT beams, the ratio of gross-to-cracked section properties (I_g/I_{cr}) is between two and three times higher than that for hypothetical steel- RCFFT samples. As such, I_e approaches I_{cr} much faster for RCFFT beams reinforced with GFRP than with steel;
46. The basic cubic parabolic form of the Branson equation is a poor mathematical shape for predicting the change in stiffness of steel and GFRP RCFFT beams. The loss in stiffness for RC- beams is much greater than that for RCFFT beams. As such, the intended nonlinear transition between gross and cracked section properties does not occur for RCFFT beams in the same way as for RC-beams.
47. New proposed equations and a proposed modification to the equations of effective moment of inertia were presented for steel and FRP-RCFFT beams. The modification is based on experimental findings, which represent the potential of empirical and semi-empirical formulations. The new equations account to the change in the confinement effectiveness and the type of internal reinforcing bars. The proposed equations were used to calculate the effective moment of inertia of the tested RCFFT beams, which in turn used to calculate the moment-deflection response. The calculated effective moment of inertia and the moment-deflection response were compared to the experimental ones. It was observed that the proposed equations gave accurate predictions over the range of variables tested parameters to affect the moment-deflection response.

Résumé et Conclusions

Résumé

L'étude suivante présente l'analyse du comportement des tubes, poteaux et poutres en PRF remplis de béton (CFFT). Elle comprend des études expérimentale et analytique. Dans le programme expérimental, les poteaux CFFT ont été renforcés intérieurement avec des barres en acier, cependant les poutres CFFT ont été renforcées avec de l'acier ou des barres en PRF de verres (PRFV). De nouveaux tubes en PRF d'enroulement filamentaire ont été utilisés comme des coffrages perdus pour les poteaux et les poutres. Des bétons de résistance moyenne et ordinaire ont été utilisés pour fabriquer les poteaux et les poutres.

Au total trente sept poteaux (courts et longs) et dix poutres prévus dans ce programme expérimental, ont été testés jusqu'à rupture. Les poteaux ont été testés en utilisant des charges concentrées et excentrées. Les poutres ont été testées à la flexion à quatre points. Les résultats expérimentaux ont fourni des informations inestimables sur le comportement des poteaux et des poutres CFFT renforcés.

En ce qui concerne les poteaux CFFT courts, les résultats d'essai de l'étude expérimentale combinés avec d'autres résultats rapportés de la littérature ont été évalués en utilisant l'analyse de régression et un certain nombre de comparaisons. Ces analyses ont été utilisées pour évaluer la validité des modèles de confinement et des équations de conception des trois guides de l'Amérique du Nord, ACI 440.2R-08, CSA S6-06 et CSA S806-02. Un modèle empirique non linéaire simple a été proposé pour la résistance ultime de confinement des poteaux CFFT. Le modèle proposé, utilisé conjointement avec le facteur de réduction, peut être utilisé pour la résistance ultime de confinement. En outre, des équations de conception étape-par-étape ont été proposées pour prédire la résistance de charge ultime factorisée des poteaux CFFT.

En ce qui concerne les poteaux CFFT élancé, des poteaux CFFT de différentes hauteurs: 305, 608, 912, 1216 et 1520 mm ont été testés sous charges de compression uniaxiale. Les effets des trois paramètres et leurs interactions sur le comportement au flambement ont été étudiés à savoir l'épaisseur de tube en PRF, la résistance du béton à la compression, et le rapport d'élancement. L'étude théorique est alors introduite pour vérifier l'exactitude des formules de la charge critique de flambement existantes. Des analyses ont été faites pour comprendre l'effet du rapport d'élancement sur la charge critique de flambement des poteaux CFFT axialement chargés. Ceci nous a entraînés d'introduire les formules de flambement des poteaux CFFT, la courbe de résistance et un exemple de conception pour ces poteaux CFFT.

En ce qui concerne les poutres CFFT, au total, dix échantillons de poutres prévus dans cette étude expérimentale, approximativement de 213 mm de diamètre et 2.00 m de longueur, ont été testés à la flexion à quatre points. Six poutres CFFT renforcées et quatre poutres circulaires en béton conventionnel renforcé avec et sans armatures spirales ont été fabriquées dans le programme expérimental pour étendre la base de données des poutres CFFT renforcées. Des barres en PRF de verre et des barres en acier conventionnel ont été utilisées pour le renforcement du béton des poutres. Cinq des poutres d'essai ont été fabriquées en utilisant un béton de résistance normale (30 MPA), et cinq poutres en utilisant un béton de résistance moyenne (45 MPA). L'étude analytique comprend l'analyse des CFFT testés en utilisant la théorie conventionnelle de poutres pour prédire la limite élastique et ultime. En outre, les réponses de moment - déflection et les moments d'inertie efficaces des poutres CFFT renforcées testées ont été analysés en utilisant différentes équations disponibles dans la littérature, les codes (ACI 318-08; CSA A23.3-04; SAA 2001) et les guides de conception (ACI 440.1R-06; ISIS 2001). Les résultats obtenus à partir de chaque analyse ont été comparés aux résultats expérimentaux correspondants. Basant sur les résultats de cette comparaison et les résultats expérimentaux trouvés. Une modification aux équations de conception existantes pour prédire le moment d'inertie efficace a été présentée

Conclusions

Les conclusions générales que l'on peut tirer de cette étude expérimentale et analytique sont comme suit:

Poteaux CFFT renforcés

Poteaux CFFT courts sous chargement concentrique

1- Les résultats expérimentaux de cette étude indiquent que le confinement fourni par les tubes en PRF de verre améliore les capacités portantes et la ductilité des poteaux.

2- Les réponses de contrainte-déformation dans les directions axiale et latérale des poteaux CFFT renforcés et non renforcés sont bilinéaires. La première pente de la réponse dépend fondamentalement du noyau de béton, cependant la deuxième pente dépend principalement de la rigidité circonférentielle du tube en PRF.

3- Les barres d'acier longitudinales fournissent une action significative qui retarde la dilatation du noyau de béton à l'intérieur de CFFT en améliorant de ce fait la ductilité des poteaux CFFT.

4- Les modes de rupture des échantillons de CFFT courts ont été caractérisés principalement par des ruptures de tubes en PRF dans la direction circonférentielle.

5- La capacité portante de CFFT est considérablement plus haute que le poteau conventionnel en béton armé. L'amélioration de la résistance dépend de la rigidité du tube en PRF dans la direction circonférentielle. Néanmoins, l'augmentation de l'épaisseur des tubes en PRFV a amélioré significativement les capacités de charges ultimes des échantillons testés.

6- Les résultats d'essai ont indiqué que la charge limite des poteaux CFFT s'est produite au niveau approximativement égal à 60% de la charge ultime.

7- Limitant le f_{LFRP} d'être $\leq f_c'$ par CSA S6-06 et limitant la résistance à la traction circonférentielle de PRF à 0.004 de son module élastique par CSA S806-02 conduit à une prédiction conservatrice de la résistance à la compression du béton confinée.

8- Les modèles de confinement de CSA S6-06 et de CSA S806-02 ont montré des prédictions conservatrices, cependant l'ACI est légèrement moins conservatrice (quand les facteurs de réduction sont utilisés pour les trois codes).

9- Les modèles de confinement calibrés pour le béton confiné en acier ne s'appliquent pas aux CFFT.

10- Les guides de conception de l'ACI 440.2R-08, de CSA S6-06 et de CSA S806-02 surestiment la capacité de charge axiale factorisée pour les poteaux CFFT renforcés et non renforcés, tandis que les prédictions de l'ACI ont été moins conservatrices.

11- Les équations de conception des codes pour la capacité de charge axiale factorisée doivent traiter le niveau de fissuration ou le niveau de charge limite des poteaux en PRF-confinés.

12- Pour la résistance du béton jusqu'au 60MPa, un modèle confiné est proposé

$$f_{cc}^{'} = f_{c}^{'}\left[0.7 + 2.7\left(\frac{f_{lFRP}}{f_{c}^{'}}\right)^{0.7}\right]$$

13- Basant sur les résultats d'essai de poteaux CFFT renforcés et non renforcés dans cette étude avec d'autres données rapportées de la littérature, l'expression suivante est proposée pour la capacité de charge ultime factorisée :

- Poteaux CFFT renforcés

$$P_r = 0.85\phi k_{cr}\left[k_{cc}f_{cc}^{'}(A_g - A_s) + f_y A_s\right]$$

- Poteaux CFFT non renforcées

$$P_r = 0.80\phi k_{cr}\left[k_{cc}f_{cc}^{'}A_g\right]$$

où,

a. k_{cc} est un nouveau facteur introduit pour tenir compter du rapport de la résistance en place des poteaux CFFT à la résistance de cylindre CFFT, $(f_{cc(column)}^{'}/f_{cc(cylinder)}^{'})$. k_{cc} est pris égale à 0.80 et 0.75 pour les poteaux CFFT renforcés et non renforcés, respectivement.

b. un nouveau produit ($k_{cr} = 0.6$) est proposé pour tenir compte du début d'écoulement de l'acier et de la fissuration du béton pour les poteaux confinés en PRF

c. La valeur de produit de 0.85 ou de 0.80 est introduite comme facteur de réduction de la résistance pour des excentricités inattendues pour les colonnes CFFT renforcées et non renforcées, respectivement.

Colonnes CFFT élancées sous charge axiale concentrique

14- L'effet du confinement des tubes de PRF a contribué à l'augmentation de la résistance et rigidité axiale des colonnes élancées.

15- L'efficacité du confinement diminue à mesure que l'élancement augmente; la rupture des colonnes élancées est due au flambement des ces dernières avant la rupture du PRF.

16- Le gain de résistance pour les colonnes élancées diminue avec l'augmentation de la résistance du béton utilisé.

17- L'augmentation de l'épaisseur des tubes de PRFV augmente d'une manière significative la résistance des colonnes élancées.

18- Le diagramme contrainte-déformation des colonnes élancées en béton, confinées dans des tubes de PRFV est bilinéaire.

19- Le mode de rupture des colonnes élancées, confinées par des tubes de PRF est dû au flambage (instabilité).

20- L'augmentation de l'élancement des colonnes confinées par des tubes de PRF de 12 à 20 a diminué la résistance en compression uniaxiale de 13 à 23%. la résistance à la compression uniaxiale des colonnes élancées à été réduite de 13 à 23 % en fonction de la résistance du béton et de l'épaisseur du tube de PRF, et ceci avec l'augmentation de l'élancement de 2 à 20

21- un modèle simplifié pour trouver l'élancement critique a été proposé pour les colonnes confinées par tubes de PRF. La valeur trouvé avec ce modèle est en accord avec l'élancement trouvé dans la littérature.

22- l'élancement critique est légèrement affecté par l'épaisseur du tube et la résistance à la compression du béton, il baisse avec l'augmentation de l'épaisseur du tube

Colonnes CFFT courtes sous charge axiale excentrée

23- Le comportement des colonnes confinées, sous charge excentrée est complètement différent de celui sous charge concentrique.

24- La résistance en compression des colonnes confinées dans des tubes de PRF, sous charge excentrée e/D de 0.10, 0.2, 0.3 et 0.4 a été diminuée de 48, 61, 71 et 77 % respectivement, par rapport à la même colonne sous charge concentrique.

25- L'augmentation de l'excentricité augmente les déformations axiales et latérales.

26- Le diagramme contrainte-déformation des colonnes en béton, confinées dans des tubes de PRF sous charge excentrée est non linaire, et comprend une branche descendante après le pic. La pente de la branche descendante augmente avec l'excentricité.

27- Le mode de rupture des colonnes confinées avec des tubes de PRF dépend du type de chargement; pour le chargement concentrique, on obtient une rupture du tube de PRF accompagné du flambement des armatures longitudinales en acier. alors que pour le chargement excentrique, elle est due à des déformations axiales et latérales excessives.

Poutre CFFT renforcés

28- Toutes les poutres en CFFT testées cette étude ont rompu en flexion. Le mode de rupture e flexion prédominant est la rupture à en traction du tube de PRF dans la direction longitudinale avec ruptures des barres d'armature du côté tendu. Toutefois, une rupture diagonale en traction dans la travée de cisaillement ainsi qu'une rupture en compression par cisaillement ont été les modes de ruptures finaux des poutres témoins en Béton Armé sans et avec spirale en acier respectivement. Ceci a montré que le tube en PRF a changé le mode de rupture de la rupture en cisaillement à la rupture en flexion.

29- Toutes les poutres renforcées avec des barres d'acier ou de PRF ont exhibés une rupture progressive et séquentielle, conduisant à un comportement pseudo-ductile remarquable.

30- Les résultats expérimentaux ont montré que les poutres confinés par des tubes en PRF ont montré une basse déflexion, un plus haut niveau de charges d'apparition de fissures, une plus grande ductilité, une plus grande rigidité et une meilleure résistance comparée à la poutre renforcée avec une spirale d'acier.

31- À partir des courbes de déformation circonférentielle à mi-travée des poutres testées, il a été confirmé que les tubes en PRF ont été activés pour confiner le noyau en béton de la poutre. Les poutres acier-CFFT ont montré un plus grand niveau de confinements que les poutres en FRP-RCFFT.

32- Il a été trouvé que le confinement donné par les tubes en PRF améliore la rigidité en traction des poutres testées, ce qui à son tour augmenté le moment d'inertie effectif de la poutre testée après fissure tel que comparé avec les poutres conventionnelles en Béton Armé.

33- Pour un béton de résistance normale et moyenne, les résultats d'éssais ont montré que le rapport de la résistance des poutres PRF-CFFT à celui des poutres acier-CFFT était de 60%. Ce rapport est approximativement égal à la racine cubique du quotient de la rigidité axiale entre les barres de PRF de verre et l'acier $\sqrt[3]{\rho_{fl} E_{fl} / \rho_{sl} E_{sl}}$. En d'autres parts, la ductilité des poutres renforcées CFFT dépend significativement du type de renforcement interne. La ductilité des poutres acier- CFFT est substantiellement plus élevée que celle des poutres PRF- CFFT.

34- Il a été observé que l'effet des deux types de béton considérés dans cette étude sur le comportement à la flexion des poutres CFFT était non significatif. Il a été observé que la résistance, la déflexion et la ductilité des poutres en CFFT ont été significativement affectées par la rigidité axiale des tubes en PRF. D'un autre coté, il a été trouvé que le ratio moyen de

la résistance expérimentale à la flexion était égal à la racine 3.5 du quotient de la rigidité axiale (module d'élasticité axial multiplié par l'épaisseur du tube en PRF).

35- Les équations données par les normes ACI 318-08 et ACI 440.1R-06 pour les structures en béton renforcées avec des barres d'acier et de PRF, respectivement, ainsi que chacune des normes A23.3 et CAN-CSA S6-06 sous-estiment les modules de rupture des poutres CFFT. Les résultats expérimentaux ont indiqués que le moment de fissure des poutres CFFT s'est produit à un niveau de charge plus élevé que celui des poutres en Béton Armé. En se basant sur les résultats d'essais, une modification au code et aux équations de dimensionnement a été suggéré pour la prédiction du module de rupture des poutres CFFT

36- La théorie conventionnelle des poutres peut être utilisée pour l'analyse et le dimensionnement des poutres CFFT, en assumant que l'interface entre le tube et le béton est complètement développée. Les procédures traditionnelles ont été trouvées acceptables pour la prédiction des moments ultime et plastique de la condition de la section transversale des poutres sous-renforcées en PRF acier- CFFT. La précision de l'analyse théorique des procédures a trait avec les valeurs mesurées. La déformation en bas des barres d'acier ou de PRF a été utilisée comme référence et le ratio de la profondeur de l'axe neutre a été déterminé en utilisant deux nouvelles équations empiriques proposées.

37- Les résultants expérimentaux des poutres CFFT testées en flexion quatre points avec des propriétés variées ont révélé que les modèles courants conventionnels ou modifiés disponibles dans la littérature, dans les normes (ACI 318-08; CSA A23.3-04; SAA 2001) et les lignes directrices de dimensionnement (ACI 440.1R-06; ISIS 2001) pour la prédiction du moment d'inertie effectif des poutres renforcées avec des barres d'acier ou de PRF, respectivement, surestiment les déflexions dans ces poutres et nécessitent par conséquent d'être révisés.

38- Pour les poutres renforcées CFFT, la transition entre les propriétés de la section brute et transversale est graduelle. La forme parabolique cubique de base de l'équation de Branson est une forme mathématique faible pour la prédiction du changement dans la rigidité des poutres en acier ou PRF-CFFT. La perte de rigidité des poutres CFFT est beaucoup moindre que celle des sections renforcées d'acier ou de PRF. En tant que tel, la transition non linéaire prévue entre les propriétés de la section brute ou fissurée ne se produit pour les poutres CFFT de la même façon que pour les éléments flexionnels non confinés renforcés d'acier ou de PRF.

39- Dans le cas des composantes de CFFT renforcées d'acier ou de RPF, le comportement observé sous charge de flexion était significativement différent de composantes en béton

renforcées d'acier ou de PRF. Ceci était attribuable au confinement du cœur de béton et à la contribution axiale du tube de PRF, qui du fait contribue au comportement global en flexion et améliore la raideur en tension des poutres CFFT. La raideur en tension des poutres RCFFT renforcées d'acier et de PRF prédite par les équations disponibles (composantes en béton renforcées d'acier ou de PRF) s'en retrouve sous-estimée et les déformations prédites sont donc surestimées.

40- La forme actuelle de Ie, telle que recommandée par les codes et guides de conceptions nord américains, sous-estime ce paramètre pour les poutres confinées de tube de PRF-verre et renforcées d'acier et de PRF.

41- Dans le cas des poutres CFFT renforcées d'acier et de PRFV, la transition entre les propriétés de section moyenne et à l'état fissuré est beaucoup plus graduelle que pour les poutres en béton renforcées conventionnelles.

42- Le rapport des propriétés de section moyenne/fissurée (Ig/Icr) des poutres CFFT renforcées de PRFV est entre deux et trois fois plus élevé que celui d'échantillons hypothétiques de type CFFT renforcés d'acier. Le paramètre Ie tend donc vers Icr beaucoup plus vite pour les poutres de CFFT renforcées de PRFV que celles renforcées d'acier.

43- La forme cubique parabolique élémentaire de l'équation de Branson constitue une mauvaise fonction mathématique pour prédire le changement en rigidité des poutres CFFT renforcées d'acier ou de PRFV. La perte en rigidité des poutres en béton renforcé est beaucoup plus grande que celle des poutres CFFT. La transition non-linéaire attendue entre les propriétés de section moyenne et fissurée des poutres CFFT ne se produit pas de la même façon que pour les poutres en béton renforcés.

44- De nouvelles équations ainsi qu'une modification à l'équation de moment d'inertie effectif ont été proposées pour les poutres CFFT renforcées d'acier et de PRF. La modification est basée sur des observations expérimentales, qui englobent le potentiel des formulations empiriques et semi-empiriques. Les nouvelles équations tiennent compte de la différence dans l'efficacité du confinement et du type de barre de renforcement interne. Les équations proposées ont été utilisées pour calculer le moment d'inertie effectif des poutres CFFT évaluées, qui a ensuite servit à calculer la réponse moment/déflexion. Le moment d'inertie effectif et la réponse moment/déflexion calculées ont été comparés à ceux obtenus expérimentalement. Il a été observé que les équations proposées fournissent des prédictions précises sur l'intervalle de variation évalué pour les paramètres affectant la réponse moment-déflexion.

8.3 Recommendations for Future Work

Based on the findings and conclusions of the current study, the following recommendations are made for future research:

1. More research is needed to study the effect of internal reinforcement ratio on the behaviour of CFFT beams.
2. Research is needed to systematically investigate the size effect on the flexural strength of RCFFT beams.
3. Additional experimental works on large scale RCFFT beams are needed to investigating the applicability of the proposed equations of this study to predict the effective moment of inertia.
4. Research is needed to quantify the compressive strength of short and slender CFFT columns reinforced with glass or carbon FRP bars.
5. More experiments works on large scale RCFFT columns are needed to investigate the applicability of the proposed equations of this study to predict the yield and ultimate compressive strength of RCFFT columns.

REFERENCES

AASHTO, (2009), "American Association of State Highway and Transportation Officials," pp. 104.

Abdalla, H. A., (2002) "Evaluation of deflection in concrete members reinforced with fibre reinforced polymer (FRP) bars," Journal Composite Structure, Vol. 56, pp. 63-71.

Ahmad, I., (2004) "Shear Response and Bending Fatigue Behavior of Concrete-Filled Fiber Reinforced Polymer Tubes," Ph.D. Thesis, North Carolina State University, Raleigh, NC, 195 p.

Ahmad, I., Zhu, Z., and Mirmiran, A., (2005), "Behavior of short and deep beams made of concrete-filled fiber-reinforced polymer tubes," Journal of Composite for Construction, Vol. 12, No. 1, pp. 102-110.

Ahmad, I., Zhu, Z., and Mirmiran, A., (2006) "Splicing of precast concrete-filled FRP tubes," Journal of Composite for Construction, Vol. 10, No. 4, pp. 345-356.

Ahmad, I., Zhu, Z., and Mirmiran, A., (2008), "Behavior of Short and Deep Beams Made of Concrete Filled Fiber-Reinforced Polymer Tubes" ASCE Journal of Composites for Construction, 6(2):123-132.

Almusallam, T.H., Al-Salloum, Y.A. 2001. "Ultimate strength prediction for RC beams externally strengthened by composite materials". Composites: Part B, 32, 609-619.

Al-Sayed, S.H., Al-Salloum, Y.A., and Almusallam, T.H., (2000), "Performance of glass fiber reinforced plastic bars as a reinforcing material for concrete structures," Journal Composites Part B: Engineering, Vol. 31, Issues 6-7, pp. 555-567.

American Concrete Institute (ACI). (2008), "Guide for the design and construction of externally bonded FRP systems for strengthening concrete structures," ACI-440.2R-08 Committee, Farmington Hills, Mich.

American Concrete Institute, (ACI) Committee 440, (2006), "Guide for the design and construction of concrete reinforced with FRP bars (ACI 440.1R-06)," American Concrete Institute, Farmington Hills, MI, 2006, 44 pp.

ACI Committee 440, (2003), "Guide for the Design and Construction of Concrete Reinforced with FRP Bars (ACI 440.1R-03)," American Concrete Institute, Farmington Hills, MI, 42 pp.

American Concrete Institute (ACI). (2008), "Building code requirements for structural concrete," ACI-318-08, Farmington Hills, Mich.

ASTM. (2008a). "Standard test method for apparent hoop tensile strength of plastic or reinforced plastic pipe by split disk method." *D 2290-08*, West Conshohocken, Pa.

ASTM. (2008b). "Standard test method for tensile properties of plastics." D 638-08, West Conshohocken, Pa.

ASTM. (2009). "Standard specification for deformed and plain carbon steel bars for concrete reinforcement." A615/A615M-09, West Conshohocken, Pa.

Benmokrane, B., and Masmoudi, R., (1996), "FRP C-bar as reinforcing rod for concrete structures," Proceedings of ACMBS 1996, Montreal, QC, Canada, pp. 181-188.

Benmokrane, B.; Chaallal, O.; and Masmoudi, R., (1996), "Flexural Response of Concrete Beams Reinforced with FRP Reinforcing Bars," ACI Structural Journal, Vol. 93, No. 1, , pp. 46-55.

Benmokrane, B., El-Salakawy, E. F., El-Ragaby, A., and Lackey, T., (2006), "Designing and testing of concrete bridge decks reinforced with glass FRP bars," Journal Bridge Engineering, Vol. 11, No. 2, pp. 217–229.

Becque, J., Patnaik A.K. and Rizkalla., S.H., (2003), "Analytical models for concrete confined with FRP tubes", Journal Composites for Construction, ASCE, Vol. 7 No. 1, pp. 1–8.

Bažant, Z. P.; and Cedolin, L., 1991, "Stability of Structures: Elastic, Inelastic, Fracture and Damage Theories," New York: Oxford University Press. pp. 1011.

Bisby, L. A., Dent, J. S., and Green, M. F., (2005), "Comparison of confinement models for fibre-reinforced polymer-wrapped concrete," ACI Structural Journal, Vol. 102, No. 4, pp. 596-604.

Bischoff, P. H., and Paixao, R., (2004), "Tension stiffening and cracking of concrete reinforced with glass fiber reinforced polymer (GFRP) bars," Can. J. Civ. Eng., Vol. 31, No. 4, pp. 579–588.

Bischoff, P. H., (2005), "Reevaluation of Deflection Prediction for Concrete Beams Reinforced with Steel and Fiber Reinforced Polymer Bars," Journal of Structural Engineering, Vol. 131, No. 5, pp. 752-767.

Bischoff, P. H., and Scanlon, A., (2007), "Effective moment of inertia for calculating deflections of concrete members containing steel reinforcement and fiber-reinforced polymer reinforcement," ACI Structural Journal, V. 104, No. 1, pp. 68-75.

Bischoff, P. H., (2007), "Deflection calculation of FRP reinforced concrete beams based on modification to the existing Branson equation," Journal of Composites for Construction, Vol. 11, No. 1, pp. 4-14.

Branson, D. E., (1965), "Instantaneous and time-dependent deflections of simple and continuous reinforced concrete beams." HPR Rep. No. 7, Part 1, Alabama Highway Dept., Bureau of Public Roads, Alabama (Dept. of Civil Engineering and Auburn Research Foundation, Auburn Univ., Aug. 1963).

Branson, D. E., (1977), "Deformation of Concrete Structures, McGraw-Hill, New York, 576 pp.

Canadian Standard Association (CSA). (2002), "Design and construction of building components with fibre-reinforced polymers," CSA-S806-02, CSA Rexdale BD, Toronto.

Burgueno, R., Davol, A., and Seible, F., (1998), ''The carbon shell system for modular bridge components,'' Proc., 2nd Int. Conf. on Composites in Infrastructure (ICCI'98), 341–354.

Canadian Standard Association (CSA), (2004), "Design of concrete structures), CSA standard CAN/CSA-A23.3-04, Rexdale, Ont.

Canadian Standard Association (CSA). (2006), "Canadian Highway bridge design code," CAN/CSA-S6-06, Toronto, Ont.

Carey, S. A., and Harries, K. A., (2005), "Axial behavior and modeling of confined small-, medium-, and large-scale circular sections with carbon fiber-reinforced polymer jackets," ACI Structural Journal, Vol. 102 No.1, pp. 62-72.

Chaallal, O., Hassan, M., and LeBlanc, M., (2006), "Circular columns confined with FRP: experimental versus predictions of models and guidelines," Journal of Composite for Construction, Vol. 10, No. 1, pp. 4-12.

Charkas, H., Rasheed, H.A., and Melhe, H., (2003), "Rigorous procedure for calculating deflections of fiber-reinforced polymer-strengthened reinforced concrete beams," ACI Structural Journal, V. 100, No. 4, pp. 529-539.

Cole B.L., (2005), "Flexural and shear performances of reinforced concrete filled fibre reinforced polymer tubes. M.Sc. Thesis. Queen's University, Kingston, Ont., Canada, p. 201.

Cole, B., and Fam, A., (2006), "Flexural load testing of concrete-filled FRP tubes with longitudinal steel and FRP rebar," Journal of Composites for Construction, Vol. 10, No. 2, pp. 161-171.

Cusson, D., and Paultre, P., (1995), "Stress-strain model for confined high-strength concrete," Journal of Structural Engineering, Vol. 121, No. 3, pp. 468–477.

Davol, A., Burgueno, R., and Seible, F., (2001), "Flexural behaviour of circular concrete filled FRP shells," Journal of Structural Engineering, Vol. 127, No. 7, pp. 810-817.

De Lorenzis, L.; and Tepfers, R., 2003, "Comparative Study of Models on Confinement of Concrete Cylinders with Fibre Reinforced Polymer Composites," Journal of Composites for Construction, ASCE, Vol. 7, No. 3, pp. 219-237.

Demers, M., and Neale, K.W. (1998), "Confinement of reinforced concrete columns with fibre reinforced composite sheets–an experimental study," Can. J. Civ. Eng., Vol. 26, pp. 226-241.

El-Mihilmy, M., and Tedesco, J. W., (2000), "Deflection of reinforced concrete beams strengthened with fiber-reinforced polymer plates," ACI Structural Journal, Vol. 97, No. 5, pp. 679-688.

El-Sayed, A. K., El-Salakawy, E. F., and Benmokrane, B., (2006), "Shear Strength of FRP-Reinforced Concrete Beams without Transverse Reinforcement," ACI Structural Journal, Vol. 103, No. 2, pp. 235- 243.

Fam A. Z., (2000), "Concrete-filled fiber reinforced polymer tubes for axial and flexural structural members," Ph.D. thesis. The University of Manitoba, p. 261.

Fam A. Z., and Rizkalla S., (2001), "Behavior of axially loaded concrete-filled circular fiber reinforced polymer tubes," ACI Structural Journal, Vol. 98, No. 3, pp. 280–9.

Fam, Z. A., and Rizkalla S., (2002), "Flexural behaviour of concrete-filled fiber reinforced polymer circular tubes," Journal of Composites for Construction, (ASCE), Vol. 6, No. 2, pp. 23–32.

Fam, A., Green, R., and Rizkalla, S., (2003a), "Field application of concrete-filled FRP tubes for marine piles," ACI Special Publication, SP-215-9, pp. 161-180.

Fam, A.; Pando, M., Filtz, G., and Rizkalla, S., (2003b), "Precast composite piles for the route 40 bridge in Virginia using concrete-filled FRP tubes," PCI Journal, Vol. 48, No. 3, pp. 32-45.

Fam, A., Flisak, B., and Rizkalla, S. (2003c) "Experimental and Analytical Modeling of Concrete-Filled FRP Tubes Subjected to Combined Bending and Axial Loads" ACI Structural J, Vol. 100, No. 4, pp. 499-509.

Fam, A., and Rizkalla, S., (2003), "Large scale testing and analysis of hybrid concrete /composite tubes for circular beam-column applications," Journal Construction and Building Materials (Elsevier), Vol. 17, pp. 507-516.

Fam, A., and Mandal., (2006), "Prestressed concrete-filled fiber-reinforced polymer circular tubes tested in flexure," PCI Journal, Precast/Prestressed Concrete Institute Vol. 51, No. 4, pp. 42-54.

Fam, A., Cole, B., and Mandal, S., (2007), "Composite tubes as an alternative to steel spirals for concrete members in bending and shear," Journal Construction and Building Materials, Vol. 21, pp. 347–355.

Fam, A., and Cole, B., (2007), "Tests on reinforced CFFT beams of different shear spans," Can. J. Civ. Eng., Vol. 34, No. 3, pp. 311–322.

Fam, A., and Son, J-K., (2008), "Finite element modeling of hollow and concrete-filled fiber composite tubes in flexure: Optimization of partial filling and a design method for poles," Journal Engineering Structures, Vol. 30, pp. 2667–2676.

Fam, A., (2008), "Development of a novel pole using spun-cast concrete into FRP tubes," PCI Journal, Vol. 53, No. 3, pp. 100-113.

Fardis, M.N. and Khalili, H.H., (1981), "Concrete encased in fiber glass-reinforced plastic", ACI Material Journal, Vol. 78, pp. 440–446.

Fardis, M.N. and Khalili, H.H., (1982), "FRP-encased Concrete as a Structural Material," Magazine of Concrete Research, Vol. 34, pp. 191–202.

Gilbert, R. I., (1999), "Deflection calculation for reinforced concrete structures-why we sometimes get it wrong," ACI Structural Journal, Vol. 96, No. 6, pp. 1027-1033.

Gilbert, R. I., (2006), "Discussion of 'Reevaluation of deflection prediction for concrete beams reinforced with steel and fiber reinforced polymer bars' by Peter H. Bischoff." Journal Structural Engineering, Vol. 132, No. 8, pp. 1328–1330.

ISIS Canada, (2001), "Reinforcing concrete structures with fibre reinforced polymers," Design Manual No. 3, ISIS Canada, Winnipeg, Manitoba, Canada.

Jaffry, S. A. D., (2001), "Concrete filled glass fibre reinforced polymer (GFRP) shells under concentric compression," M. Sc. theses, Univ. of Toronto- Toronto, ON, Canada.

Hadi MNS., (2007), "Behaviour of FRP strengthened concrete columns under eccentric compression loading", Journal Composite Structure, Vol. 77, pp. 92–96.

Kaynak, C., Erdiller, E.S., Parans, L., and Senel, F., (2005), "Use of split-disk tests for the process parameters of filament wound epoxy composite tubes," Journal Polymer Testing, Vol. 24, pp. 648-655.

Karbhari, V. M., and Gao, Y., (1997), "Composite jacketed concrete under uniaxial compression-verification of simple design equations," Journal of Materials in Civil Engineering, Vol. 9, No. 4, pp. 185-193.

Karbhari, V.M., Seible, F., Burgueño, R., Davol, A., Wernli, M., and Zhao, L., (2000), "Structural characterization of fiber-reinforced composite short- and medium-span bridge systems," Journal Applied Composite Material, Vol. 7, No. 2-3, pp. 151–182.

Karbhari, V.M., (2004), "Fiber reinforced composite bridge systems-transition from the laboratory to the field," Journal Composite Structures, Vol. 66, pp. 4-16.

Kim, S., (2007), "Behavior of high-strength concrete columns," Doctoral thesis, North Carolina State University, Raleigh, North Carolina.

Kurt, C.E., (1978), "Concrete-filled structural plastic columns". Journal Structural Division, ASCE, Vol. 104, No. 1, pp. 55-63.

Lam, L., and Teng, J. G., (2002), "Strength models for fiber-reinforced plastic-confined concrete," Journal of Structural Engineering, ASCE, Vol. 128, No. 5, pp. 612-623.

Lam, L., and Teng J.G., (2003), "Design-oriented stress–strain model for FRP confined concrete," Journal Construction and Building Materials, Vol. 17, No. 6 & 7, pp. 471-89.

Lam, L., and Teng J.G. (2004), "Ultimate condition of FRP-confined concrete," Journal Composite for Construction, ASCE., Vol. 8, No. 6, pp. 539–48.

Li, J., and Hadi MNS., (2003), "Behaviour of externally confined high strength concrete columns under eccentric loading," Journal Composite Structure, Vol. 62, No. 2, pp. 145–53.

Lyse, I., and Kreidler, C. L., (1932), "Fourth progress report on column tests at Lehigh University." ACI Journal, Vol. 28, pp. 317-46.

Mandal S., (2004), "Prestressed concrete-filled fiber reinforced polymer tubes," M.Sc. Thesis. Queen's University, Kingston, Ont., Canada, p. 204.

Mandal S., and Fam, A., (2006), "Modeling of prestressed concrete-filled circular composite tubes subjected to bending and axial loads," Journal of Composites for Construction, ASCE, Vol. 132, No.3, pp. 449–459.

Mander, J. B., Priestley, N. J. M., and Park, R., (1988), "Theoretical stress-strain model for confined concrete," Journal of Structural Engineering, Vol. 114, No. 8, pp. 1804-1826.

Mandal, S., Hoskin, A., and Fam, A., (2005), "Influence of concrete strength on confinement effectiveness of fiber-reinforced polymer circular jackets," ACI Structural Journal, Vol.102, No.3, pp. 383-392.

Masmoudi, R., Thériault, M., and Benmokrane, B., (1998), "Flexural behaviour of concrete beams reinforced with deformed fibre reinforced plastic reinforcing rods," ACI Structural Journal, Vol. 95, No. 6, pp. 665-76.

Mirmiran, A., and Shahawy, M., (1996), "New concrete-filled hollow FRP composite column," Composites Part B: Engineering, Vol. 27B, No. 3-4, pp. 263-268.

Mirmiran, A., and Shahawy, M., (1997a), "Behavior of concrete columns confined by fiber composites," Journal of Structural Engineering, Vol. 123, No. 5, pp. 583–590.

Mirmiran, A., and Shahawy, M., (1997b), "Dilation characteristics of confined concrete," Journal Mechanics of Cohesive-Frictional Materials, Vol. 2, pp. 237-249.

Mirmiran, A., Shahawy, M., Samaan, M., El Echary, H., Mastrapa, J. C., and Pico, O., (1998), "Effect of column parameters on FRP-confined column," Journal Composite for Construction, Vol. 2, No. 4, pp. 175-185.

Mirmiran, A., Shahawy, M., El Khoury, C. and Naguib, W., (2000), "Large beam-column tests on FRP-filled composite tubes," ACI Structural Journal, Vol. 97, No. 2, pp. 268–276.

Mirmiran, A., Shahawy, M., and Beitleman, T., (2001), "Slenderness limit for hybrid FRP concrete columns," Journal of Composites for Construction, ASCE, Vol. 5, No.1, pp. 26-34.

Mirmiran, A., Shao, Y., and Shahawy, M., (2002), "Analysis and field tests on the performance of composite tubes under pile driving impact," Composite Structures, Vol. 55, No. 2, pp. 127-135.

Mirmiran, A., and Shahawy, M., (2003), "Composite pile: A successful drive," Journal Concrete International, Vol. 25, No. 3, pp.89-94.

Miyauchi, K., Inoue, S., Kuroda, T., and Kobayashi, A., (1999), "Strengthening effects of concrete columns with carbon fiber sheet," Transactions of the Japan Concrete Institute, Vol. 21, pp. 143-150.

Mohamed, H., and Masmoudi, R., (2007), "Behavioral Characteristics for FRP Composites Pole Structures: Nonlinear Finite Element Analysis" CSCE 2007 Annual General Meeting, Yellowknife, Northwest Territories, June 6-9.

Mohamed, H., and Masmoudi, R., (2008a), "Compressive Behaviour of Filament Winded GFRP Tube-Encased Concrete Columns" Fourth International Conference on FRP Composites in Civil Engineering (CICE2008), 22-24 July 2008, Zurich, Switzerland.

Mohamed, H., and Masmoudi, R., (2008b), "Characteristic behaviors of GFRP tube-encased concrete columns" CSCE 2008 Annual General Meeting, Québec, QC, 10 to 13 Jun.

Mohamed, H., and Masmoudi, R., (2008c), "Compressive behaviour of reinforced concrete filled FRP tubes," ACI Special Publications, SP-257-6, pp. 91-108.

Mohamed, H., and Masmoudi, R., (2009a), "Behavior of FRP tubes-encased concrete columns under concentric and eccentric loads," COMPOSITES & POLYCON 2009, American Composites Manufacturers Association, January 15-17, Tampa, FL USA.

Mohamed, H.; and Masmoudi, R., (2009b), "Assessment of Confinement Models for Concrete Confined with FRP Tubes," American Society for Composites and Canadian Association for Composite Structures and Materials, proceedings on CD-Rom, September 15 to 17, University of Delaware in Newark, Delaware, USA.

Mohamed, H., and Masmoudi, R. (2010) "Axial Load Capacity of Reinforced Concrete-Filled FRP Tubes Columns: Experimental versus Theoretical Predictions" Journal of Composites for Construction, ASCE, Vol. 14, No. 2, pp. 1-13.

Mota, C.; Alminar, S.; and Svecova, D., (2006), "Critical review of deflection formulas for FRP-RC members," Journal of Composites for Construction, Vol. 10, No. 3, pp. 183-194.

Naguib, W., and Mirmiran, A., (2002a), "Time-dependent behavior of FRP confined concrete columns," ACI Structural Journal, Vol. 99, No. 2, pp. 142–148.

Naguib, W., and Mirmiran, A., (2002b), "Flexural creep tests and modeling of concrete-filled fiber reinforced polymer tubes," Journal of Composites for Construction, Vol. 6, No. 4, pp. 272-279.

Ozbakkaloglu, T., and Saatcioglu, M., (2004), "Rectangular stress block for high-strength concrete," ACI Structural Journal, Vol. 101, No. 4, pp. 475-483.

Pando M, Fam A, Lesko J, Filz G., (2003), "New bridge piers using load bearing concrete-filled GFRP tubes," Field application of FRP reinforcement: case studies, ACI SP-215-10; pp.181–200.

Park, R., and Paulay, T., (1975), "Reinforced concrete structures," John Wiley & Sons Inc, New York, 769 p.

Parvin1, Z., and Wang, W., (2001), "Behavior of FRP jacketed concrete columns Under Eccentric Loading," Journal of Composites for Construction, Vol. 5, No. 3, pp. 146-152.

Parvathaneni, K., Iyer, L., and Greenwood, M., (1996), "Design and construction of test mooring pile using superprestressing," Proceeding of Advanced Composite Materials in Bridges and Structures, Montreal, pp. 313-324.

Pessiki, S., Harries, K.A., Kestner, J.T., Sause R. and Ricles. J.M., (2001), "Axial behavior of reinforced concrete columns confined with FRP jackets," Journal of Journal Composite for Construction, ASCE, Vol. 5 No. 4, pp. 237–245.

Pilakoutas, K., and Mortazavi, A.A., (1997), "Ductility through external confinement of RC members with FRP," In Non-metallic (FRP) reinforcement for concrete structures. Japan Concrete Institute,1: pp. 225–232.

Qasrawi, Y., and Fam, A., (2008), "Flexural load tests on new spun-cast concrete-filled fiber-reinforced polymer tubular poles," ACI structural Journal, Vol. 105, No. 6, pp. 750-759.

Rafi, M. M., Nadjai, A., and Ali, F., (2006) "Experimental testing of concrete beams reinforced with carbon FRP bars," Journal of Composite Materials, Vol. 41, No. 22, pp. 2657-2673.

Rafi, M. M., and Nadjai, A., (2009) "Evaluation of ACI 440 deflection model for fiber-reinforced polymer reinforced concrete beams and suggested modification," ACI Structural Journal, V. 106, No. 6, pp. 762-771.

Rizkalla, S., and Mufti, A., (2001), "Reinforcing Concrete Structures with fibre Reinforced Polymers," Design Manual No. 3, ISIS Canada, Winnipeg, MB, Canada.

Rizkalla, S., Hassan, T. and Hassan, N., (2003), "Design Recommendations for the use of FRP for Reinforcement and Strengthening of Concrete Structures," Journal of Progress in Structural Engineering and Materials, Vol. 5, No. 1, pp. 16-28.

Rocca, S., Galati, N., and Nanni, A., (2008), "Review of design guidelines for FRP confinement of reinforced concrete columns of noncircular cross sections," Journal Composite for Construction, Vol. 12, No. 1, pp. 80-92.

Saafi, M., Toutanji, H. A., and Li, Z., (1999), ''Behavior of concrete columns confined with fiber reinforced polymer tubes,'' ACI Material Journal, Vol. 96, No. 4, pp. 500–509.

Saatcioglu, M., and Razvi, S. R., (1992), "Strength and ductility of confined concrete," Journal Structural Division, Vol. 118, pp. 1590–1607.

Samaan, M., Mirmiran, A., and Shahawy, M., (1998), ''Model of concrete confined by fiber composites,'' Journal Structural Engineering, Vol. 124 No. 90, pp. 1025–1031.

Seible, F., (1998), ''Innovative designs for pPedestrian bridges,'' Proceeding., Developments in Short and Medium Span Bridge Engineering'98.

Seible, F., V. M. Karbhari, and R. Burgueno., (1999), "King Stormwater Channel and I-5/Gilman Bridges," Structural Engineering International, Vol. 9, No. 4, pp. 250–253.

Shao, Y., and Mirmiran, A., (2004), "Nonlinear cyclic response of laminated glass FRP tubes filled with concrete" Journal Composites Structure, Vol. 65, pp. 91–101.

Shao, Y., and Mirmiran, A., (2005) "Experimental investigation of cyclic behavior of concrete-filled fiber reinforced polymer tubes" Journal of Composites for Construction, Vol. 9, No. 3, pp. 263-273.

Shao, Y., Aval, S., and Mirmiran, A., (2005) "Fiber-element model for cyclic analysis of concrete-filled fiber reinforced polymer tubes" Journal of Structural Engineering, Vol. 131, No. 2, pp. 292-303.

Shawn, A. C., and Kent, A. H., (2005), "Axial behavior and modeling of confined small-medium-, and large-scale circular sections with carbon fiber-reinforced polymer jackets" ACI Structural Journal, Vol. 102, No. 4, pp. 596-604.

Sheikh, S.A., Jaffry, S.A.D., and Cui, C., (2007), "Investigation of glass-fibre-reinforced-polymer shells as formwork and reinforcement for concrete columns." Can. J. Civ. Eng., Vol. 34, No. 3, pp. 389-402.

Son, J-K., and Fam, A., (2008), "Finite element modeling of hollow and concrete-filled fiber composite tubes in flexure: Model development, verification and investigation of tube parameters," Journal Engineering Structures, Vol. 30, pp. 2656–2666.

Spadea, G., Bencardino, F., Swamy, R.N., (2000), "Optimizing the performance characteristics of beams strengthened with bonded CFRP laminates,". Journal Materials & Structures, Vol. 33, pp. 119-26.

Spoelstra, M. R., and Monti, G., (1999), "FRP-Confined Concrete Model," Journal of Composites for Construction, V. 3, No. 3, Aug, pp. 143-150.

Standards Association of Australia (SAA). (2001), "Australian standard for concrete structures," AS 3600-2001, SAA, Sydney, Australia.

Teng, J.G., Chen, J.F., Smith, S.T., Lam, L., (2002), "FRP strengthened RC structures". John Wiley & Sons, New York, NY.

Richart, F. E.; Brandtzaeg, A.; and Brown, R. L., (1929), "The Failure of Plain and Spirally Reinforced Concrete in Compression," Bulletin 190, University of Illinois Engineering Experimental Station, Champaign, Ill.

Thériault M, Neale KW., (2000), "Design equations for axially loaded reinforced concrete columns strengthened with fibre reinforced polymer wraps,". Can. J. Civ. Eng., Vol. 27, 1011–1020, NRC, Canada.

Toutanji, H. A., (1999), "Stress-strain characteristics of concrete columns externally confined with advanced fiber composite sheets," ACI Material Journal, Vol. 96, No. 3, pp. 397–404.

Toutanji, H. A., and Saafi, M., (2000), "Flexural behavior of concrete beams reinforced with glass fiber-reinforced polymer (GFRP) bars," ACI Structural Journal, V. 97, No. 5, pp. 712-719.

Toutanji, H. A., and Deng, Y., (2003), "Deflection and crack-width prediction of concrete beams reinforced with glass FRP rods," Construction and Building Materials, Vol. 17, pp. 69-74.

Yost, J. R.; Gross, S. P.; and Dinehart, D. W., (2003), "Effective moment of inertia for glass fiber-reinforced polymer-reinforced concrete beams," ACI Structural Journal, Vol. 100, No. 6, pp. 732-739.

Yuan, W., and Mirmiran, A., (2001), "Buckling analysis of concrete-filled FRP tubes," International Journal of Structural Stability and Dynamics, Vol. 1, No. 3, pp. 367-383.

Wu, G., Lu, Z.T., and Wu. Z.S., (2006), "Strength and ductility of concrete cylinders confined with FRP composites," Journal Construction and Building Materials, Vol. 20, pp. 134–148.

Wu, G., Lu, Z., and Wu, Z., (2003), "Stress–strain relationship for FRP-confined concrete cylinders." Proc., 6th Int. Symp. on Fibre-Reinforced Polymer (FRP) Reinforcement for Concrete Structures (FRPRCS-6), K. H. Tan, ed., Vol. 1, World Scientific, Singapore, 551–560.

Zhao L, Burgueno R, Rovere HL, Seible F, Karbhari VM., (2004), "Preliminary evaluation of the hybrid tube bridge system," Report No. TR-2000/4, Department of Structural Engineering, University of California, San Diego, CA; p. 1–56.

Zhu, Z., Ahmad, I., and Mirmiran, A., (2005), "Effect of column parameters on axial compression behavior of concrete-filled FRP tube," Advances in Structural Engineering, Vol. 8 No. 4, pp. 443-449.

Zhu, Z., Ahmad, I., and Mirmiran, A., (2006), "Seismic performance of concrete-filled FRP tube columns for bridge substructure," Journal of Composite for Construction, Vol. 11, No. 3, pp. 359-370.

Zhu, Z., Ahmad, I., and Mirmiran, A., (2009), "Fatigue modeling of concrete-filled fiber-reinforced polymer tubes," Journal of Composite for Construction, Vol. 13, No. 6, pp. 582-590.